



HAL
open science

Impact of meso-scale heterogeneities on the mechanical behaviour of concrete : insights from in-situ x-ray tomography and E-FEM modelling

Olga Stamati

► **To cite this version:**

Olga Stamati. Impact of meso-scale heterogeneities on the mechanical behaviour of concrete : insights from in-situ x-ray tomography and E-FEM modelling. Mechanics of materials [physics.class-ph]. Université Grenoble Alpes [2020-..], 2020. English. NNT : 2020GRALI023 . tel-02923399

HAL Id: tel-02923399

<https://theses.hal.science/tel-02923399>

Submitted on 27 Aug 2020

HAL is a multi-disciplinary open access archive for the deposit and dissemination of scientific research documents, whether they are published or not. The documents may come from teaching and research institutions in France or abroad, or from public or private research centers.

L'archive ouverte pluridisciplinaire **HAL**, est destinée au dépôt et à la diffusion de documents scientifiques de niveau recherche, publiés ou non, émanant des établissements d'enseignement et de recherche français ou étrangers, des laboratoires publics ou privés.

THÈSE

Pour obtenir le grade de

DOCTEUR DE L'UNIVERSITÉ GRENOBLE ALPES

Spécialité: **2MGE : Matériaux, Mécanique, Génie Civil, Electrochimie**

Arrêté ministériel: 25 mai 2016

Présentée par

Olga STAMATI

Thèse dirigée par **Yann MALECOT**, Professeur, Université Grenoble Alpes, et
codirigée par **Edward ANDÒ**, Ingénieur de Recherche, CNRS, et
Emmanuel ROUBIN, Maître de Conférences, Université Grenoble Alpes

préparée au sein du **Laboratoire 3SR**
dans **l'École Doctorale I-MEP2 - Ingénierie - Matériaux Mécanique, Environnement, Énergétique, Procédés, Production**

Effet des hétérogénéités sur le comportement mécanique du béton à l'échelle mésoscopique: apports de la micro-tomographie à rayons-x *in-situ* combinée à une modélisation E-FEM

Thèse soutenue publiquement le **12/05/2020**,
devant le jury composé de :

M. Jean-Baptiste COLLIAT

Professeur, Université de Lille, Examineur, Président

M. François HILD

Directeur de Recherche CNRS, ENS Paris-Saclay, Rapporteur

M. Julien YVONNET

Professeur, Université Paris-Est Marne-la-Vallée, Rapporteur

Mme Camille CHATEAU

Chargée de Recherche, École des Ponts ParisTech, Examinatrice

M. Ryan HURLEY

Assistant Professor, Johns Hopkins University, Examineur

M. Yann MALECOT

Professeur, Université Grenoble Alpes, Directeur de thèse

M. Edward ANDÒ

Ingénieur de Recherche, CNRS, Co-encadrant de thèse

M. Emmanuel ROUBIN

MCF, Université Grenoble Alpes, Co-encadrant de thèse



Acknowledgments

This thesis is an outcome of a three years work in Laboratoire 3SR, during which I have been fortunate enough to meet and collaborate with some extraordinary individuals.

First and foremost the supervisors of this project. Eddy, Manu and Yann, simply thanks to each one of you. Thank you for your guidance since I started my master's project with you, 4 years ago, with hardly knowing what a computer terminal is, or having performed any experiment in my life. I have learnt so many things from you during our discussions over meetings, working sessions, lunches, and coffee breaks. Thank you for building a *team* based on mutual respect and not authority. Thank you for your patience, your trust, your interest and above all, thanks for giving me the freedom – that I essentially needed – to drive this PhD on my own way. I'm sure, in years to come, you will continue to be a great source of inspiration to students that are willing to set their own path.

Next, I would like to express my sincere gratitude to all the members of the jury: the president Mr. Jean-Baptiste Colliat, the two reviewers Mr. François Hild and Mr. Julien Yvonnet, and the two examiners Ms. Camille Chateau and Mr. Ryan Hurley for the time they spent reading thoroughly my manuscript and their constructive feedback and remarks. Thank you especially for your understanding regarding the unusual events that occurred between my submission and my video-defense. It was honestly an honour having such a jury and a pleasure to discuss the various aspects of my work. I certainly regret the fact that this discussion did not happen in person.

Thanks in general to all the people in 3SR, who make this lab a really great working environment. Great thanks especially to Pascal Charrier for his fundamental help with the experimental part of this work. Pascal, you should know that 3SR is lucky to have you on board! Many thanks to Denis Caillerie, who although being a retired professor, was always willing to spend time replying to any question and considerably contributed to laying down the basis of the full-field measurements part of this work. Thanks to Alejandro Ortega for the very effective working sessions on the numerical part of this project. Grazie Cino, for always being there to discuss even the silliest of my questions – honestly, your enthusiasm for science is infectious! Thanks Alessandro and Ben for every scientific discussion we had during these 3 years, that were by far precious. Thanks Eleni S., Eleni K. and Alexandra for all the support and the moments we shared. Thanks Kyrillos.

To finish, and since it's important to remember where we come from, many thanks to my professor back in Greece, Nikos Klimis, who I was lucky to meet as an undergraduate student and somehow is one of the principal reasons I ended up being here. Finally, without any need of deliberation and only as a small gesture of appreciation, deep thanks to my family.

Abstract in English

This doctoral thesis investigates the impact of the meso-scale heterogeneities of concrete (aggregates and macro-pores) on its macroscopic mechanical response. A combined numerical and experimental approach is adopted to study the progressive evolution of the 3D fracturing processes of micro-concrete specimens under uniaxial tension, uniaxial compression and triaxial compression.

Part of the originality lies in the exploration of multiple loading paths on concrete samples of realistic composition (including cement, sand, aggregates and water) and in the *in-situ* nature of the experiments conducted. The experimental campaign is performed inside an x-ray scanner, which allows the internal structure of the material to be non-destructively captured and its evolution from the intact (before loading) until the damaged (after unloading) state to be followed and quantified. The 3D images coming from the scans are first analysed in order to quantitatively describe the morphology of the meso-structure (aggregates, mortar matrix and macro-pores). A timeseries analysis of the set of images coming from each *in-situ* test follows, which allows for the measurement of the 3D kinematic fields (displacement and strain fields) throughout the experiments.

On the numerical side, the identified morphologies coming from the intact scans are given as an input to a FE meso-model with enhanced discontinuities. The originality of the numerical simulations comes from their 3D nature and the consideration of the actual meso-structure of the micro-concrete specimens, based on the segmentation of the three phases of the material. After a calibration of the model in uniaxial tension, its predictive ability is challenged under different loading paths in compression.

An extensive comparison is presented between experimental and numerical observations, in terms of macroscopic responses, displacement fields, fracturing processes and failure patterns. The typical asymmetric behaviour of concrete in tension and compression, as well as the increase of strength and ductility with the increase of confinement are sufficiently captured numerically. Starting from an x-ray scan, it is shown that the model is able to satisfactorily reproduce some of the basic characteristic features of the failure modes observed experimentally for the different loading paths studied.

While validating the numerical results and through a combination of numerical and experimental observations, the significant impact of the meso-scale heterogeneities on the local failure mechanisms is revealed. It is shown that, for the studied material, the shape and location of the largest aggregates and macro-pores are essentially driving the fracture patterns under simple tension, simple compression, and triaxial compression. The good correspondence between experiments and model strongly suggests that the explicit representation of these heterogeneities is the key feature that allows the predictive power of the model. A further insight into the impact of the meso-structure is obtained by investigating virtual concrete morphologies, generated by modifying the real meso-structures coming from the scans.

Résumé en Français

Ce travail de thèse s'intéresse à l'effet des hétérogénéités du béton à l'échelle mésoscopique (granulats et porosités d'air occlus) sur son comportement mécanique à l'échelle macroscopique. Pour ce faire, les processus de déformation et de fissuration d'échantillons de micro-béton soumis à différentes sollicitations (traction, compression simple ou compression confinée) sont analysés en comparant des résultats expérimentaux de mesures de champs 3D avec des simulations d'échantillons de béton numérique.

Outre le matériau étudié, représentatif d'un béton, l'originalité des essais expérimentaux vient de leur caractère "in situ" et de la multi-axialité des chargements étudiés. Les essais sont en effet réalisés dans un tomographe à rayons-x, donnant ainsi accès à la structure tridimensionnelle du matériau (de façon non-destructive) tout au long de l'expérience, de l'état initial intact à la rupture. Les images tridimensionnelles sont également utilisées pour identifier et quantifier la morphologie de la mésostructure dont les phases d'intérêt sont les granulats, la macro-porosité et le mortier. De plus, la série d'images obtenue permet de mesurer des champs cinématiques tridimensionnels (déplacement et déformation), à différents stades du chargement, pour chacun des essais.

Ces mesures permettent d'alimenter un modèle Éléments Finis mésoscopique en lui fournissant une mésostructure réaliste et en permettant de calibrer ses paramètres. Il est choisi ici d'identifier le modèle à l'aide des essais de traction simple et d'analyser la prédiction de ce dernier pour les autres types de sollicitations réalisées. L'originalité des simulations numériques vient de leur caractère tridimensionnel et de la prise en compte d'une "vraie" mésostructure de micro-béton basée sur une segmentation tri-phasique du matériau (macro-pores, granulats et mortier).

Une comparaison des résultats expérimentaux et numériques est proposée en confrontant les réponses macroscopiques, les champs cinématiques locaux ainsi que les faciès de fissurations. L'asymétrie des résistances du béton en traction et en compression est bien retrouvée par le modèle ainsi que l'augmentation de la ductilité de la réponse avec la pression de confinement. En outre, le modèle est capable de reproduire de façon satisfaisante les modes de rupture des différents chargements et états de confinement étudiés.

L'analyse de la pertinence des prédictions du modèle mésoscopique permet de confirmer l'importance primordiale qu'une représentation réaliste des hétérogénéités a sur le développement des mécanismes de rupture locaux. Nous montrons que c'est principalement la forme et la position des plus grosses hétérogénéités (granulats et macropores) qui vont influencer le processus de fissuration du béton étudié, quelle que soit la sollicitation. Les prédictions faites avec le modèle nous encouragent à croire que la représentation explicite de la morphologie réelle est l'ingrédient clé de la bonne concordance observée, entre expérience et modélisation. A ce sujet, une étude numérique sur l'impact des formes sur le comportement est finalement conduite.

Contents

Contents	8
1 Introduction	11
1.1 Background and synthesis of the main objective of this thesis	11
1.2 Structure of this thesis	20
2 Experimental campaign	23
2.1 Studied material: scale and morphology	23
2.1.1 Characteristic sizes of the specimens	24
2.1.2 Specimen preparation	25
2.2 X-ray scanning of micro-concrete	27
2.2.1 Brief introduction to x-ray tomography	27
2.2.2 X-ray facility at Laboratoire 3SR	30
2.3 Description of the apparatus	32
2.3.1 Apparatus for uniaxial tension	34
2.3.2 Apparatus for uniaxial compression	35
2.3.3 Apparatus for triaxial compression	36
2.4 Testing procedure	38
2.4.1 Test set-up	38
2.4.2 Description of an <i>in-situ</i> test	40
2.4.3 Calibration of the apparatus	42
2.5 <i>In-situ</i> experiments conducted	43
2.5.1 Uniaxial tension	44
2.5.2 Uniaxial compression	45
2.5.3 Triaxial compression	47
2.5.4 Summary of macroscopic mechanical responses	50
2.6 Concluding remarks	50
3 Identifying the micro-structure and following its evolution	53
3.1 Extraction of the morphology	54
3.1.1 Post-reconstruction steps	55
3.1.2 Phase identification	57
3.1.3 Morphological measurements	61
3.1.4 Validation of the segmentation procedure	63
3.2 Methodology for following the micro-structural evolution	65
3.2.1 Basic principles of Digital Volume Correlation (DVC)	65
3.2.2 Combined regularly-spaced and discrete local DVC techniques	73
3.2.3 Estimation of measurements uncertainty	77
3.3 3D kinematic fields and fracture patterns from <i>in-situ</i> experiments	82

3.3.1	Uniaxial tension	83
3.3.2	Uniaxial compression	85
3.3.3	Triaxial compression	90
3.4	Concluding remarks	96
4	Numerical framework	97
4.1	FE meso-model description	98
4.1.1	Local kinematics enhancement	99
4.1.2	Phenomenology and resolution scheme	101
4.2	Application to micro-concrete	103
4.2.1	Accounting for the morphology imaged through x-rays	104
4.2.2	Application of boundary conditions	107
4.2.3	Calibration of material parameters	108
4.2.4	Numerical prediction	112
4.3	Concluding remarks	118
5	Link between experimental and numerical observations	119
5.1	Macroscopic responses comparison	120
5.2	Fracturing process and failure patterns comparison	125
5.2.1	Uniaxial tension	126
5.2.2	Uniaxial compression	131
5.2.3	Triaxial compression	136
5.3	Further insights into the role of morphology	144
5.3.1	Influence of macro-pores	144
5.3.2	Modelling heterogeneities as spheres	149
5.4	Concluding remarks	154
6	Conclusions and Perspectives	157
6.1	Summary	157
6.2	Perspectives	160
6.2.1	Elastic properties identification based on experimental kinematic fields	160
6.2.2	Numerical meso-model	166
6.3	Conclusions	169
	Bibliography	171
	Appendices	182
A	Technical drawings of the 7075 T6 aluminium alloy cell	183
B	Mechanical tests outside of the x-ray cabin	185

Chapter 1

Introduction

This chapter introduces the subject area of this doctoral work, putting it into historical perspective, as well as briefly describing recent work in the most closely related fields. After having laid down the historical context and the synthesis of the main objective of this thesis, the structure of the work itself is then introduced in Section 1.2.

1.1 Background and synthesis of the main objective of this thesis

Composite nature of concrete

Composite materials, such as cementitious ones, consist of several constituent phases of significantly different properties, that when combined, produce a material with *emergent* characteristics, different from its individual components. When it comes to investigate the mechanical behaviour of such materials, one of the fundamental challenges is to quantitatively relate information obtained at a finer scale to the emergent macroscopic properties. The concept of the observation scale and the role of heterogeneities become thus of major importance.

Concrete is a composite cementitious material widely used in the world, with its current worldwide consumption estimated in the order of 17 billion metric tonnes per year [Ashby, 2012]. Even though the environmental impact of concrete is significant (contributing 8% to the worldwide emissions of CO₂), it is still essential for some sensitive infrastructures, such as dams, nuclear power plants, wind turbine foundations, *etc.* Considering the fact that the development of modern cement-based materials dates back to the nineteenth century, the mechanical behaviour of concrete has been investigated over decades. However, as the Latin word *concretus* (growing together) suggests, due to its highly heterogeneous nature, its failure mechanisms are complex phenomena and still constitute a very active area of research.

The quasi-brittle behaviour of concrete observed at the macro-scale is strongly influenced by the morphology and the properties of its material constituents and their mutual interactions over a large range of different length scales: from nano- to meso-scale, referring to nm (hydrated cement scale) and cm (largest aggregates scale), respectively [Mehta, 1986, Weerheijm, 2013, Basheer *et al.*, 2005]. Research is, therefore, increasingly redirected towards both an experimental and a numerical investigation of concrete at different range of scales, with the selection of an appropriate level of investigation depending on the characteristics of the response sought. Provided that many details on the length

scales of concrete can be found in the literature (see for instance [Mehta, 1986, Garboczi et Bentz, 1993, Huet, 1993]), only a brief discussion is made herein.

The macro-scale is the typical scale of the analysis of structures, whereby concrete is considered as a homogeneous material. At the meso-scale, concrete can be viewed as a three phase geomaterial, constituted of aggregates and macro-pores embedded within a mortar matrix (mix of cement paste and fine sand). Macro-porosity refers to the pores being much larger than the capillary voids (about 10 nm). It corresponds to both the entrained air voids (usually ranging from 50 to 500 μm) and the entrapped air voids, which can be almost as large as the largest aggregates, depending on the concrete workability. At a lower level of observation, the so-called micro-scale, the heterogeneous structure is composed of cement matrix and micro-pores, both giving the subscale representation of the mortar matrix. At this scale, the crystals of the hydrated cement paste are mainly investigated, practically how they grow and interact (see for instance [Ioannidou *et al.*, 2014]). A system of capillary pores with a size of 0.02 to 10 μm exists, together with gel pores in the cement paste with size of 50 nm. Micro-pores play an important part in desiccation, shrinkage and creep, whereas macro-pores are more influential in determining the strength and fracture patterns of the material [Mehta, 1986].

Concrete meso-models

[Zaitsev et Wittmann, 1981] were the first to consider the composite concrete structure as a multi-level hierarchical system by introducing four different characteristic levels: macro-level, meso-level, micro-level and nano-level. Among these observation scales, the meso-scale has been found the most useful for studying the influence of the heterogeneities on the macroscopic behaviour ([Kim et Al-Rub, 2011, Wriggers et Moftah, 2006, Wang *et al.*, 2015, Häfner *et al.*, 2006]) and is also the scale at which this doctoral work focuses.

More specifically, at the meso-scale the presence of both aggregates and macro-pores in the concrete mix, with various sizes and shapes, results to an heterogeneous stress field, even under uniform loading, leading to stress concentrations and initial micro-cracking around the weakest regions (usually the interfaces). With increasing load, these micro-cracks grow and coalesce into one (or several) critical macro-crack(s) resulting to the macroscopic failure of the material. Consequently, the meso-scale is a scale of interest to study the local failure mechanisms of concrete and therefore, in recent years, many numerical meso-models have been developed.

These meso-models involve an explicit representation of the meso-structure and are built upon a local behaviour of the different phases. Their strength originates exactly from this physical structural effect, with the degradation modelling kept simple and yet producing complex macroscopic mechanisms. Meso-models can be used to reveal the influence of the meso-scale heterogeneities on the global response by easily changing global descriptors, such as phase volume fractions, aggregates and macro-pores size distributions, aggregates shape, or the mechanical properties of each phase, being an effective and practical alternative to experimental studies. A multi-scale approach could also be achieved by using the meso-model as a constitutive law at the macro-scale [Zaitsev, 1985].

After the first “numerical concrete” meso-model was introduced by [Zaitsev et Wittmann, 1981] (see Fig. 1.1), over the years a large number of meso-models for concrete have been developed, based on different theories (fracture mechanics, damage mechanics, plasticity theory, *etc*), that fit within the context of continuum models (using the Finite Element Method), discrete models (using for example the Discrete Element Method) or a combi-

nation of them, by introducing discontinuities within continuum models. A brief review of some notable examples is given in the following.

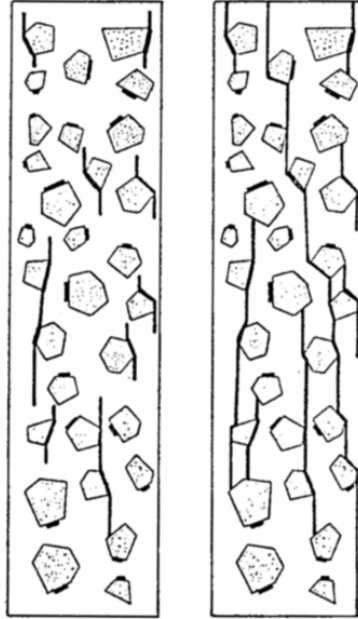


Figure 1.1: First “numerical concrete” meso-model by Zaitsev and Wittmann: crack patterns for two different load levels in normal concrete predicted by a “computer experiment” (extracted from [Zaitsev et Wittmann, 1981])

[Bažant *et al.*, 1990] have performed mesoscopic studies of concrete using a truss model to realistically simulate the spread of cracking and its localisation. [Schlangen et Van Mier, 1992] were the first to use a lattice model simulation of typical failure mechanism and crack face bridging in concrete. A 3D lattice model was later developed by [Lilliu et van Mier, 2003] to study the fracture process in concrete. A 2D DEM based particle model was used by [Azevedo *et al.*, 2008] to study fracture process in concrete under uniaxial tension and compression. [Poinard *et al.*, 2011] used a model that combined the lattice system of cohesive interactions with the classical DEM contact interactions to reproduce concrete behavior under high confinement. 3D DEM models were also used by [Suchorzewski *et al.*, 2017] and [Nitka et Tejchman, 2018] to investigate concrete fracture at the mesoscopic level.

A 2D FE meso-model was used by [Tejchman *et al.*, 2010] to investigate the fracture process zone of a notched concrete beam. A 3D FE meso-model was used by [Wriggers et Moftah, 2006] for unconfined compression tests and by [Dupray *et al.*, 2009] to simulate the behavior of concrete under triaxial compression at high mean stress. A 3D FE meso-model was also used by [Huang *et al.*, 2015] to understand the fracture behaviour of concrete under simple tension and compression.

More recently, FE models enhanced with discontinuities (see Fig. 1.2) have been also developed to study the fracture mechanisms of concrete at the meso-scale, see for example [Benkemoun *et al.*, 2010] and [Roubin *et al.*, 2015b]. The latter category, and particularly a meso-model that fits within the context of the Embedded Finite Element Method (E-FEM) is the approach followed in this work. Please note that a description of the main ingredients of the model is given in Chapter 4.

No matter the selected approach, two main aspects have to be considered in these models; the morphological description of the meso-structure and how to account for the

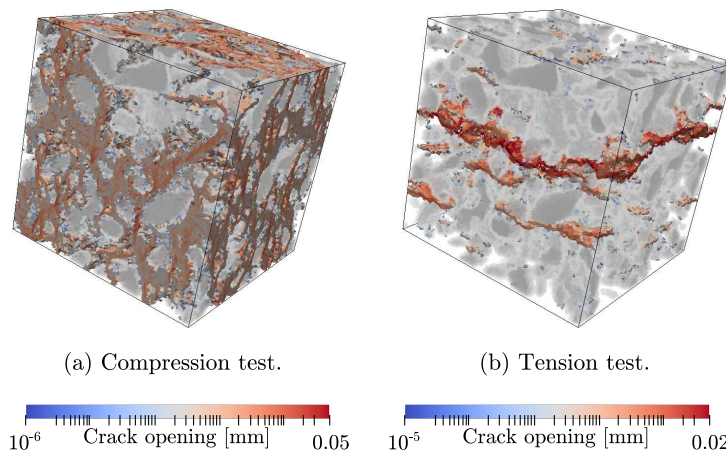


Figure 1.2: Macroscopic crack paths for simple tension and compression tests predicted by a FE meso-model enhanced with discontinuities (extracted from [Roubin *et al.*, 2015b])

quasi-brittle behaviour of the material. The way the latter is addressed among the different approaches is discussed in Chapter 4. The former aspect, concerning the morphological description of the meso-structure is discussed in the following.

Morphological description of the meso-structure

In meso-models, the most common method to address the morphological description of the meso-structure is the generation of artificial morphologies in a direct or an indirect way. An indirect way means that the different phases are not explicitly taken into account, but rather the heterogeneous material properties are modelled as spatially-varying random fields. Such approaches have been used in FE meso-models [Yang *et al.*, 2009] or lattice meso-models [Leite *et al.*, 2004].

However, the most typical approach in meso-scale modelling is the use of morphological models to explicitly account for the different phases. Several methods for packing ideal geometrical objects can be found in the literature with different optimisation procedures and geometrical shapes (see for example [Wittmann *et al.*, 1985, Bažant *et al.*, 1990, Schlangen et Van Mier, 1992, Wang *et al.*, 1999, Wriggers et Moftah, 2006]). In such approaches, aggregates of different shapes and sizes are artificially generated and randomly distributed in the numerical concrete sample, with the mortar matrix filling the space between the particles. Usually, the different realisations of the random geometrical configurations satisfy basic statistical characteristics of the real material and the size distribution of aggregates follows a given grading curve. As an illustration, a sphere packing of aggregates using the collective rearrangement algorithm [Bezrukov *et al.*, 2002] is shown in Fig. 1.3a. Recently as an alternative, [Roubin *et al.*, 2015a] proposed a morphological model based on excursion sets of correlated random fields that produces complex randomly shaped morphologies, which are more representative of the actual irregular aggregates found in the meso-structure of concrete (see Fig. 1.3b).

However, all of the aforementioned approaches actually assume *a priori* the morphology, facing thus limitations regarding the representativeness of the generated meso-structures, which can have important consequences on the mechanical response of the model. Often a volume fraction can be targeted, but global descriptors such as surface areas, mean curvature or topology can be very far from realistic. Moreover, quantita-

tive validation of these models with experimental results is relatively hard. To overcome this, in recent years, real meso-morphologies are obtained in 2D (through cameras or microscopes) or in 3D (through magnetic resonance imaging (MRI) or x-ray and neutron tomography) by taking advantage of recent advances in non-destructive imaging combined with image analysis. This is the approach followed in this study, in particular the use of x-ray tomography in order to obtain a realistic representation of concrete's meso-structure as described below.

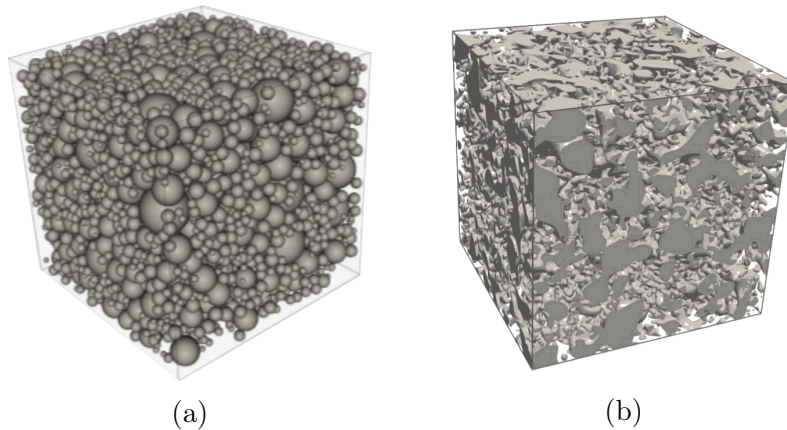


Figure 1.3: Artificial meso-structures of cementitious materials: (a) sphere packing of aggregates (extracted from [Vallade, 2016b]), (b) randomly shaped aggregates based on excursion sets of correlated random fields (extracted from [Roubin *et al.*, 2015a])

Concrete meso-structure imaged through x-rays

X-ray tomography is a non-destructive imaging technique which is based on the ability of x-rays to penetrate through matter (undergoing an attenuation) that permits the visualisation of the internal micro-structure of the material. Although the origins of x-ray tomography sit firmly in the medical sphere dating back in the 1960s, it is a technique well adapted in the field of materials science and since its early use in this domain (see [Baruchel *et al.*, 2000, Salvo *et al.*, 2003]) it has become a very powerful tool.

Very briefly, x-ray tomography is a method of reconstructing a 3D field of x-ray attenuation coefficients within an object by assembling 2D radiographic images (projections) taken at different angles. These attenuation coefficients vary according to the energy spectrum of the incident x-rays and the material elemental composition (especially the atomic number), as well as the density of the investigated object. It is exactly this variation (in attenuation) that makes x-rays so suitable for studying the internal structure of multiphase heterogeneous materials, such as concrete at the meso-scale. An extensive review of more than 400 studies that applied x-ray tomography to cementitious materials can be found in the recent paper of [Brisard *et al.*, 2020]. A description of the most important features of x-ray tomography as they apply in this work is given in Chapter 2. In what follows, a short review of previous works that used x-ray tomography to study concrete at the meso-scale is given.

To start with, various studies extracted valuable quantitative information regarding the internal meso-structure of concrete. [Garboczi, 2002] used 3D tomographic images of concrete to perform a mathematical shape analysis of aggregates using spherical harmonic functions. [Masad, 2004] used x-ray tomography to quantify the internal structure of

asphalt mixes in terms of air void distribution and aggregate packing. [Gallucci *et al.*, 2007] employed x-ray tomography to characterise the pore structure in cement paste, while [Lu *et al.*, 2006] and [Cnudde *et al.*, 2009] to characterize the pore structure in concrete.

X-ray tomography has been also applied in a number of studies to investigate the internal damaged micro-structure of concrete. For instance, it was used by [Wang *et al.*, 2003] to quantify the damage parameters of asphalt concrete specimens and by [Schlangen, 2008] to determine the level of damage by measuring the crack tortuosity. In a different study [Suzuki *et al.*, 2010] estimated the damage in concrete samples extracted from a canal wall by means of crack distribution.

Considering the rich information provided by the tomographic data, the link between x-ray tomography and meso-models has received increasing attention. As a first step, and related to the previous discussion concerning the representativeness of the meso-structure, realistic morphologies coming from x-ray scans have been introduced to numerical concrete meso-models. For instance, [Man et van Mier, 2008] extracted the aggregate structure from concrete x-ray images and introduced it to a 3D lattice model, in order to study the fracture of concrete subjected to three-point bending. [Wang *et al.*, 2014] performed 3D FE simulations of asphalt concrete mixtures based on the micro-structures obtained from x-ray images. [Ren *et al.*, 2015] developed a three-phase (aggregates, voids, cement paste) 2D meso-scale FE model based on x-ray concrete images to simulate crack propagation under uniaxial tension (see Fig. 1.4).

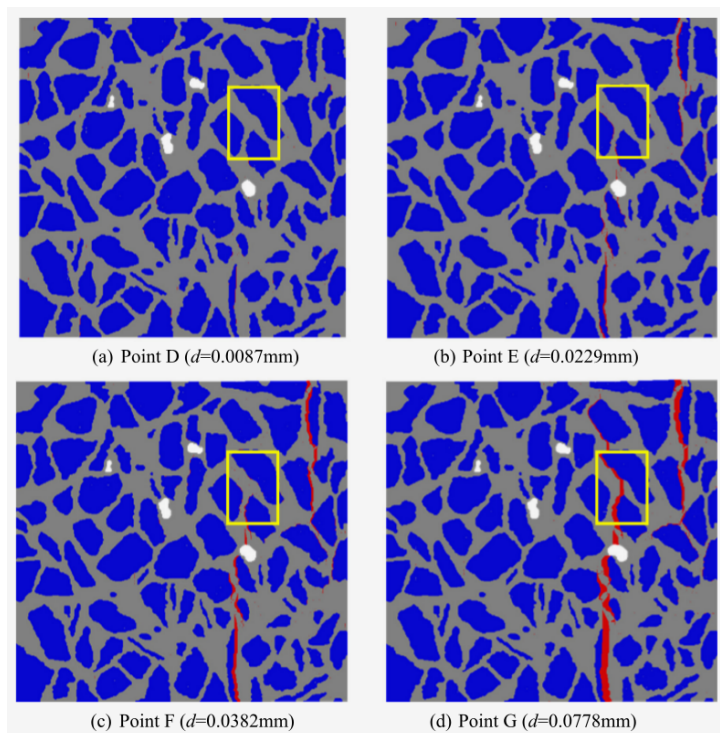


Figure 1.4: Macro-crack propagation during a 2D uniaxial tensile FE simulation based on realistic morphology coming from an x-ray scan (extracted from [Ren *et al.*, 2015])

Meanwhile, by performing several x-ray scans of a single sample, the evolution of various phenomena was non-destructively investigated, such as the characterisation of damage induced by leaching in mortar [Burlion *et al.*, 2006] or a sulfate attack in cement paste [Stock *et al.*, 2002]. In the same context, *ex-situ* mechanical tests were conducted to investigate the fracture process of concrete under triaxial compression [Poinard *et al.*,

2012] (see Fig.1.5) or uniaxial cyclic loading [Obara *et al.*, 2016]. It should be mentioned, however, that during an *ex-situ* test, the specimen needs to be unloaded and then removed from the loading frame in order to be scanned.

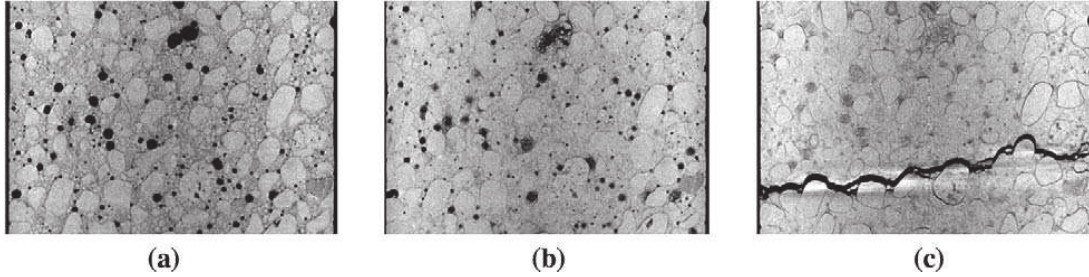


Figure 1.5: Vertical slices extracted from the tomographic scans during an *ex-situ* triaxial compression test on a cylindrical (7 cm in diameter and 14 cm in height) concrete specimen: (a) undamaged, (b) after the hydrostatic cycle at 650 MPa confinement and (c) after the failure (extracted from [Poinard *et al.*, 2012])

***In-situ* mechanical tests in concrete**

Unlike an *ex-situ* test, one of the great advantages that x-ray tomography provides is the ability to perform *in-situ* mechanical tests, which are the type of experiments conducted in this work. During such experiments the internal micro-structure of the sample is scanned at several loading stages, revealing important information about the actual evolution of the fracturing process. However, due to the supplementary constraints imposed by the use of x-rays, these *in-situ* tests differ principally from the widely used standard ones, both in terms of the specimen size (which has to be significantly smaller) and in terms of the instrumentation, since specific experimental facilities are required.

Consequently, studies which involve *in-situ* experiments in cement-based materials are less common in literature. Notable examples are [Landis *et al.*, 1999] and [Landis *et al.*, 2007] who performed *in-situ* compression tests on small mortar specimens to study the internal crack growth (through the evolution of the porosity) during loading. Recently, [Hurley et Pagan, 2019] presented a combination of *in-situ* x-ray tomography and 3D x-ray diffraction to study the fracture network growth and the evolution of aggregate stress tensors of a 1 mm³ concrete cube (made of portland cement and single-crystal quartz aggregates) during a uniaxial compression test. A 3D view of the sample showing the voids and fractures, together with aggregates whose measured axial stress component exhibits a decrease greater than 10 MPa between two loading steps is shown in Fig. 1.6.

Apart from the experimental investigation of the fracturing process of concrete, *in-situ* mechanical tests offer the opportunity for a direct link between experiments and simulations. As a first step towards this direction, the morphology obtained from the intact (before loading) x-ray scan can be introduced to a numerical meso-model. Recently for example, [Yu *et al.*, 2018] studied the fracture evolution of a 40 mm³ concrete cube under uniaxial compression, involving a qualitative comparison between the prediction of a three-phase 3D FE meso-model based on the intact x-ray image and direct observations on the x-ray images obtained during the *in-situ* test.

This study was limited, though, to a qualitative comparison between experimental and numerical observations. However, one of the key aspects of an *in-situ* test is that the series of 3D images, when coupled with specific full-field measurement techniques, provide

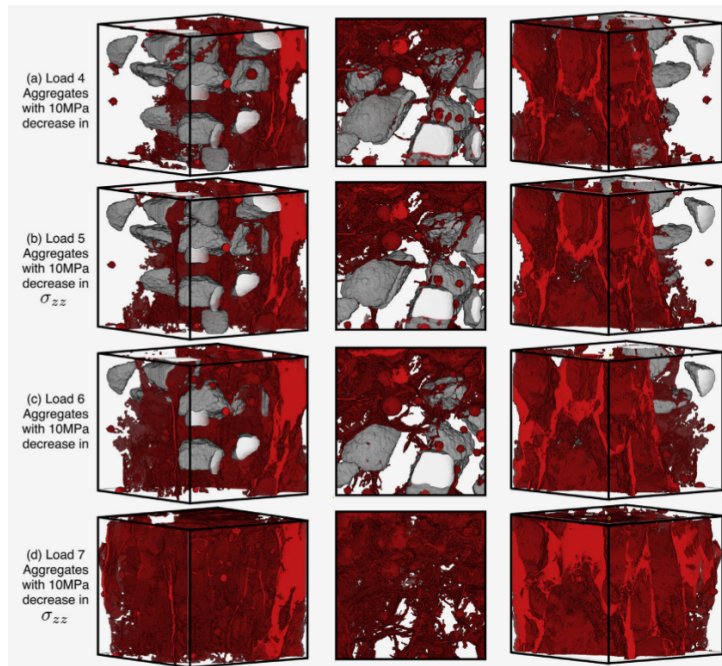


Figure 1.6: 3D views showing voids and fractures, together with aggregates with a decrease (more compression) in the measured σ_{zz} more than 10 MPa during an *in-situ* uniaxial compression test on a 1 mm^3 concrete cube (extracted from [Hurley et Pagan, 2019])

direct access to experimental kinematic fields. Among the existing full-field measurement techniques, Digital Volume Correlation (DVC) has undergone a rapid development in the last decades and is also the technique adopted in this work. Please note that a description of the most important features of the DVC technique applied in this study is given in Chapter 3. It is briefly mentioned here that DVC allows the measurement of 3D displacement fields between two acquired images, offering unprecedented advances in the micro-scale understanding of the mechanical behaviour of materials.

For example, the DVC technique was used in [Hild *et al.*, 2013] to analyse the damage mechanism during an *ex-situ* drying test of a cementitious composite. Recently, [Chateau *et al.*, 2018] presented an image subtraction technique based on DVC to detect and extract the complex network of micro-cracks that progressively developed in a lightweight concrete sample submitted to uniaxial compression. A 3D view through the detected crack network at specific loading steps is shown in Fig. 1.7.

It is worth mentioning that only experimental observations of the localisation process were involved in these studies. However, the experimental kinematic fields can be directly compared to the predictions of a numerical model that is built based on the realistic meso-structure coming from the intact x-ray scan bridging, thus, the gap between experiments and simulations. Due to the advanced experimental and numerical techniques required, studies on the fracturing process of cementitious materials that involve a direct comparison between model and experiments are still rare in literature.

A notable example is [Nguyen *et al.*, 2016] who studied the initiation and propagation of the complex 3D cracking network on lightweight concrete samples under simple compression through a direct quantitative comparison between model and experiment. The prediction of a continuum mechanics-phase field model based on the micro-structure obtained from the intact x-ray scan was compared to the experimental crack paths obtained

from a DVC analysis of the *in-situ* data (see Fig. 1.8). Another recent example comes from [Yang *et al.*, 2017] who investigated the initiation and propagation of damage in a concrete cube during a Brazilian test. The x-ray image of the scan before loading was introduced to a 3D FE meso-model and the numerical predictions were compared to the DVC results obtained from the *in-situ* experiment. In both studies, valuable information concerning the impact of the underlying meso-structure on the fracturing process was obtained.

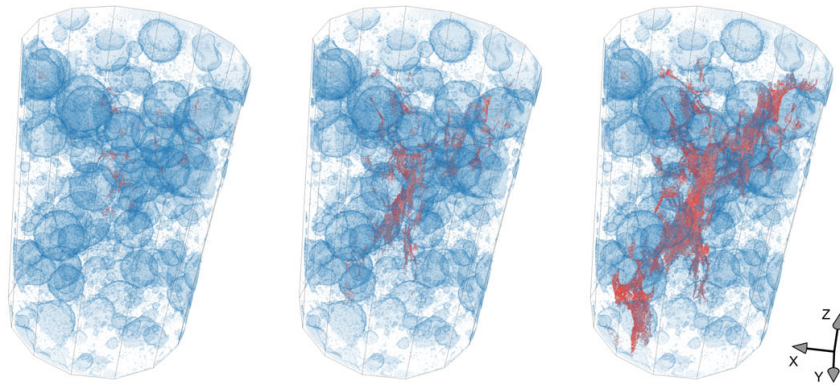


Figure 1.7: 3D views of the crack network (red) propagation through the segmented porosity (blue) at discrete loading steps during an *in-situ* uniaxial compression test on lightweight concrete (extracted from [Chateau *et al.*, 2018])

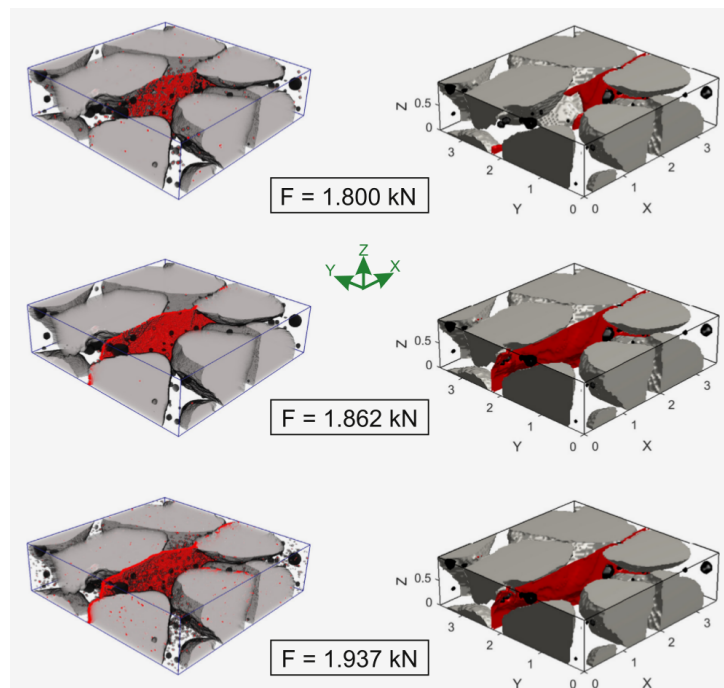


Figure 1.8: Comparison between experimental crack (left) obtained from microtomography and from phase field method (right) of a lightweight concrete sample subjected to simple compression for different loading steps (extracted from [Nguyen *et al.*, 2016])

Synthesis of the main objective of this thesis

To summarise, the aforementioned studies do not intend to extensively cover the entire subject area of this doctoral work, but rather to lay down the historical context by briefly describing recent works in the most closely related fields. This short bibliographic review has shown that despite the significant progress made over the years, the fracture processes of concrete still constitute a very active area of research. It is understood that the mechanical behaviour of concrete is governed by its heterogeneity, with the meso-scale found to be the key scale of interest to study the impact of the local failure mechanisms on the macroscopic response. The literature review reveals that relatively few recent works have taken into account the real meso-structure of the material. Combined numerical and experimental studies of the fracturing process of concrete samples with realistic composition are still very rare in literature. The few available works focus on the mechanical response under simple compression or indirect tension.

There are no clues (at least to the author's knowledge) of previous studies that investigated both numerically and experimentally the progressive evolution of the 3D fracturing process of concrete under multiaxial loading. This is especially true for concrete samples of realistic composition subjected to uniaxial tension and triaxial compression. On one hand, direct tensile tests provide direct insights into the fundamental mechanisms of concrete fracture and serve as a way for interpreting macroscopic failure under more complicated loading conditions, such as confined or unconfined compression tests. On the other hand, the confined behaviour of concrete is important when it comes to investigate the mechanical response of the material in real cases, which are encountered in structural applications involving massive constructions or prestressed concrete structures, like the ones mentioned in the beginning of this chapter.

The studies mentioned in this section have paved the way for the principal inspiration of this thesis, which is to shed some light on the impact of the meso-scale heterogeneities of concrete on its fracturing process under a number of different loading paths. This is achieved by studying concrete samples of realistic composition, which includes cement, sand, aggregates and water, and not only mortar or cement paste, as it is usually done. The proposed methodology consists, on one hand, in performing *in-situ* mechanical tests which coupled with DVC allow an experimental quantitative characterisation of the mechanical behaviour and the fracturing process of the material. On the other hand, the identified morphologies coming from the intact x-rays scans are given as an input to a FE meso-model with enhanced discontinuities, so that a direct quantitative comparison between experimental and numerical observations is made. Part of the novelty that this work brings is that the proposed experimental-numerical approach is applied not only to uniaxial tension or compression, but to a combination of different loading paths, including for the first time triaxial compression.

1.2 Structure of this thesis

This doctoral work aims to provide a further insight on the impact of the meso-scale heterogeneities of concrete on its macroscopic mechanical response. The mechanical behaviour of small specimens of concrete of realistic composition (including cement, sand, aggregates and water) is studied under: uniaxial tension, uniaxial compression, and triaxial compression. The methodology proposed herein is a combined experimental-numerical strategy: experimental observations coming from x-ray *in-situ* mechanical tests coupled

with full-field measurements are compared to predictions of a FE meso-model with enhanced discontinuities which is built based on the morphologies coming from the x-ray scans of the intact samples.

The thesis is divided into four main chapters as follows:

Chapter 2: Experimental campaign

Chapter 2 details the experimental work conducted in this study, starting by introducing the studied material and the factors that determine the scale and morphology of the samples tested. Section 2.2 presents a brief introduction to the most important features of x-ray tomography, as they apply to this work. A description of the Laboratoire 3SR x-ray tomograph follows, providing technical details of the source and acquisition system used in this study. The developed experimental set-up compatible with the x-ray scanner of Laboratoire 3SR is then presented in Section 2.3, with a detailed description of the specific apparatus used for each type of test. The testing procedure followed for each test is described in Section 2.4, along with the calibration of the apparatus used for each test. The conducted experimental campaign is described in Section 2.5, with 8 in total *in-situ* tests performed: two uniaxial tension tests, three uniaxial compression tests and three triaxial compression tests at 5 MPa, 10 MPa and 15 MPa confining pressures. A description of each test is given, together with a discussion of the macroscopic responses.

Chapter 3: Identifying the micro-structure and following its evolution

Chapter 3 details the analysis of the 3D images coming from the *in-situ* mechanical tests described in Chapter 2. Section 3.1 focuses on the analysis of a *single* 3D image, with the objective of identifying the imaged morphology (aggregates, mortar matrix and macro-pores) and, in turn to quantitatively characterise it. The principal technical challenge of separating the solid phase into aggregates and mortar matrix is discussed. The segmentation procedure developed in this work is described, along with its validation, leading to a quantitative characterisation of concrete's meso-structure. Section 3.2 presents the adopted method to analyse the 3D images coming from each *in-situ* test as an evolving set in time, in particular, Digital Volume Correlation (DVC). A short introduction on the DVC approach used in this work is given, together with the description of the specific implementations required to address the challenges imposed by the *in-situ* tests conducted herein. Section 3.3 is dedicated to a detailed description of the measured 3D kinematic fields, as well as the observed failure patterns coming from each *in-situ* mechanical test.

Chapter 4: Numerical framework

Chapter 4 presents the FE meso-model employed in this work to numerically investigate the mechanical behaviour of the studied material. In Section 4.1 two different kinds of kinematics enhancements in the context of E-FEM are introduced, in order to address on one hand, the explicit representation of the heterogeneities (aggregates and macro-pores embedded into the mortar matrix) and on the other hand, the modelling of the local discrete failure mechanisms. Section 4.2 focuses on the application of the meso-model to the micro-concrete samples. An illustration of the creation of the FE mesh based

on the identified morphologies coming from the x-ray scans is firstly given, along with a description of the boundary conditions applied for each test. The identification of the model in simple tension is presented and its predictive ability is challenged under different loading paths in compression.

Chapter 5: Link between experimental and numerical observations

Chapter 5 presents a systematic comparison between the experimental and numerical observations of the studied material's mechanical behaviour. In Section 5.1 for selected tests, the prediction of the model is compared to the corresponding experiments in terms of macroscopic responses, displacement fields, fracturing processes and failure patterns. The onset and evolution of the fracturing process, along with the different failure modes are discussed both numerically and experimentally. Section 5.2 focuses on the role of the underlying morphology on the mechanical macroscopic response. Virtual morphologies are generated by modifying the real morphologies coming from the x-ray scans, with the objective to offer a further insight into the impact of the different phases.

Chapter 6: Conclusion and perspectives

Chapter 6 summarises the principal parts of this work and discusses some suggestions for future work.

Chapter 2

Experimental campaign

This chapter details the experimental work conducted in this study to investigate the impact of the meso-scale heterogeneities of concrete on its macroscopic mechanical response. Three different mechanical tests are selected: uniaxial tension, uniaxial compression, and triaxial compression. The particularity of the tests presented is that they are performed inside an x-ray scanner, in particular the one in Laboratoire 3SR. This kind of mechanical tests, also called *in-situ*, consists in performing a series of tomographic scans while the specimen is under load. The main advantage of performing such tests is that, apart from obtaining the typical macroscopic responses (in terms of force-displacement curves), the internal structure of the material is also non-destructively captured and its evolution from the intact (before loading) until the damaged (after unloading) state is followed and quantified (as detailed in Chapter 3). However, due to the supplementary constraints imposed by the use of x-rays, these *in-situ* tests differ principally from the widely used standard ones, both in terms of the specimen size (which has to be significantly smaller) and in terms of the instrumentation, since specific experimental facilities are required.

The chapter starts by introducing the studied material, detailing the factors that determine the scale and morphology of the characteristic sample tested, followed by a description of its preparation procedure. The experimental facilities and the specific equipment used are then presented, with a description of the testing procedure following. Where possible, common features found in all types of tests are gathered and presented together, whereas detailed information referring specifically to each type of test is added where needed. Finally, the conducted experimental campaign is presented, with a description of each of the tests performed and the mechanical responses obtained.

2.1 Studied material: scale and morphology

Typically, mechanical tests with homogeneous stress state on plain concrete specimens are performed either on cubes or cylinders. International standards accept either sample types and provide values for the corresponding characteristic (compressive) concrete strength in terms of both cylindrical and cubical specimens [BSI, 2004], [ASTM, 2003]. From a mechanical point of view, due to the Poisson effect and the friction between the specimen and the loading plates, the stress state in a cube under compression is neither homogeneous nor uniaxial. There is a confinement effect that results in an increase of the strength. The same effect occurs in a cylindrical specimen, however, due to the higher slenderness ratio which is typically 2 : 1, (as opposed to 1 : 1 for cubes) it is considered that the friction effect vanishes in a zone in the middle of the sample [BSI, 2004],[ASTM, 2003], [Neville

et al., 1995]. Besides, during a tomographic scan, the object is rotated around a vertical axis, which makes the choice of cylindrical specimens quite suitable, since the shape of domain that carries full information (for all projection angles) is almost cylindrical for a cone x-ray beam. Consequently, the shape of the concrete samples tested in this work is chosen to be cylindrical with a typical slenderness ratio of 2 : 1.

Having selected the shape, the following question that naturally arises concerns the size of the cylindrical sample. Considering that the main objective of this work is the investigation of the local failure mechanisms of concrete at meso-scale, specimens with significant heterogeneities are required, which will give a direct insight on the impact of both the mechanical and the morphological properties of each phase (aggregates, macro-pores, mortar matrix) on the macroscopic mechanical response of the material. In other words, the objective is to create samples with rather small dimensions compared to the size of the largest heterogeneities as explained in the following.

2.1.1 Characteristic sizes of the specimens

Choice of specimen size

The final choice of the characteristic specimen size is affected by a number of factors. To begin with, the specimen must be of a sufficient size with respect to the largest heterogeneities so that it has some mechanical resistance and some relevance to real concrete. Furthermore, the use of x-ray tomography to obtain a 3D image of the micro-structure, implies a trade-off between the field of view, *i.e.*, sample size, and the spatial resolution, *i.e.*, the smallest heterogeneity that can be identified in the image. In the case considered, the smallest heterogeneities are the smallest macro-pores, with a physical size of about 100 μm . This encourages a pixel size of at least 20 $\mu\text{m px}^{-1}$ in order to be able to describe (recognise them in the image) these pores coarsely, having around 5 pixels across the diameter. As it will be explained in detail in Section 2.2, because of the cone x-ray beam used here, the effect of geometric magnification and the size of the pixels on the detector, this pixel size limits the field of view (*i.e.*, sample size) to around 30 mm. Consequently, the specimen must be designed so as to fit completely inside this field of view.

Apart from being imaged with x-rays, the specimens are mechanically loaded *in-situ* in the x-ray scanner of Laboratoire 3SR. This means that their dimensions and failure force must be in agreement with the limitations of the mechanical loading system. The current limitation of the loading system is a maximum load capacity of 500 N in tension and 10 kN in compression. For a tensile concrete strength of around 3.5 MPa this results to a maximum sample diameter of around 13 mm, while for a compressive strength of around 35 MPa this results to a maximum sample diameter of around 19 mm.

The points above direct towards a small specimen size, meaning that a *micro-concrete* is automatically selected, which is a concrete with a maximum aggregate size (*i.e.*, D_{max}) of a few millimeters. In preliminary tests performed, it has not been possible to core a specimen smaller than 10 mm. Making a trade-off between the different constraints, cylindrical specimens are chosen of 11 mm in diameter and 22 mm in height. Such a size, considering the tensile concrete strength of about 3.5 MPa, means a tensile failure load that should not exceed 350 N, which is compatible with the system mentioned above. Another characteristic scale to be chosen is the size of the largest heterogeneities (*i.e.*, size of largest aggregates) that is detailed in the following along with the concrete composition.

Concrete composition

The concrete composition is given in Table 2.1, with a mix proportion corresponding to an ordinary concrete in terms of both strength and slump (*i.e.*, workability), known as R30A7 [Gabet, 2006]. R30A7 concrete mixture has been designed with the aim of creating a composition with characteristics of standard concrete, which can be studied on a laboratory scale, and it has been extensively studied under various loading paths (see [Vu, 2007], [Gabet *et al.*, 2008], [Piotrowska, 2013], [Lukic, 2018]). It has an expected compressive strength of 30 MPa after 28 days with a slump of 7 cm measured by Abrams cone test. The mix proportion is 1 : 3 : 3.8 : 0.6, by weight of cement: sand: aggregates: water. Typically, it contains rolled siliceous aggregates with a maximum size of 8 mm, a size that considering the specimen size selected in this work, can not be respected.

It is generally accepted that in order to reduce test variability to an acceptable level, the ratio of the sample diameter over maximum aggregate size should not be below a minimum of 3 or 4. ASTM standard, for example, requires the diameter of the test cylinder to be at least 3 times the nominal maximum aggregate size [ASTM, 2003]. Considering that a cylinder of 11 mm in diameter is chosen for this work, rolled, siliceous aggregates (chemical composition: $SiO_2 > 97.3\%$) coming from Mios (France), with a maximum size of 4 mm are finally selected. The choice of such an aggregate size satisfies the objective to create small samples compared to the size of the largest heterogeneities, with aggregates being both quite large to hope some discrepancy between different specimens, but also small enough to have a behaviour which is still representative of concrete.

Table 2.1: Composition of concrete mixture

Aggregates D 0.5/4 [kg/m^3]	1008
Sand $D_{max} = 1800 \mu m$ [$kg/m^3 s$]	838
Cement CEM I 52.5 N PM ES CP2 (Vicat) [kg/m^3]	263
Water [kg/m^3]	169
Density [kg/m^3]	2278

2.1.2 Specimen preparation

The choice to test such small specimens of concrete implies that their preparation differs from the ordinary standard concrete specimens. As a first step of the micro-concrete samples preparation, the standard concrete preparation procedure is followed, by mixing the composite materials (see Table 2.1), in this case with a benchtop rotary mixer. Afterwards, two alternative methods are developed to obtain the desired size of samples: a) pouring the freshly mixed concrete directly into moulds of the desired dimensions (11 mm in diameter and 22 mm in height) or b) casting larger concrete blocks and then coring samples of the desired dimensions.

Method A: Moulding samples of the desired size

Regarding the first method, an aluminium mould of dimensions 30x30 cm, with 36 cylindrical holes of 11 mm in diameter and 28 mm in height is designed, so as to directly obtain the cylindrical samples without needing to core them. At the bottom edge of the mould, an aluminium plate is bolted, leaving the top edge free in order to pour the freshly mixed concrete. Before pouring the mix, oil is applied to the inside each of the cylindrical holes

to reduce friction and facilitate the removal of the samples. After pouring, a second aluminium plate is screwed into the top edge of the mould, which is then conserved for 28 days in water. By the end of this period, the time to extract the samples has arrived, revealing that this method does not work as intended. Firstly, during the casting it has been proven difficult to pour the liquid concrete mix into the small cylinders, as a result, many of the larger aggregates not to enter into the holes. Moreover, a strong reaction between concrete and aluminium is observed, making it difficult to pull the samples out from the mould. Besides, a strong side effect due to trapped air is observed, resulting in the creation of big holes in the specimens outer surface. For all these reasons, this method is not the one finally adopted for the preparation of the micro-concrete specimens.

Method B: Core-drilling samples of the desired size

Conversely, casting concrete in cylindrical moulds of about 10 cm³ in volume and then coring samples of the desired dimensions is the method finally adopted. Again, before pouring the freshly mixed concrete, oil is applied inside the moulds to reduce friction. Vibration follows the pouring and then the mix is sealed with plastic cover to prevent loss of any moisture content during the initial phase of hydration for three days. By the end of this period, the concrete cylinders are removed from their moulds and stored for 28 days in a container filled with water saturated with lime to avoid any calcium hydroxide leaching out of concrete, reducing its strength.

The reason behind the use of cylindrical moulds, is the later use of a lathe machine for coring the samples. In particular, a non rotary tool-bit (Diprotex PCD CPMB 120412) optimised for concrete materials is used, where the specimen has to be a cylinder, which is spinning, while the core bit is kept fixed. However, the use of such a machine has been proven to be unsuitable, since the cylindrical core is breaking inside the tool-bit while the whole block is still spinning.

As an alternative, a drilling machine (DIAMANT Evolution DK17) with a diamond instrumented core bit of 16 mm external and 11 mm internal diameter is used to core concrete samples of the desired size (see Fig. 2.18a). This time, the concrete block is fixed and the core bit is rotating and moving downwards. One of the main advantages of diamond core drills is that no impact is applied to the surface being drilled. Diamonds work by grinding away with friction and friction produces heat, which means that a constant water supply is necessary to keep the bit cool.

Coring concrete samples of 11 mm in diameter and around 24 mm in height is a delicate procedure which has to be performed patiently (by moving the core bit relatively slowly and smoothly downwards) having the concrete block well fixed (as shown in Fig. 2.18a). The extracted cylindrical cores are then cut to a nominal 23 mm length with a diamond wire (see Fig. 2.18b) leaving an additional 1 mm margin. As a last step of the preparation procedure, both surfaces are rectified with a rectification machine (grindstone granulometry 252 µm) shown in Fig. 2.18c). Since the parallelism between the two edges of a uniaxial or triaxial concrete specimen have to be as perfect as possible (to avoid introducing any bending moments), the rectification procedure is done extremely carefully and checked with a standard gauge comparator. Once the above steps are completed, the micro-concrete sample, shown in (see Fig. 2.18d), is ready to be tested. As a general remark, the preparation of such small samples is of considerable technical difficulty.

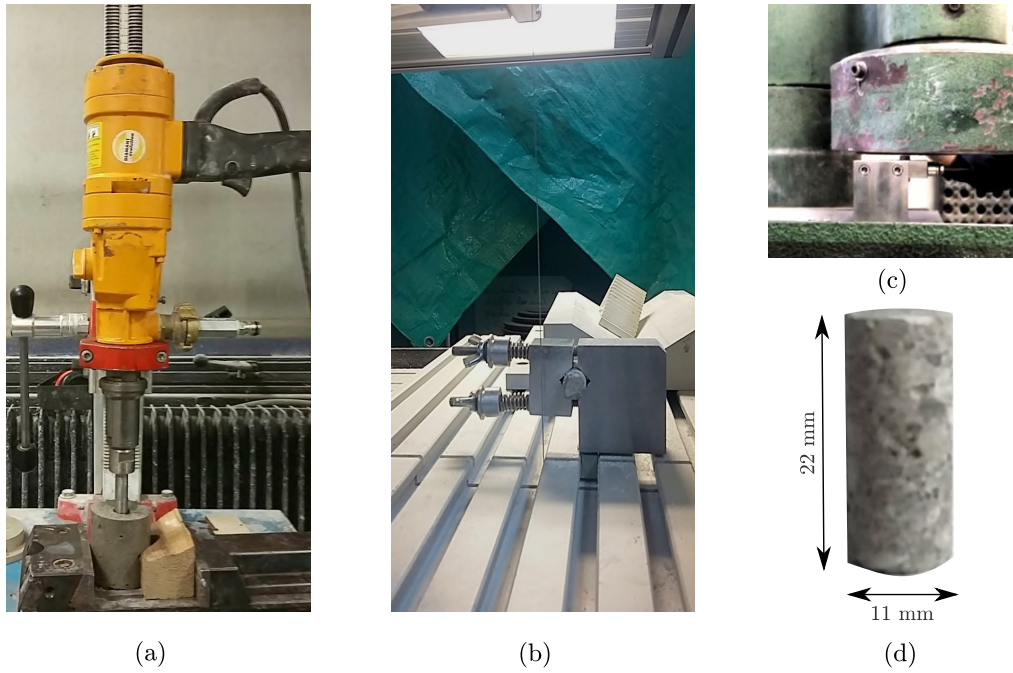


Figure 2.1: Micro-concrete sample preparation procedure: (a) core-drilling, (b) cutting with a diamond wire, (c) edge rectification and (d) cylindrical micro-concrete sample

2.2 X-ray scanning of micro-concrete

As explained in the introduction of this work, one of the primary objectives is to obtain a realistic representation of the heterogeneous meso-structure and follow its evolution over time as it progresses under load. This is achieved by non-destructive 3D imaging, in particular x-ray computed tomography, where the visualisation of the internal micro-structure is based on variations in density and atomic composition of the investigated object as explained briefly in the following.

2.2.1 Brief introduction to x-ray tomography

Interaction of x-rays with matter

X-rays, discovered in 1895 by Wilhelm Conrad Röntgen, are a form of high-frequency electromagnetic radiation, produced by accelerating electrons. Three things can occur when an x-ray photon meets with matter: absorption, scattering or no interaction at all. The probability of an x-ray photon to interact with a *particular* atom is low, however, this probability increases for a very large number of atoms in a small volume of solid. Any interaction removes the photon from the beam (through scattering or absorption) and this loss of photons is called *attenuation*, a term referring to the beam, not to individual photons.

The attenuation of a parallel beam of monoenergetic photons as it travels through a homogeneous medium of a constant thickness can be described by the Beer–Lambert law:

$$I = I_0 e^{(-\mu x)} \quad (2.1)$$

where: I_0 and I are, respectively, the reference and the transmitted intensity of the beam, x is the linear distance that the beam travels inside the medium and μ is the total linear attenuation coefficient. The larger the travelled distance or the higher the attenuation coefficient μ , the smaller the amount of the transmitted photons. The total linear attenuation coefficient, μ , also called macroscopic cross section, expresses the logarithm of the probability of photon interaction per unit distance travelled. It depends on the photon energy of the beam, the atomic number of the material, and the material density, as explained below.

Because the mass of the material itself provides the attenuation, a coefficient more accurately characterising the material, is the, density-independent, mass attenuation coefficient: $\mu_m = \frac{\mu}{\rho}$ (in m^2/kg). This is a measure of the degree of absorption or scattering of radiation per unit mass, characterising how easily the material can be penetrated by the x-ray beam. The mass attenuation coefficient for an heterogeneous material is given by:

$$\mu_m = \frac{\mu}{\rho} = \sum_i^n w_i \frac{\mu_i}{\rho_i} \quad (2.2)$$

where: w_i and $\frac{\mu_i}{\rho_i}$ are the weight fraction and mass attenuation coefficient, respectively, of the i th constituent element of the material. To understand how the attenuation coefficient relates to the physical properties of the material and the energy of the x-ray beam, one should understand how x-rays interact with matter.

Among the different attenuation processes that can occur when x-rays interact with matter, for the material studied and the x-ray photons energy considered in this work, the contributions from an absorption reaction, called photoelectric effect and a scattering reaction called Compton scattering are the most dominant ones (see [Malhotra et Carino, 2003], [Ketcham et Carlson, 2001]).

In a photoelectric absorption event, an x-ray photon is involved in an inelastic collision (*i.e.*, the kinetic energy is not conserved) with an electron orbiting the nucleus of an atom, giving up all of its energy and therefore being absorbed. Absorption can only take place if the photon energy is equal to or greater than the electron binding energy. For a given photon energy, the probability of a photoelectric effect occurring is proportional to the density of the material and the atomic number cubed. While, for given material, the probability of photoelectric interactions occurring drops drastically as the photon energy is increased (inversely proportional to the cube of the photon energy, see [Markowicz, 1993], [Bushberg et Boone, 2011]). The significant point is that tightly bound electrons in materials with a high atomic number are more likely to be involved in photoelectric absorption because the binding energies are closer to the x-ray energies.

The second process of attenuation concerned here is the Compton (incoherent) scatter, where an x-ray photon collides with a loosely bound electron in the outer shell, loses part of its energy and is deflected into a new direction. It occurs when a photon has a much greater amount of energy than the binding energy of the electron, effectively considering the electron as “free”. For a given photon energy, the amount of Compton scattering is a function of the density of the material and relatively independent of the atomic number.

The practical importance of the distinction between these two mechanisms is that their relative contribution is a function of the energy of the incident x-rays, with photoelectric absorption dominating at low energies (and high atomic number), below 100 keV, whereas Compton scattering dominating at higher energies (up to 15 MeV). As a result, low-energy x-rays are more sensitive to differences in composition than higher energy ones. The

photon energy of the x-ray beam should be adjusted to each application, so as to give sufficient transmission through the object and at the same time provide good contrast in the image (as explained in the following section).

To briefly summarise, x-rays are a type of radiation, able to penetrate through matter undergoing an attenuation. The attenuation coefficient μ varies according to the energy spectrum of the incident x-rays and the material elemental composition, especially the atomic number, as well as the material density. It is exactly this variation (in attenuation) that makes x-rays so suitable for studying the internal structure of multiphase heterogeneous materials, such as concrete at the meso-scale.

Projections, reconstruction and artefacts

As stated briefly in the introduction, x-ray tomography is a method of reconstructing a 3D field of x-ray attenuation coefficients within an object. This is achieved by acquiring different projections of the object (also called radiographs) at many angular positions, as it rotates around a vertical axis. For each rotation angle, projections are recorded as the line integral of the material attenuation along the path of the x-rays, by recording in each point of a detector (described below) the amount of photons passing on a given ray-path through the material. The process of recovering the 3D internal structural information from a number of finite projections is known as reconstruction.

Reconstruction is an inverse problem, where starting from these line integral attenuation measurements in certain directions a function is sought, which is the field of these attenuation coefficients inside the sample. A number of algorithmic techniques have been developed to solve this problem, with the inverse Radon transform [Radon, 1917] (mapping a function from line integrals at different directions) providing the mathematical basis. In this work, a filtered back-projection algorithm [Feldkamp *et al.*, 1984] is used which is an analytical inversion of the Radon transform in Fourier space. This algorithm is available in the XAct software provided by RX-Solutions (Annecy, France) and is used to reconstruct the 3D field of x-ray attenuation coefficients inside the micro-concrete specimens.

A number of artefacts can affect the quality of the final image, with beam-hardening being the most frequently encountered one for a polychromatic (detailed in the next section) x-ray beam. Very briefly, as the x-ray beam passes through the specimen, the lower energy parts of the spectrum are attenuated more easily and thus the mean energy of the x-ray beam is increased (“hardened”). This results in an unequal repartition of the linear attenuation coefficients in the reconstructed image, with the edges of the specimen appearing brighter than the center, even if the material is the same throughout [Mukunoki *et al.*, 2004]. There are different filters that can be applied during the acquisition and reconstruction to alleviate this artefact. In this study, due to the experimental set-up used and more specifically the pressure vessels (described in the following section), the effect of beam-hardening is not considered that significant. Note, however, that when both the set-up and the filters proved insufficient, post-processing image analysis operations can be applied to correct the beam-hardening artefact, as detailed in the following chapter. Another common artefact encountered in x-ray images is the ring artefact. This occurs when a miscalibrated or defective pixel in the detector generates in the reconstructed image a bright (or dark) ring centered on the pixel, corresponding to the location of the rotation axis [Hsieh *et al.*, 2009]. A good calibration of the detector and a suitable filter during the reconstruction can minimise the effect of this artefact.

Apart from artefacts, accumulated noise during the acquisition and reconstruction can highly reduce the quality of the final image. A detailed reference to sources and processes of noise related to x-ray tomography is out of the scope of this work (see for instance [Davis et Elliott, 2006]). It should be mentioned, however, that herein in order to increase the signal to noise ratio (SNR) in the final image, a number of projection images at each angle are averaged. In the same context, the scanning parameters are carefully chosen so as to decrease the blurring in the image, as discussed in the following while describing the main components of the tomograph used in this study.

2.2.2 X-ray facility at Laboratoire 3SR

Laboratoire 3SR (Grenoble) hosts a specialised laboratory tomograph built by RX-Solutions (Annecy, France). The main components of this tomograph (and of any micro-CT tomograph) are:

- the x-ray source
- the rotation stage
- the x-ray detector

In this type of set-up the source and the detector are kept fixed in space, while the specimen is rotated. These components are housed inside a lead-lined cabin shown in Fig. 2.2 and a detailed description of each one of them is given just below.

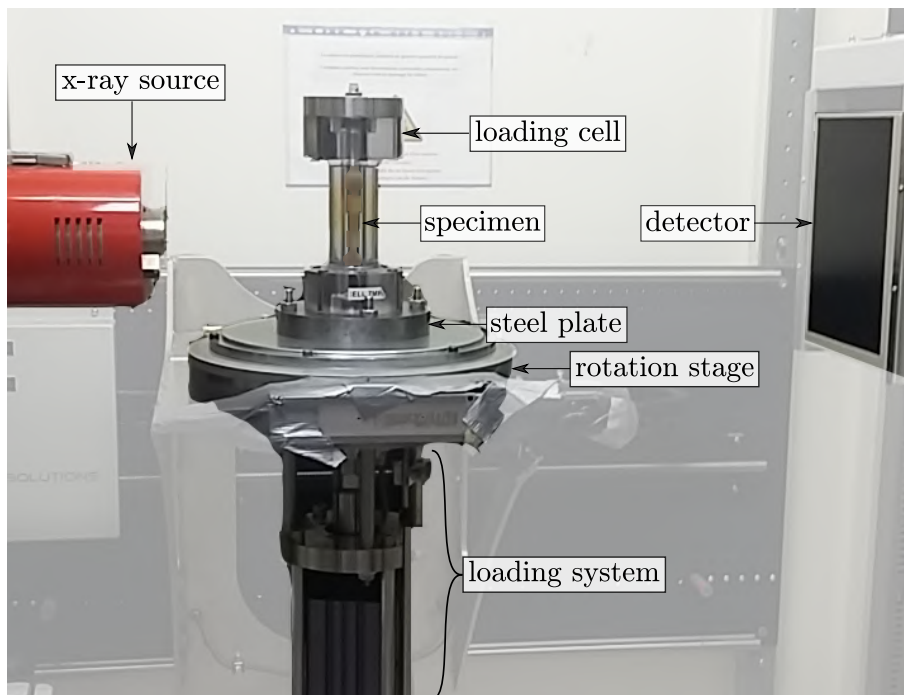


Figure 2.2: Labelled photo (with background faded) of *in-situ* x-ray facility at Laboratoire 3SR. Note that the depicted set-up is used for an *in-situ* uniaxial tensile test

Source

X-ray radiation is created by converting energy from accelerated electrons into x-ray photons, with a detailed description being out of the scope of this work. Herein, this energy conversion takes place within an x-ray tube (micro-focus vacuum tube in this case), sealed inside the x-ray source (Hamamatsu Corporation L12161 – 07 150 kV) that can be seen on Fig. 2.2 on the left. The energy conversion causes the accelerated electrons to strike a metal (Tungsten in this case) target from which x-rays are emitted. Generally, most of the kinetic energy is converted into thermal energy, leaving a very small amount available for the production of x-rays.

Because of the mechanisms involved in the production of the x-ray photons (see [Markowicz, 1993]), the source used here is polychromatic, which means that it emits photons having a wide spectrum of energies. The emitted x-ray beam is divergent (conical), with the origination point being a “spot” on the target and the emitted beam diverging out in a conical shape. The source operates in three different spot sizes: small, medium and large, which are related to the power applied to the tube, which itself is a function of the voltage and the current applied (detailed just below). The spot size plays an important role in the final resolution of the radiograph, since if it is bigger than the projected pixel size, then the spatial resolution is affected. In general, as the spot size increases, so does the amount of blurring in the acquired image, which means that the image becomes less sharp.

Apart from the spot size, three principle electrical quantities can be adjusted in this type of source: a) the voltage applied to the tube, b) the electrical current that flows through the tube, and c) the exposure time (*i.e.*, the duration of x-ray production). The operational range is 40 to 150 kV for the applied voltage and between 10 and 500 μA for the applied current, allowing a range of different sample sizes and densities to be imaged. By adjusting the applied voltage, the speed of the accelerated electrons changes and, in turn, so does the range of the x-ray photon energies. As the applied voltage increases, more higher energy photons are included in the beam, thus raising its average energy. By adjusting the current, the amount of the accelerated electrons changes and, in turn, so does the number of the generated photons (*i.e.*, the *flux* of the beam changes). Changes in current affect the quantity of x-rays, without producing any energy shift in either side of the spectrum. The energy spectrum (as explained in the previous section) affects the relative attenuation of the x-rays as they penetrate through matter, with higher energy x-rays penetrating more effectively than lower energy ones. The flux of the x-ray beam affects the signal to noise ratio (SNR), thus the contrast of the image. However, higher intensities require often a larger spot size which results in a smaller final resolution and an increased blurring in the image.

Detector

X-rays photons that have been transmitted through the material are recorded by a detector. The detector used here is depicted in Fig. 2.2 on the right. It measures the flux (number of x-ray photons per area and per unit time) of the incident beam and not the energy of the arriving photons, which means that it is energy insensitive. It is an indirect amorphous silicon (a-Si) flat-panel detector (Varian PaxScan 2520DX), which converts the x-ray photons arriving in its surface into visible light through a thick (700 μm) layer of caesium iodide (high x-ray absorption) scintillator. Directly behind the scintillator layer, there is an array of amorphous silicon (almost immune to radiation damage) and

thin film transistors (TFTs) whose function is to receive this visible light, convert it into electrical signal and thus into a digital image.

The total pixel area of the detector (where the intensity of the x-rays photons is measured) measures 244×195 mm, counting 1920×1536 pixels, which means that a pixel size in the detector is $127 \mu\text{m}$. Even though there is both a fixed number of pixels in the detector and each of these pixels has a fixed size, a range of different spatial resolutions can be achieved in the final image (from 7 to $100 \mu\text{m}$ in this case), thanks to the combination of the conical beam and the geometric magnification effect. Translation of the specimen closer to the x-ray source makes the specimen enlarged to the detector, thus, the spatial resolution (which determines the smaller object that can be seen) increases. However, this results in both decreasing the field of view and increasing the blurring of the image.

In this study, the detector is calibrated in the beginning of each different type of mechanical test. The specimen is translated very close to the source, which is set to operate in small or medium spot size depending on the test. This results to a voxel size of $13 \mu\text{m}$, achieving a spatial resolution that captures efficiently the smallest considered heterogeneities (macro-pores of about 0.1 mm). Such a voxel size means that the magnification factor is around 9.5 , decreasing the field of view to 25.5×20.5 mm, ensuring though, that the specimen (22 mm in height and 11 mm in diameter) fits completely inside. The fact that the specimen is positioned far from the detector, on one hand, decreases the probability that scattered x-rays reach the detector, but on the other hand, increases the blurring in the image, which is compensated by operating the source in small or medium spot size mode.

In general, by taking into account the fundamental principles and trade-offs involved, through sensible compromises, the setting parameters can be adjusted in order to maximise the contrast between features of interest in the final image, while minimising artefacts that may arise. The exact set of scanning parameters for each mechanical test performed in this work is a function of each specific set-up used and is given in Section 2.5, where each test is specifically detailed.

Rotation stage

The rotation stage is installed between the x-ray source and the detector, as depicted in Fig. 2.2. It is a hollow ring that rotates, allowing experimental equipment to be installed below and above it. It is mounted on a translation trolley that allows to position the specimen at the desired distance from the source, achieving the desired geometric magnification and thus the desired pixel size. On top of the rotation stage a steel disk is mounted with a 10 cm hole in the centre. A steel plate is mounted on top of it with a 10 mm hole in the centre. The loading cell, which contains the specimen (as shown in Fig. 2.2) is mounted on top of this steel plate. A detailed description of these pieces of equipment is given just below.

2.3 Description of the apparatus

A suitable experimental set-up compatible with the x-ray scanner of Laboratoire 3SR is developed, allowing the micro-concrete specimens to be scanned while they are under load. As stated in the introduction of this chapter, three different mechanical tests are performed: uniaxial tension, uniaxial compression and triaxial compression, with a specific apparatus used in each test which are described in this section. Regardless of the

loading path, there are two main components found in all tests: a loading system and a loading cell.

Loading system

Uniaxial tension or compression tests imply that an axial force (tensile or compressive) is applied to the specimen. In case of a triaxial test, the specimen is first subjected to an isotropic compression under the level of the desired confining pressure: $\sigma_1 = \sigma_2 = \sigma_3$. Thereafter the specimen is axially compressed by applying a deviatoric loading, which means that σ_1 is increased, while $\sigma_2 = \sigma_3$ remain constant and equal to the cell pressure. In all cases the axial force (tensile or compressive) is applied by a ram, which differs depending on the test and is driven by a loading system.

The loading system of Laboratoire 3SR can be seen in Fig. 2.2 and Fig. 2.5, is designed by Andò and manufactured by Nominal Concept, France. It is based on an electric motor which generates a rotation that is then turned into a vertical movement of the loading head (either upwards or downwards), allowing a displacement control of the experiment. As shown in Fig. 2.2 and Fig. 2.5, it is suspended below the rotation stage by four tie steel bars, which pass through the circular disk and the steel plate (mentioned above while describing the rotation stage). It has a maximum load capacity of 15 kN, a speed range from 0.1 to 100 $\mu\text{m min}^{-1}$ and the motor is driven remotely from a computer used for data acquisition.

The axial force applied by the ram to the specimen is measured by a forcemeter (which differs depending on the test), installed onto the loading head and being always in contact with the loading ram. The load capacity for the forcemeter in tension is 500 N (shown in Fig. 2.3), while for the one in compression is 10 kN (shown in Fig. 2.4). The vertical displacement of the loading head is measured with an axial Linear Variable Differential Transformer sensor (LVDT), attached in one of the steel bars (see Fig. 2.3). Strain gauges are not used herein in order to avoid creating artefacts on the 3D x-ray images, which means that such an instrumentation does not allow a direct measurement of the circumferential strain of the specimens. However, such a measurement can be obtained from the analysis of the timeseries of the reconstructed images as detailed in the next chapter. Note here that both the LVDT and the forcemeters are calibrated at the beginning of each different type of mechanical tests.

Loading cell

Due to the supplementary constraints imposed by the use of x-rays, no matter the type of mechanical test (and regardless of the stress path), the entire load frame is built upon a loading cell which is bolted in the circular steel plate (mentioned above and shown in Fig. 2.2) in order to equilibrate the load applied to the specimens. This cell needs to be stiff enough to carry the return force, but also made from a material which does not block the x-rays. Consequently, there is a clear trade-off between the rigidity and strength of the cell and its transparency to x-rays.

For the uniaxial tests, a low x-ray absorption plexiglas cell (PMMA) is used, designed for triaxial testing of rocks with 7 MPa confining pressure [Alikarami *et al.*, 2015]. It is shown as a sketch in Fig. 2.3 and Fig. 2.4, but also in place in Fig. 2.2. It has a cylindrical hole of 20 mm diameter all the way through and a reduced wall thickness of 15 mm in the central part, where the x-ray beam is going to pass through. This particular “I” shape

of the cell provides the necessary rigidity, but also enables it to be translated very close to the x-ray source, reaching to a higher spatial resolution. The fact that it is made of a transparent plastic, allows visual monitoring during the test.

Regarding the triaxial compression tests, taking into account that the strength of concrete increases with the confinement, there is certainly a need for reaching much higher force levels, while sustaining the desired cell pressure. Considering previous results on triaxial compression tests on R30A7 concrete composition ([Poinard *et al.*, 2012], [Gabet *et al.*, 2008]), as well as the limitations of the loading system (15 kN maximum load capacity) and the forcemeter (10 kN maximum load capacity), a maximum confining pressure of 15 MPa can be reached. A compromise between the existing pieces of experimental equipment, the rigidity, the strength and the transparency to x-rays of the designed material, lead finally to a design of a new I-shaped, high pressure 7075 T6 aluminium alloy cell, visible in Fig. 2.5, which is based on an initial design by Erminio Salvatore. Note that the technical drawings of this cell are presented in Appendix A.

Its dimensions are similar to the plexiglas one, fitting with the rest pieces of equipment, but this time, with an external diameter of 30 mm and a reduced wall thickness of 5 mm, in order to decrease the probability of the x-ray beam being attenuated as it passes through. It is dimensioned for a combined loading scenario of a 45 kN axial force on the external face of the cell and a 30 MPa confining pressure in the internal cylinder. A linear elastic calculation on *SolidWorks* with a Von Mises failure criterion lead to 122 MPa maximum deviatoric stress. Considering that the strength of the aluminium alloy used is about 500 MPa this results in a safety factor of 4 in terms of stress.

Despite the reduced wall thickness, the probability that the x-ray beam is attenuated as it passes through the aluminium alloy cell (higher atomic number and density) is higher compared to the plexiglas one. This means that an increased power of the x-ray beam is required for the triaxial tests. It should be mentioned, however, that this high pressure cell acts as an effective x-rays filter by absorbing the low energy x-rays, thus minimising beam-hardening artefacts. Unlike the plexiglas cell, a visual monitoring of the test is not possible.

2.3.1 Apparatus for uniaxial tension

In general, a direct tensile test in concrete is difficult to perform, due to the brittle behaviour of the material, with a normalised testing protocol not having been developed. In this study, in order to perform a direct *in-situ* tensile test in micro-concrete specimens (as published in [Stamati *et al.*, 2019]), a mechanism that grips the specimen and pulls it uniaxially is designed, which is shown in Fig. 2.3. This is done by gluing the top and bottom surfaces of the cylindrical specimen (label No. 4) to two specifically designed aluminium caps (label No. 5) with a high strength two-component epoxy resin (Sikadur-52), which is cured for at least 48h before each test. To avoid any stress concentration or failure on the axial faces of the specimen and to ensure good centering, the shape of the caps is designed as shown in Fig. 2.3.

In each aluminum cap there are threads for bolting a ball-joint (label No. 3) in order to ensure that the applied load remains as axial as possible. The ball-joints allow free rotation in the two planes normal to the loading direction, thus eliminating any bending moment due to potential defects in parallelism. The top ball-joint is screwed into a designed steel platen (also called specimen holder, label No. 1), which is in turn bolted into the plexiglas

cell (label No. 2). A steel cylindrical ram of 10 mm diameter is designed (label No. 8), which is screwed into the bottom ball-joint in one end and into the forcemeter in the other end, as per [Salvatore *et al.*, 2016]. A HBM C9-500 N forcemeter is used with a maximum 500 N load capacity (label No. 9), which corresponds to a limit strength of around 5 MPa for a specimen of 11 mm diameter (a strength of around 3.5 MPa is expected). Note that due to the low stiffness of the ball-joints used, the capture of the post-peak response is out of the scope of this work.

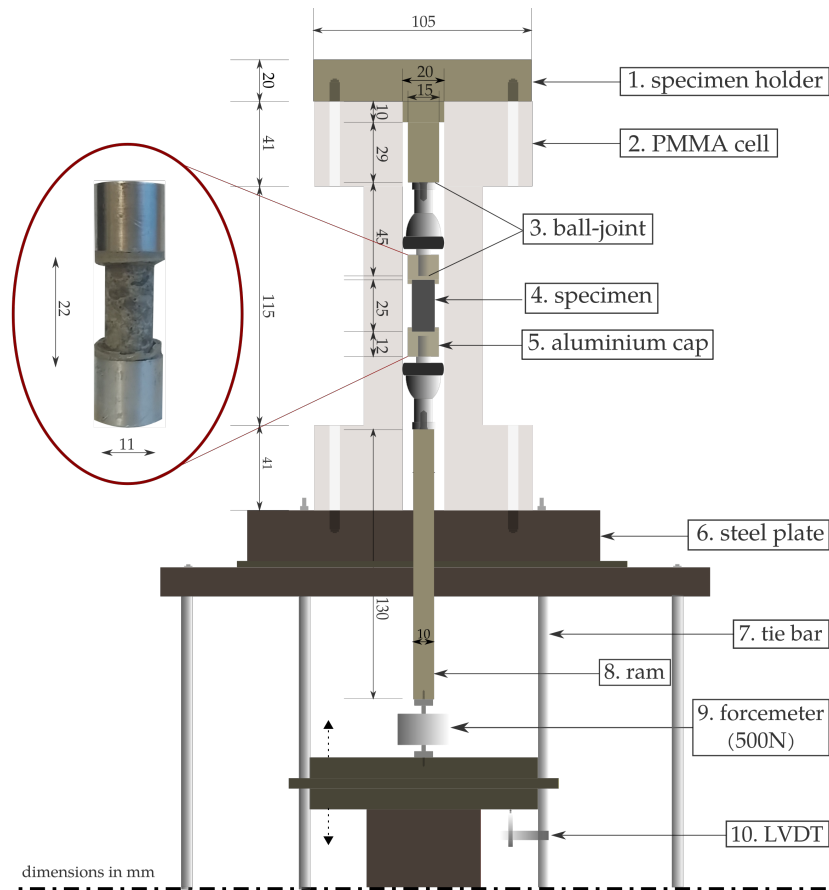


Figure 2.3: Sketch of the designed load frame for uniaxial tension tests

2.3.2 Apparatus for uniaxial compression

Most of the required equipment for conducting a uniaxial compression test is available in Laboratoire 3SR, mainly pieces designed for *in-situ* experiments on rocks and sands. As already mentioned, similarly to the uniaxial tension test, the plexiglas transparent cell is used. The only piece of equipment that needed to be manufactured is a two-part specimen alignment mechanism (compression bolt), made of steel. Likewise the ball-joints used in tension, this mechanism allows only rotation movement around the loading axis, eliminating any bending moments, erasing thus perpendicularity and parallelism defects of the specimen faces. As shown in Fig. 2.4, the compression bolt (label No. 5) is placed in-between the bottom surface of the specimen (label No. 4) and the ram (label No. 6).

In order to hold both the specimen and the compression bolt in place, a neoprene membrane (label No. 3) is used (internal diameter of 10 mm and thickness of 0.5 mm. The membrane is cut to size, stretched around both the specimen and the pivot mechanism,

and then stretched over top platen (specimen holder label No. 1) so as to cover at least few millimeters. The top platen is in turn bolted into the plexiglas cell (label No. 2). Attention should be paid to ensure that the sample axis is vertical and well-centered with respect to the the loading ram. This is done by inspecting its position either by eye or later with the help of the x-rays, by acquiring a radiograph before the first scan. The ram used is a steel cylinder of 10 mm in diameter, this time, with one flat and one hemispheric end (label No. 6). The hemispheric end is the one in contact with the compression bolt, creating a small contact area so as to minimise moment transfer. A HBM C2-10 kN forcemeter is used with a maximum 10 kN load capacity (label No. 8), which corresponds to a strength of around 100 MPa for a specimen of 11 mm diameter, value way larger than the expected one (not more than 40 MPa).

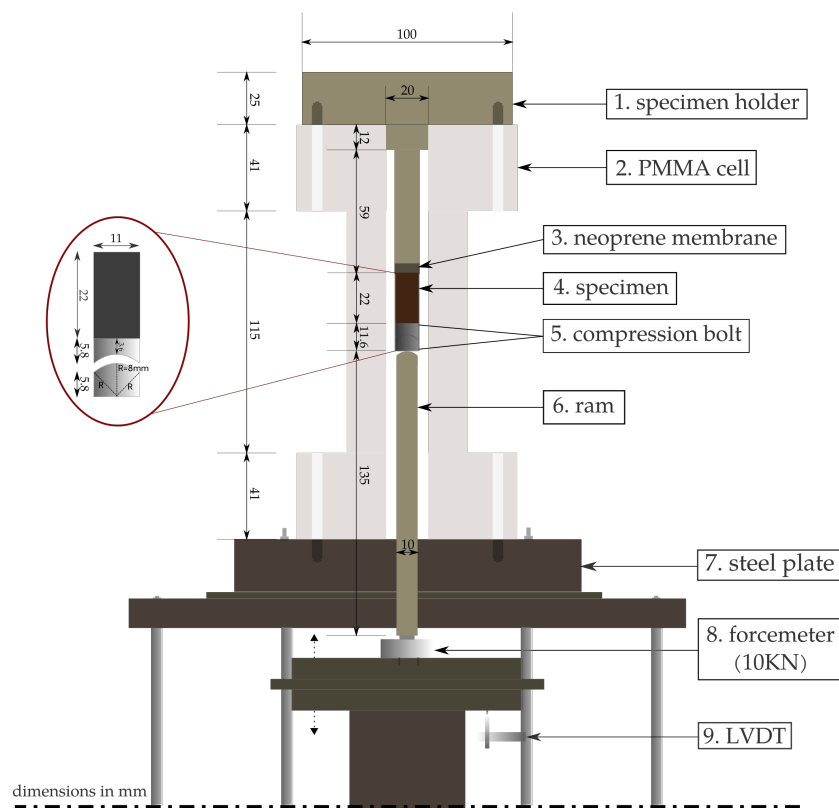


Figure 2.4: Sketch of the designed load frame for uniaxial compression tests

2.3.3 Apparatus for triaxial compression

Concerning the triaxial compression test, the forcemeter, ram, pivot mechanism and specimen holder are the same as the ones used for the uniaxial compression case (shown in Fig. 2.4). The plexiglas cell is replaced by the high pressure aluminium alloy cell described before, which sustains the desired confining pressure and provides the required strength and rigidity. The aluminium cell is bolted into the circular steel plate, which not only equilibrates the forces carried from the cell, but also seals the bottom of the cell with an O-ring.

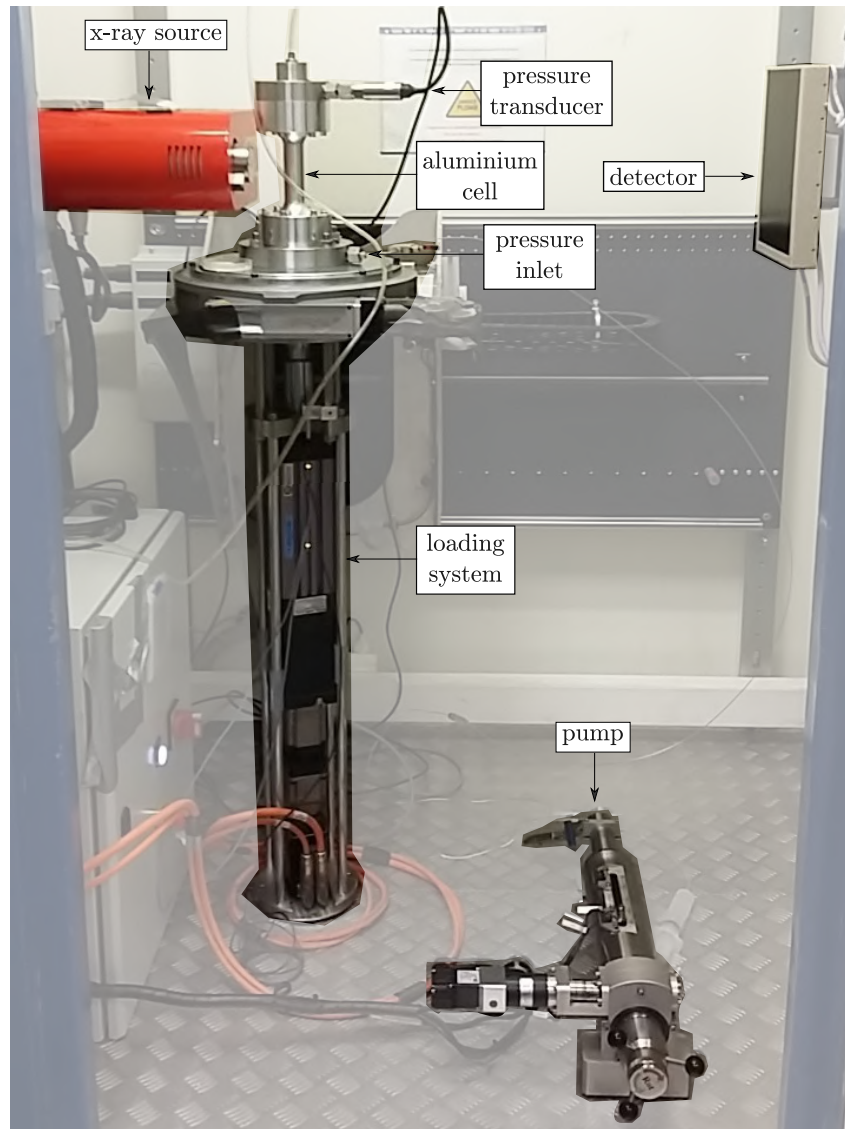


Figure 2.5: Set-up for triaxial compression tests. The designed high pressure aluminium loading cell is shown in place (mounted on the rotation stage), along with the pump used for the application of the confining pressure

The additional requirement of a triaxial test is drainage lines between the top and the bottom of the loading cell. The circular bottom steel plate has a tap on the outside (shown in Fig. 2.5) that allows both filling the cell with the confining fluid, which is water in this study, and the confining pressure to be applied. A Sanchez VPSSH 6–700 pump is used (shown in Fig. 2.5) which allows a fine control of the confining pressure, by adjusting the pump control system to the pressure value set.

A neoprene membrane is used, again, to hold both the specimen and the compression bolt in place, as well as to ensure a watertight seal, while the confining pressure is applied. This time, a triple layer of membrane is used to avoid any piercing due to punching of the membrane through the macro-pores that may be found on the specimen's surface. Again, attention should be paid to ensure that the sample axis is vertical and well-centered with respect to the the loading ram. This is actually double checked with a radiograph before applying the confining pressure, as described in the next section.

The upper platen (or specimen holder), makes a seal with the top part of the cell and

has a hollow steel tube, that allows vacuum to be applied, useful while stretching the membrane around the sample, but also to keep the sample in place during the application of the confinement. This tube is also convenient for identifying if the membrane is pierced, since in such a case, water will flow through the hole, around the specimen and finally flow out of the top of the specimen holder. The upper platen has also a tap on the outside (shown in Fig. 2.5), linked to a pressure transducer which reads the real pressure level inside the cell.

2.4 Testing procedure

2.4.1 Test set-up

Regardless of the experiment performed, the first step is to set up the loading system outside of the x-ray cabin. The forcemeter (500 N or 10 kN depending on the test) and the LVDT are then installed onto the loading head and on one of the tie bars, respectively, and the whole set is then installed under the rotation stage inside the x-ray cabin. Thereafter, the steel disk and the bottom steel plate are slid into the tie bars of the loading system and bolted onto the rotation stage and on the disk, respectively (see Fig. 2.2 and Fig. 2.5). The last component to be installed is the specimen holder; the steel platen that carries the specimen about to be tested. However, there are some steps in the installation procedure specifically followed for each type of test as explained just below.

Uniaxial tension

In case of uniaxial tension, after the installation of the loading system below the rotation stage, the plexiglas cell is bolted onto the circular steel plate. Afterwards, the mechanism which grips and pulls the specimen is assembled, with the whole assembly done from top to bottom, as shown in Fig. 2.6. Note that the specimen is already glued into the aluminium caps, since it takes at least 48 hours for the glue to reach its strength. The two ball-joints are then screwed into the top and bottom aluminium caps.

The specimen holder (top steel platen shown in Fig. 2.3) is turned upside down, with the steel piston facing up (see Fig. 2.6a). The top ball-joint of the assembly ball-joints-caps-specimen is then attached to it (see Fig. 2.6b). Afterwards, the loading ram is screwed into the bottom ball-joint (see Fig. 2.6c). At this point, the specimen holder is turned again upside down and carefully is transferred and lowered in the top surface of the loading cell (see Fig. 2.6d). The assembly ball-joints-specimen-ram passes through the cylindrical tube, until the bottom part of the ram appears through the hole of the circular steel plate (where the loading cell is bolted). Note that the dimensions of all the designed pieces have been carefully measured, ensuring that part of the ram would appear through the circular plate. The loading head is then moving upwards, until the forcemeter (already installed on the top of the loading head) reaches the ram. At this stage, by closely monitoring the force (to avoid applying an undesirable tensile load), the ram is very carefully screwed into the forcemeter, with the top plate (specimen holder) following this rotation movement to facilitate the bolting. As a last step, the top plate is carefully bolted into the top of the loading cell, still by closely monitoring the force, to avoid applying this time an undesirable compression load.

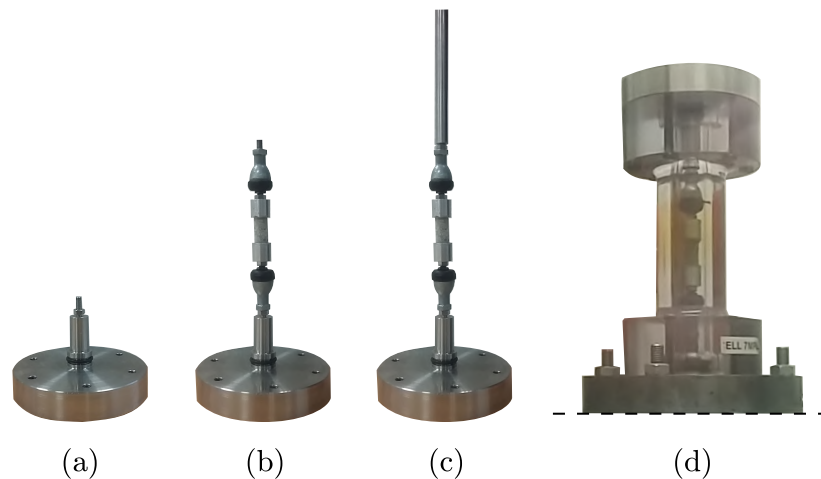


Figure 2.6: Installation of the specimen into the loading cell during a uniaxial tensile test: (a) the specimen holder is turned upside down, (b) the specimen with the ball-joints is attached to it (c) the ram is screwed into the bottom ball-joint (d) the specimen holder is turned upside down and lowered in the top surface of the loading cell (which is already bolted into the steel plate)

Uniaxial and triaxial compression

In case of uniaxial and triaxial compression, after the installation of the steel plate the ram is slowly slid downwards through the circular plate until it gets into contact with the forcemeter, which is already installed on the top of the loading head. Note that the circular plate makes a seal with the ram, essential in the triaxial test. The pressure vessel (PMMA or aluminium depending on the test) is then bolted into the circular plate, creating a seal with an O-ring. After the installation of the loading cell, in case of a triaxial test, the cell is filled carefully from the top with tap water at room temperature with a syringe. The length between the top edge of the ram and the top of the cell is measured, so as to ensure that enough space is left for the specimen holder and the specimen. Attention should be paid on this step while conducting a triaxial test, since no visual monitoring is possible.

The membrane (triple layer for the triaxial tests) is then stretched around the specimen and the compression bolt, as shown in Fig. 2.7b (for a uniaxial compression test). The specimen holder is then turned, as previously, upside down (with the steel piston facing up) and the specimen with the alignment mechanism are installed into it with the membrane stretched around them (see Fig. 2.7c). After having ensured that there is enough space left between the top edge of the ram and the top of the pressure vessel, as a last step (see Fig. 2.7d), the specimen holder is turned again upside down, pushed down slowly and bolted in the top surface of the cell creating a seal with an O-ring.

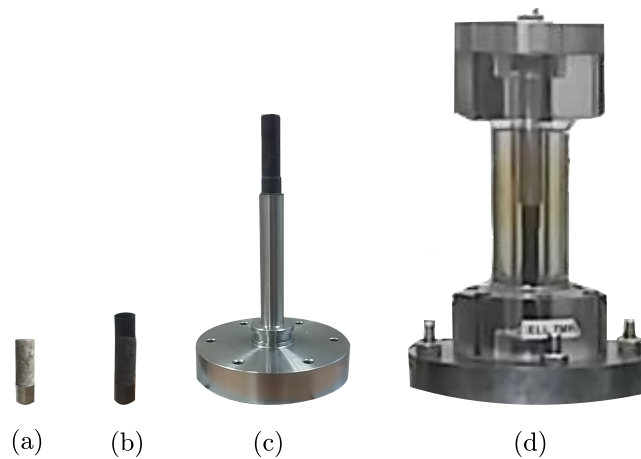


Figure 2.7: Installation of the specimen into the loading cell during a uniaxial compression test: (a) the compression bolt is positioned into the bottom surface of the specimen, (b) the neoprene membrane is stretched around the specimen and the compression bolt (c) the membrane (holding the specimen and the compression bolt in place) is stretched around the steel piston of the specimen holder (d) the specimen holder is turned upside down and lowered in the top surface of the loading cell (which is already bolted into the steel plate)

2.4.2 Description of an *in-situ* test

Once the set-up is ready, with the specimen mounted on the loading cell and positioned at the desired distance from the source (that is kept fixed during the whole test), the *in-situ* experiment can be conducted. As already mentioned, an *in-situ* experiment consists in performing multiple tomographic scans while the sample is under load. The number of scans depends on the type of test performed and are conducted at different loading steps. The objective of the selected loading steps is to have at least: one scan in the initial configuration (called reference scan), one, if possible, in the elastic regime, a number of them in intermediate load values before the peak and one last after failure. Since the exact tensile or compressive strengths of the specimens are not known *a priori*, the selected loading steps are chosen approximately by combining information concerning the concrete composition, the dimensions of the specimen and several preliminary mechanical tests performed in this work outside the x-ray scanner.

Reference scan

In case of a triaxial test, the first tomographic scan is performed after the application of the confining pressure. The ram needs first to get in contact with the compression bolt, which is in contact with the bottom surface of the sample. Since the aluminium cell allows no visual monitoring of the test, the x-rays are turned on, the field of view is centered at the bottom edge of the compression bolt and a series of radiographs are acquired while the ram is moving very slowly upwards (see Fig. 2.8)

These radiographs are also useful to examine whether the specimen is tilted and in such a case, the specimen holder is removed and the specimen is fixed by hand. By closely monitoring the level of force, when the ram gets in contact with the pivot mechanism (see Fig. 2.8 on the right), the LVDT is set to zero and the data acquisition (axial force, axial displacement and cell pressure) is started. The confining pressure is then applied with

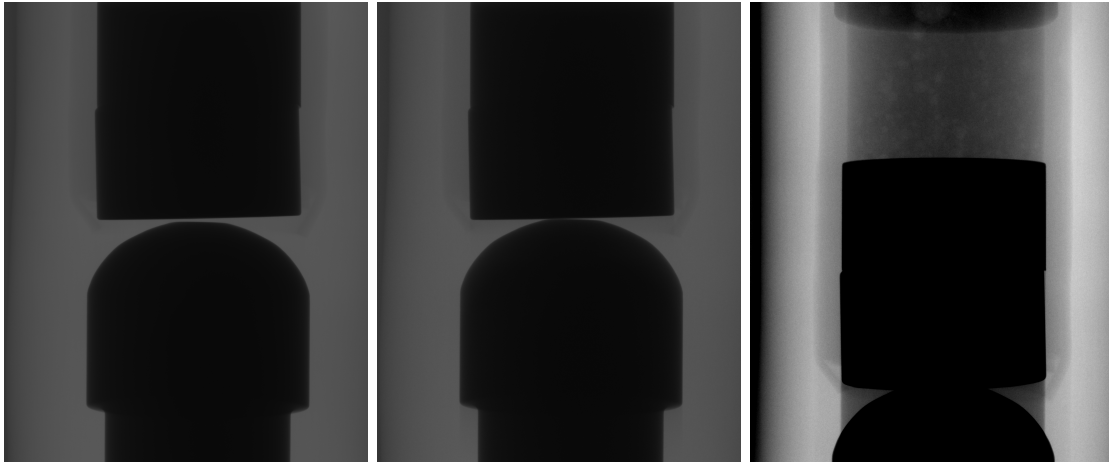


Figure 2.8: Series of radiographs acquired before the application of the confinement during a triaxial test. The ram is approaching the compression bolt, which is in contact with the bottom part of the sample (visible in the last radiograph)

the Sanchez pump (shown in Fig. 2.5) connected to the bottom steel plate through a cell pressure inlet. To detect possible leaks in the membrane, a stream of x-rays radiographs are acquired during the confinement step. Leaks can be identified by noticing a relatively large deformation of the membrane due to a big macro-pore in the specimen's outer surface and observing water coming out of the tube connected at the top of the specimen holder (shown also in Fig. 2.5). When the desired pressure level is reached, and if no leaks have been found, a first tomographic scan is performed under isotropic compression.

Concerning the uniaxial compression tests, the first tomographic scan is performed after the ram is in contact with the bottom part of the sample. As above, a series of radiographs are acquired while the ram is moving slowly upwards, with the field of view centered at the bottom part of the specimen. Again, in case of observing that the specimen is tilted, the specimen holder is removed and the specimen is fixed by hand. By closely monitoring the force level, the moment when the ram gets in contact with the bottom part of the sample, the data acquisition (axial force and axial displacement) start and the LVDT is set to zero. At this point and prior to any load application the first tomographic scan is performed.

In case of a tensile experiment, the ram is already bolted into the aluminium cap which is glued into the bottom part of the sample (see Fig. 2.6). Once the installation procedure is completed with the specimen positioned at the desired distance from the source, the LVDT is set to zero and the data acquisition (axial force and axial displacement) start. At this point and prior to any load application the first tomographic scan is performed.

Scans during loading

When the first scan is completed, an axial load (tensile or compressive depending on the test) is applied by moving the ram (downwards or upwards) with a fixed displacement rate until the second loading step is reached. At this stage, the displacement is stopped and the second tomographic scan is performed. After this scan has finished, the specimen is loaded again, with the same displacement rate, until the next load step is reached. This procedure continues until the last scan, the one after the failure of the material, is

conducted.

2.4.3 Calibration of the apparatus

Due to the instrumentation used, with the LVDT installed in one of the tie bars (see Fig.2.3 and 2.4), the measured axial displacement corresponds to the *total* displacement of the system, including the response of the apparatus (different for each test), as well as the response of the micro-concrete samples. The external force (either compressive or tensile) is applied to each of the components with the same magnitude, while the amount of the total deformation is the sum of the relative deformation of each component, which depends on their relative stiffness (*i.e.*, corresponding to a system of springs in series). Since a different apparatus is used for each type of mechanical test, a calibration outside the x-ray scanner is required for each one of them, in order to estimate and subtract the elastic stiffness of the apparatus from the global response.

In case of tension, a calibration is performed by conducting a uniaxial tensile test, with the set-up being the one depicted on Fig. 2.3 and the testing procedure identical to the one described above. This time, however, the two aluminium caps are glued together, *i.e.*, there is no micro-concrete sample in between them, estimating thus directly the apparatus stiffness. Once the whole system is in place, the data acquisition (axial force and axial displacement) is started. The ram starts to move downwards, with two cycles of loading-unloading following, reaching to a maximum force of 400 N as depicted in Fig. 2.9a. A non-linear effect can be seen in the response, which can be attributed both to the soft plexiglas cell and the ball-joints used. Note that this non-linearity will be taken into account while subtracting the part of the apparatus stiffness from the global response of the *in-situ* tensile tests presented in the following section.

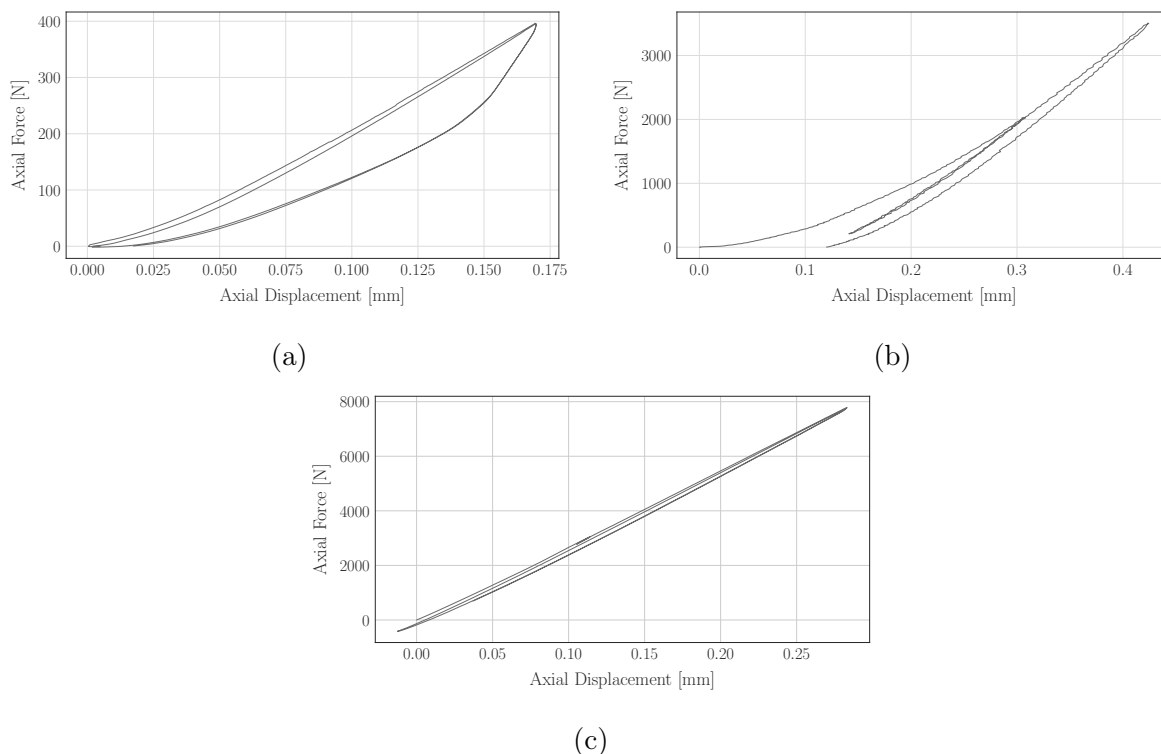


Figure 2.9: Estimation of the apparatus stiffness: (a) uniaxial tension, (b) uniaxial compression (c) triaxial compression

In case of compression tests, the calibration is performed with the set-up being the one depicted on Fig. 2.4 for a uniaxial case and on Fig. 2.5 for a triaxial case. The installation procedure is identical to the one described previously for each type of test, with the only difference being the substitution of the micro-concrete sample with a 20 mm in height and 10 mm in diameter steel sample. In case of triaxial compression, a 15 MPa confining pressure is firstly reached before the application of the deviatoric load. Once the set-up is ready, the data acquisition (axial force and axial displacement) is started and the ram moves upwards, with two cycles of loading-unloading followings. A maximum axial force of 3500 N is reached in uniaxial compression (see Fig. 2.9b), while a maximum deviatoric force of 8000 N is reached for triaxial compression (see Fig. 2.9c). The steel sample exhibits a linear elastic behaviour with a known stiffness which is then subtracted from the global response in order to end up only with the response of the apparatus. As per the tensile case, a non-linear effect can be seen in the response of the simple compression test, which can be attributed to the contact effect between the two-part compressive bolt (see Fig. 2.4) and the steel sample. Due to the confining pressure, such an effect does not occur in triaxial compression. Note that in both cases the stiffness of the apparatus is calculated during the second loading cycle.

The calculated stiffness values are gathered in Table 2.2, showing that, indeed, the relative stiffness of the apparatus used in each type of test is different, with the tensile one being the least stiff. Due to the significant non-linear response observed in this case, the measurement uncertainties are higher and therefore an upper and lower limit for the estimated stiffness are also given. The uniaxial compression apparatus is much stiffer than the tensile one, in particular four times stiffer, but still the aluminium cell used in triaxial compression is twice stiffer than the plexiglas one used in simple compression. As already mentioned, the estimated relative stiffness of each apparatus will be subtracted from the calculated global response of the corresponding *in-situ* experiment presented in the following section.

Table 2.2: Estimated apparatus stiffness

Test type	Stiffness [N/mm]
Uniaxial tension	2692 ± 6
Uniaxial compression	12780
Triaxial compression	26500

2.5 *In-situ* experiments conducted

The experimental campaign conducted in this work consists of a study of the mechanical response of cylindrical micro-concrete samples (22 mm in height and 11 mm in diameter) under: uniaxial tension, uniaxial compression, and triaxial compression. In total, 8 *in-situ* tests are conducted:

- 2 uniaxial tension tests (T-01 and T-02),
- 3 uniaxial compression tests (C-01, C-02 and C-03) and
- 3 triaxial compression tests at 5 MPa (TX5-01), 10 MPa (TX10-01) and 15 MPa (TX15-01) confining pressures.

Apart from these tests, 14 preliminary tests are performed outside of the x-ray cabin to check and validate the different experimental apparatus and obtain an overall idea of the expected failure strengths and failure patterns of the material (see Appendix B).

An exact description of each test with the specific parameters used is detailed in this section, along with a discussion of the mechanical responses. The reconstructed 3D images obtained during the *in-situ* tests are also presented, mainly as a supplementary information on the global response. A further analysis of these images will be covered extensively in the following chapter. Note that all the *in-situ* tests are gathered in Fig. 2.19, presented at the end of this chapter, containing information concerning the type, the name, and the failure stress of each test, along with the central vertical greyscale slices coming from the tomographic scans.

2.5.1 Uniaxial tension

In total, four tomographic scans are performed for each of the two uniaxial tensile tests: the reference scan, one at 150 N, one at 250 N and one after the failure of the specimens. The voltage and current of the x-ray source are set to 125 kV and 80 μ A, with the source operating in a small spot size and the voxel size set to 13 μ m. Projections are acquired in 1120 different angular positions between 0° and 360°, as the specimen is rotated around a vertical axis and six images of each angle are averaged in order to reduce the noise. The total duration of each scan is 1h50'.

Fig. 2.10 and 2.11 show the experimental macroscopic stress-strain curves of the two tensile experiments, after subtracting the strain corresponding to the elastic stiffness of the apparatus (see Section 2.4.3) and assuming a level of zero stress in the specimen after the material failure. The loading steps where the tomographic scans are carried out are indicated along with the reconstructed 3D images of the specimens. Note that due to the polycarbonate cell and the ball-joints used, the loading system is not stiff enough, resulting to a high elastic deformation of the whole loading frame during the post-peak unloading phase, which is not possible to capture.

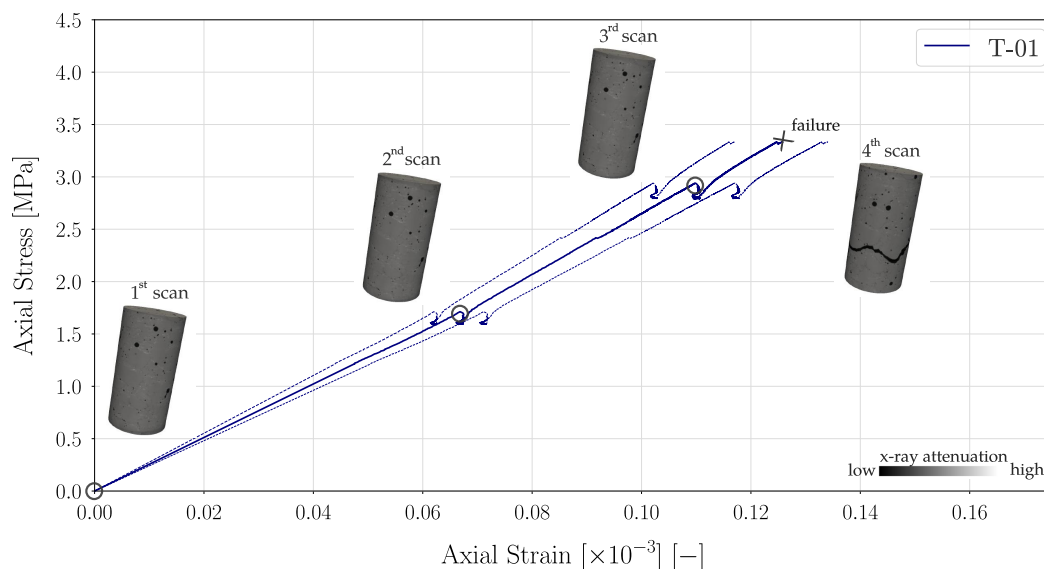


Figure 2.10: Macroscopic stress-strain curve for the first uniaxial tension test performed *in-situ* in the x-ray scanner

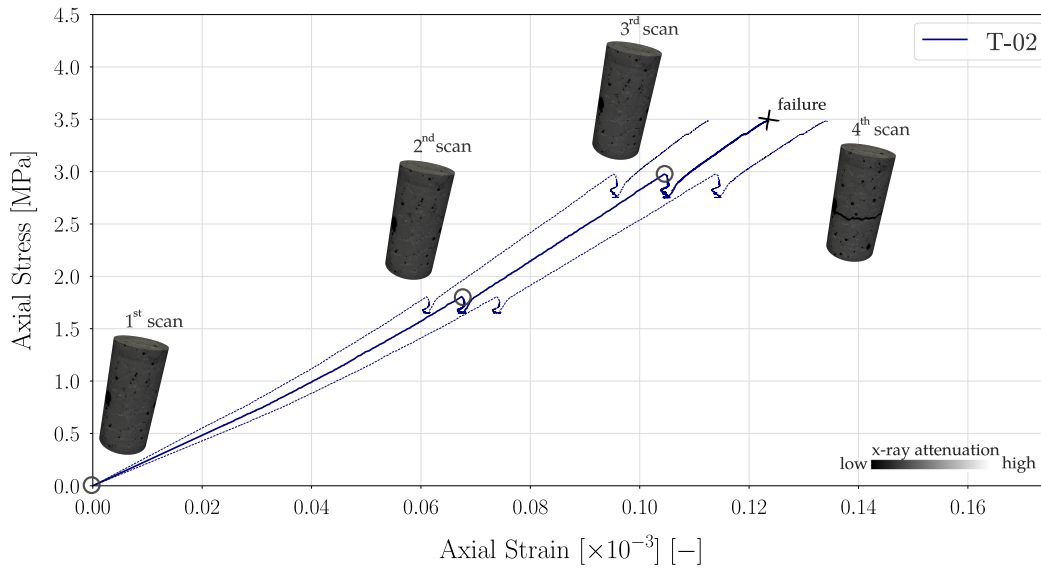


Figure 2.11: Macroscopic stress-strain curve for the second uniaxial tension test performed *in-situ* in the x-ray scanner

The two tests have relatively similar macroscopic responses, exhibiting the typical quasi-brittle behaviour expected in a tensile test in concrete. Despite the small size of the samples, the values of the measured tensile strengths, 3.2 MPa and 3.5 MPa, are very close to ordinary concrete specimens. As discussed in the previous section (see Table 2.2), because of the soft loading system used, the measurement uncertainties for the elastic moduli are high resulting to an upper and lower limit (dashed lines in Fig. 2.10 and 2.11). However the estimated values range between 24 to 33 GPa and are still representative of concrete.

Concerning the failure patterns, the design with the aluminium caps and the ball-joints worked successfully, since failure on the axial faces of the specimens did not occur. A typical behaviour of concrete under uniaxial tension is observed, with a clear macro-crack, normal to the direction of loading (typical for fracture mode I) appearing in the 3D images of the post-peak scans. However, from qualitative visual inspection, no obvious micro-structural change is visible in the images between the initial and the two following scans. As explained in detail in the following chapter, following the micro-structure while it is deforming before such a brittle failure, will be a challenge for the tools presented in this work.

2.5.2 Uniaxial compression

The same loading-unloading paths are followed in the three *in-situ* compression tests, with a first loading until 2000 N, an unloading until 200 N and a second loading until failure. However, neither the number of tomographic scans nor the loading steps are kept constant between the three tests. This is justified by the fact that loading is interrupted at different points (in order to perform a scan), attempting to catch significant changes in the macroscopic response, which is carefully followed during each test. In any case, apart from the reference and the post-peak scan, in all of the tests, a scan at 2000 N is performed, during the first loading cycle, and one at 2500 N, during the second loading cycle.

Due to the plexiglas cell used, the scanning parameters are identical to the ones used in uniaxial tension (described just above) with a voxel size of $13\ \mu\text{m}$ and a 1h50' scanning time for each test. In the same spirit, a quasi-brittle failure is observed and the loading system is not stiff enough to capture the post-peak response.

Fig. 2.12, 2.13 and 2.14 present the macroscopic responses of the three uniaxial tests. The strain corresponding to the elastic stiffness of the apparatus is subtracted and a level of zero stress in the specimen is assumed after the material failure. The responses obtained are typical of a concrete specimen being uniaxially compressed, with compressive strengths about 10 times higher compared to the tensile ones. The tangent stiffness is slightly decreasing during the loading, whereby the material becomes damaged due to micro-cracking. The measured compressive strengths and Young's moduli range between 32 to 39 MPa and 26 to 28 GPa, respectively.

A contact effect can be observed in the beginning of the loading between the two-part compressive bolt (see Fig. 2.4) and the specimen. However, the failure patterns as revealed from the post-peak 3D images, do not suggest that bracing cones (due to boundary conditions) have occurred. More complex failure patterns are observed when compared to the failure mode in tension. Similarly to the tensile experiments, no obvious micro-structural change is visible by eye in the 3D images before the peak.

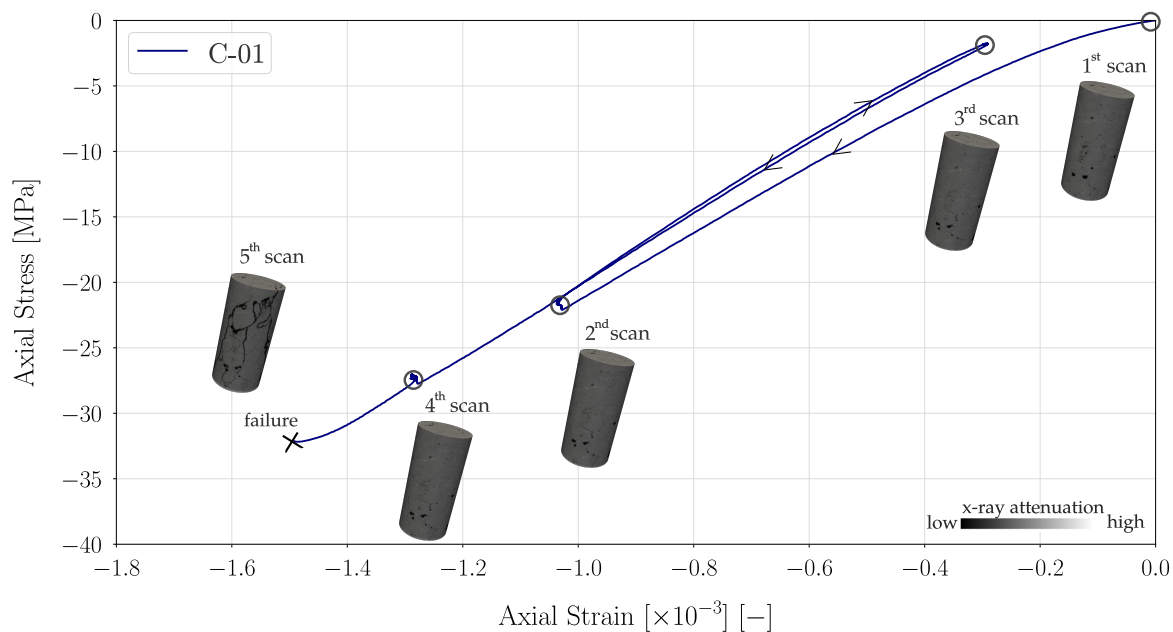


Figure 2.12: Macroscopic stress-strain curve for the first uniaxial compression test performed *in-situ* in the x-ray scanner

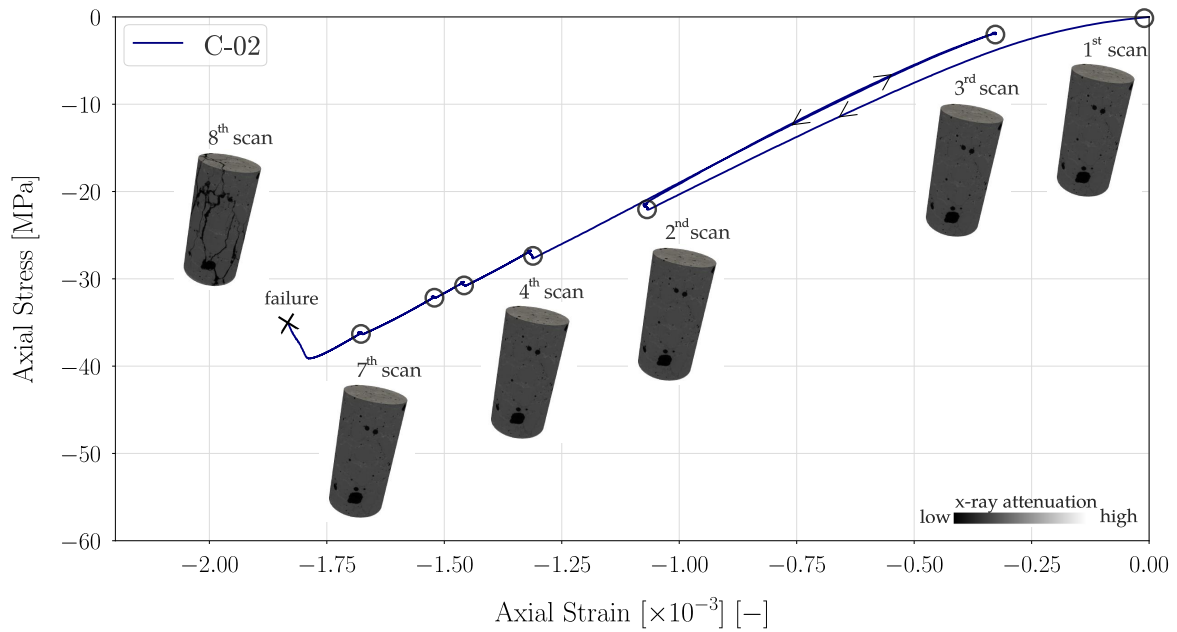


Figure 2.13: Macroscopic stress-strain curve for the second uniaxial compression test performed *in-situ* in the x-ray scanner

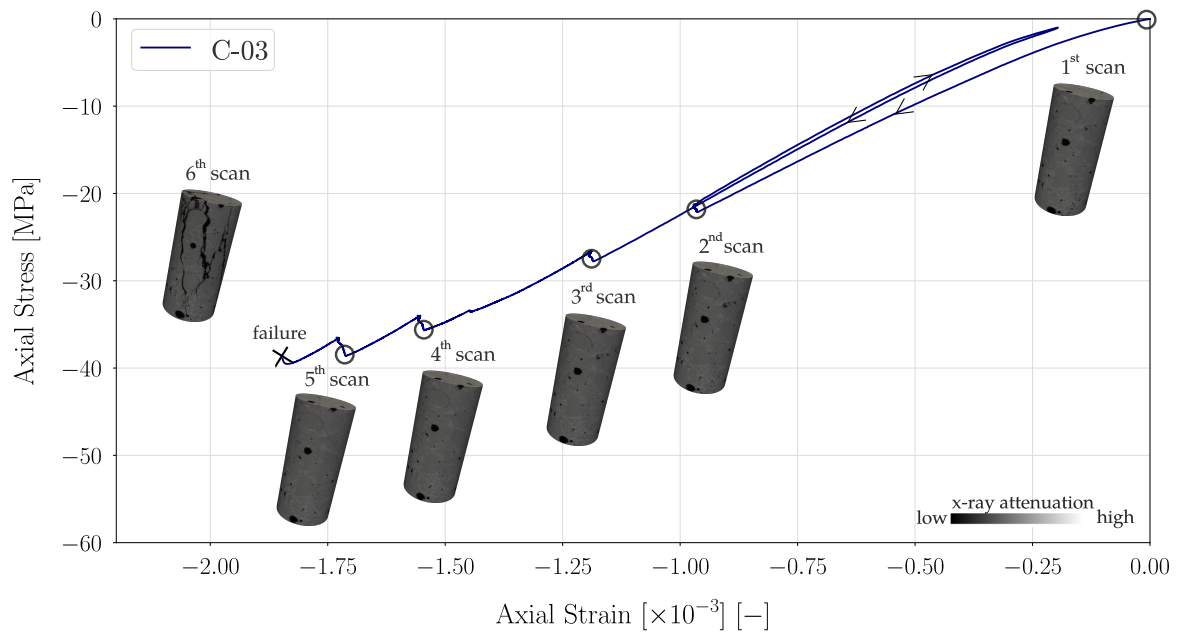


Figure 2.14: Macroscopic stress-strain curve for third uniaxial compression test performed *in-situ* in the x-ray scanner

2.5.3 Triaxial compression

For each level of confinement (5 MPa, 10 MPa and 15 MPa), one *in-situ* test is conducted, with different number of scans for each test. Apart from the reference and the post-peak scans, a third scan is conducted at relatively low force values (elastic regime). As above, by carefully following the macroscopic response, the loading is interrupted at certain points

attempting to catch significant micro-structural changes. It should be mentioned here that for the *in-situ* test at the highest confining pressure (15 MPa), the limit of the force-meeter load capacity (10 kN) is reached and as a result, the loading had to be interrupted. However, the macroscopic response suggests that failure has already occurred.

For the triaxial compression tests, due to the high pressure aluminium cell used (with a higher probability of attenuating the x-rays passing through), the voltage and current of the x-ray source are set to 135 kV and 100 μ A, respectively, with the source operating in a medium spot size, whereas the pixel size is maintained at 13 μ m as per previous scans. Again, projections are acquired in 1120 different angular positions between 0° and 360°, as the specimen is rotated around a vertical axis, while this time, seven images of each angle are averaged in order to reduce the noise. The total duration of each scan is increased to 2h20'.

The deviatoric part of the macroscopic responses is shown in Fig. 2.15, 2.16 and 2.17, for an increasing level of confinement, after subtracting the strain corresponding to the elastic stiffness of the apparatus. A typical triaxial response of concrete is observed, with a linear elastic phase in the beginning of the loading, followed by a loss of rigidity due to micro-cracking. The deviatoric stress is increased until the peak deviatoric stress is reached, whereafter strain softening occurs. As the confinement increases, the samples undergo a peak stress which is increasing, as well as the level of relaxation during scanning is increasing. Another trend that is confirmed is the passage from brittle to ductile behaviour, corresponding to the transition between fracture mode I and fracture mode II [Reynouard *et al.*, 2010].

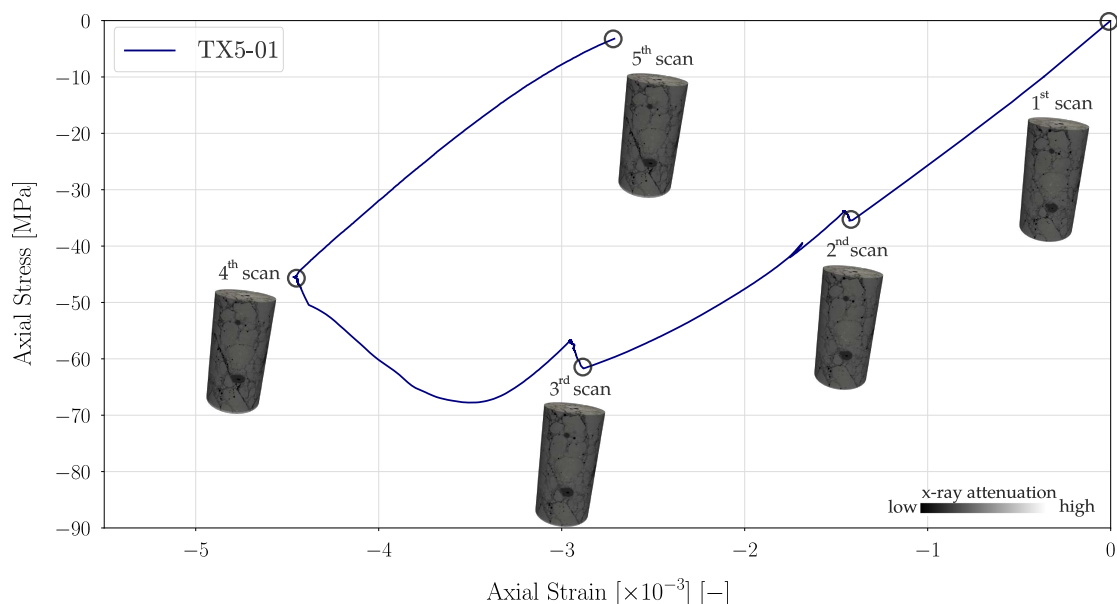


Figure 2.15: Deviatoric part of the macroscopic stress-strain curve for triaxial compression test under 5 MPa confinement performed *in-situ* in the x-ray scanner

This transition can also be observed in the failure patterns as revealed by the reconstructed 3D images obtained from the last scan, which differ significantly according to each level of confinement. For the lower confinements (5 MPa and 10 MPa) the specimens fail macroscopically on a sliding inclined plane. For the highest level of confinement, even though the macroscopic curve indicates that the plateau of the stress has been reached,

no failure of the specimen is visible in the last 3D image, suggesting that a completely different failure mechanism has occurred. Again, the investigation and quantification of the micro-structural deformation during the loading (discussed in the following chapter) are expected to shed some light on the different failure mechanisms that appeared.

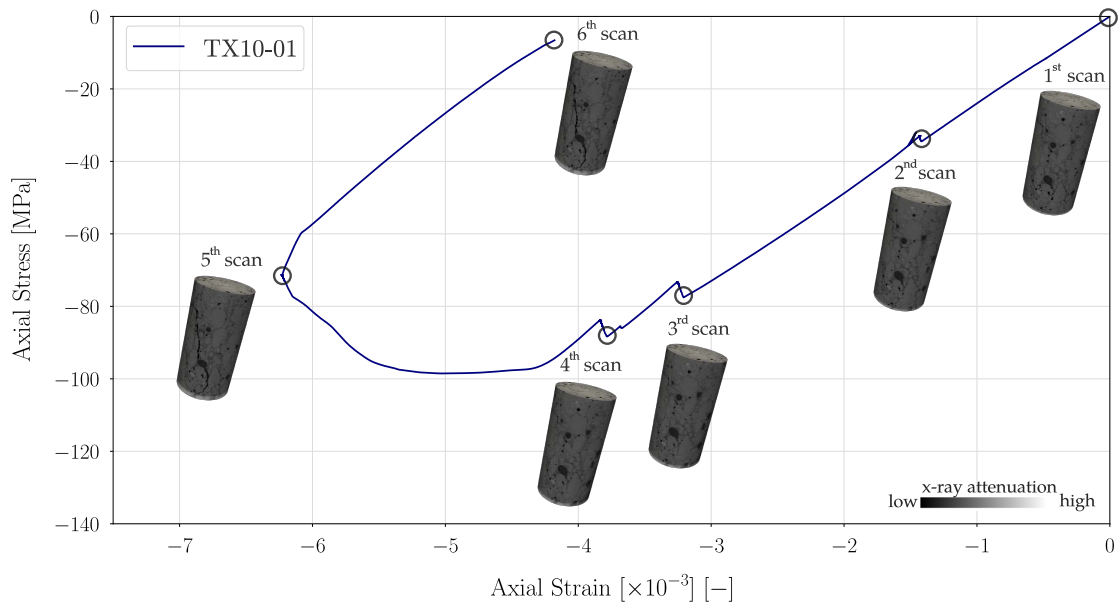


Figure 2.16: Deviatoric part of the macroscopic stress-strain curve for triaxial compression test under 10 MPa confinement performed *in-situ* in the x-ray scanner

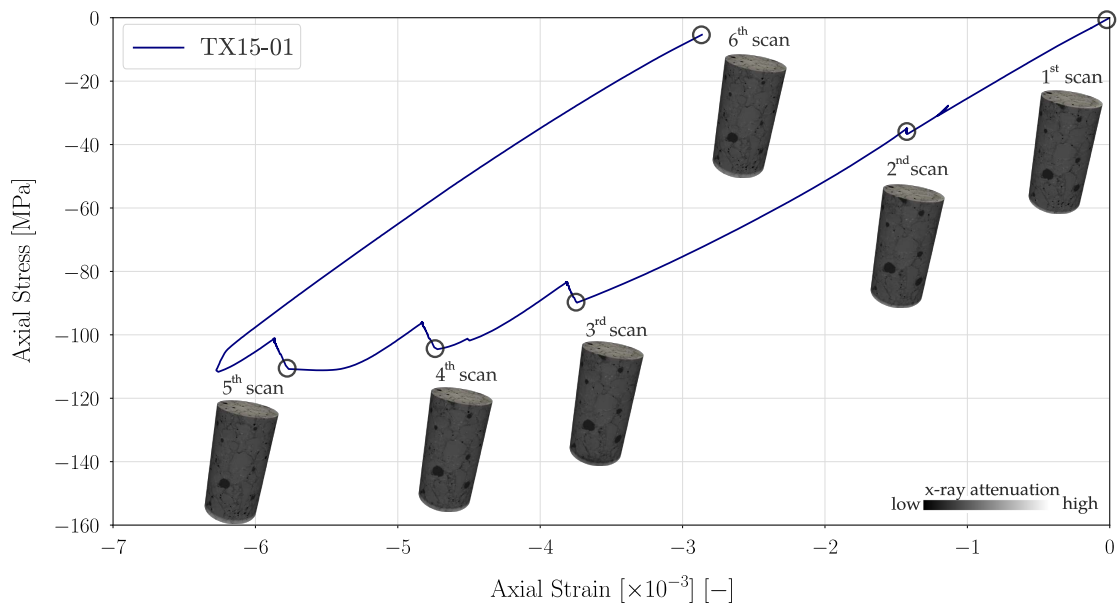


Figure 2.17: Deviatoric part of the macroscopic stress-strain curve for triaxial compression test under 15 MPa confinement performed *in-situ* in the x-ray scanner

2.5.4 Summary of macroscopic mechanical responses

To summarise, the macroscopic responses, in terms of axial stress as a function of axial strain, of all the *in-situ* mechanical experiments are gathered and presented in Fig. 2.18. While the specimens' size is admittedly small compared to their heterogeneities, their mechanical responses seem to be representative of the ordinary concrete from which the micro-concrete composition is derived. The typical asymmetrical macroscopic failures in tension and compression are observed, whereby starting both from a symmetric elastic behaviour, it is clear that for compression the transition to a non-linear behaviour is obtained for a larger macroscopic stress compared to tension. Moreover, with an increasing level of confinement (from 0 to 15 MPa) the peak compressive stress appears later and the transition from brittle to ductile behaviour is revealed, indicating that the micro-concrete specimens are mechanically representative.

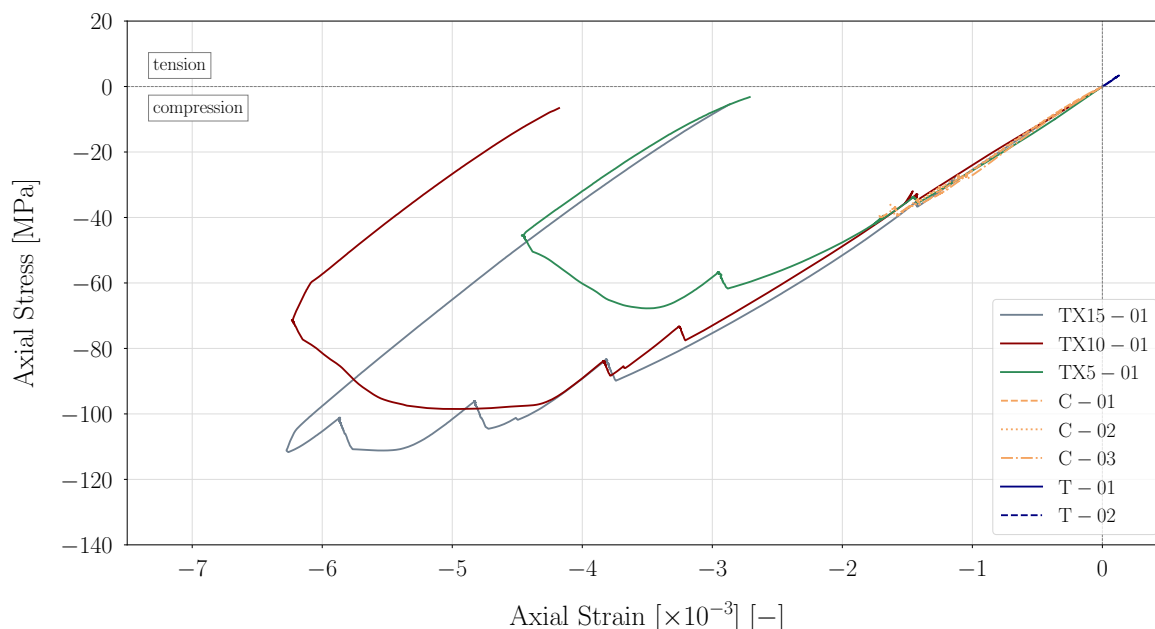


Figure 2.18: Combined macroscopic responses of all the *in-situ* tests conducted: TX refers to triaxial compression tests, C refers to uniaxial compression tests, T refers to uniaxial tension tests

2.6 Concluding remarks

This chapter presented the experimental campaign conducted in this work. The use of x-ray tomography combined with a mechanical loading system imposed certain size limitations on the examined specimens. The trade-off between the different constraints led to a preparation of cylindrical micro-concrete samples measuring 11 mm in diameter and 22 mm in height. The developed experimental set-up compatible with the x-ray scanner of Laboratoire 3SR was then presented, with a detailed description of the specific apparatus used for each type of test. In total 8 *in-situ* mechanical tests were performed: two uniaxial tension tests, three uniaxial compression tests and three triaxial compression tests at 5 MPa, 10 MPa and 15 MPa confining pressures. Despite their admittedly small size, the specimens tested were proven mechanically representative, offering interesting

information concerning the mechanical behaviour of the material under the different stress paths studied. However, the main advantage of performing *in-situ* tests is that, apart from obtaining the typical macroscopic responses (in terms of stress-strain curves) the evolution of the internal micro-structure during the loading is also followed. This is achieved through the analysis of the 3D images coming from these tests which is the subject of the following chapter.

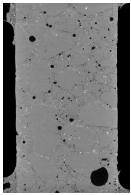
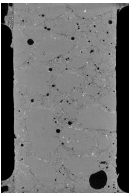
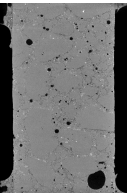
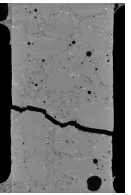
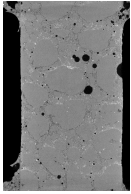
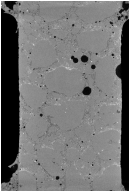
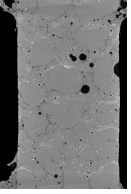
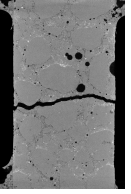
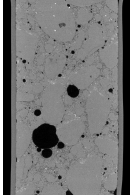
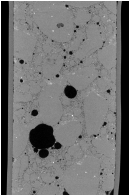
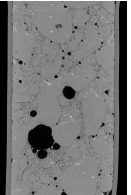
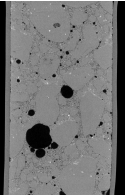
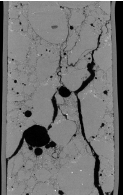
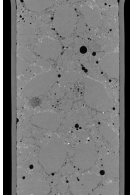
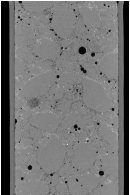
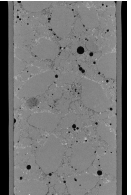
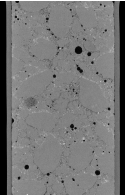
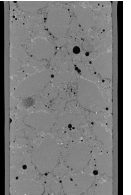
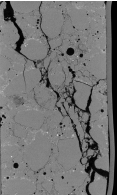
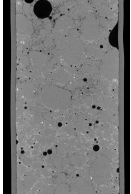
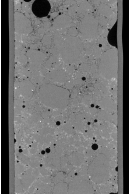
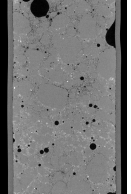
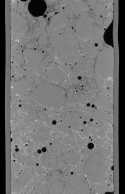
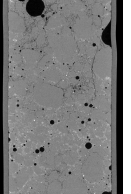
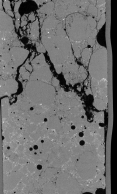
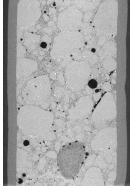
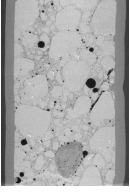
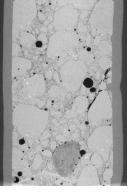
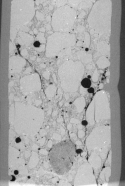
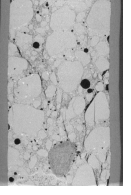
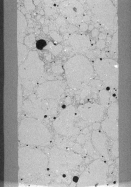
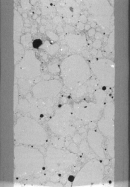
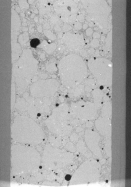
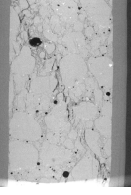
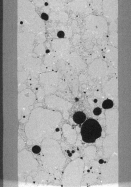
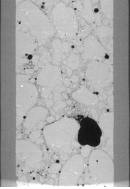
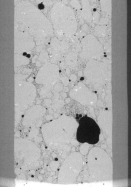
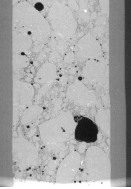
	Test name	Peak stress	1 st scan	2 nd scan	3 rd scan	4 th scan	5 th scan*	6 th scan*
uniaxial tension	T-01	3.2 MPa					n/a	n/a
	T-02	3.5 MPa					n/a	n/a
uniaxial compression	C-01	32.1 MPa						n/a
	C-02	38.8 MPa						
	C-03	39.5 MPa						
triaxial compression	TX5-01 (p=5 MPa)	67.6 MPa						n/a
	TX10-01 (p=10 MPa)	98.1 MPa					n/a	n/a
	TX15-01 (p=15 MPa)	111.5 MPa**					n/a	n/a

Figure 2.19: Table with all the *in-situ* mechanical tests gathered, containing the name of each test, the failure stress (deviatoric for the triaxial tests) and the central vertical slices of the reconstructed 3D images coming from the tomographic scans performed during each test. * For C-02 and C-03 not all scans are shown. ** This stress corresponds to the highest force value recorded before interrupting the loading, due to the excess of the forcemeter's load capacity

Chapter 3

Identifying the micro-structure and following its evolution

This chapter details the analysis of the 3D images coming from the *in-situ* mechanical tests presented in Chapter 2, where small cylindrical micro-concrete samples (*i.e.*, 22 mm in height and 11 mm in diameter) are loaded until failure inside the x-ray scanner of Laboratoire 3SR, under uniaxial tension, uniaxial compression and triaxial compression. The obtained 3D images, acquired at different stages of increasing load during each test, represent a 3D field of x-ray attenuation coefficients inside the micro-concrete specimens, given as scalar greyscale functions. The scanning parameters have been chosen carefully, serving well one of the primary objectives of this study, which is to obtain a realistic representation of the heterogeneous meso-structure of concrete, with all the different phases visible in the greyscale 3D images (as depicted in Fig. 3.1).

A straightforward interpretation of these greyscale images is linked with the morphological characterisation of the meso-structure. This is achieved, in the first place, through the identification of the different phases, and in the second place, through their quantitative characterisation. The question that naturally arises is related then to the way this identified morphology evolves under load and, in turn, to the way this micro-structural evolution can be followed and quantified. At this point, it needs to be mentioned that the analysis of the 3D images presented in this chapter, and generally all over this work, is performed with the open source software `spam` [Stamati *et al.*, 2020], principally developed in Laboratoire 3SR, with parts of it, initially developed to cover the needs of this work.

This chapter describes the analysis of the 3D images coming from the *in-situ* experiments, first considering only a *single* 3D image and characterising the morphology of the meso-structure and afterwards, considering the whole *set* of 3D images (coming from each *in-situ* test) and characterising the evolution of the identified morphology over time. The chapter starts by illustrating a representative example of an x-ray 3D image of micro-concrete, introducing the technical challenge related to the identification of the different phases that arises when concrete is imaged with x-rays. The description of the developed segmentation procedure (and published in [Stamati *et al.*, 2018]) follows, along with its validation, leading to a quantitative characterisation of concrete's meso-structure. The chapter then proceeds into the analysis of the 3D images as an evolving set in time, detailing the method used here to compare and analyse images of deforming materials, in particular Digital Volume Correlation (DVC). A short introduction to the DVC approach adopted in this work follows, together with the description of the specific implementations required to address the challenges imposed by the *in-situ* experiments on micro-concrete

considered herein. The last part of this chapter is dedicated to a detailed description of the measured 3D kinematic fields, as well as the observed failure patterns coming from each *in-situ* mechanical test.

3.1 Extraction of the morphology

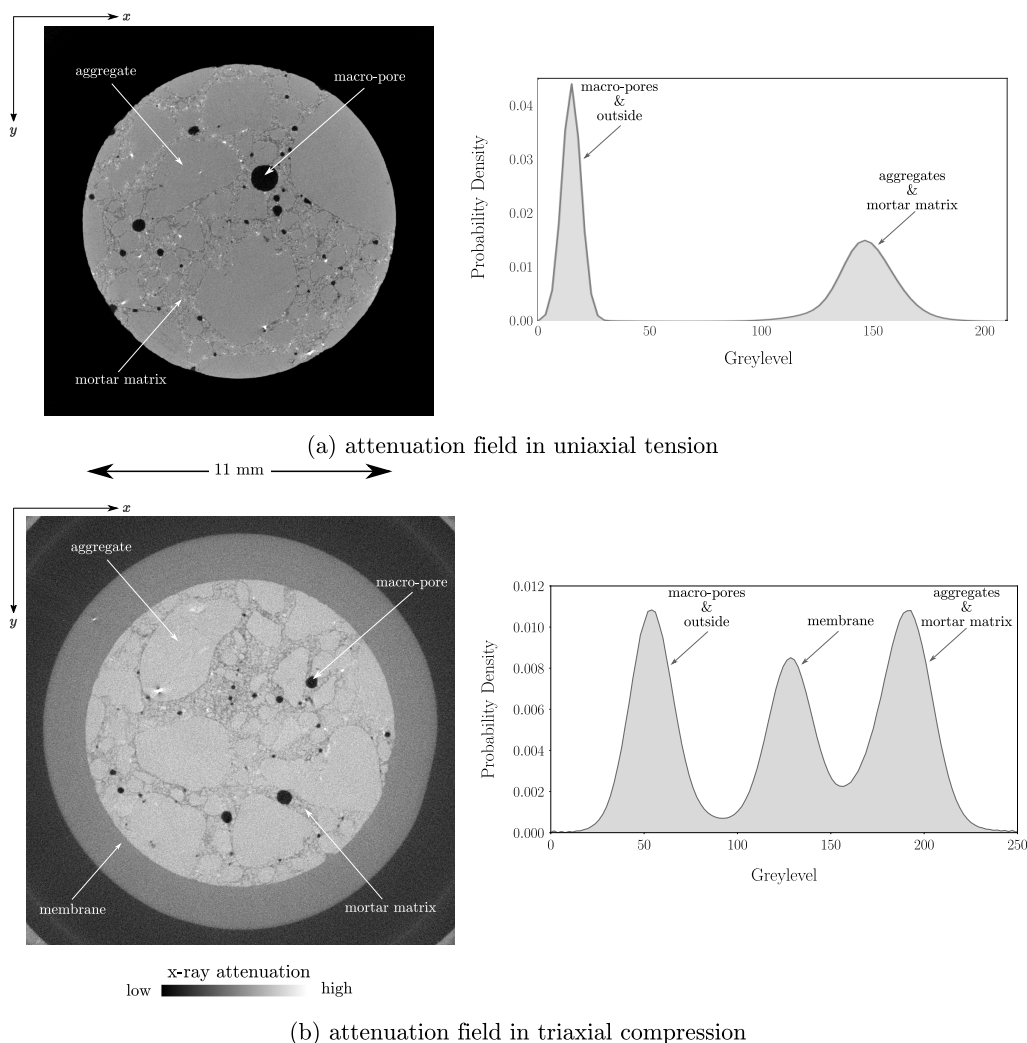


Figure 3.1: Representative horizontal slices and greylevel histograms of the corresponding reconstructed 3D volumes for a uniaxial tension (top) and a triaxial compression (bottom) test. The different phases of concrete's meso-structure are easily distinguishable by eye in both images

Fig. 3.1 shows the mid-height horizontal slices of the reconstructed 3D images coming from the reference (before loading) scans of a uniaxial tension (top) and a triaxial compression (bottom) test. Note that the dynamic ranges of the reconstructed greylevels are different for each test. It should be reminded here that, due to the different loading cells used (see Section 2.3), the scanning parameters for uniaxial and triaxial tests are different. The voxel size is maintained at $13 \mu\text{m px}^{-1}$ for all the tests conducted in this work, however the reconstructed volume in the triaxial test is bigger, due to the surrounding membrane. As explained in Chapter 2, in all cases the scanning parameters are chosen carefully, in order to represent sufficiently the meso-structure of concrete. It can be seen

that in these two images the three different phases (aggregates, macro-pores and mortar matrix) are easily identifiable.

Since an x-ray image represents a reconstructed field of x-ray attenuation coefficients inside the scanned sample, where the greylevel is high, the attenuation is high, corresponding roughly to a dense area. Consequently, macro-pores appear black (lower x-ray attenuation), while coarse aggregates and mortar matrix (mix of finer aggregates and sand) share shades of grey (higher x-ray attenuation). When the constituted materials have similar x-ray attenuation coefficients, which happens to be the case of what exactly described just above (aggregates embedded into mortar matrix), a considerable difficulty is added to the phase identification procedure. In fact, aggregates and mortar matrix are distinguished in these images more because of their *texture* than due to their relative *contrast*, since their greylevels are very close.

This is also depicted in the computed histograms of Fig. 3.1, which show the distribution of the greylevels inside the micro-concrete specimens and the surrounding air. On the top row, the peak on the left represents the void phase together with the outside of the specimen (lower x-ray attenuation), while a peak on the right corresponds to the solid phase (higher x-ray attenuation). The separation, thus, between solid and void phases can be achieved with relative ease, due to their obvious density contrast, whereas, the separation of the solid phase into aggregates and mortar matrix is not straightforward and constitutes a technical challenge addressed in this section.

Note that in the greylevel histogram of the triaxial test, a range of greyvalues correspond to the surrounding neoprene membrane, with an x-ray attenuation in-between the void and the solid phases. This renders the identification and removal of the membrane a necessary initial step before proceeding into a phase segmentation. Besides identifying the border of the cylindrical specimen, in order to facilitate the segmentation procedure, a series of post-reconstruction image analysis operations are required, as explained in the following.

3.1.1 Post-reconstruction steps

Due to imperfections resulted from coring (see Section 2.1.2), the shape of the specimens is not a perfect cylinder, which requires the actual shape of the boundary to be identified. This is achieved here by traversing vertically through the 3D images and finding in every 2D slice the contours (by joining all the continuous points along the boundary which have the same intensity), as implemented in the Python open source library OpenCV [Bradski, 2000]. The biggest identified contour is kept, which represents the outer surface of the membrane (in compression) or the perimeter of the specimen itself (in tension). A so-called binary “mask” image is then defined for each slice by setting all the pixels inside the identified perimeter to one, while the remaining to zero.

Concerning the compression tests, in order to identify the inner surface of the membrane, an erosion (*i.e.*, basic morphological operation for shrinking the identified binary shapes in an image) of the mask is performed. Assuming that the membrane deforms uniformly, the radius of the spherical structuring element used (detailed in Section 3.1.3), corresponds to its thickness. Alternatively, assuming a perfect cylinder, a 3D mask could have been also defined by simply keeping only those pixels of every 2D slice for which their radial distance is smaller or equal than the radius of the specimen. Note that in both cases, by summing the voxels of the binary mask, the total volume of the specimen is directly computed.

Proceeding now into the imaged micro-structure, as discussed in Section 2.2.1, the reconstructed image contains a certain amount of random noise (which is typically modelled as Gaussian), as well as a number of well-known artefacts, such as beam-hardening (due to the polychromatic source used) and rings. Although filters are applied during the acquisition and reconstruction, a series of image analysis operations are still essential for reducing the noise level and correcting the artificially nonuniform spatial distribution of the greyvalues due to beam-hardening.

As a first step, the artificial darkening of the inside of the cylindrical specimen is corrected radially by collecting greyvalues of a representative number of aggregates (highest greyvalues) and macro-pores (lowest greyvalues) which are hand-picked to cover the whole surface (see Fig. 3.2). These values are then linearly fitted with respect to their radial position, separately for each material. A corrected greyvalue for each voxel is obtained as a function of the specimen's radius based on the following equation:

$$GV^{\text{new}}(r) = \frac{GV(r) - GV^{\text{p}}(r)}{GV^{\text{a}}(r) - GV^{\text{p}}(r)} \quad (3.1)$$

where $GV^{\text{new}}(r)$ is the corrected greyvalue for each voxel, r is the distance (in pixels) of every voxel to the centre of the specimen, $GV(r)$ is the initial greyvalue of each voxel, $GV^{\text{p}}(r)$ and $GV^{\text{a}}(r)$ are the fitted initial greyvalues of the macro-pores and aggregates at a distance r , respectively. As a further step, an anisotropic diffusion filter [Perona et Malik, 1990] is applied in order to decrease the noise level, which smooths the image preferably along the directions of weak gradients. The constant conductance parameter in the basic anisotropic diffusion equation is set to a low value (three greylevels) in order to preserve better the image features, mainly the edges of the objects.

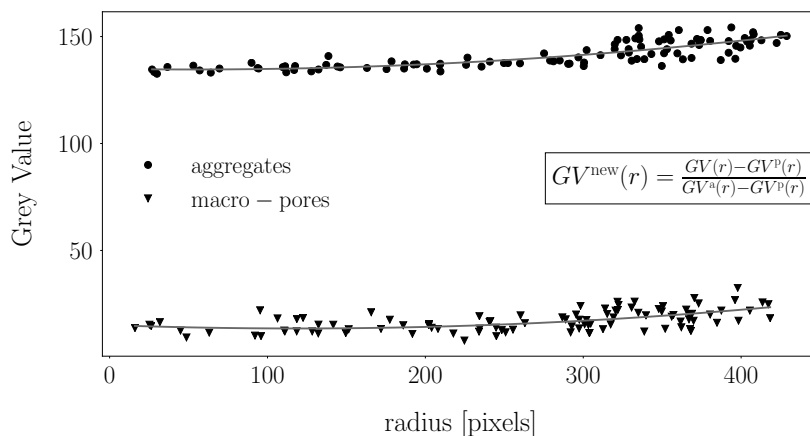


Figure 3.2: Beam-hardening artefact correction by a new repartition of the greyvalues based on their radial position

As an illustration of the post-reconstruction steps, for the representative central horizontal slice of the tensile test depicted on the top row of Fig. 3.1 the result of the application of the mask image, combined with the denoising and beam-hardening correction operations, are depicted in Fig. 3.3. The specimen border is identified and the corrected slice is shown together with the vertical profiles of greyvalues crossing the specimen's center before and after the corrections. The noise level has been reduced from 6.9 to 3.4 greylevels. The effect of the beam-hardening artefact is also reduced, since the artificially lower greyvalues in the center of the cylindrical specimen are corrected. Once

these post-reconstruction steps are completed, the identification of the different phases follows.

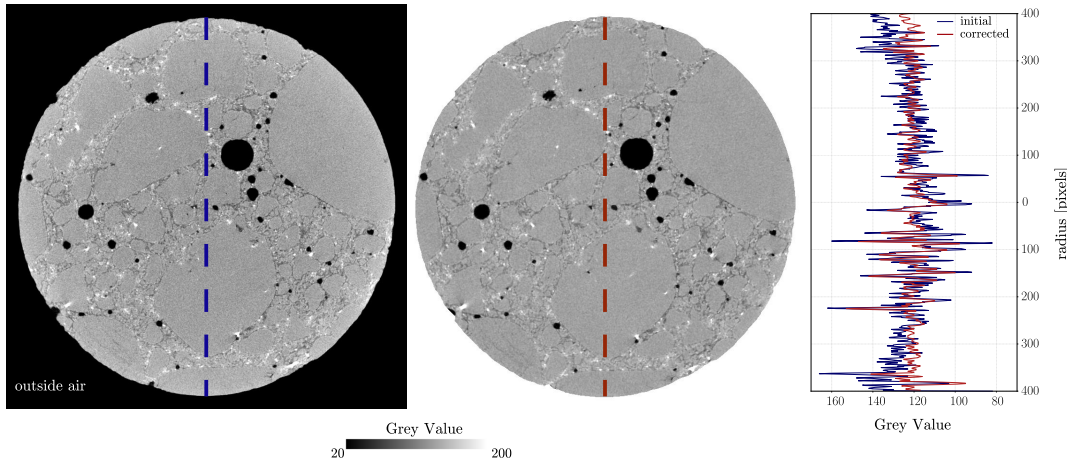


Figure 3.3: Horizontal slice before (left) and after (middle) the beam hardening-artefact correction, the application of the mask image and the denoising operation, presented with a vertical profile of greyvalues (crossing the center of the slice) before and after the corrections

3.1.2 Phase identification

From the computed greylevel histograms it is shown that the segmentation of the macro-pores can be done based on the absolute greyvalues of each phase, by determining the threshold corresponding to the transition between solid and void. The thresholding operation binarises the image, *i.e.*, creating a binary black-and-white image, (such as the mask image described above), by replacing all voxels with greyvalues equal or smaller than some fixed constant - the threshold value - with ones, and all the remaining voxels with zeros (or *vice versa*).

As mentioned in Chapter 1, the porosity observed at the meso-scale refers only to the entrapped air porosity formed during the mixing of concrete, which is known as macro-porosity. In cases where the volume fraction of air in the fresh concrete has been measured with an aerometer and provided that the scanning resolution is good enough (voxel size $\ll 50 \mu\text{m}$), the chosen threshold value should lead to a calculated macro-porosity close to the one measured, determining, thus, the threshold value from a physical measurement. In this work, since such a physical measurement is not available, the macro-porosity is calculated for a range of different threshold values between the two peaks of the corrected histogram and the threshold is selected as the minimum between these two peaks. The calculated macro-porosity as a function of the threshold value and the resulting binary image containing only the macro-pores are depicted in Fig. 3.4.

Moving now to the solid phase segmentation, as already mentioned, the relative contrast between aggregates and mortar matrix is low, resulting in a combined peak in the computed histogram (see Fig. 3.1). At the scale of observation, however, mortar matrix is a more heterogeneous material compared to aggregates. This means that the *variation* of greyvalues inside this material should be more irregular, a characteristic which ends up being the key for their separation. Instead of separating the solid phase based on the *absolute* greyvalues (related to the density of the material), a separation based on the

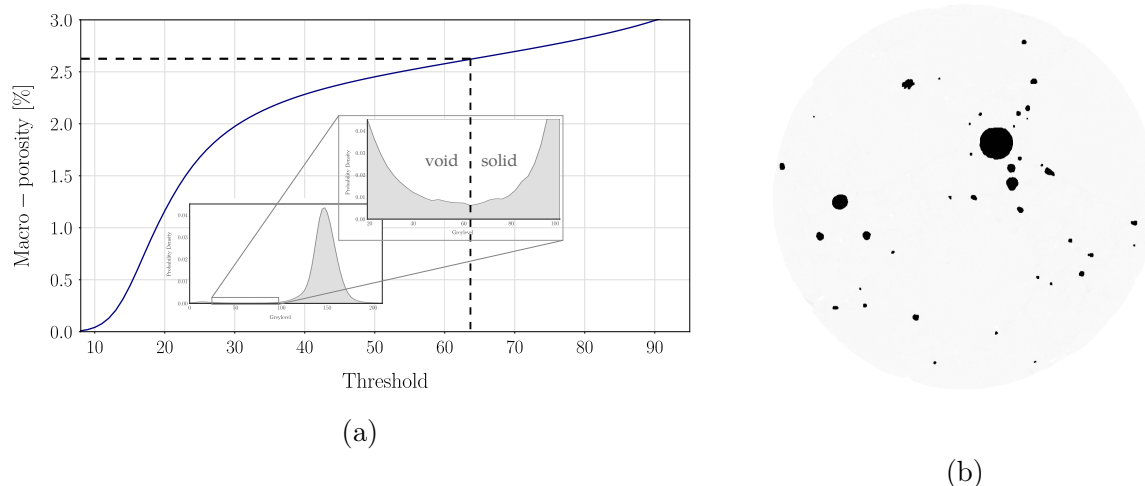


Figure 3.4: Segmentation of macro-pores based on the mean greyvalues of each phase: (a) relation between the selected threshold and the resulted macro-porosity. The optimal threshold value is chosen to be the minimum value between the two peaks of the histogram. (b) binary slice of the macro-pores

variation of the greyvalues (related to the homogeneity of the material) is the approach adopted in this work. From an image analysis point of view, this difference (in homogeneity) can be revealed by an application of a spatial variance filter. More specifically, a sequence of morphological operations and filters using structuring elements are needed in order to achieve the segmentation of the solid phase in the micro-concrete specimens studied herein as detailed below.

As a first step, the variance map of the corrected 3D image is calculated, based on a selected structuring element, given by the formula: $\text{VAR}(X) = E(X^2) - E(X)^2$, where $E(X)$ is the averaged greyscale image over the structuring element. Here it should be mentioned that a structuring element is a binary matrix, defined by its shape and size, that selects a local neighbourhood around a voxel of interest. There is a fair amount of liberty in the choice of the structuring element strongly affecting the result of the morphological operation. Setting the size of the structuring element is similar to setting the observation scale, while by choosing a particular shape of the structuring element, is a way of differentiating some objects (or parts of objects) from others, according to their shape or spatial orientation [Serra, 1983]. Here, the *size* is defined as the length of the edge of the cube that contains the structuring element.

As a general rule, the bigger the structuring element size, the higher the deterioration of the shape of the segmented aggregates. Consequently, the structuring element should be just large enough to separate low and high variance regions, while remaining sufficiently small to capture the smallest aggregates to be segmented, but also to preserve the details of the aggregates' shapes. To evaluate this shape deterioration, the variance filter is applied to a set of already segmented aggregates (coming from the segmentation procedure), for different sizes and shapes (cubes and spheres) of structuring elements. The percentage of voxels affected by the filter application is given in Fig. 3.5. The volume (*i.e.*, the sum of the ones contained in the binary matrix) of the structuring element is the dominant parameter that affects the final result, with the shape being a second order parameter.

For the *in-situ* tests studied here, a spherical structuring element of 9 voxels size is

selected, which considering that the voxel size in the reconstructed images is $13\ \mu\text{m}$, means that the smallest object to be captured is $0.1\ \text{mm}$. Note that as shown in Table 2.1, the micro-concrete composition considered herein consists of aggregate sizes ranging between 0.5 and $4\ \text{mm}$. The computed variance map of the representative horizontal slice is shown in Fig. 3.6a. Afterwards, by isolating with a thresholding operation the lower variance areas (aggregates and macro-pores) and discarding the already identified macro-pores (see Fig. 3.4), a binary image containing only the segmented aggregates is obtained (see Fig. 3.6b).

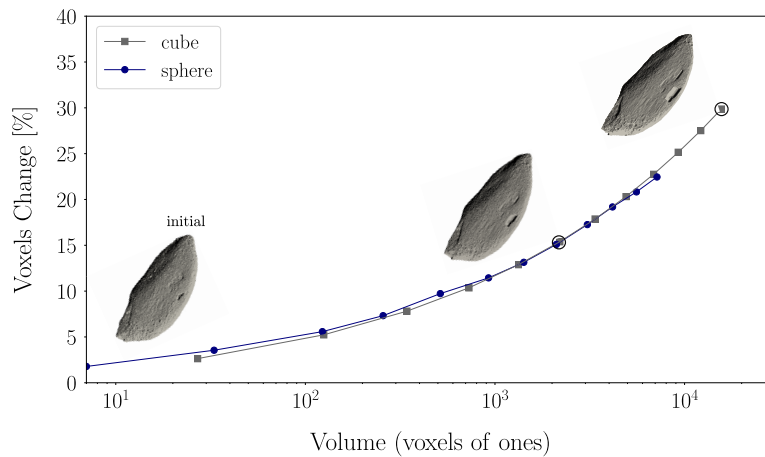


Figure 3.5: Deterioration of the aggregates' shape after the application of the variance filter as a function of the volume (number of ones) of the structuring element. Illustrative example of an aggregate's morphological evolution between the initial state and after the application of a variance filter with a cubical structuring element of 15 and 25 voxels size

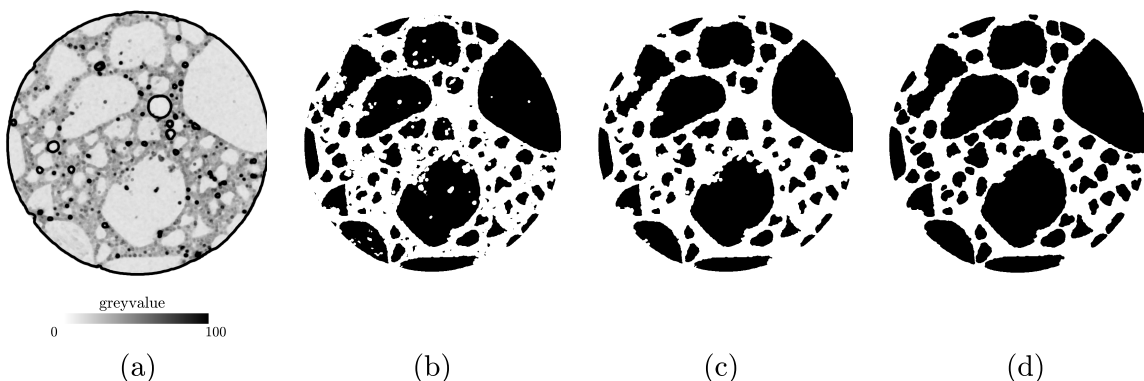


Figure 3.6: Developed procedure for extracting the aggregates from a 3D image coming from a concrete x-ray scan: (a) calculation of the variance map based on a specific structuring element, (b) thresholding the variance image and keeping only the aggregates (low variance regions), (c) morphological noise removal, filling holes and discarding the small size objects and (d) morphological dilation to retrieve the original size and shape of the objects yielding the final binary image of the segmented aggregates

In order to retrieve the original size and shape of the identified aggregates, a series of morphological filters is then applied. The morphological noise is firstly removed by an application of an opening morphological operation (*i.e.*, a dilation of the erosion of the image), followed by a filling holes operation for closing the artificially created holes inside the aggregates. Afterwards, based on the aggregate's size distribution curve used for the casting of the micro-concrete samples (see Table 2.1), any objects with a size smaller than 0.5 mm are discarded (see section 3.1.4 for details), leading to the image depicted in Fig. 3.6c. As a last step, a dilation is performed to retrieve the original size of the aggregates, with a structuring element of the same shape and half the size as the one used for the variance filter, leading to the final binary image of segmented aggregates (see Fig. 3.6d).

The segmentation procedure described above results in two 3D binary images: one containing the macro-pores and one containing the aggregates. The combination of these two binary images with the remaining space inside the mask image (*i.e.*, corresponding to the mortar matrix) leads to the segmented discrete 3D image, where each phase of concrete's meso-structure is identified, as shown in Fig. 3.7.

By combining now the trinarised image with the initial greyscale one, the distribution of the greylevels inside each phase is obtained. From the probability density functions depicted in Fig. 3.8, it is shown that the mean values of aggregates and mortar matrix are indeed very close: 137 and 135, respectively, revealing that a separation of the solid phase based on a single (mean) threshold value would have been impossible. However, the difference in variation is rather clear, demonstrating that the proposed segmentation procedure based on a variance filter is a simple and effective tool.

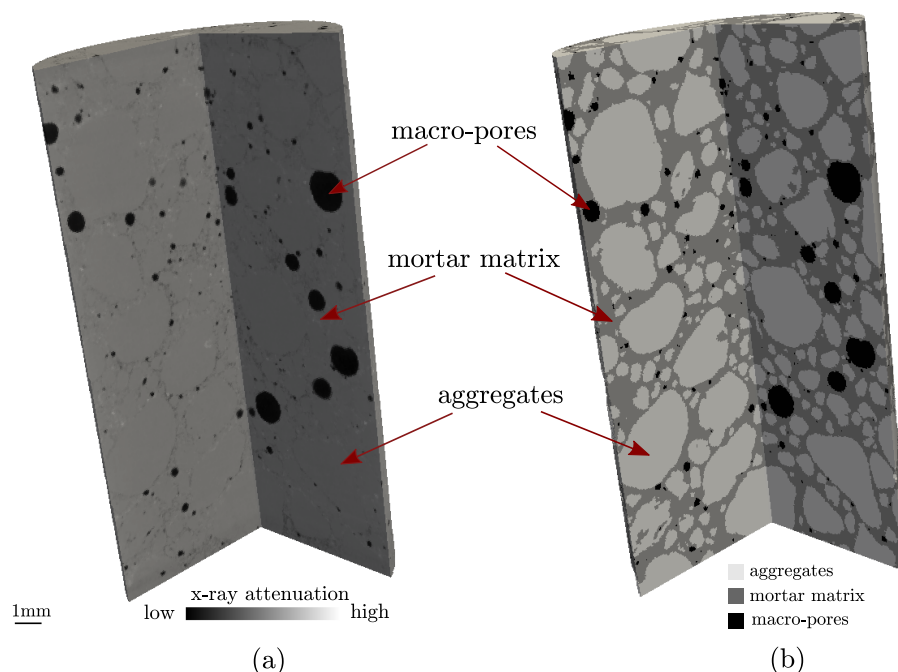


Figure 3.7: Illustrative example of phase identification on the reference (before loading) scan of the T-01 uniaxial *in-situ* tensile test: (a) reconstructed greyscale 3D image, (b) segmented 3D image, where each phase of concrete's meso-structure is identified (aggregates, macro-pores and mortar matrix)

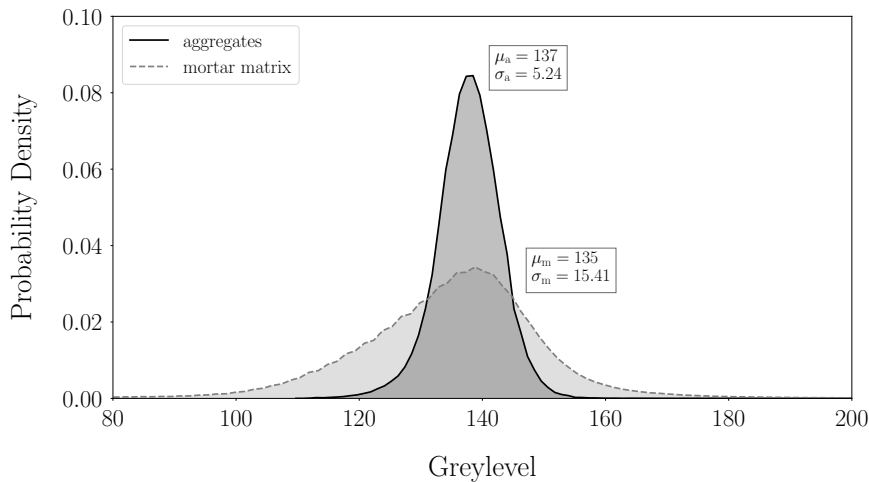


Figure 3.8: Distribution of greyvalues inside the aggregates and mortar matrix in the reference greyscale image of the T-01 test. The resulting mean values and standard deviations are respectively equal to 137 and 5.24 for aggregates, while 135 and 15.41 for mortar matrix

It should be mentioned here that the reference scan of the first uniaxial tension test (T-01) has been selected as an illustration of the phase identification procedure. The exact same steps are followed for all the *in-situ* tests conducted in this work, leading to segmented 3D images for all the different micro-concrete samples studied.

3.1.3 Morphological measurements

Once the three phases are separated, a quantitative characterisation of the morphology is possible. Individual aggregates and macro-pores can be identified by traversing the binary 3D image of each phase and assigning to all voxels that are in contact with each other (*i.e.*, belonging to each particle) a single, unique positive integer, *i.e.*, label number, creating thus a so-called “labelled” image. The labelling of the individual particles can be done using a so-called connected component analysis, based on a selected structuring element that defines the type of connectivity between neighbouring voxels. Here, in order to ensure that touching aggregates are identified as different, a simplified interface to the ITK morphological watershed algorithm [Beare et Lehmann, 2006] is used to label the binary images, as implemented in `spam`.

Starting from a labelled image, a number of particle characteristics can easily be computed, the most straightforward being the volume (in voxels) of each labelled object (by summing the number of voxels having the same label number). The curve showing the relationship between sieves with specific openings as a function of the percentage of the aggregate’s volume passing each sieve, known as grain size distribution, is widely used for characterising aggregates. This curve is known to affect the compacity of the granular skeleton and consequently the mechanical response of concrete [Mehta, 1986, Garboczi et Bentz, 1993]. By computing the diameter of a sphere that would have the same volume with the one of each labelled aggregate (which is not spherical), a so-called equivalent sphere diameter can be used to define the size of each aggregate and relate it, in turn, with the sieve size. Note that the step of discarding the smaller size particles mentioned during the segmentation procedure, is actually based on this calculation of equivalent diameters of the identified objects.

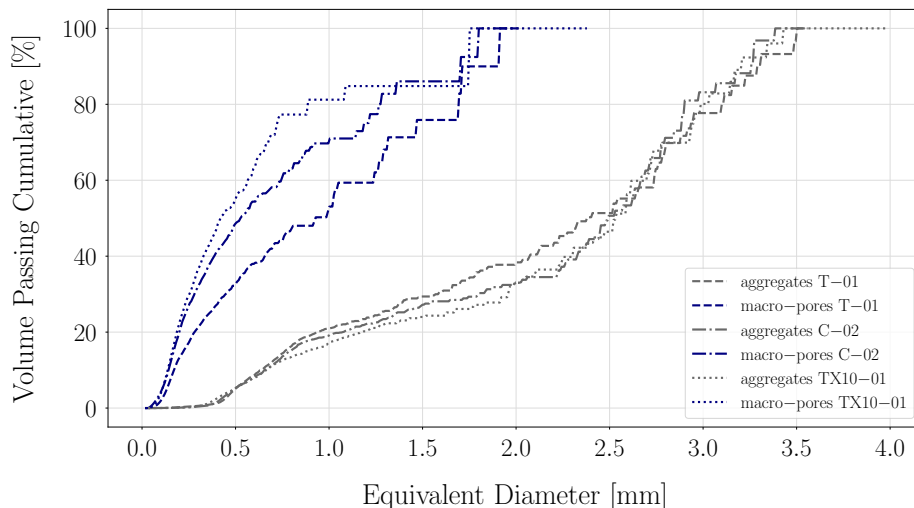


Figure 3.9: Aggregates and macro-pores size distribution curves for three tested samples

For roughly spherical objects, such as the macro-pores considered here, their size is unambiguously defined by their diameter. Aggregates and macro-pores size distribution curves can then be obtained, as shown in Fig. 3.9 for three representative tested samples. It should be kept in mind that the micro-concrete composition considered herein consists of aggregate sizes ranging between 0.5 and 4 mm (see Table 2.1), values that are in accordance with the computed size distribution curves shown in Fig. 3.9. It can be observed that the discrepancy of the computed sizes between the different tests is lower for aggregates compared to macro-pores, which is expected, since the latter are randomly created during the mixing of concrete [Neville *et al.*, 1995]. It is also shown that the objective to create samples with rather small dimensions compared to the size of the largest heterogeneities is achieved. About 50% of aggregates measure equivalent diameters higher than 2.5 mm and about 30% of macro-pores' measure equivalent diameters higher than 1 mm.

Table 3.1: Volume fraction (VF) for each phase calculated from the segmented 3D images coming from the reference (before loading) scans of each mechanical test performed

Test	Macro-pores VF [%]	Aggregates VF [%]
T-01	2.6	50.1
T-02	2.9	49.7
C-01	3.9	51.3
C-02	2.6	49.4
C-03	3.3	45.3
TX5-01	1.7	47.9
TX10-01	1.9	45.7
TX15-01	2.7	42.9

Besides the sizes of the identified objects, global descriptors, such as the volume fraction of each phase can be easily calculated. Table 3.1 gathers for each mechanical test the calculated volume fraction of each phase coming from the segmented 3D images of the reference (before loading) scans. The computed macro-porosity ranges between 1.7 and 3.9%, while the percentage of aggregates ranges between 42.9 and 51.3%. More detailed

measurements and a number of particle characteristics can also be made, computing for instance the surface area, the shape and the orientation of each identified object, with a description of some of these measurements and their potential effect on the macroscopic mechanical response discussed in Chapter 5.

3.1.4 Validation of the segmentation procedure

Since one of the primary objectives of this work is to reveal the impact of the meso-scale heterogeneities of concrete on its macroscopic mechanical response, the realistic representation of the heterogeneous meso-structure is of major importance. This renders the reliability and the quality of the segmentation procedure presented above crucial.

In this context, as a first step of the validation procedure, an x-ray scan of a representative set of aggregates used for an ordinary concrete mix (largest aggregate size of about 1 cm) embedded into a gel is performed (see Fig. 3.10a).

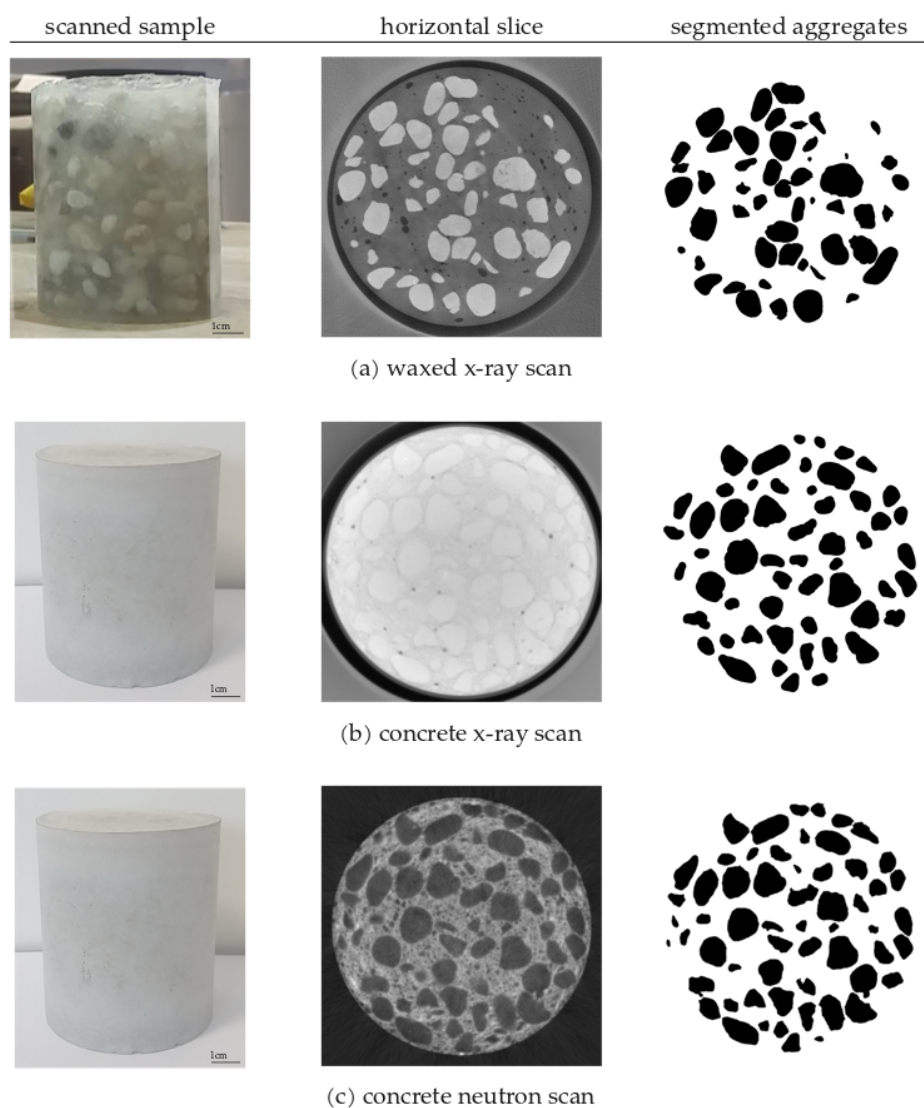


Figure 3.10: Validation of the aggregates segmentation procedure. A representative set of coarse aggregates is scanned three times and extracted as 3D binary images: (a) embedded in gel, (b) casted as regular concrete and scanned with x-rays, (c) same concrete sample scanned with neutrons

The gel is selected here as the surrounded material, since it limits the contacts between aggregates, while it decreases the probability of the x-ray beam being attenuated as it passes through it. A direct extraction of the set of aggregates is then possible, by simply thresholding the reconstructed 3D image, yielding a binary 3D image of the aggregates, without having performed any image analysis operations that might have affected any of their morphological characteristics.

The exact same set of aggregates is then used to cast a *real concrete* sample and a second x-ray scan follows with a voxel size of $50\ \mu\text{m}$. The developed phase identification procedure is applied, resulting to a second binary 3D image of the same set of aggregates. A cubical structuring element of 25 voxels size is used for the variance filter, meaning that this time, aggregates smaller than $1.3\ \text{mm}$ can not be captured (see Fig. 3.10b). As a further validation step, a neutron tomography scan is performed on the same concrete specimen (see Fig. 3.10c). It should be mentioned here that the neutron attenuation coefficient of the same material can be very different compared to the x-ray one, due to the different physics involved when neutrons interact with matter. It is exactly this difference in the attenuation coefficients (providing, in fact, complementary attenuation fields) that makes the combination of these two imaging modalities an extremely valuable tool for the study of various meso-scale mechanisms in concrete (see for example [Trtik *et al.*, 2011, Roubin *et al.*, 2019]). In the presented case, there is an obvious difference in contrast between the different phases in the reconstructed 3D image coming from the neutron scan, which clearly discriminates aggregates from mortar matrix. Consequently, a third binary 3D image of the same set of aggregates is obtained through a simple thresholding operation based on the absolute (mean) greyvalues.

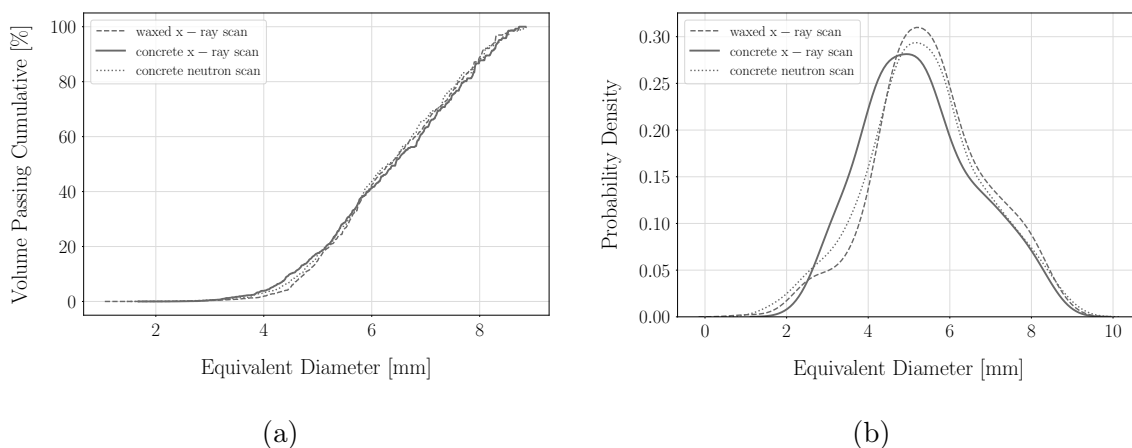


Figure 3.11: Comparison of the aggregate size distribution curves coming from the 3 different scans: (a) cumulative distribution function, (b) density function (where the y axis is normalized frequency so that $\int = 1$)

For a qualitative comparison, Fig. 3.10 presents the scanned sample, along with the middle horizontal greyscale 2D slice coming from the reconstructed 3D image of each scan and the corresponding binary image of the segmented aggregates. To give a more quantitative evidence, the three different binary 3D images of the same set of aggregates are labelled (as explained in the previous section) and the particle size distribution curves of the extracted aggregates are plotted in Fig. 3.11. The comparison of these three curves although satisfactory, is not enough to prove that indeed, the extraction from the concrete x-ray scan is necessarily successful.

For this reason, the binary images of the scanned concrete samples coming from the two different modalities (x-rays and neutrons) are locally compared, by registering them (*i.e.*, aligning them, as explained in the second part of this chapter) by eye and then subtracting from one another. The number of voxels that do not coincide after the registration of these two images is equal to 4% of the sample's volume. Assuming that the segmented image obtained from neutron tomography is the reference, this provides a quantitative order of magnitude of the error of the x-rays scan segmentation procedure. Note that this error would probably be even lower with the images of the micro-concrete samples actually studied in this work (voxel size of 13 μm), for which unfortunately no neutron scan was performed. In any case, according to this validation, the proposed method leads to a reliable separation of the three phases and consequently to a realistic representation of concrete's meso-structure.

3.2 Methodology for following the micro-structural evolution

The first part of this chapter detailed the developed procedure, where starting from an x-ray scan of micro-concrete, specific image analysis tools are applied to finally obtain a trinary 3D image, where each phase of the material's meso-structure is separated. Phase identification is crucial in order to study the impact of the meso-scale heterogeneities (aggregates and macro-pores) of concrete on its macroscopic response, which requires, in the first place, these heterogeneities to be individually accessed and quantified. Having identified the morphology, the characterisation and quantification of the micro-structural evolution as the load progresses is the question that naturally arises.

Full-field measurement techniques have been proven an extremely powerful tool in experimental solid mechanics to address this issue, providing direct access to experimental kinematic fields. Among them, the technique used in this work, Digital Image Correlation (DIC), dating back in the early 1980s [Lucas *et al.*, 1981, Peters et Ranson, 1982, Sutton *et al.*, 1983] has been extensively used for obtaining kinematic fields from digital images, being a robust and accurate method. Its extension in 3D, Digital Volume Correlation (DVC), initially emerged in 1999 [Bay *et al.*, 1999] has undergone a rapid development in the last decades. More specifically, the DVC technique coupled with data coming from *in-situ* experiments provide the full 3D displacement field between a reference and a deformed state, allowing unprecedented advances in the micro-scale understanding of the mechanical behaviour of materials.

In what follows, the basic principles involved in the so-called "local" DVC approach adopted in this work are detailed, along with the specific implementations required to address the challenges imposed by the *in-situ* experiments on the micro-concrete samples studied here.

3.2.1 Basic principles of Digital Volume Correlation (DVC)

Formulation of correlation procedure

The basic principle of DVC is finding a transformation that links two 3D images of the same sample acquired at different deformation increments. Generally, the first image is referred to as the "reference" image $f(\mathbf{x})$ and the second, acquired after an increment of deformation, as the "deformed" image $g(\mathbf{x})$, where f and g are scalar functions of the

spatial coordinates, denoting the greyvalues at each discrete 3D voxel spatial position $[z, y, x]$.

The DVC procedure followed in this work is implemented in the open source software `spam` [Stamati *et al.*, 2020] based on the formulations found in [Lucas *et al.*, 1981], [Hild et Roux, 2012] and [Tudisco *et al.*, 2017]. A deformation function, called hereafter Φ , is sought, such that the material point in the position \mathbf{x} in the reference image corresponds to the same material point in the position $\mathbf{x}' = \Phi \cdot \mathbf{x}$ in the deformed image. For any voxel position in the region of interest the following expression can then be written:

$$f(\mathbf{x}) = g(\Phi \cdot \mathbf{x}) \quad (3.2)$$

known as the equation of optical flow (or the greylevel conservation), which is the basic assumption behind digital volume (or image) correlation.

At this point, different choices can be made for the deformation function in order to regularise the system. In the present case, the deformation function is considered linear and homogeneous, with 12 degrees of freedom, accounting for affine transformations: translation, rotation, normal and shear strain. Following a standard practice in stereoDIC [Sutton *et al.*, 2009], it is expressed in homogeneous coordinates and represented by a 4×4 matrix Φ with a trivial padded last row and 12 unknowns which reads:

$$\Phi = \begin{bmatrix} \Phi_{zz} & \Phi_{zy} & \Phi_{zx} & t_z \\ \Phi_{yz} & \Phi_{yy} & \Phi_{yx} & t_y \\ \Phi_{xz} & \Phi_{xy} & \Phi_{xx} & t_x \\ 0 & 0 & 0 & 1 \end{bmatrix} \quad (3.3)$$

The first three rows of the fourth column describe rigid-body translations $[t_z, t_y, t_x]$ and the top corner 3×3 sub-matrix corresponds to the familiar, from continuum mechanics, deformation gradient tensor, \mathbf{F} . A right Cauchy polar decomposition theorem is used to decompose this 3×3 tensor into rotations, normal and shear strains, *i.e.*, $\mathbf{F} = \mathbf{R} \cdot \mathbf{U}$. By padding a unit coordinate to the position vector $\mathbf{x} = [z, y, x, 1]$ (*i.e.*, homogeneous coordinates), the mapping of coordinates is achieved such that: $\mathbf{x}' = \Phi \cdot \mathbf{x}$.

The point \mathbf{x} in the reference image has integer voxel coordinates, while the point $\mathbf{x}' = \Phi \cdot \mathbf{x}$ in the deformed image has, in general, non-integer coordinates. Therefore, its greylevel can only be evaluated by means of some interpolation scheme, making use of the greylevels of the neighbouring voxels. By interpolating the greyvalues of all the voxels, a *corrected* image can then be constructed, as $\tilde{g}(\mathbf{x}) = g(\tilde{\Phi} \cdot \mathbf{x})$, with $\tilde{\Phi}$ being a trial deformation function. Generally, different choices of interpolation schemes exist, among them, spline interpolations of various orders are available in `spam`, with zero order being a nearest neighbour interpolation, first order a trilinear, third order a cubic, *etc.* In this work, a trilinear interpolation scheme is used in the coarser scale of analysis (see below), for speeding up the whole procedure, while for obtaining the final corrected deformed image in the finest level of resolution, a third order interpolation scheme is used (more computationally expensive).

Due to acquisition noise and other sources of imperfection [Grédiac et Hild, 2013], [Hild et Roux, 2012], Eq. (3.2) is actually never strictly satisfied. Therefore, it is normally formalised to tolerate white Gaussian noise and is written in a weak form over the domain of interest (containing more than 1 voxel). The correlation procedure consists then in minimising an objective function that is based on a suited similarity measure between the reference image, $f(\mathbf{x})$, and the deformed one, $\tilde{g}(\mathbf{x})$, corrected by $\tilde{\Phi}$.

The similarity criterion used here, compatible with the assumption of white Gaussian noise [Buljac *et al.*, 2018], is the sum of squared differences (SSD) formulating the objective function as:

$$\eta^2 = \frac{1}{2} \sum_{\mathbf{x} \in \Omega} \left(f(\mathbf{x}) - g(\tilde{\Phi} \cdot \mathbf{x}) \right)^2 \quad (3.4)$$

where η^2 is the error over the considered domain, Ω , representing the quality of the match between the two images. The solution of the DVC procedure is hence the deformation function Φ that minimises the functional:

$$\Phi = \underset{\tilde{\Phi}}{\operatorname{argmin}} \mathcal{T}(\tilde{\Phi}) \quad \text{where} \quad \mathcal{T}(\tilde{\Phi}) = \eta^2 \left(f(\mathbf{x}), g(\tilde{\Phi} \cdot \mathbf{x}) \right) \quad (3.5)$$

Following the formulation written in [Lucas *et al.*, 1981] that takes advantage of the spatial gradient of the image, a first order Taylor expansion is used to linearise the system about a solution $\tilde{\Phi}$. As proposed in [Tudisco *et al.*, 2017] (see Eq. (5)-(13)), a Gauss-Newton iterative scheme is implemented to solve the non-linear problem of the minimisation procedure, consisting in successive corrections of the estimated deformation function, assuming that the corrections $\delta\Phi$ remain small:

$$g(\Phi^{(n+1)} \cdot \mathbf{x}) = g(\Phi^{(n)} \cdot \mathbf{x}) + \nabla g(\Phi^{(n)} \cdot \mathbf{x}) \cdot \delta\Phi^{(n+1)} \cdot \Phi^{(n)} \cdot \mathbf{x} \quad (3.6)$$

where ∇g is the augmented gradient vector of the deformed image expressed in homogeneous coordinates, *i.e.*, $\nabla g = [g_{,z}, g_{,y}, g_{,x}, c_0]$, with the 4th component c_0 not yet defined. This equation is made more compact by introducing $\mathbf{x}^{(n)} = \Phi^{(n)} \cdot \mathbf{x}$ and the corrected image at iteration (n): $\tilde{g}^{(n)}(\mathbf{x}) = g(\Phi^{(n)} \cdot \mathbf{x})$:

$$g(\Phi^{(n+1)} \cdot \mathbf{x}) = \tilde{g}^{(n)}(\mathbf{x}) + \nabla \tilde{g}^{(n)}(\mathbf{x}) \cdot \delta\Phi^{(n+1)} \cdot \mathbf{x}^{(n)} \quad (3.7)$$

The objective function is then expanded up to the second order in $\delta\Phi^{(n+1)}$ yielding:

$$\begin{aligned} \mathcal{T} \left[\Phi^{(n+1)} \right] = \sum_{\mathbf{x} \in \Omega} & \left[[\eta^2] + ([\eta^2]_{,2}) \left(\nabla \tilde{g}^{(n)} \cdot \delta\Phi^{(n+1)} \cdot \mathbf{x}^{(n)} \right) \right. \\ & \left. + \frac{1}{2} ([\eta^2]_{,22}) \left(\nabla \tilde{g}^{(n)} \cdot \delta\Phi^{(n+1)} \cdot \mathbf{x}^{(n)} \right)^2 \right] \end{aligned} \quad (3.8)$$

where the notations $[\eta^2]_{,2}$ and $[\eta^2]_{,22}$ refer to the partial derivatives with respect to the second argument once or twice, respectively and η^2 as well as its derivatives are computed at point $(f, \tilde{g}^{(n)})$. As proposed in [Tudisco *et al.*, 2017], in the spirit of Voigt notation of the strain matrix, the components of the matrix $\delta\Phi_{ij}^{(n+1)}$ are relabelled in a single index m , such that $\delta\Phi_{i(m)j(m)}^{(n+1)} = \delta\Phi_m^{(n+1)}$. Differentiating the above equation with respect to $\delta\Phi^{(n+1)}$ and solving for the zero-point leads to the determination of $\delta\Phi^{(n+1)}$ from the linear system:

$$M_{mp}^{(n)} \delta\Phi_p^{(n+1)} = A_m^{(n)} \quad (3.9)$$

where the Hessian and the Jacobian, respectively take the form:

$$M_{mp}^{(n)} = \sum_{\mathbf{x} \in \Omega} \left(x_{j(m)} \tilde{g}_{,i(m)}^{(n)} \right) \left(x_{j(p)} \tilde{g}_{,i(p)}^{(n)} \right) \quad (3.10)$$

$$A_m^{(n)} = \sum_{\mathbf{x} \in \Omega} (f - \tilde{g}^{(n)}) \left(x_{j(m)} \tilde{g}_{,i(m)}^{(n)} \right) \quad (3.11)$$

In these equations x_j refers to the j -th component of the vector \mathbf{x} (including the padded unit coordinate), while $\tilde{g}_{,i}$ refers to the first three components of the vector $\nabla \tilde{g}$ (excluding the 4th c_0 component), so that the unknown $\delta \Phi$ is a 12-component vector.

The correction of the deformation function at iteration $(n + 1)$ is performed multiplicatively around the identity matrix:

$$\Phi^{(n+1)} = \Phi^{(n)} (\mathbf{I} + \delta \Phi^{(n+1)}) \quad (3.12)$$

allowing large transformations to be captured. Note that in case of small transformations, an additive correction (*i.e.*, $\Phi^{(n+1)} = \Phi^{(n)} + \delta \Phi^{(n+1)}$) could be performed.

It should be mentioned here that greylevel gradients are computed as centered finite differences. In order to avoid recomputing the gradient of the corrected deformed image (*i.e.*, $\nabla \tilde{g}^{(n)}(\mathbf{x})$) in every iteration (which can be computationally expensive), the gradient of the reference image can be used, so that the matrix \mathbf{M} is computed once and for all and only the vector \mathbf{A} is updated on each iteration [Roux *et al.*, 2008], [Pan *et al.*, 2014].

The convergence of this iterative procedure allows the measurement of the deformation function Φ that minimises the functional of Eq. (3.4) to be obtained. The convergence criterion as implemented in `spam` is based on the norm of the deformation function increment between two successive iteration steps. In this study it is set as: $\|\delta \Phi\| < 10^{-6}$. A maximum number of iterations (here 300) is set as a limit to stop the iterative procedure in case that the convergence criterion is not satisfied. The iterative algorithm is also interrupted based on divergence conditions. These are set as limits on displacement changes: *i.e.*, a component of the translation vector is bigger than 50% of the maximum dimension of the reference image, volumetric changes: *i.e.*, the volumetric strain is bigger than 300%, and global error changes: *i.e.*, the normalised greylevel residual (see below) at the current iteration is twice bigger than the one at the previous iteration.

Correlation residuals

The quality of the match at the end of the correlation procedure is of utmost importance, with the best indicator being the so-called “residual field”: $\eta(\mathbf{x}) = |f(\mathbf{x}) - g(\Phi \cdot \mathbf{x})|$ over the whole considered domain. It is a “voxelwise” measure of the relevance of the proposed solution corresponding to the difference (in greylevels) between the images in the reference and the deformed configuration, after the latter has been corrected by the measured deformation function. Regions with high greylevel residual values correspond to features in the fields that were not captured by the correlation procedure: noise and artefacts, divergence problems or model phenomenological errors, such as for example, unexpected discontinuities in the displacement field, *i.e.*, cracks.

The residual field is a valuable and simple way of assessing the level of uncertainty in the kinematics measurement by performing correlations between images that no deformation has occurred, as it will be discussed in Section 3.2.3. Moreover, provided that the deformation function Φ used here accounts only for linear transformations, residual fields are very useful indicators of non-linear transformations, such as cracks. The use of correlation residual fields to detect and extract cracks has been already illustrated through various examples (see for instance [Hild *et al.*, 2013, Chateau *et al.*, 2018] related to cementitious materials) and is also applied in this work, as shown in Section 3.3.

“Binning” or “multiscale” approach

The regularised functional presented above is generally smooth and convex around the global minimum allowing gradient-based methods to converge successfully after a few iterations. However, in cases of large deformations (large compared to the correlation length of the micro-structure (see Section 3.2.2)), the convergence might be difficult, since the applicability of the Taylor expansion is questionable. In other words, if the initialisation of the deformation Φ is too far from the actual solution, the above algorithm may diverge or converge to a local minimum. In order to resolve this problem, a coarse-fine strategy is followed here, known as “multiscale” approach [Lucas *et al.*, 1981, Hild et Roux, 2006, Helfen *et al.*, 2007], which consists in performing progressive correlations using previously obtained deformation functions on a coarser scale as an initial condition to a finer scale.

Usually, the bin levels are chosen as geometric series of 2^l . A 2-binning corresponds to averaging the greylevels of $2 \times 2 \times 2$ neighbouring voxels, dividing thus by 2 the number of voxels in each direction, a 4-binning dividing by 4 the number of voxels in each direction, *etc.* Once the largest transformations have been accounted for by a successful correlation at a given level of “binning”, the solution is used to initialise a correlation in a smaller “binning” level (finer scale) progressively restoring details (higher frequencies) on images, until the final step of the multiscale approach is reached, which is the correlation of the original images, without any loss of information. An illustrative example of this multiscale approach is given just below, in the context of presenting the registration between two images.

Registration of a pair of images

The formulation of the correlation procedure presented above is based on the minimisation of the sum of the squared differences, with respect to the unknown degrees of freedom, over the considered domain Ω . Provided that the iterative algorithm will only converge if the initial estimation of Φ is close to the right solution, in this work, as an initial step, all voxels belonging to each image are considered as the domain Ω and hence an overall deformation function is computed, which roughly maps all of the reference image to the deformed one. This results to an overall alignment between the two images, known as “registration” (non-rigid in this case), which is described by a *single* homogeneous deformation function, Φ_{reg} . In this study, the registration is performed at downscaled “binned” images, benefiting from the robustness and the speed-up offered by the multiscale coarse-fine procedure described above.

As an illustration the registration algorithm is run for the pair of images coming the second step of a uniaxial compression test, firstly at a bin-2 level and then at the original images, using the result of the bin-2 level as an initial guess. Fig. 3.12 presents the calculated rigid-body motion over the cumulative iterations. It is shown that the majority of the rigid-body motion is accounted for with the “binned” images, with the registration at a bin-1 level converging at a slightly different solution. This is especially true for the translation in the axial direction, which is also the direction of loading. Note that a registration performed directly on the original images converges (to the same transformation) after 24 iterations, which is computational more expensive compared to a total 14 iterations with the multiscale approach.

In case of a pure rigid-body translation, registering two images involves just a homogeneous displacement of all points, being accounted for by simply adding to every coordinate

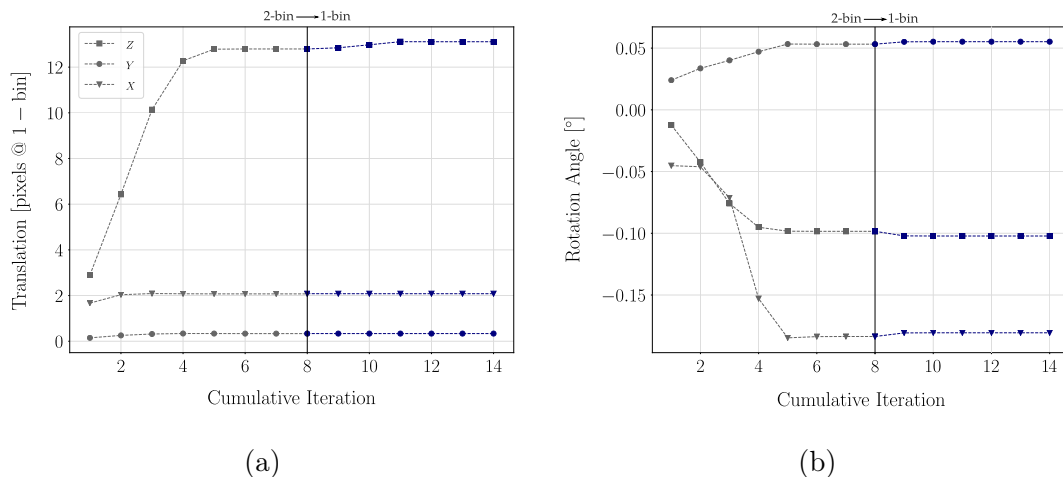


Figure 3.12: Illustration of the registration algorithm run for two binning levels in a pair of images coming from a uniaxial compression test. The computed Φ_{reg} is multiplicatively decomposed into translations (left) and rotations (right) over the cumulative iterations. Note that translations of the bin-2 level are scaled to binning 1 voxel size (*i.e.*, multiplied by 2)

of the reference image the calculated translation vector. However, if the transformation is anything other than a pure translation, the centre of application of registration becomes important. Consider, for example, a homogeneous deformation function that describes a rigid-body rotation around the vertical axis of the specimen, with all the points moving in circles (perpendicular to the axis of rotation) apart from the fixed ones, which correspond to the straight line of the axis of rotation. This time, the linear mapping between the two images, or in other words, the application of registration, involves the calculation of the angular displacement for every non-fixed point, which makes the origin of the registration important.

In `spam` and consequently in this work, the choice was made to define the point of application of the registration as the centre of the reference image. Thus, continuing with the rotation example above, the last column of this computed Φ_{reg} (which corresponds to the translation vector) is written: $[0, 0, 0, 1]$, meaning that there is no translation of the center of the image. Applying this Φ_{reg} to any other point (not belonging to the vertical axis of the image) will result in adding an angular displacement to this zero translation vector.

This is how, in a more general case of more complex transformations, the registration (*i.e.*, a single deformation function evaluated at the centre of the reference image) is applied at any point in the image, resulting to a homogeneous deformation *field*, which maps all the points of the considered domain to a new configuration. Note that the measured registration function, as an initial guess, can be applied at any point of the considered domain, not only “voxelwise”, but also in a coarser scale, at coordinates of arbitrarily distributed points. These coordinates can correspond for example to the points of a regularly-spaced grid (or even the nodes of a FE mesh, in case of a global correlation) as described right below.

“Local” correlation

The local DVC approach followed in this work consists in creating a regular grid of points in the reference configuration by subdividing the region of interest into a set of inde-

pendent subvolumes, or zones of interest (ZOIs), known as correlation windows. Cubical correlation windows are well suited to data coming from tomography, since the 3D images provide a convenient grid sampled in voxels. The “local” aspect of the procedure involves the extraction of these cubic subvolumes from the reference image (centered around each point of the grid) and the independent calculation of a linear deformation function for each one of them, following the iterative procedure described above. This time, the considered domain Ω is the extracted subvolume and the iterative procedure consists in gradually deforming each subvolume of the deformed configuration so as to best match the subvolume of the reference configuration.

As already mentioned, for the iterative algorithm to converge, each local calculation should start close enough to the right solution. The application of the computed registration (*i.e.*, Φ_{reg}) to each point of the grid (*i.e.*, \mathbf{x}) leads to the extraction of a subvolume in the deformed image around the mapped position of the grid point (*i.e.*, $\mathbf{x}' = \Phi \cdot \mathbf{x}$). This is most of the times an essential initial guess. Alternatively, in cases where a quite complex and/or heterogeneous deformation field maps the two images, with a single Φ_{reg} not providing an adequate initial guess for the grid points to converge, a coarse nearest-pixel displacement guess, known as “pixel search” can be performed. In this study, due to the stiff until failure mechanical response of the micro-concrete specimens, the application of the calculated registration Φ_{reg} to each point of the grid was found an adequate initial guess.

By combining the independently computed deformation functions for each correlation window, a *field* of discrete deformation functions is retrieved for the whole region of interest, not to be confused with the homogeneous deformation field obtained through the registration procedure. The deformation function evaluated at each measurement point of the grid is the result of an averaging process over each ZOI, *i.e.*, each correlation window, whereas the deformation function coming from the registration is a result of an averaging process over the whole region of interest (ROI), *i.e.*, the whole image.

Consequently, the deformation field coming from the local DVC approach is (in general) heterogeneous throughout the specimen. It is exactly these non-homogeneous deformations (which can not be described by a single deformation function) that are needed to be captured for the micro-scale understanding of the fracturing processes. Note that this locally measured DVC field (evaluated at every grid point) can then be interpolated at each voxel position, resulting to a corrected deformed image, this time mapped by a field of deformation functions.

The size of the extracted subvolume and the spacing of the measurement points can be chosen independently, by selecting a spacing smaller than the window size (*i.e.*, overlapping ZOIs), equal to the window size (*i.e.*, contiguous ZOIs) or bigger than the window size (*i.e.*, separate ZOIs). In this work, the spacing of the grid points is set equal to the window size, ensuring that the measured kinematics exhibit no correlation between different discrete estimations, or in other words, ensuring the statistical independence of the corresponding error [Grédiac et Hild, 2013]. Concerning the error in the measured field, the size of the selected window is crucial and directly affects the relevance of the measured kinematics, as it will be discussed in detail in Section 3.2.3.

It is worth mentioning here that since linear deformation functions are computed independently for each correlation window, no continuity is imposed in the sought displacement field between the separate windows, which is the underlying difference between “local” and “global” DVC approaches (see for example [Hild et Roux, 2012]). Furthermore, the independent calculation performed for each correlation window is well suited for a par-

allelisation scheme, implemented in `spam` through an MPI interface, which significantly reduces the computational time for the whole correlation procedure.

Strain calculation and invariants

The local DVC procedure described so far yields a set of independent measurements that can be seen as a field of deformation functions for the whole image. The displacement field can be then obtained by extracting the translation component of each Φ . This field reveals valuable information about the evolution of the fracturing processes, however, the subsequent estimation of the derived strain field is essential to complete the understanding of the localised deformation throughout the specimen.

Strain is a continuum-mechanics state variable reflecting the deformation that a material undergoes. Concentration of strains in narrow bands, *i.e.*, strain localisation, is usually encountered in quasi-brittle materials and is used to describe the transition from a spatially continuous deformation process to a discontinuous one. The distinction between strain localisation (weak discontinuity) and cracking (strong discontinuity) is not trivial and highly depends on the observation scale. Herein, in order to describe the fracturing process of the studied micro-concrete samples, both the strain fields and the correlation residual fields (indicating cracks) will be used.

In `spam`, the calculation of the strain field relies on the transformation gradient, which is a local characterisation of the motion. Local strains are computed based on a local variation of the displacement field (*i.e.*, relative displacements of neighbouring measurement points). The implemented method for calculating the displacement gradient coming from a local correlation is based on the displacements of 8 neighbouring points laid in a structured cubic grid. The measured displacement vectors at every grid point are used as nodal displacements of a finite element mesh, made of 8-noded elements. Or in other words, a linear mapping of the measured regularly-spaced displacement field inside an 8-noded quadratic quadrilateral element (Q8) is performed. At the centre of each 8-noded element, the 3×3 transformation gradient tensor \mathbf{F} is then defined as:

$$\mathbf{F} = \mathbf{I} + \nabla \mathbf{u} \quad (3.13)$$

where \mathbf{I} is the identity matrix and $\nabla \mathbf{u}$ is the displacement gradient.

The calculated transformation gradient tensor \mathbf{F} contains, however, components of the material rotations, inherent in the measured kinematic field, which do not represent any intrinsic material response to external loading. Therefore, following the large (finite) strain framework, a right Cauchy polar decomposition theorem is used to decompose the transformation gradient into a stretching followed by a rotation: $\mathbf{F} = \mathbf{R} \cdot \mathbf{U}$. With \mathbf{U} representing the symmetric right stretch tensor, measuring the change in the local shape and \mathbf{R} the orthogonal rotation tensor, measuring the change of local orientation. The strain tensor, characterising length and angle changes, is then defined as: $\mathbf{U} - \mathbf{I}$.

A multiplicative decomposition of the stretch tensor \mathbf{U} into an isotropic (*i.e.*, spherical) and deviatoric part is implemented in `spam`, in order to extract scalars representative of the volume and shear distortion of the material at the measurement point. Following the formulation derived by Denis Caillerie the multiplicative decomposition of the strain tensor is written as:

$$\mathbf{U} = \mathbf{U}_{\text{iso}} \cdot \mathbf{U}_{\text{dev}} \quad \text{with} \quad (3.14)$$

$$\mathbf{U}_{\text{iso}} = J^{1/D} \cdot \mathbf{I} \quad \text{and} \quad (3.15)$$

$$\mathbf{U}_{\text{dev}} = \frac{1}{J^{1/D}} \cdot \mathbf{U} \quad (3.16)$$

where J is the determinant of the transformation gradient tensor and D the dimensions of the problem. As a first invariant of the strain tensor, the *volumetric* strain is given by the Jacobian matrix, defined as: $\varepsilon^V = J - 1$. As a second invariant of the strain tensor, the *deviatoric* strain is defined as the Euclidean norm of the decomposed deviatoric part: $\varepsilon^D = \|\mathbf{U}_{\text{dev}} - \mathbf{I}\|$.

It should be mentioned here that in order to evaluate the strain field, the gradient of the raw displacement field needs to be computed. This operation implies the computation of the gradient of raw experimental data, which typically come with a certain level of error and noise, accumulated through the acquisition, reconstruction and the correlation procedure, as discussed in Section 3.2.3.

In this work, the deformation field is evaluated in a regularly-spaced grid being as fine as possible, while ensuring reliability of the measurements (see Section 3.2.3). The measured raw displacement field is then post-processed before proceeding into a strain calculation. As a first step, the displacements of the grid points that did not correlate successfully (either they did not converge to the right solution or simply diverged) are replaced by a weighted influence of the displacements of the closest 12 successfully correlated points. Afterwards, in order to smooth the corrected displacement field, a 3D median filter is applied, with a structuring element (see Section 3.1.3) of one voxel radius, in order to reduce the risk of oversmoothing the field and, thus, losing mechanical information.

3.2.2 Combined regularly-spaced and discrete local DVC techniques

DVC (and DIC) utilises a texture that should be the signature of each volume (or surface) considered, simply transported by the sought deformation function from one configuration to the other, as stated in Eq (3.2). The performance of the correlation procedure is strongly affected by the correlation function of the considered texture, meaning that the latter needs to exhibit an internal character. In a 2D case, where the surface of the material is observed with a camera, the correlation procedure is usually facilitated by applying onto the surface an optimised speckle pattern, creating thus, an artificial texture. Unlike the 2D case, the real micro-structure of the material is used in tomography, relying on the texture in the bulk of the material. A broad range of greyvalues is then required, as well as high contrast between neighbouring voxels, which is not always guaranteed by the natural texture of the studied material.

Some materials characterised by their natural heterogeneity, can be privileged, since their heterogeneities can behave like a natural speckle pattern, with the contrast and variation of greylevels between different phases being suitable for image correlation. The existence of heterogeneities does not guarantee, though, the performance of the correlation procedure, since it might happen that the texture *inside* these heterogeneities is actually poor. This happens to be the case of the micro-concrete specimens considered herein, with coarse aggregates embedded into a mortar matrix, not even mentioning the – by definition – textureless macro-pores.

From a physical point of view, aggregates and mortar matrix are actually a set of individual particles, albeit of significantly different sizes. When captured at $13\ \mu\text{m}$ voxel size, these different sizes result in different characteristic distributions of greyvalues around each material's mean, which, as was shown in Section 3.1, ended up being the key characteristic of their separation (*i.e.*, greylevels inside aggregates exhibiting 3 times lower variance compared to mortar matrix). The local contrast and, thus, the texture inside these two materials differs significantly.

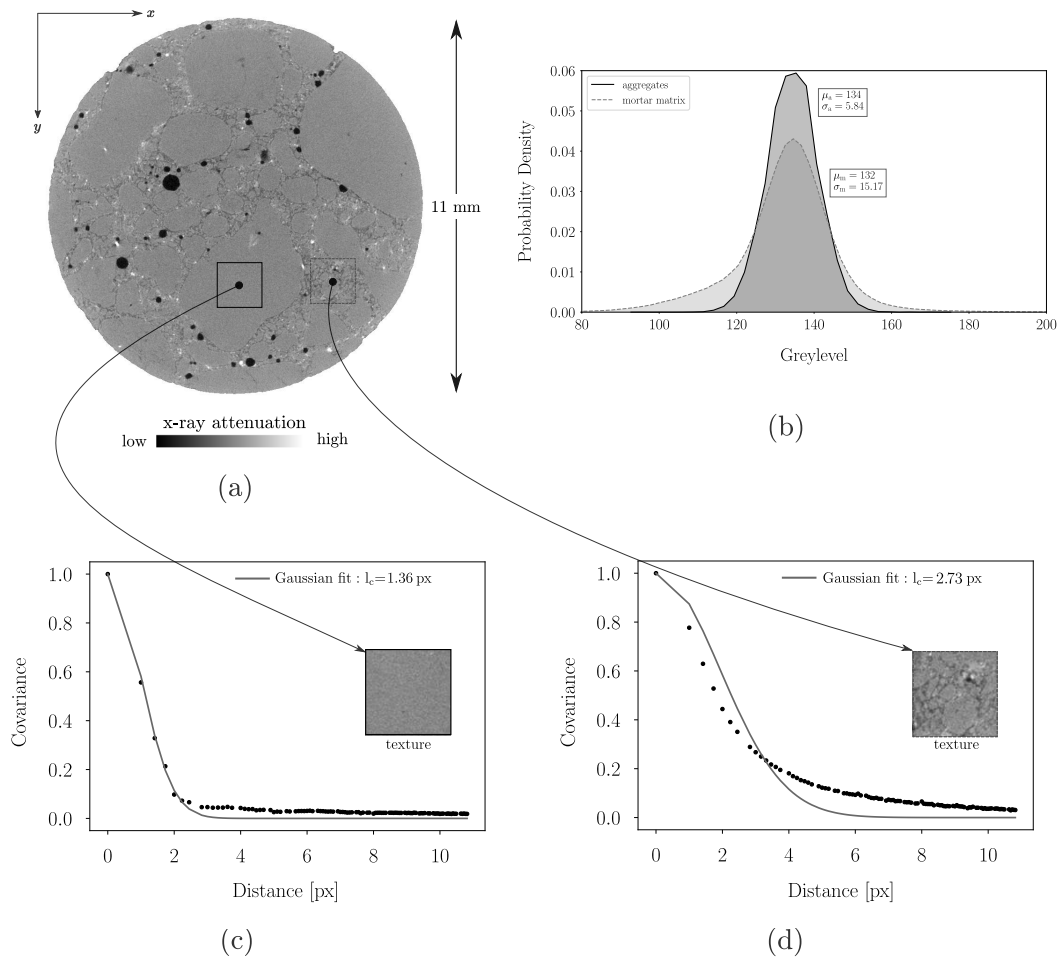


Figure 3.13: Correlation length of the micro-concrete's texture, captured at $13\ \mu\text{m}$ voxel size, calculated for a cube cropped inside an aggregate (bottom left) and inside the mortar matrix (bottom right)

To quantify this difference, as an illustration, a cube is cropped inside each of the two phases and the correlation lengths of the extracted textures are calculated (see Fig. 3.13). It should be mentioned here that the correlation length is the characteristic distance over which the normalised pair correlation function (*i.e.*, covariance) of the signal decays to 50%. When the correlation length is too small, *i.e.*, in the order of one pixel, the signal might no longer be distinguished from the noise. Usually, a good compromise is to deal with textures for which the correlation length is greater than a few pixels and smaller than the window size, in the order of 2 to 5 pixels (see [Hild et Roux, 2012, Grédiac et Hild, 2013]).

As depicted in Fig. 3.13 (bottom), the computed correlation length inside the cropped

aggregate is quite low, close to the order of the pixel size (1.3 pixels), whereas the correlation length of the cropped cube inside the mortar matrix is double (2.7 pixels). Such a small correlation length calculated inside aggregates, reveals the lack of texture inside this material, meaning that a highly spatially resolved correlation is rather ill-fated inside these inclusions. In other words, a quite fine 3D regular grid, necessary to capture small micro-structural changes, imposes far too small subvolumes to capture features inside the textureless coarse aggregates.

To circumvent this problem, a new DVC technique is adopted in this work, which consists in correlating the matrix material and the coarse aggregates separately and merging afterwards the calculated deformation fields. More specifically, as a first step, the considered images are registered to roughly map one onto the other, by calculating a single Φ_{reg} , which is then used as an initial guess for the two different correlations that follow.

Fig. 3.14 shows an illustrative example of the proposed procedure, whereby on the top row on the left the central vertical slices of the greyscale images coming from an *in-situ* compression test are shown. A regular grid of points is defined in the reference greyscale image (see Fig. 3.14b), being as fine as possible, while ensuring reliability of the measurements (*i.e.*, window size of 31 voxels, as discussed in detail in Section 3.2.3). After applying the computed Φ_{reg} to each point of the grid, a local correlation is performed which results to a field of deformation functions evaluated at every grid point. Fig. 3.14e depicts the central vertical slice of the decomposed axial displacement field. Correlation windows for which the iterative procedure failed to converge are shown as grey points in Fig. 3.14d and can also be easily identified from their extreme displacement values. It can be seen that these points fall mostly inside aggregates.

Independently from the regularly-spaced correlation, coarse aggregates are segmented from the reference greyscale image, following the procedure detailed in Section 3.1 (*i.e.*, based on their low variance) and then labelled (see Section 3.1.4), as depicted in Fig. 3.14c. This labelled image serves as a mask for the “discrete” correlation (in the style of [Hall *et al.*, 2010, Andò *et al.*, 2012]) that follows. In this case, instead of defining cubical windows on a regular grid, arbitrarily shaped correlation windows are used, centered in the centre of mass of each labelled aggregate, defining the smallest box that each aggregate fits inside (the so-called “bounding box”). This means that the reference configuration is described now by the 3D greyscale image, as well as the labelled 3D image of the coarse aggregates, with the set of quantitative particle-based measurements that it involves. After applying the computed Φ_{reg} to the centre of mass of every labelled aggregate, the greyvalues corresponding to each aggregate are masked, extracted as subvolumes and matched with the deformed configuration (according to the iterative procedure detailed in Section 3.2.1). The displacement vectors calculated in the centre of mass of each aggregate are shown in Fig. 3.14f.

The two independent correlations described so far yield two separate fields of discrete deformation functions, attributed roughly to the same region of interest (*i.e.*, the whole image), but calculated on different zones of interest: one on regularly-spaced contiguous cubic windows and the other on each aggregate’s bounding box. The local grid measurements whose correlation procedure did not converge due to being inside an aggregate can now be replaced with the help of the discrete correlation. In order to achieve this, the labelled image is firstly projected onto the regularly-spaced grid, so that the grid points that fall inside each labelled aggregate are identified. Then, for each aggregate the deformation function evaluated in its centre of mass is applied to the grid points that fall inside it (see Fig. 3.14g). The resultant field is then merged with the regularly-spaced deformation

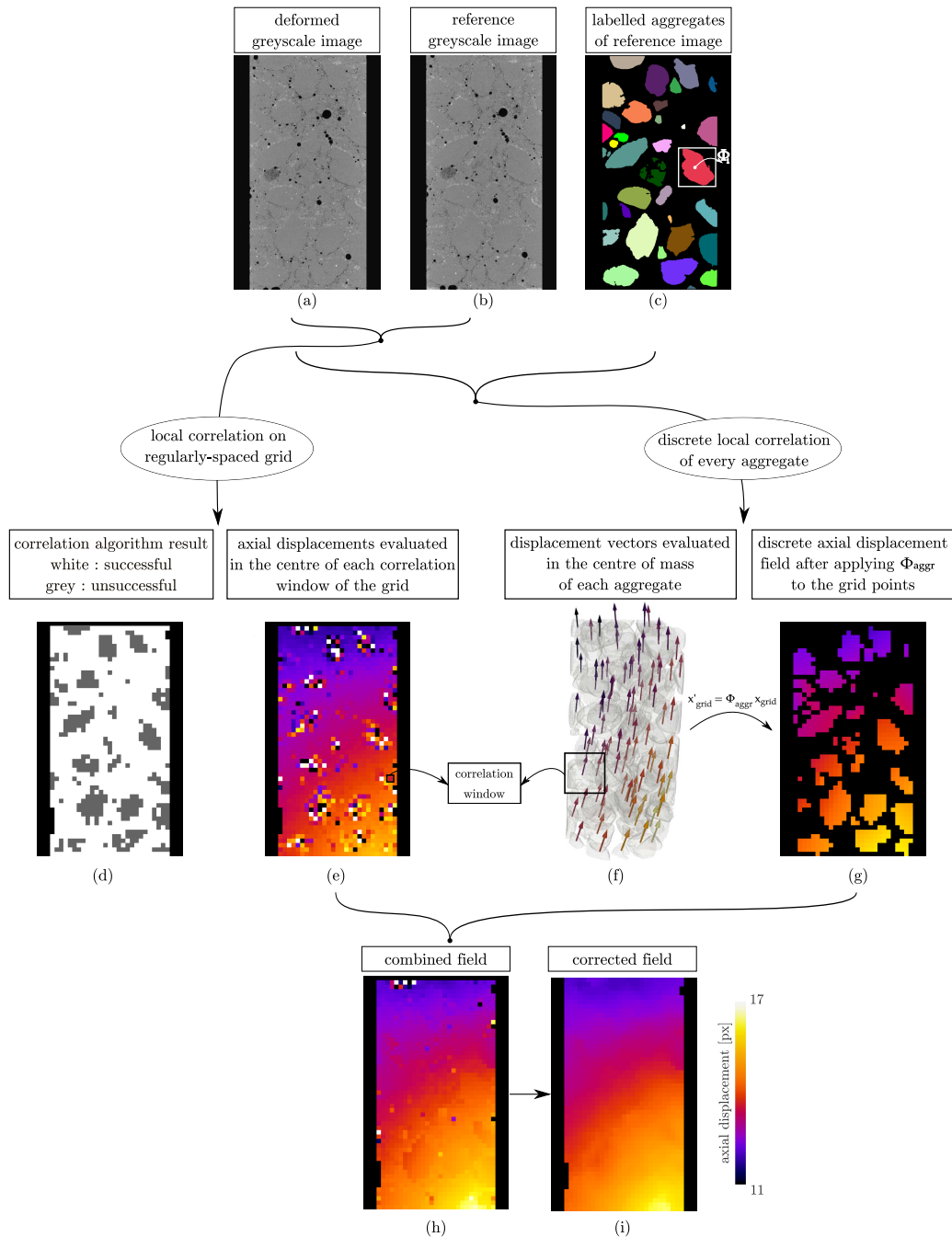


Figure 3.14: Illustration of the proposed combination of the regularly-spaced and discrete local DVC techniques in a pair of images coming from the C-02 *in-situ* compression test

field, leading to the final combined field (see Fig. 3.14h). This field, although obviously improved compared to the original one (see Fig. 3.14e), contains still a few points with extreme displacement values, either belonging to an aggregate that did not correlate successfully (see top left of the field) or to points in the original grid corresponding to the other two phases (mortar matrix or macro-pores) that also failed to correlate. It is this combined field that is then post-processed; corrected by the mean weighted deformation values of the closest neighbours and filtered (see Fig. 3.14i). Note that the strain fields are derived from the merged and corrected displacement field.

It should be mentioned here that the procedure presented above results in a nonuni-

form deformation field inside each aggregate. If, for instance, the deformation function of an aggregate encodes a rigid-body rotation around its centre of mass, this will be accounted for by a final nonuniform regularly-spaced displacement field inside this aggregate. As an alternative to the technique adopted here, the deformation functions of the grid points falling inside aggregates could have been estimated by interpolating the deformation functions of the successfully correlated grid points falling at the interfaces between aggregates and mortar matrix. This is actually how the correlation windows that might fall completely inside large textureless macro-pores (and thus fail to converge) are treated during the step of the field correction (replaced by a weighted influence of the closest well-correlated points).

3.2.3 Estimation of measurements uncertainty

Uncertainty in measured kinematic fields

Image correlation gives a direct access to experimental kinematic fields and in the sake of measurement reliability, it is of fundamental importance to estimate the levels of uncertainty evolved in the kinematics measurement and, in turn, the metrological performance of the procedure. Sources of errors can be:

- intrinsic to the DVC procedure, related to errors coming from the interpolation of greyvalues at non-integer positions [Schreier *et al.*, 2000] or related to the choice of the kinematic basis [Schreier et Sutton, 2002], [Bornert *et al.*, 2009] which is unable to describe the actual transformation (deformation function accounting for affine transformations in the considered case), and
- independent to the adopted DVC procedure, related to noise associated with image acquisition and reconstruction processes [Roux et Hild, 2006], [Bornert *et al.*, 2009], [Dautriat *et al.*, 2011].

Different ways have been developed to evaluate the correlation procedure and various works extensively studied the levels of uncertainties and sources of errors involved in DVC techniques, either by studying synthetic cases (see for example [Hild et Roux, 2012]), or in real cases by creating artificial transformations (see for example [Doumalin et Bornert, 2000, Dautriat *et al.*, 2011], with a detailed discussion being out of the scope of this work.

In this study, the uncertainty level of the measured kinematics is estimated by conducting a so-called “repeated” scan, which consists in performing two subsequent scans of the same micro-concrete sample, with some rigid-body motion between the two acquisitions, but without any mechanical loading. The set-up and the scanning parameters of the “repeated” scan are identical to the ones used for the *in-situ* experiments (see Section 2.4). Generally, the reference scan (*i.e.*, the first scan conducted during each *in-situ* experiment described in Section 2.5) could have been repeated twice, resulting to a unique double scan for each experiment, associated with the specific texture of each micro-concrete sample. However, here, in the sake of simplicity, two different “repeated” scans are conducted: one for the uniaxial tests by using the plexiglass pressure vessel and the scanning parameters described in Section 2.4 and a second one for the triaxial tests by using the aluminium high pressure vessel and the specific scanning parameters described again in Section 2.4.

Fig. 3.15 (top row) depicts the central vertical slices of the repeated scan for the uniaxial tests, with the slice extracted from the first scan shown on the left and the slice extracted from the subsequent second scan shown on the middle. Their initial absolute

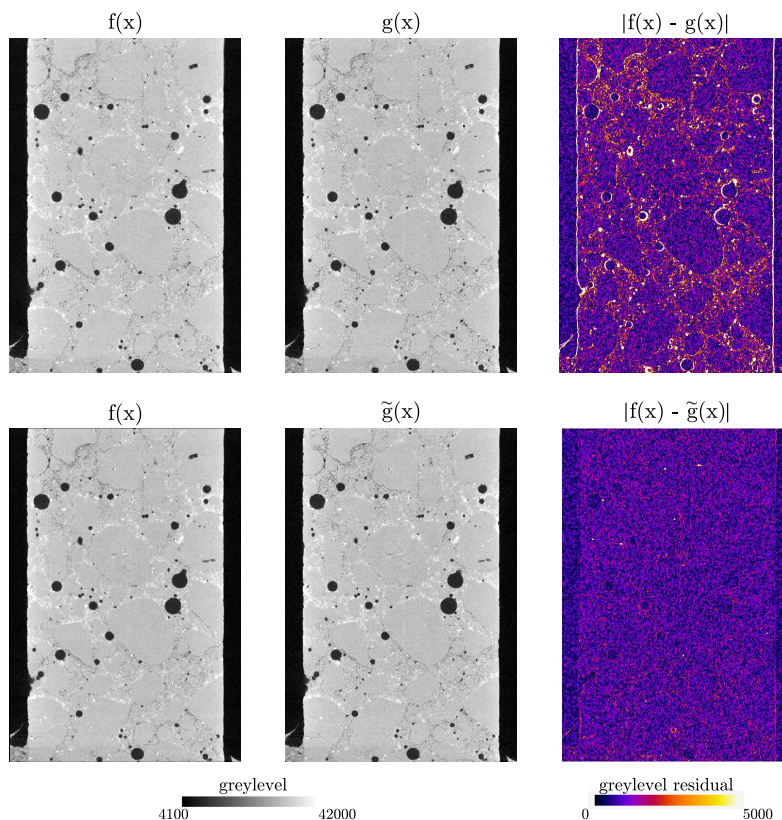


Figure 3.15: Registration of the “repeated” scan for the uniaxial tests. (Top): central vertical slices of the two scans along with their initial difference, (Bottom): central vertical slices of the reference image (same as above), the registered second image and their difference after their registration

difference (top right) is calculated by subtracting voxelwise the greyvalues in the two images and keeping the absolute value of their difference. This difference image, which is clearly not zero, demonstrates that even though no mechanical loading has occurred, there is some rigid-body motion between the two configurations, as well as accumulated noise throughout the acquisition and the reconstruction procedure.

The difference image $|f(\mathbf{x}) - \tilde{g}(\mathbf{x})|$, where $\tilde{g}(\mathbf{x})$ corresponds to the image of the second scan after the application of the measured Φ_{reg} , is depicted on the bottom right of Fig. 3.15. As is apparent by comparing this image to the initial difference on the top row, the registration between the two images leads to their alignment and to a significantly reduced intensity in the difference image. The underlying micro-structure is no more visible, revealing that the measured deformation function applied to the image of the first scan creates a good correspondence to the image of the second scan. Note that the standard deviation of the difference image $|f(\mathbf{x}) - \tilde{g}(\mathbf{x})|$ is 460 greylevels, which is very close to the noise level in the original greyscale images (450 greylevels). After the subtraction of the measured rigid-body motion, the remaining non-zero intensity values in the difference image are an indicator of the measurement uncertainty, which as discussed above, is attributed to the inherent noise of the data and is intrinsic to the DVC procedure.

This measurement uncertainty is then quantified for a deformation field coming from a local correlation. To achieve this, a series of local DVC computations are performed in the “repeated” scans for a range of different sizes of contiguous (*i.e.*, ensuring statistical

independence of the corresponding error) cubical correlation windows. The rigid-body motion obtained through the registration is subtracted from the measured deformation fields and the resultant displacement fields are then corrected and filtered, in order to proceed into the strains calculation. Any displacement (or strain) that deviates from zero after the subtraction of the rigid-body motion is attributed to errors in the measured kinematics, with the standard deviation of the resultant displacement and strain fields giving an estimation of the measurement uncertainty. Note that correlation windows that fall completely inside large aggregates (and thus fail to converge, see Section 3.2.2) are not considered for this parametric analysis.

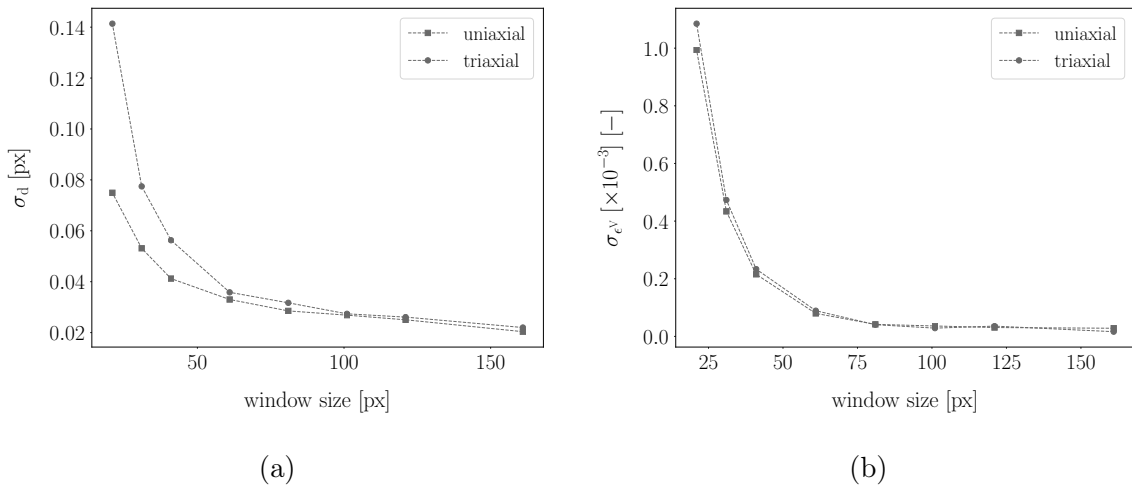


Figure 3.16: Estimation of measurement uncertainties for uniaxial and triaxial *in-situ* experiments as a function of the window size for a local correlation: (a) standard displacement uncertainty, (b) standard volumetric strain uncertainty

Fig. 3.16 presents the evolution of the standard displacement and strain uncertainties as a function of the correlation window size calculated from the two different “repeated” scans, one corresponding to the uniaxial and another corresponding to the triaxial tests. A well known trend is observed [Hild et Roux, 2012, Grédiac et Hild, 2013], whereby the larger the window size, the smaller the uncertainty. This trend, confirmed again here, implies that there is a clear trade-off between the spatial resolution of the measurement and the level of the measurement uncertainty, which is actually linked to the underlying DVC (or DIC) formulation and not to the specific implementation used in **spam**. Note here, that due to the different scanning parameters and pressure vessels used, the measured uncertainty is slightly higher for the triaxial tests, highlighted mainly for the smaller window sizes. This is likely due to the lowered transmission and therefore higher noise in the scans.

A complex heterogeneous kinematic field requires many measurement points (smaller contiguous correlation windows) in order to be accurately described at the expense, though, of higher uncertainties which can dominate the signal for very small windows. A compromise is therefore required, which is strongly related to the particular experiment conducted, the material studied and the scale of the mechanisms of interest. In the presented case, the window size selected for the local correlation analysis of the *in-situ* experiments on micro-concrete is 31 voxels (*i.e.*, 0.4 mm), which means that any measured displacement smaller than 0.05 px for the uniaxial tests and 0.08 px for the triaxial tests

falls below the uncertainty level. As discussed in Section 3.2.2, the choice of this correlation window size excludes the coarser aggregates, which are independently correlated in a (much larger) zone of interest, which is defined by their bounding box.

Uncertainty in measured elasticity modulus

Starting from an experimentally measured displacement field, macroscopic mechanical properties of the examined micro-concrete specimens can be derived. More specifically, by evaluating the relative difference of the calculated displacements in the direction of loading on the top and bottom surface of the cylindrical specimens, the macroscopic Young's modulus can be computed, which is given from the following expression:

$$E = \frac{\sigma}{\epsilon} = \frac{FH}{Az} \quad (3.17)$$

where:

- F is the measured force level during the experiment,
- A is the measured surface area of each specimen,
- z is the difference between the measured displacements of the considered points and
- H is the initial distance between the two measurement points.

The error analysis presented above calls for caution, when defining this material property based on the measured kinematic fields. An estimation of the global error associated with the Young's modulus measurement (ΔE) can be derived, by calculating the relative errors of the measured quantities: F, A, z, H, with respective errors: ΔF , ΔA , Δz and ΔH that is written:

$$\Delta E = \left| \frac{H}{Az} \right| \Delta F + \left| \frac{F}{Az} \right| \Delta H + \left| \frac{FH}{A^2 z} \right| \Delta A + \left| \frac{FH}{Az^2} \right| \Delta z \quad (3.18)$$

where:

ΔF is the error in measuring the force during the experiment, as measured by the forcemeter, with a given by the manufacturer tolerance of 0.1 N,

ΔH is the error in measuring the distance between two points in the image, which is of the magnitude of the voxel size and can be neglected,

ΔA is the error in measuring the surface area of the specimen, which is given by: $A = \frac{\pi}{4} \times d^2$, so that $\Delta A = \frac{\pi}{2} \times d \times \Delta d$, where d is the diameter of the specimen and

Δz is the error coming from the measured displacement field, which is by far the dominant one and is directly taken from the computed displacement uncertainty coming from the "repeated" scans, as described above.

Fig. 3.17 depicts the measured Young's moduli, along with the corresponding error bars for a representative test of each different loading path conducted in this work: top row on the left for a uniaxial tension test, top row on the right for a uniaxial compression test and bottom row for a triaxial compression test. More specifically, the reference scan of each test is correlated for a range of different window sizes with the subsequent second

one (in order to remain in low levels of load and thus close to the elastic regime) and the axial displacement fields throughout the samples are extracted. Starting from the bottom edge, and traversing vertically the specimen, the axial displacements of the measurement grid points at each vertical grid position are averaged. Their relative difference (*i.e.*, z in Eq. (3.17)) is then computed for a range of different vertical distances (*i.e.*, H in Eq. (3.17)) along the sample and the Young's modulus (see Eq. (3.17)), with the corresponding error (see Eq. (3.18)) are computed for each window size.

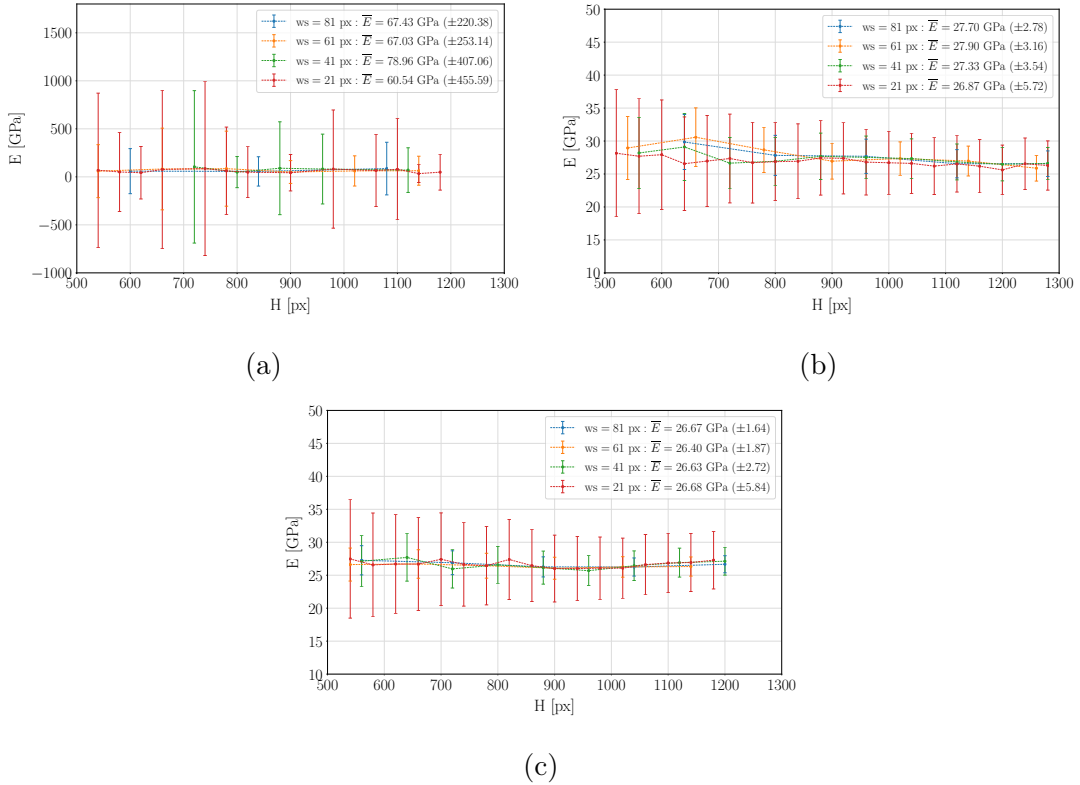


Figure 3.17: Estimation of uncertainty in measuring the Young's modulus throughout the samples for a range of correlation window sizes: (a) uniaxial tension (test T-01), (b) uniaxial compression (test C-02) (c) triaxial compression (test TX15-01)

In general, the smaller the window size and the closer the points which their relative displacement difference is calculated, the higher the computed error in the measured elasticity modulus. Concerning the uniaxial tension tests, following the micro-structure while it is deforming in such a brittle case, results unavoidably in measuring very small relative displacements inside the specimen (as will be discussed extensively in the following section). Therefore, for the tensile tests conducted in this work, the Young's modulus is not possible to be safely evaluated from the experimental kinematic fields, with errors reaching 400 GPa. On the contrary, with strengths about 10 to 30 times higher compared to the tensile ones, much higher displacements are encountered during the compression tests. For both uniaxial and triaxial compression tests the error remains low, ranging between 1 to 5 GPa, with the calculated Young's modulus in the order of 27 GPa, which is a typical value for an ordinary concrete specimen. It should be reminded, here, that the Young's moduli estimated from the experimental macroscopic stress-strain curves in compression (see Section 2.3) range also between 26 to 28 GPa.

3.3 3D kinematic fields and fracture patterns from *in-situ* experiments

In this section, based on the tools and techniques discussed so far in this chapter, the measured kinematic fields along with the observed failure patterns coming from the *in-situ* experiments on the micro-concrete specimens (see Section 2.3) are presented. The main objective is to observe and quantify the first stages of the fracturing processes at the scale of the largest heterogeneities (aggregates and macro-pores), as well as to observe and compare the different failure patterns for each loading path, as revealed from the post-peak scans. In order to underline the fact that the analysis performed in this work is in 3D and the measurements presented are 3D in nature, all the presented kinematic fields are in 3D, allowing a direct observation of the entire region of interest and its evolution throughout the experiment.

As already mentioned, for all the *in-situ* tests, the kinematic fields are obtained through a combined local DVC computation on a fine regularly-spaced grid (contiguous correlation windows with a point spacing of 30 voxels, *i.e.*, 0.4 mm) together with a “discrete” correlation of the coarser aggregates. Before proceeding into the computation of the strain fields, the combined displacement field is post-processed by firstly correcting the unsuccessfully correlated points with a weighted influence of the closest 12 successfully correlated points and then by smoothing the resultant field with a 3D median filter of 1 voxel radius.

For each mechanical test, the measured displacement accompanied by the derived strain fields are presented in terms of a total, and not incremental analysis. This means that always the first scan of each *in-situ* experiment is considered as the “reference” configuration and is mapped into the subsequent scans captured throughout the test. For the discrete correlations to be performed, the coarser aggregates of the reference images of each test are segmented and labelled. The measured kinematic fields are then compared with the damaged micro-structure after the failure of the material, however, a detailed morphological analysis of the failure patterns, themselves, is principally addressed in Chapter 5.

It should be mentioned here that for the uniaxial tests, the formed macro-cracks are of some pixels width, easily visible in the post-peak x-ray 3D images, resulting in their direct extraction by a thresholding operation based on their greyvalues. However, in the case of triaxial tests, cracks might be too narrow (*i.e.*, with widths less than the voxel size) to be visible and, in turn, extracted from the post-peak scans. A finer detection of the cracking network is then required, based on the greylevel residual fields coming from the correlation between the reference and the post-peak scan of each test.

Taking advantage of the sub-pixel nature of the DVC measurements, as already introduced in Sections 3.2.1 and 3.2.3, these fields are valuable for revealing the inevitable noise contained in the 3D images, but also errors intrinsic to the kinematics assumed by the DVC procedure. For the considered case in particular, where the sought deformation function accounts only for linear transformations, regions with high residual values at the end of the correlation procedure are indicators of discontinuities on the calculated displacement field, corresponding to cracks. Note here that regardless of the loading path, correlation residuals were calculated for all the steps before the peak throughout the different *in-situ* experiments. However, these residual fields provided no supplementary information on top of the calculated kinematic fields and, thus, are not presented.

3.3.1 Uniaxial tension

Two *in-situ* uniaxial tensile tests are performed in this work, with their macroscopic responses (depicted in Fig. 2.10 and 2.11) showing a typical quasi-brittle behaviour of concrete under uniaxial tension, with similar levels of tensile strengths (around 3.2 MPa) and a clear macro-crack appearing in the post-peak scans. The central vertical slices of the four scans conducted for each test are shown in Fig. 2.19, with no visible micro-structural change between the first and the two following scans before failure. Following the fracturing process in such a brittle response, governed from such small strains, is a real challenge for the tools presented in this chapter.

Fig. 3.18 shows the measured displacement and axial strain fields for the two tensile tests, calculated by mapping the initial scan (before loading) into the two subsequent ones, at levels of 50% and around 78%, respectively, of the peak load. The calculated displacement vectors are pointing downwards, following the direction of loading, since during the experiment the specimen is pulled downwards by moving slowly the designed ram shown in Fig. 2.3. The displacement fields of the T-01 test show a deviation of the displacement vectors away from axial symmetry, indicating that the loading is actually not purely axial, but rather a slight bending occurs. Note that slices through the kinematic fields of this test are also shown in Chapter 5. On the contrary, a smooth distribution of the displacements along the vertical axis of the sample is observed in the T-02 test, with the bottom of the specimen (where the loading is imposed) exhibiting higher displacements compared to the top. Despite the different distribution of the displacement fields observed, it is worth mentioning that both tests have close failure strengths.

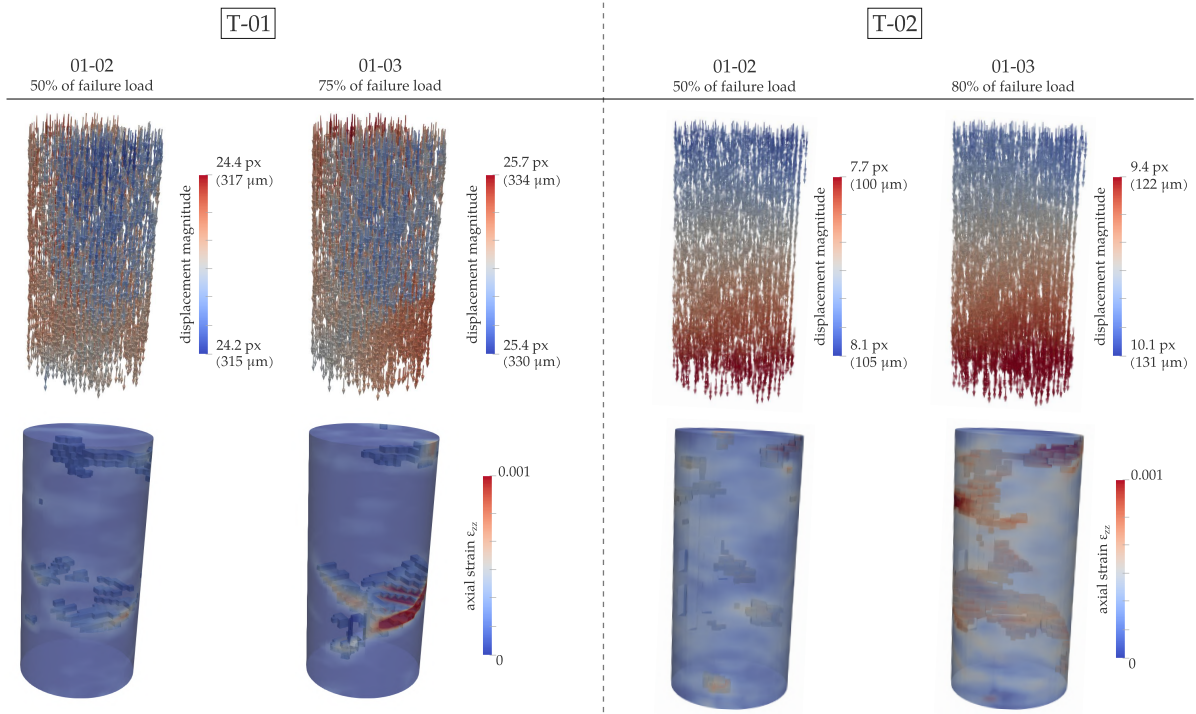


Figure 3.18: Kinematic fields in uniaxial tension. For visualisation, displacement vectors are scaled up 10 times and axial strains below 0.03% are faded. The depicted vectors are proportional to the displacement magnitude, but since ranges are small a tight colour map is applied to highlight differences. Note that slices through the kinematic fields of the T-01 test are shown in Chapter 5

Note that, due to the deformation of the loading system, large displacement steps (corresponding to rigid-body translations) are calculated in the range of 300 μm and 100 μm for the first and the second test, respectively. However, the relative displacements which correspond to the actual micro-structural change inside the micro-concrete samples are in the range of 2 to 4 μm . It should be recalled that the voxel size of the scans is 13 μm , indicating that the DVC procedure adopted herein is indeed capable of revealing kinematic inhomogeneities in the order of sub-pixel displacements. Based on the uncertainty analysis discussed in Section 3.2.3, a relative displacement of 0.2 voxels (3 μm) is still above the estimated uncertainty level, which for the selected correlation window of 31 voxels size is in the range of 0.05 voxels. However, as already mentioned in the same section, such a small range of displacements yields high levels of uncertainties in the estimated elasticity modulus (see Fig. 3.17a), meaning that a safe estimation of the Young's modulus for the tensile tests is not possible.

From the measured fields it is revealed that the response of the material is not purely elastic-brittle, since, especially for the T-01 test, even for the first correlated pair of 3D images (at a load 50% of the maximum failure load), a heterogeneous displacement field appears, indicating strain localisations and crack initiation. Indeed, as depicted by the axial strain fields of the first test, strain localisation is observed even in the first increment, with the strain field becoming increasingly inhomogeneous at 75% of the maximum failure load, whereby strain concentrations in a roughly horizontal layer throughout the specimen are observed. Concerning the second test, strain concentrations are less obvious for the first pair of correlated 3D images. However, at 80% of the maximum failure load a rather similar (compared to the first tensile test) pattern occurs, with axial strains concentrating in a roughly horizontal layer across the sample.

Concentrating now on the failure patterns themselves, as obtained by the post-peak scans, important information about the damaged internal micro-structure can be revealed. The largest heterogeneities (big macro-pores and coarser aggregates) of the initial (*i.e.*, intact) micro-structure of both samples are segmented from the reference 3D images and shown in Fig. 3.19a and 3.20a. By isolating the voids and keeping the largest connected component in the post-peak 3D images of both tests, the experimental macro-cracks are also extracted and shown in Fig. 3.19b and 3.20b. Typical macro-cracks for fracture mode I are observed, crossing roughly horizontally the cylindrical specimens, formed around the aggregates and sometimes propagating through macro-pores. In both tests, it is highlighted that the shape and location of both aggregates and macro-pores form the morphology of these macro-cracks. Note that the role of the shape and location of the heterogeneities in the mechanical response under uniaxial tension is further investigated in Chapter 5.

The identified localised strain regions in both tests, correspond very well to the location of the final macro-cracks as shown in Fig. 3.19c and 3.20c. This result reveals that the combination of an *in-situ* testing together with the adopted in this work full-field measurement technique, is proven to be indeed a valuable tool to capture and quantify the first stages of the fracturing processes, even in such a brittle and stiff case of a micro-concrete sample being uniaxially loaded under tension.

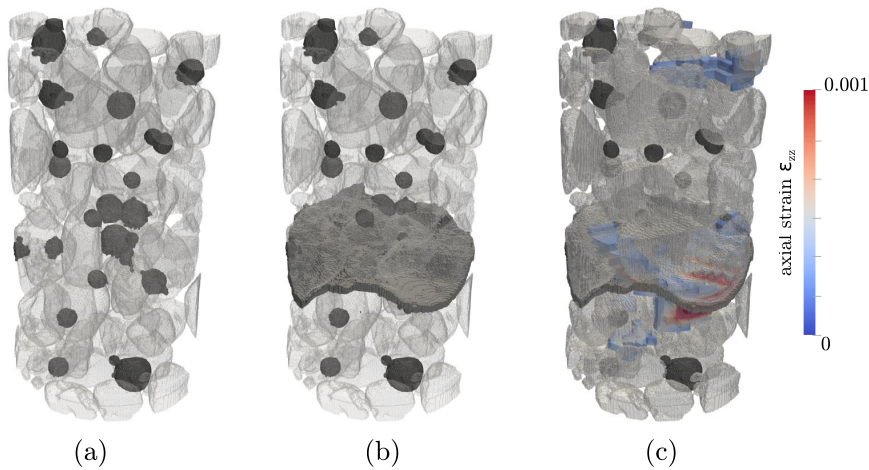


Figure 3.19: Crack patterns in T-01: (a) segmented largest heterogeneities of reference scan, (b) segmented macro-crack from the post-peak scan, (c) regions of localised strain measured at the last step overlaid with the final macro-crack

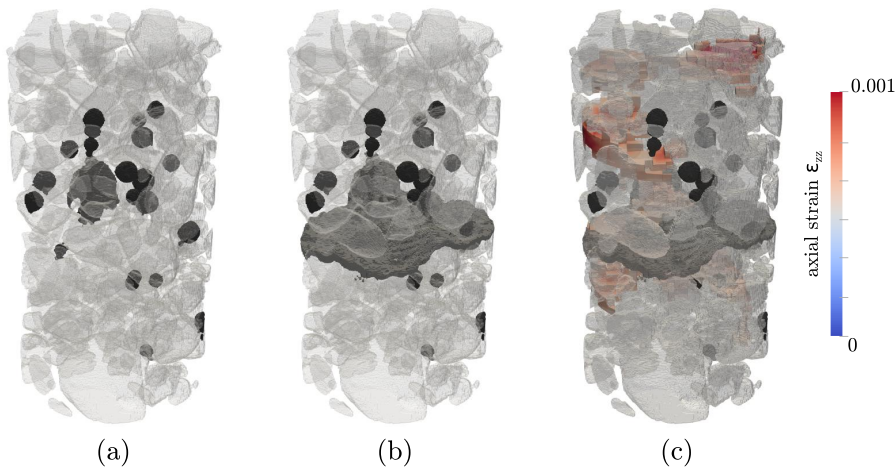


Figure 3.20: Crack patterns in T-02: (a) segmented largest heterogeneities of reference scan, (b) segmented macro-crack from the post-peak scan, (c) regions of localised strain measured at the last step overlaid with the final macro-crack

3.3.2 Uniaxial compression

The macroscopic responses obtained from the three *in-situ* uniaxial compression tests are shown in Fig. 2.12, 2.13 and 2.14. Similarly to the tensile experiments, no obvious micro-structural change is visible in the central vertical slices of the scans before the failure of the material, as shown in Fig. 2.19. However, with compressive strengths about 10 times higher compared to the tensile ones, quite larger relative displacements are expected for these tests.

Indeed, for all the three tests, relative displacement magnitudes in the order of 9 to 12 pixels (*i.e.*, around $140\ \mu\text{m}$) are measured inside the micro-concrete specimens, as shown on the top rows of Fig. 3.21, 3.22 and 3.23, with rigid-body translations in the order of 100 to $140\ \mu\text{m}$. Note that this time, the range of about 10 pixels relative displacement ensures lower (compared to tension) uncertainty levels on the estimated elasticity moduli. The displacement vectors are pointing (mostly) upwards, following the direction of loading

with the ram (shown in Fig. 2.4) slowly pushing the specimens from the bottom. It should be recalled here, that the second scan for all the three tests is performed at a 2000 N force level, just before starting the unloading path.

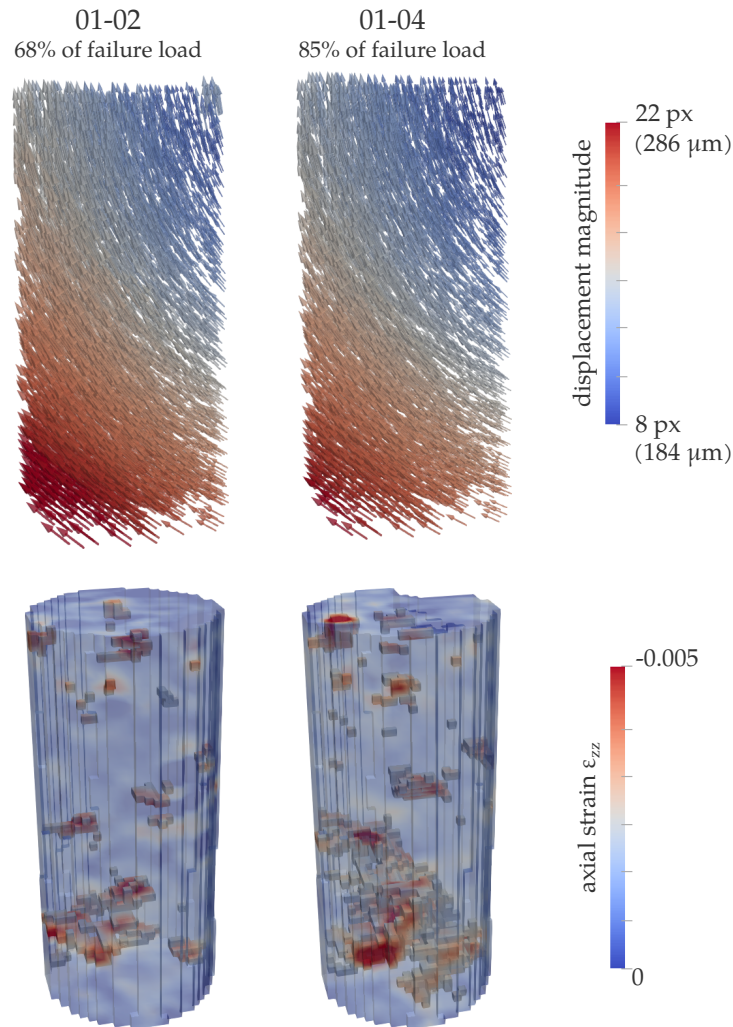


Figure 3.21: Kinematic fields in first uniaxial compression test (C-01). For visualisation, displacement vectors are scaled up 10 times and axial strains above -0.25% are faded

For the C-01 test, even for the first pair of correlated 3D images (until a 2000 N loading), the measured displacement field shows a deviation of the displacement vectors away from axial symmetry (as per the first tensile one), with discrete inclined blocks of displacement magnitudes clearly appearing. In this first step, axial strains already start to concentrate in the bottom part of the specimen, which become increasingly localised in the following step (at 85% of failure load), pointing towards a diagonal failure zone crossing the bottom of the sample. This relatively early appearance (between the first two scans) of strain localisation might explain the lower compressive strength measured for this test (32 MPa compared to 38 MPa of the rest two tests), as well as the slightly lower measured Young's modulus (24.5 GPa with a corresponding error of ± 4 GPa).

On the contrary, for the second and third compressive tests (see Fig. 3.22 and 3.23), the first pairs of correlated 3D images (again until a 2000 N loading) exhibit relatively homogeneous displacement fields and low strains levels. The Young's moduli measured

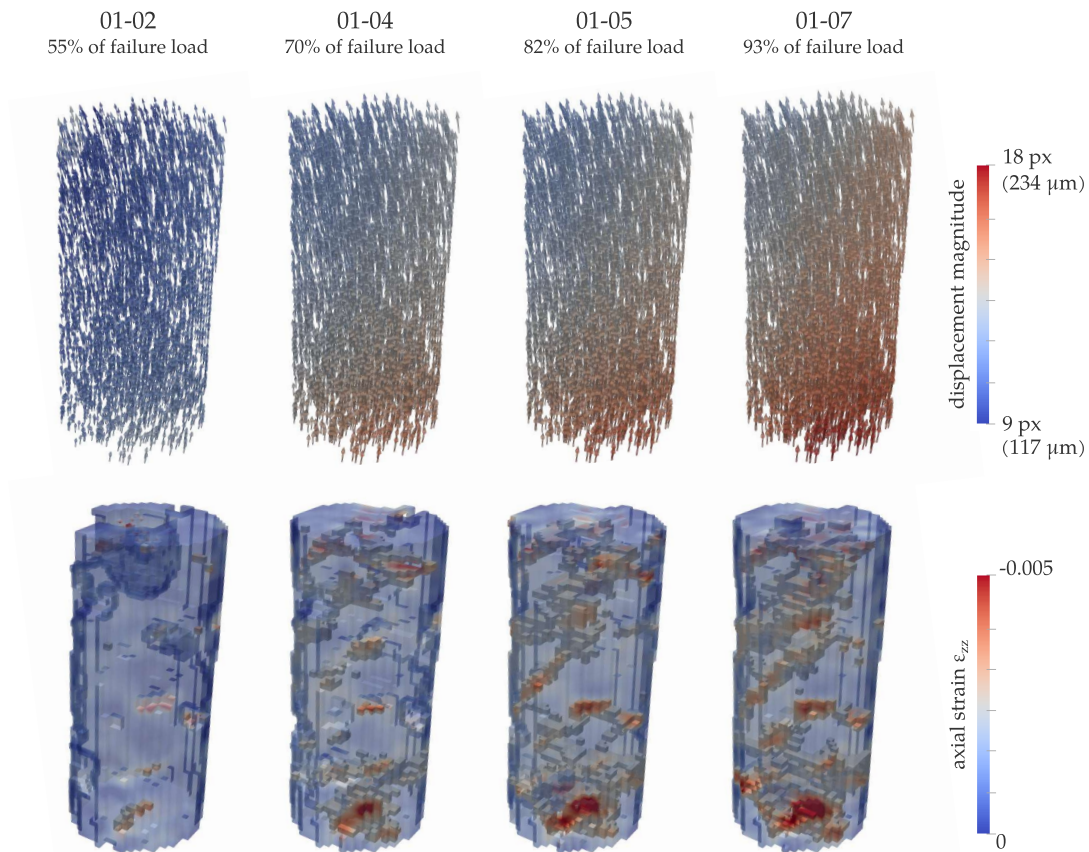


Figure 3.22: Kinematic fields in second uniaxial compression test (C-02). For visualisation, displacement vectors are scaled up 10 times and axial strains above -0.25% are faded. Note that slices through these fields are shown in Chapter 5

at this step are 27 GPa and 26.5 GPa, for the C-02 and C-03 test, respectively, with a corresponding error of ± 3 GPa for both tests. As the tests evolve, the displacement fields become more heterogeneous, with strain localisations appearing throughout the samples. Despite failing at similar compressive strengths (38 MPa), the evolution of the fracturing processes is different for these two tests. Concerning the second compressive test, the failure seems to initiate in inclined bands across the specimen appearing as concentrated axial strain regions (and also as gradients in the displacement fields), which progressively become more localised. Note that slices through the kinematic fields of this test are also shown in Chapter 5. Regarding the third compressive test, the failure initiates and then localises in the top part of the specimen, whereby two diagonal axial strain bands appear to cross each other, with the bottom part of the specimen exhibiting less significant strains.

The measured kinematic fields for all the three tests suggest mainly inclined localised regions of failure. In order to investigate the damaged micro-structure, again the largest heterogeneities of each sample are segmented and presented together with the extracted cracks from the post-peak scans. As illustrated in Fig. 3.24, 3.25 and 3.26, more complex failure patterns are observed, in all of the three tests, compared to the tensile ones. Inclined cracking networks crossing the specimens can be seen, with the identified regions of strain localisations corresponding well with parts of these networks for all the different experiments. The impact of the heterogeneities in the formation of the cracks is highlighted once more and will be further investigated for the C-02 test in Chapter 5.

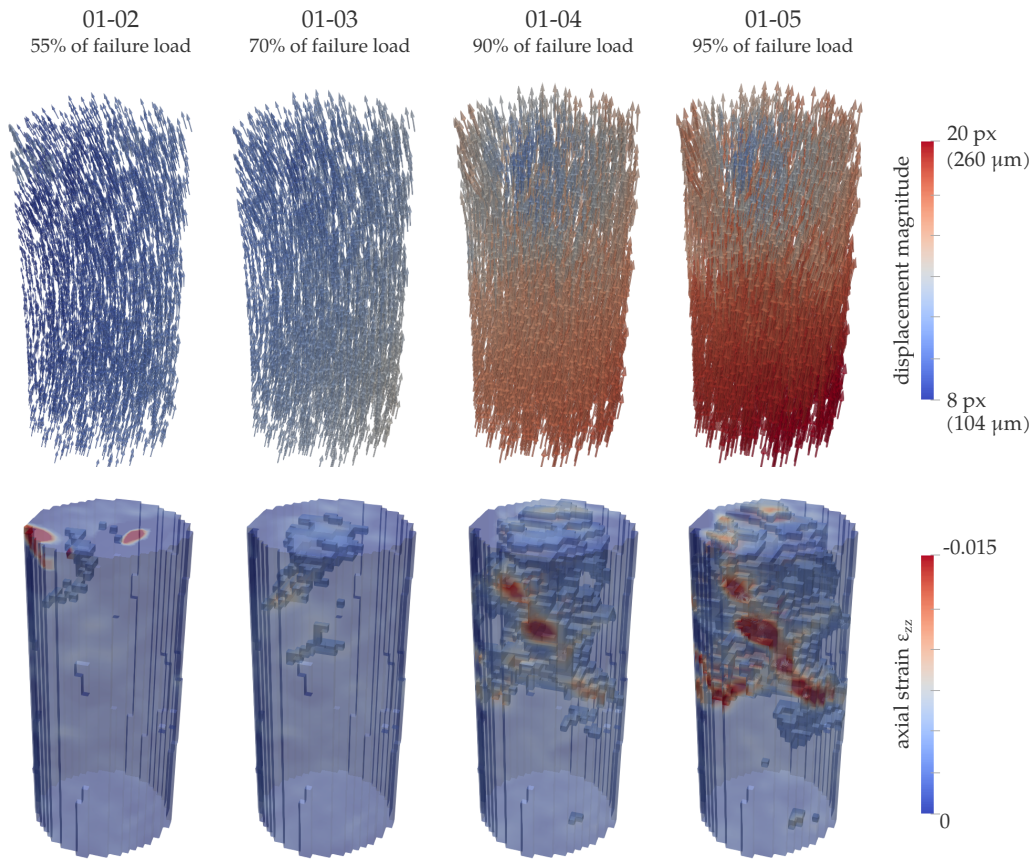


Figure 3.23: Kinematic fields in third uniaxial compression test (C-03). For visualisation, displacement vectors are scaled up 10 times and axial strains above -0.35% are faded

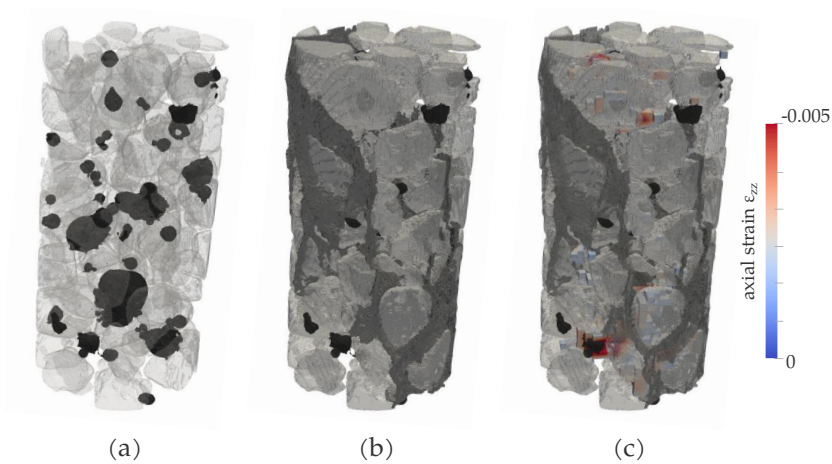


Figure 3.24: Crack patterns in C-01 test: (a) segmented largest heterogeneities of reference scan, (b) segmented macro-crack from the post-peak scan, (c) regions of localised strain measured at the last step overlaid with the final macro-crack

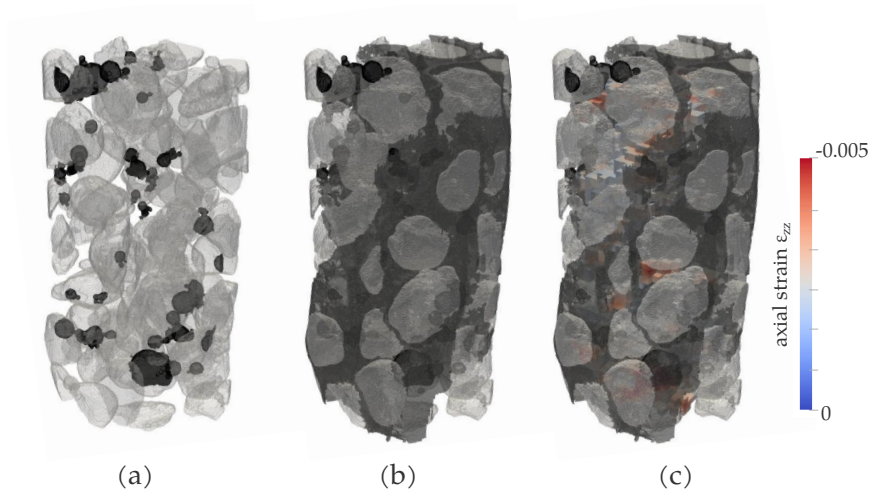


Figure 3.25: Crack patterns in C-02 test: (a) segmented largest heterogeneities of reference scan, (b) segmented macro-crack from the post-peak scan, (c) regions of localised strain measured at the last step overlaid with the final macro-crack

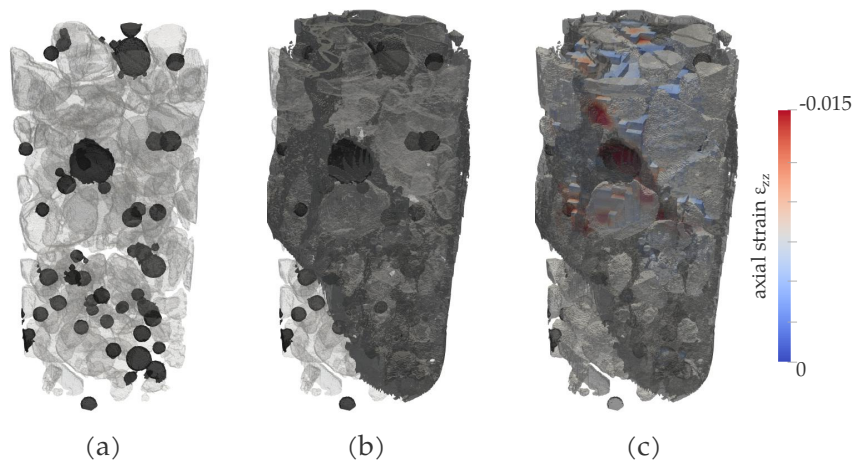


Figure 3.26: Crack patterns in C-03 test: (a) segmented largest heterogeneities of reference scan, (b) segmented macro-crack from the post-peak scan, (c) regions of localised strain measured at the last step overlaid with the final macro-crack

3.3.3 Triaxial compression

Three triaxial *in-situ* experiments are conducted in this study at 5 MPa, 10 MPa and 15 MPa confining pressures, with the obtained macroscopic responses (gathered in Fig. 2.18), showing that the peak compressive stress is increasing with an increasing level of confinement. Considering the fact that the response becomes more ductile and thus more easy to follow, for these tests (as opposed to the uniaxial ones) a correlation of the reference scan with the one captured after the failure of the samples is also performed. It should be reminded here that the test under the highest confinement had to be interrupted, since the limit of the forcemeter load capacity was reached. It is one of the cases where the measured kinematic fields are expected to shed some light on the failure mechanisms that occurred during the experiment.

Starting with the TX5-01 test, Fig. 3.27 presents the kinematic fields measured during this experiment. Note that slices through the kinematic fields of this test are also shown in Chapter 5. Due to the strong discontinuity occurring in the end of the test, a different scale bar is used for the measured fields before and after the failure of the sample. For the first pair of correlated 3D images, at 60% of the peak load, a smooth distribution of the displacements is observed, with the vectors pointing mostly upwards (although, slightly tilted on the top part), indicating the direction of the applied axial deviatoric load. As this load progresses, the magnitude of the displacement increases, with the vectors clearly tilting from the axial direction and the displacement field at 90% of the peak load becoming distinctly inhomogeneous. Reaching to the end of the test (after failure), the measured field consists of two discrete inclined blocks, with a zone of large displacement gradient in-between them.

Already at the first step, strain localisations are observed in both volumetric and deviatoric fields with regions reaching 0.5% compressive volumetric strain. In the second step, the strains are localised in two inclined zones (shear bands) crossing roughly diagonally the bottom part of the sample. One of the two bands dominates, with the localised deformation in the strain fields measured at the last step (after failure) consisting of a strong discontinuity, as indicated also by the displacement field. Note that the amplitude of the deviatoric strain measured along this band is not constant, although the physical meaning of the strain measured inside this strong discontinuity is rather lost. It is also worth mentioning that the width of this band directly depends on the spatial resolution of the local DVC procedure (*i.e.*, window size of 31 voxels) and it is not a voxel-scaled measurement as the residual field presented below.

The comparison between the identified zones of localised deformation and the failure patterns observed from the post-peak image is shown in Fig. 3.28. As revealed by the kinematic fields of Fig. 3.27, the failure seems to initiate from the bottom part of the sample, however, micro-cracks in this area are not captured by a simple thresholding of the greyvalues of the post-peak scan (see Fig. 3.28b). To observe the crack patterns in a finer scale, the greylevel residual fields coming from the correlation of the last step are also used to characterise the damaged micro-structure. The measured displacement field, evaluated at every grid point, is interpolated in every voxel position of the reference image, creating a deformed (by an heterogeneous displacement field) reference image. This deformed image is then subtracted from the post-peak one, yielding the residual field, high values of which are extracted and shown in Fig. 3.28c.

Due to the sub-pixel nature of the correlation measurements, a richer crack network is captured through the residual fields compared to a simple thresholding of the post-peak scan. Localised regions of the computed strain fields at the second step (at 90%

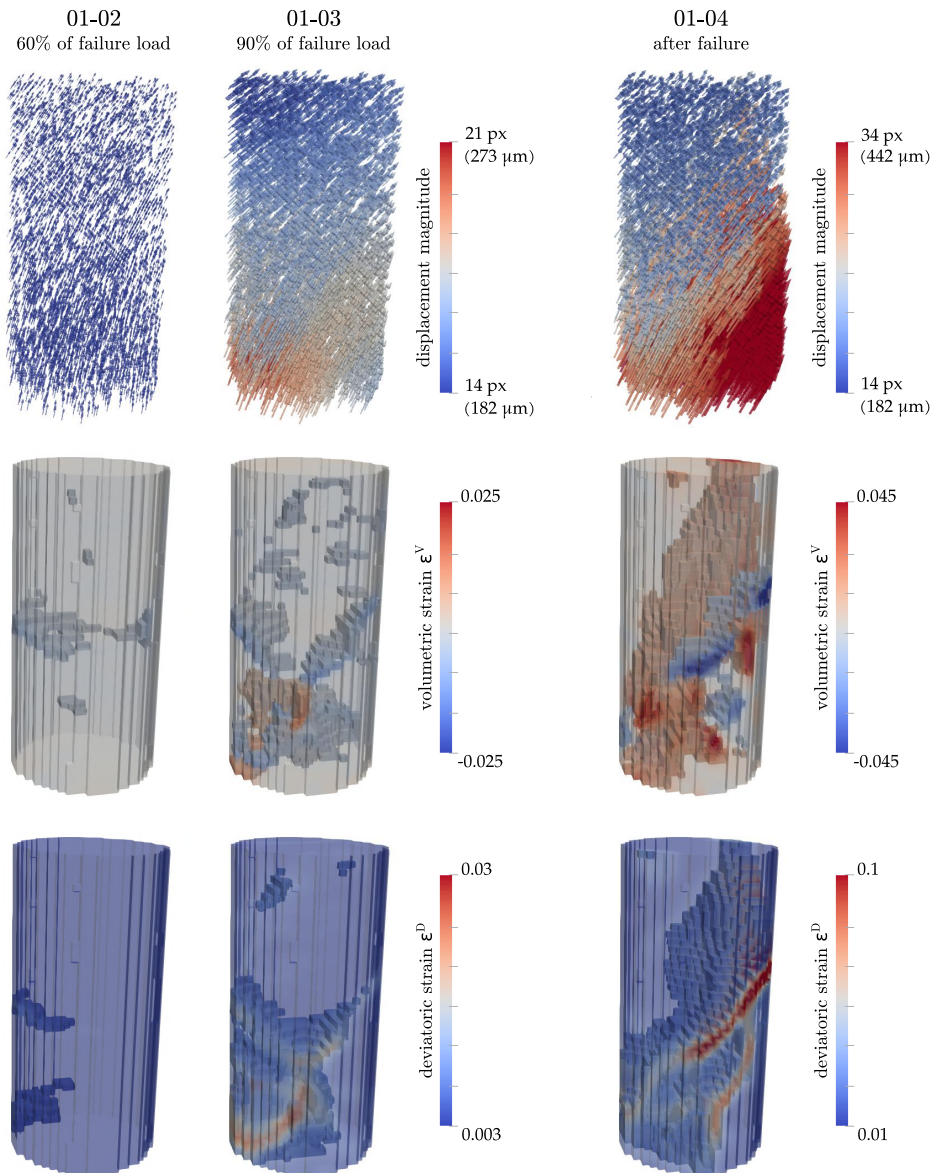


Figure 3.27: Kinematic fields in triaxial compression test under 5 MPa confinement (TX5-01). For visualisation, displacement vectors are scaled up 5 times. Positive volumetric strains lower than 0.3% and negative volumetric strains higher than -0.3%, along with deviatoric strains lower than 0.6% are faded before failure. Also positive volumetric strains lower than 1% and negative volumetric strains higher than -1%, together with deviatoric strains lower than 2.5% are faded for the last step, even though the physical meaning of strain is rather lost in such a strong discontinuity. Note that slices through these fields are shown in Chapter 5

of the peak load) coincide well with the extracted from the residual field crack network (see Fig. 3.28d). The specimen fails macroscopically on a sliding inclined plane, forming a quite complex network of cracks, which crosses the bottom half of the specimen diagonally and then traverses roughly vertically through the top part, branching around the coarser aggregates and propagating through the macro-pores.

Moving now to the triaxial compression tests at 10 MPa and 15 MPa confining pressures, since the behaviour becomes progressively more ductile (with increasing strain

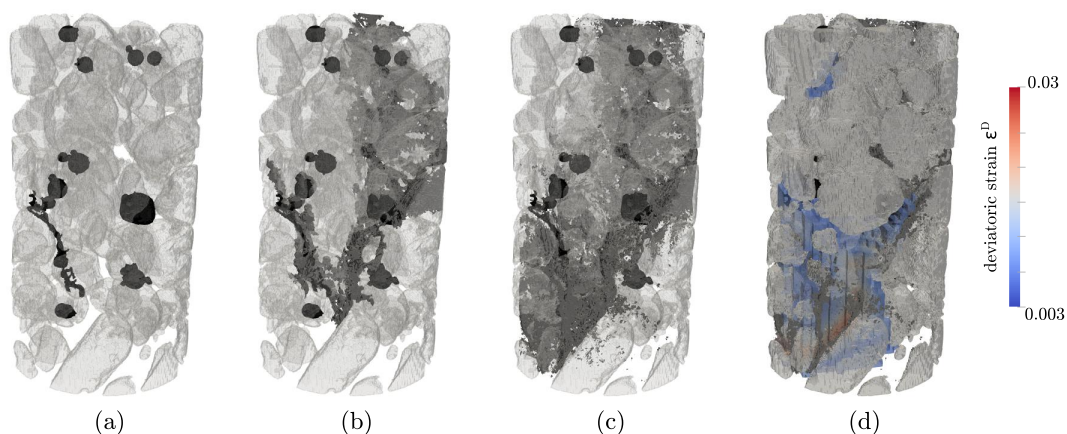


Figure 3.28: Crack patterns in TX5-01 test: (a) segmented largest heterogeneities of reference scan, (b) segmented macro-crack from post-peak scan, (c) regions of high residual values coming from the correlation between the reference and the post-peak scan, (d) regions of localised strain measured at the last step before failure overlaid with the regions of high correlation residual values

levels), a constant scale bar (different, though, for each test) is used for each of the kinematic fields calculated throughout these experiments. As shown in Fig. 3.29 and 3.30, in both tests for the first pair of correlated 3D images (at 40% of the peak load), the displacement vectors are not pointing upwards, but are rather tilted on the side, with lower computed magnitudes compared to the subsequent steps. A smooth distribution of the displacements is observed, with higher magnitudes at the bottom part (see length of the arrows), where the axial deviatoric load is applied. No strain concentrations can be observed at this stage, however, the localisation initiates well before the stress plateau with volumetric and deviatoric strain concentrations already visible in the second pair of correlated images for both tests. Despite the same trend so far, the evolution of the fracturing processes and the final failure modes are very different between these two experiments.

Regarding the TX10-01 test, as the deviatoric load increases, the displacement field becomes progressively more heterogeneous and regions with high volumetric and deviatoric strains appear at inclined bands across the specimen. Similarly to the TX5-01 test, the measured displacement field at the last step (after failure) consists of two discrete inclined blocks with a zone of a significant displacement gradient in-between them. By the end of the test, regions of high strain values concentrate at two main parallel inclined bands, even though the physical meaning of strain (as per the TX5-01 test) is rather lost in such a strong discontinuity.

Concerning the test under the highest confinement, while the deviatoric load increases, the localisation gets more pronounced, with the deviatoric strain accumulating within a shear band, which appears at the bottom part of the sample. The increase of the deviatoric strain is associated to a corresponding increase in compaction, highlighted in the volumetric strain field (negative values), whereby a formation of a compaction band slightly inclined with respect to the principal stress direction is observed. Even though this test had to be interrupted, the computed strain fields suggest that the macroscopic failure of the specimen happens on a roughly horizontal compressive shear band located at the bottom part of the sample. Note that this failure pattern can also, intuitively, be revealed by following the change of orientation of the displacement vectors during the

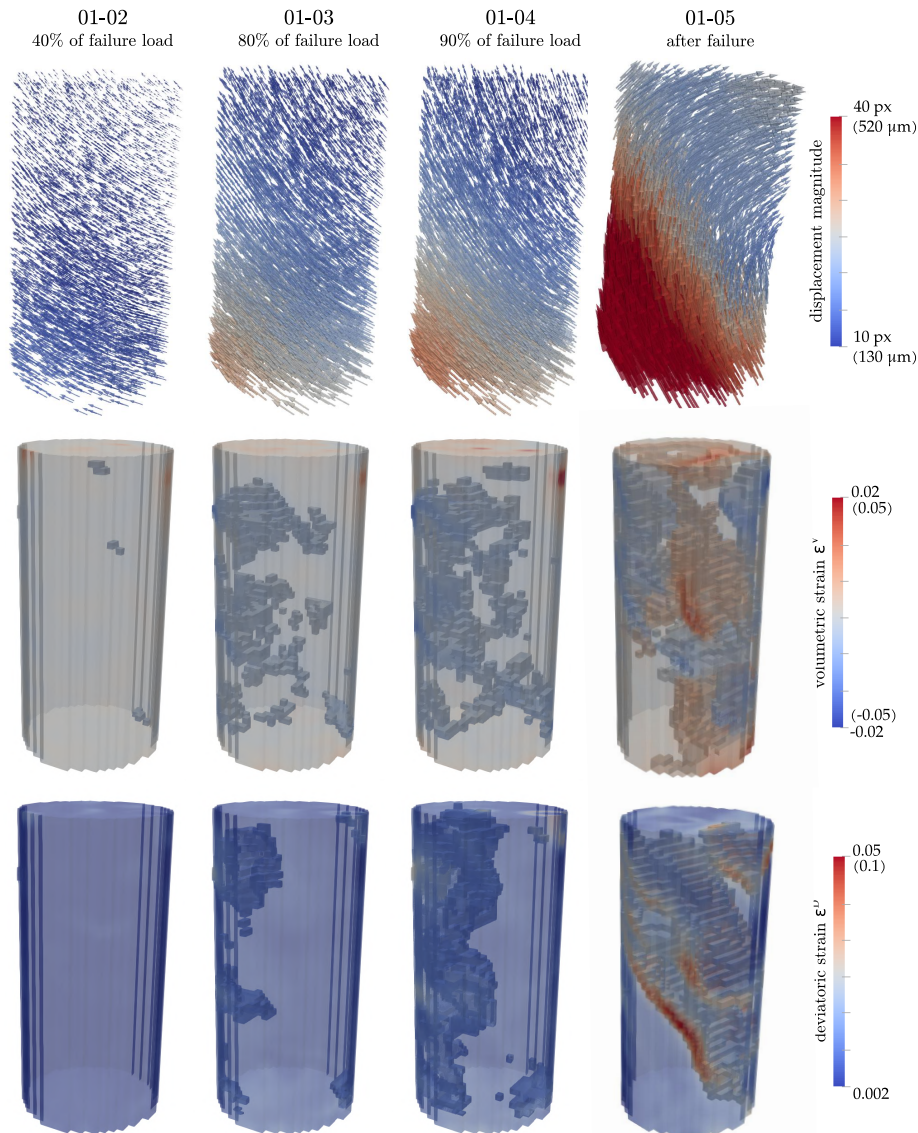


Figure 3.29: Kinematic fields in triaxial compression test under 10 MPa confinement (TX10-01). For visualisation, displacement vectors are scaled up 5 times. Negative volumetric strains higher than -0.35% and deviatoric strains above 0.8% are faded before failure. After failure (different scale bar for strains), negative volumetric strains higher than -0.55% and positive volumetric strains below 1% , together with deviatoric strains below 4% are faded, even though the physical meaning of strain (similarly to TX5-01 test) is rather lost in such a strong discontinuity

experiment. Unlike the TX5-01 and TX10-01 tests, the orientation of the displacement vectors do not remain fixed (pointing in a parallel tilt), but a discrete block in the bottom of the specimen (exhibiting the highest displacement magnitude) seems to rotate.

Concentrating on the damaged micro-structure, for the TX10-01 test, the crack network coming from the post-peak scan coincides well with the one extracted from the correlation residual field. Similarly to the TX5-01 test presented above, the specimen fails macroscopically on an sliding inclined plane, with regions of localised strains calculated at the last step before failure (90% of the failure load) being part of the created complex crack network (see Fig. 3.31).

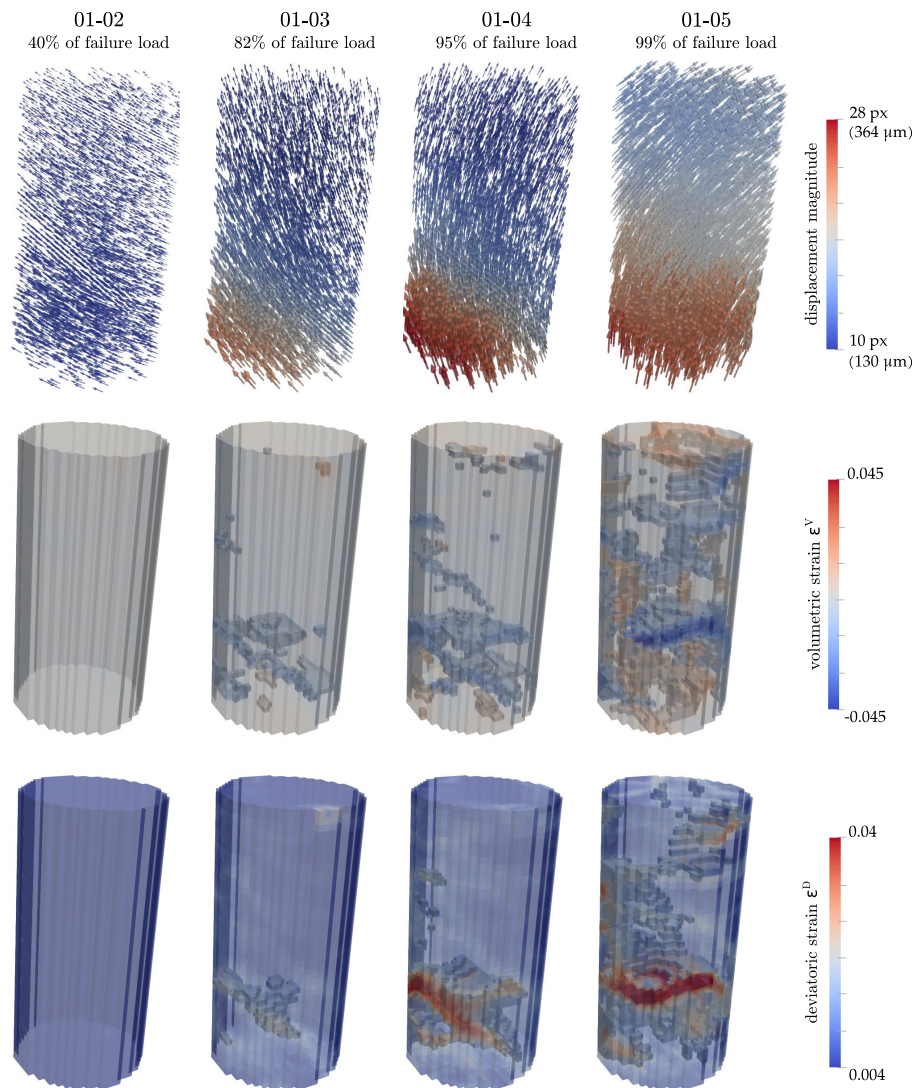


Figure 3.30: Kinematic fields in triaxial compression test under 15 MPa (highest) confinement (TX15-01). For visualisation, displacement vectors are scaled up 5 times. Negative volumetric strains higher than -0.7% and positive volumetric strains below 0.35% , along with deviatoric strains lower than 1.5% are faded. Note that slices through these fields are shown in Chapter 5

The different failure mode for the test under the highest confinement is also highlighted in the crack patterns obtained both from the residual fields of the last correlated pair of 3D images and the 3D image of the last scan, itself (see Fig. 3.32). Although few micro-cracks are also extracted in the middle of the specimen (see Fig. 3.32b), both fields indicate a high concentration of cracks principally on the bottom part of the sample. Observing the internal micro-structure, this region corresponds to a relatively high concentration of porosity (see Fig. 3.32a), suggesting that not the micro-cracking, but rather the collapsing of the macro-porous structure of the material is most likely to be the principal local damage mode that leads to the macroscopic failure of the specimen.

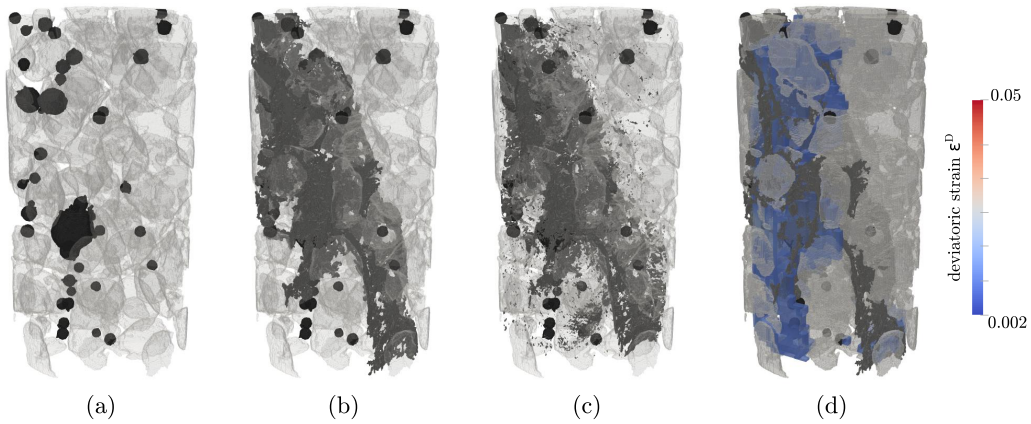


Figure 3.31: Crack patterns in TX10-01 test: (a) segmented largest heterogeneities of reference scan, (b) segmented macro-crack from post-peak scan, (c) regions of high residual values coming from the correlation between the reference and the post-peak scan, (d) regions of localised strain measured at the last step before failure overlaid with the regions of high correlation residual values

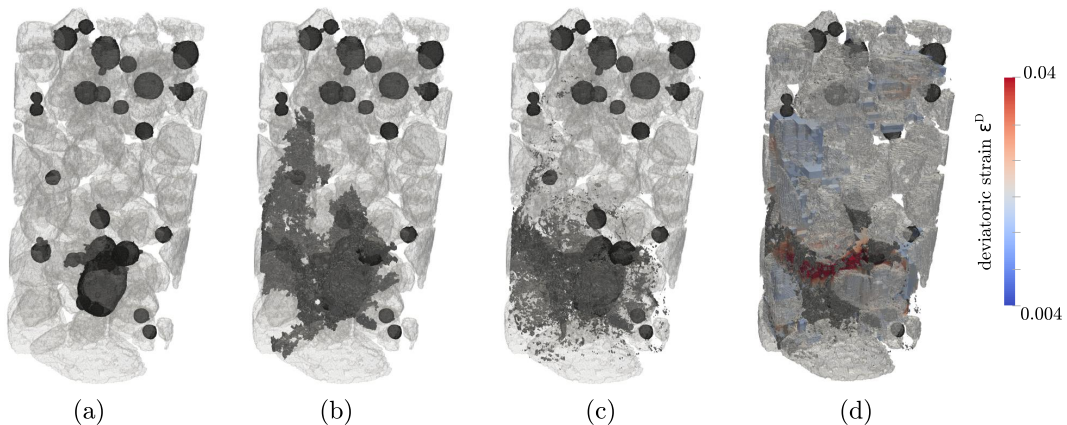


Figure 3.32: Crack patterns in TX15-01 test (highest confinement): (a) segmented largest heterogeneities of reference scan, (b) segmented macro-crack from post-peak scan, (c) regions of high residual values coming from the correlation between the reference and the post-peak scan, (d) regions of localised strain measured at the last step overlaid with the regions of high correlation residual values. Note that slices through these fields are shown in Chapter 5

3.4 Concluding remarks

In this third chapter the analysis of the 3D images coming from the *in-situ* mechanical tests on micro-concrete samples (detailed in Chapter 2) was presented. The first part of the chapter focused on the analysis of a single 3D image, starting by showing how a representative 3D greyscale image of the scanned micro-concrete samples looks like and introducing the principal challenge of separating the solid phase into aggregates and mortar matrix. The description of the developed segmentation method followed, having as a key the separation based on the variation of greyvalues inside each material (homogeneity of the material), instead of the absolute greyvalues (density of the material). From an image analysis point of view this was achieved by calculating the variance map of the greyscale image. The presented procedure was validated by comparing the same segmented set of aggregates coming from x-rays and neutron scans.

The second part of the chapter focused on the analysis of the evolution of the identified micro-structure during the tests, introducing the adopted methodology to quantify the first stages of the fracturing processes at the scale of the largest heterogeneities. The combination of a regularly-spaced and discrete (for the coarser aggregates) local DVC techniques was presented, followed by a discussion on the measurement uncertainties. In the last part of the chapter, the measured displacement and the derived strains fields for all the mechanical tests were presented and compared with the observed failure patterns coming from the post-peak scans. It was shown that the adopted DVC technique coupled with the data coming from the *in-situ* experiments offered valuable information for the micro-scale understanding of the mechanical behaviour of the studied material under the different loading paths considered.

For example in a case of uniaxial tension, relative displacements inside the samples in the range of 1/5 of the voxel size (2 to 4 μm) were measured and typical macro-cracks for fracture mode I were observed. More complex failure modes were observed for the compression tests (confined or unconfined). A notable example was the test under the highest level of confinement (15 MPa), where even though the experiment had to be interrupted since the limit of the forcemeter load capacity was reached, the measured kinematic fields revealed that a compactive shear was created.

As a general remark, thanks to the insights provided by the 3D field measurements, it was shown that the failure of concrete involves complex phenomena, attributed both to the brittleness of the material and its complex micro-structure. In order to further explore these phenomena and investigate the impact of the heterogeneities on the fracturing process of concrete, a numerical approach is employed, which is discussed in the following chapter.

Chapter 4

Numerical framework

This chapter details the numerical investigation of the mechanical behaviour of the micro-concrete specimens introduced in Chapter 2. At the meso-scale, the mechanical behaviour of quasi-brittle materials, such as the micro-concrete specimens studied here, is characterised by stress localisation and the appearance of initial micro-cracks around the weakest regions (usually the interfaces). These micro-cracks progressively grow and coalesce to develop one (or more) critical (in the sense that it percolates through the specimen) macro-crack(s), resulting to the macroscopic failure of the material. Therefore, from a numerical point of view, the two main challenges to model the quasi-brittle behaviour of the examined micro-concrete specimens at meso-scale are:

- to model the local discrete failure mechanisms
- to explicitly take into account the heterogeneities.

Concerning the former, a well-known problem arises when dealing with softening behaviours. In standard continuum constitutive models, the consideration of the material degradation by implementing strain-softening features leads to strains concentrations in narrow bands (*i.e.*, strain localisation phenomenon), which fails to provide an objective description of the localised material failure. The ellipticity of the governing differential equations is lost, which leads to an ill-posed boundary value problem [Sandler et Wright, 1984] yielding physically meaningless results, with the FE solution depending on the geometrical size of the elements [Pietruszczak et Mroz, 1981, Bažant et Belytschko, 1985]. In order to address this problem, mesh regularisations of the continuum constitutive equation can be introduced (smeared crack approach [Hillerborg, 1991, Oliver, 1989]) or a modification of the nature of those equations can be performed (non-local models, higher order continuum models, gradient based models [Pijaudier-Cabot et Bažant, 1987, Peerlings *et al.*, 1996, Needleman, 1988]).

In opposition to these approaches, FE models with embedded discontinuities have emerged as an interesting alternative to model material failure, providing specific kinematics enrichments [Dvorkin *et al.*, 1990]. More specifically, these models directly capture the physical discontinuity (*i.e.*, crack) within the material itself by enriching the continuous displacement modes of the standard FE with additional discontinuous displacements. Unlike the standard FE, a discontinuity surface is placed inside the elements irrespectively of their specific size and orientation. The released energy corresponds to the crack opening process and is dissipated into the discontinuity surface. Consequently, these methods differ from schemes that impose discontinuities at the element interfaces, with mesh dependencies no longer appearing and regularisation techniques no more required.

This enrichment technique can be classified into two broad categories; the *global* (nodal) enrichment and the *local* (element) enrichment with their principal numerical implementations known, respectively, as eXtended Finite Element Method (X-FEM) [Moës *et al.*, 1999] and Embedded Finite Element Method (E-FEM) [Ortiz *et al.*, 1987]. A detailed comparison between these two methods can be found in [Oliver *et al.*, 2006]. Herein is mentioned that additional degrees of freedom are introduced in X-FEM for the elements enhanced with discontinuities, leading to a higher flexibility but also to a higher computational cost. On the other hand, the computational cost is relatively lower for E-FEM, attributed to the inherent local aspect of this method, with an inexpensive equation solving and condensation at the element level. This allows to preserve the global size of the problem, without adding any global unknowns no matter the number of discontinuities (cracks) that may appear. In the presented case, considering the complex crack patterns (involving crack coalescence and branching) inherent in the fracturing process of micro-concrete and the choice to keep the local behaviour as simple as possible, the meso-model used follows the E-FEM formulation.

It is worth mentioning that the kinematics enhancements have been originally introduced in E-FEM to model material degradation. However, their local aspect and light framework has naturally led to their application for different purposes, such as to model material heterogeneities (see Section 4.1.1). A local kinematic enhancement that captures the contrast in material properties within an element provides a convenient tool for interface modelling, without the need to insert additional elements to account for interfaces. This kind of local enhancement coupled with a realistic representation of the meso-structure and an appropriate meshing technique, addresses the second crucial issue regarding the mechanical modelling of heterogeneous materials at the meso-scale; which is the explicit representation of heterogeneities within a FE context.

The chapter starts by introducing the FE meso-model used in this work, mainly focusing on its basic ingredients. The introduction of two different kinds of kinematics enhancements in the context of E-FEM is described, in order to address both the explicit representation of the morphology and the modelling of the local discrete failure mechanisms. The phenomenological law that enables the consistency between the discontinuity kinematics and the continuum constitutive model is then introduced. The second part of the chapter focuses on the application of the meso-model to the micro-concrete specimens studied in this work. An illustrative example of the creation of the FE mesh based on the identified morphology coming from an x-ray scan is given, along with a detailed description of the boundary conditions applied for each of the different loading paths considered. The identification of the numerical parameters of the model based on the first *in-situ* tensile experiment follows. In the last part of this chapter, new morphologies coming from the remaining *in-situ* tests are introduced to the meso-model and without any further identification, the model is asked to predict the mechanical responses for the different loading paths.

4.1 FE meso-model description

Over the years, a large number of numerical meso-models for concrete have been developed (see Chapter 1), based on different theories (fracture mechanics, damage mechanics, plasticity theory, *etc*), that fit within the context of continuum models (using the Finite Element Method), discrete models (using for example the Discrete Element Method) or a combination of them, by introducing discontinuities within continuum models. As al-

ready mentioned in the introduction of this chapter, the numerical model used in this work belongs to the latter category, whereby the explicit representation of the heterogeneous morphology and the modelling of the local discrete failure mechanisms are handled by a double kinematics enhancement within the context of the E-FEM. In what follows, only the main ingredients of the model are presented, while a detailed description can be found in [Roubin *et al.*, 2015b, Roubin, 2013] and [Benkemoun *et al.*, 2010].

4.1.1 Local kinematics enhancement

Accounting for the morphology

In the context of FE, the methodology most frequently used for the representation of a morphology is the so-called *adapted mesh method*. It roughly consists in firstly placing the nodes at the interfaces, which is followed by a volumetric meshing of each phase. Each element of the generated mesh is essentially on one or the other side of the interface, physically meaning that it is occupied by one of the constitutive materials of the considered morphology. Adapted meshes lead to a very accurate description of the morphology, at the expense, though, of complex and time costly meshing algorithms in order to ensure good element shapes. This is especially true for complicated geometries, which happens to be the case of the meso-structure studied herein. In addition to this, particular attention has to be paid on the modelling of the interfaces (*i.e.*, debonding mechanism), by introducing for example zero thickness elements (*i.e.*, cohesive bands) [Barenblatt, 1962].

In this work, an alternative meshing technique is adopted, referred to as *non-adapted mesh method* [Moës *et al.*, 2003]. As a first step, regardless of any morphology, an unstructured FE mesh is generated, with randomly and evenly distributed nodes in space. The second step consists in *projecting* the heterogeneous morphology onto the generated FE mesh. This morphological projection consists in looping over each element and identifying in which phase of the morphology each node belongs. On one hand, when all nodes of an element belong to the same phase, the element is a classical FE occupied by one of the constituted materials. On the other hand, an element with nodes belonging to two different phases is split into two parts by a physical interface, inheriting material properties of each of the two phases.

Following the E-FEM formulation, in order to account for this material discontinuity, a kinematic enhancement is introduced by means of a jump in the strain field within the element, called hereafter *weak discontinuity*. This idea dates back in late 1980s in the pioneer work of Ortiz [Ortiz *et al.*, 1987] to model localisation bands in the context of the E-FEM. The application of weak discontinuities to model material heterogeneities has been introduced later in [Sukumar *et al.*, 2001] in the context of X-FEM followed by the works of [Markovic *et al.*, 2005], [Ibrahimbegovic et Melnyk, 2007] and [Hautefeuille *et al.*, 2009] in the context of E-FEM.

The morphological projection leads to two different kinds of elements, those that have all their nodes within the same phase (aggregates, macro-pores or mortar-matrix for the studied case) and those that have nodes in two different phases, which are the ones enhanced by a weak discontinuity. The strain inside an element after this enhancement is written in the Voigt notation as:

$$\boldsymbol{\varepsilon} = \mathbf{B}\mathbf{d} + \mathbf{G}_w[|\boldsymbol{\varepsilon}|] \quad (4.1)$$

The first term contains the standard FE strain field, where \mathbf{d} is the vector which contains the degrees of freedom corresponding to the nodal displacements multiplied by

the standard strain interpolation matrix \mathbf{B} (derivatives of the shape functions). The second term contains the weak discontinuity vector $[[\boldsymbol{\varepsilon}]]$ (*i.e.*, the strain jump), which is a set of new unknowns, multiplied by a matrix \mathbf{G}_w that contains a Heaviside function at the interface, representing the interface geometry. This geometrical information accounts for the volume fraction of each phase inside the element, along with the orientation of the respective interface (*i.e.*, interface vector \mathbf{n}). Both the volume fraction of each phase and the interface vector are computed during the morphological projection, regardless of any mechanical state. Note that it is assumed that the discontinuity surface inside a weakly enhanced element is flat (*i.e.*, \mathbf{n} is constant over the interface).

Accounting for the local failure mechanisms

Micro-cracking is the local failure mechanism considered here, being the key phenomenon to represent material degradation and, in turn, to reproduce the quasi-brittle behaviour of the studied heterogeneous material. From a kinematics point of view, micro-cracks can be characterised as jumps in the displacement field, representing thus the discontinuous aspect of them. In order to account for these displacement discontinuities (jumps), the FE are enhanced, this time, by another set of local kinematics, referred to as *strong discontinuity*.

[Dvorkin *et al.*, 1990] were the first to develop a method able to deal successfully with strong discontinuities, introducing localisation lines in FE, providing a first solution insensitive to the mesh size. The strong discontinuity by means of a displacement jump has been introduced in [Simo *et al.*, 1993] within a FE framework and further developed in [Simo et Oliver, 1994, Oliver, 1996, Wells et Sluys, 2001]. The strain inside an element after this enhancement is written in the Voigt notation as:

$$\boldsymbol{\varepsilon} = \mathbf{B}\mathbf{d} + \mathbf{G}_s[[\mathbf{u}]] \quad (4.2)$$

where the first term is still the standard FE strain, while the second term corresponds to the strong discontinuity. $[[\mathbf{u}]]$ is a vector of new unknowns containing the displacement discontinuity components (*i.e.*, directly corresponding to the crack opening), multiplied by the matrix \mathbf{G}_s that contains a Dirac-delta function at the interface, which represents the position and the orientation of the crack. Note here that, as opposed to the weak discontinuity, the strong discontinuity is not known prior to any mechanical calculation and, thus, both a localisation and an initiation criterion should be introduced, as explained in Section 4.1.2.

Double kinematics enhancement

As first introduced in [Benkemoun *et al.*, 2010], in case of debonding, the two enhancements can be linearly combined leading to the following strain formulation:

$$\boldsymbol{\varepsilon} = \underbrace{\mathbf{B}\mathbf{d}}_{\text{standard}} + \underbrace{\mathbf{G}_w[[\boldsymbol{\varepsilon}]] + \mathbf{G}_s[[\mathbf{u}]]}_{\text{enhanced}} \quad (4.3)$$

Fig. 4.1 gathers the three types of discontinuity settings that can occur inside a 4-noded tetrahedron element. It illustrates how the presented formulation permits a material interface (modelled by a weak discontinuity) to fail (modelled by a strong discontinuity), thus modelling debonding [Roubin *et al.*, 2015b]. It should be noted here, that in the case

where both weak and strong enhancements are present inside an element, the position and the orientation of the strong discontinuity is set the same to the weak one (*i.e.*, material interface). This means that the crack is forced to open following the material geometry. In case of no difference in material properties inside the element, the crack opens following a local governing law presented below, with the discontinuity surface appearing in the barycentre of the element.

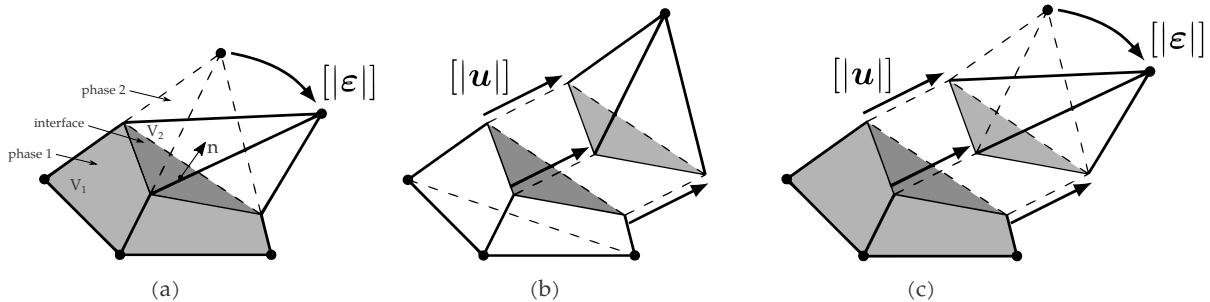


Figure 4.1: 4-noded tetrahedron element with: (a) one weak discontinuity, (b) one strong discontinuity and (c) both weak and strong discontinuity

4.1.2 Phenomenology and resolution scheme

The double kinematics enhancement described so far enriches the standard finite element approximation by discontinuous shape functions, introducing two additional set of unknowns in the global mechanical problem; one being the weak discontinuity vectors $[[\boldsymbol{\varepsilon}]]$ and the other the crack openings $[[\boldsymbol{u}]]$. Note that no matter the type of discontinuity considered in an element (weak, strong or both), it is assumed that it follows a single discontinuity surface, dividing the finite element Ω_e into two sub-domains Ω_e^\oplus or Ω_e^\ominus (with $\Omega_e = \Omega_e^\oplus \cup \Omega_e^\ominus$). It should be also mentioned that the additional degrees of freedom introduced by these enhancements have an internal character, which means that they are solved, locally, on the element level. From a computational point of view, this is a significant advantage of the E-FEM formulation, since the number of the global degrees of freedom remains constant, strictly defined by the number of nodes of the mesh.

The behaviour law can be written as a function of the two enhancements, combining continuous and discontinuous quantities, following the Discrete Strong Discontinuity Approach (DSDA) [Oliver, 2000]. More specifically, the part of the element that corresponds to a strong discontinuity is governed by its own constitutive law, which complements the behaviour law attributed to the bulk of the material, which remains continuous and is governed by a selected stress-strain law. Here, following the general spirit of simplicity in the meso-scale modelling, the stress-strain law is assumed to be linear-elastic, but in general can be inelastic (see for example [Oliver, 1996]). Since the material properties can differ depending on whether they are evaluated in Ω_e^\oplus or Ω_e^\ominus , the behaviour law is written as:

$$\boldsymbol{\sigma}(\boldsymbol{d}, [[\boldsymbol{\varepsilon}]], [[\boldsymbol{u}]]) = \begin{cases} \boldsymbol{C}^\oplus \boldsymbol{\varepsilon}^\oplus = \boldsymbol{C}^\oplus (\boldsymbol{B}\boldsymbol{d} + \boldsymbol{G}_w^\oplus [[\boldsymbol{\varepsilon}]] + \boldsymbol{G}_s [[\boldsymbol{u}]]) & \text{in } \Omega_e^\oplus \\ \boldsymbol{C}^\ominus \boldsymbol{\varepsilon}^\ominus = \boldsymbol{C}^\ominus (\boldsymbol{B}\boldsymbol{d} + \boldsymbol{G}_w^\ominus [[\boldsymbol{\varepsilon}]] + \boldsymbol{G}_s [[\boldsymbol{u}]]) & \text{in } \Omega_e^\ominus \end{cases} \quad (4.4)$$

where the tensor \boldsymbol{C} is the Hooke operator, which contains the elastic material properties of each phase; *i.e.*, the Young's modulus E and the Poisson ratio ν .

Note that \mathcal{C} remains constant during the mechanical solution, which means that the softening does not come from the material degradation, but rather through kinematic considerations attributed to the modification of the vector $[[\mathbf{u}]]$ (*i.e.*, crack opening). The energy is dissipated, thus, through the discontinuity surface, which plays the role of softening regularisation, yielding a mesh-independent solution [Simo *et al.*, 1993]. As discussed in the introduction of this chapter, this is a significant difference to strain-softening plasticity models or damage models known for their sensitivity to the discretisation. It should be mentioned here that one of the main requirements imposed in this formulation is that the continuity of the traction vector is respected in the discontinuity surface, ensuring that the constitutive model is still consistent after the activation of a strong discontinuity (see [Roubin, 2013] for more details).

Following the DSDA approach, the non-linear failure mechanism is described through a local governing law at the discontinuity surface formulated as a so-called traction-separation law (equivalent to a cohesive law), which links the traction transmitted over the discontinuity surface (stress state) to the displacement jump (crack opening). The discrete approach is activated when a certain stress state within an element is reached; the tensile strength σ_y , which should be considered as a meso-scale material characteristic. This is expressed by the following tension-based Rankine localisation criterion:

$$\Phi_l = \mathbf{T} \cdot \mathbf{n} - \sigma_y \quad (4.5)$$

where \mathbf{n} is the discontinuity orientation vector and $\mathbf{T} = \boldsymbol{\sigma} \cdot \mathbf{n}$ (in matrix format) is the traction vector at the discontinuity surface.

The above localisation criterion specifies also the orientation of the crack, where two different cases should be considered. In case of an element with shared material properties, the crack opens at the interface between each phase. The normal vector \mathbf{n} is considered to be the orientation of the material interface, which is known prior to any mechanical application. In case of an element not enhanced by a weak discontinuity, the Rankine criterion postulates that the normal vector \mathbf{n} is the direction of the largest principal stress, defined simply by the first eigenvalue of the stress tensor inside the element. Here it should be noted that in both cases (with or without a weak discontinuity), when the localisation occurs ($\Phi_l \geq 0$), the orientation of the crack is recorded and remains fixed.

Once the localisation has occurred, the failure mechanism is driven by an opening criterion. In the sake of simplicity in the meso-scale modelling, a basic single traction criterion and brittle softening is used here, with the hardening function decreasing exponentially with respect to the crack magnitude:

$$\Phi_o = \mathbf{T} \cdot \mathbf{n} - \sigma_y \exp\left(-\frac{\sigma_y}{\mathcal{G}_f}[u]\right) \quad (4.6)$$

where \mathcal{G}_f is another meso-scale material characteristic, denoting the fracture energy of each phase (corresponding to the amount of energy necessary to create a fully opened crack) and $[u] = \|[u]\|$ is the norm of the crack opening vector, which leads to a local brittle behaviour. Note that as \mathcal{G}_f tends to 0 (or ∞), the response becomes brittle (or ductile). Since this law provides information only on the norm $[u]$ of the crack vector $[[\mathbf{u}]]$, it is assumed here that the orientation of this vector is the same as \mathbf{n} . This means that the evolution only of the first component of the traction vector is governed by the displacement jump, corresponding thus to a mode I crack opening. It is important to note that under this assumption no relative sliding of the crack faces is considered.

The described behaviour law, which makes possible the consistency between strong discontinuity kinematics and a continuum constitutive model, is presented in Fig. 4.2:

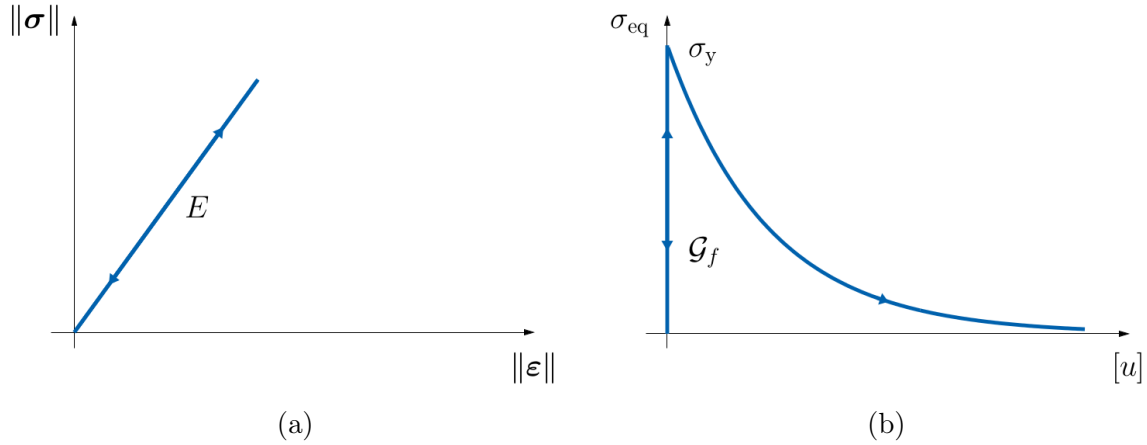


Figure 4.2: From [Roubin *et al.*, 2015b] Elastic/brittle behaviour: (a) behaviour outside the discontinuity interface for a 1D case, (b) behaviour at the discontinuity interface

As mentioned above, following the Embedded FE formulation [Oliver, 1996, Wells et Sluys, 2001, Roubin *et al.*, 2015b], the equations added by the presence of the enhanced parts of the strain field are solved at the element level, by performing a local resolution. This means that the internal variables $[\|\boldsymbol{\varepsilon}\|]$ and $[\|\boldsymbol{u}\|]$ are computed for a fixed value of the nodal displacements \boldsymbol{d} within each FE. Note also that in the presented case, an analytical solution exists in order to solve the local non-linear problem of the considered opening criterion (see Eq. (4.6)), leading to a light local framework, where no local Newton procedures are necessary (see details in [Roubin, 2013]). Once the local variables are computed, a static condensation [Wilson, 1974] allows the system to keep the same size as without enhancements (*i.e.*, there are no additional global unknowns) and the nodal displacement increments are computed from the solution of the global equilibrium equation of the system. As already mentioned, this specific feature of the embedded formulation allows for preserving the global size of the system (which is defined by the number of nodes), regardless of the number of cracks or the complexity of the geometry.

The presented framework is implemented in the FE code FEAP [Taylor, 1987] and the implemented quasi-Newton BFGS resolution scheme coupled with an iterative solver (Conjugate Gradient) is used to solve the non-linear set of equations of the global system.

4.2 Application to micro-concrete

After the description of the basic characteristics of the FE meso-model, it is now tested on the micro-concrete specimens introduced in Chapter 2. In what follows, an illustration of the morphological projection described in Section 4.1 is given, based on the identified morphology coming from the first *in-situ* tensile test (see Section 3.1). A description of the application of the different boundary conditions required for each loading path follows. The calibration of the meso-model is then presented, where the numerical parameters are identified based on the macroscopic response of the first *in-situ* tensile experiment (see Section 2.5). Without performing any further numerical identification, the model is then

challenged by predicting the macroscopic responses of the remaining *in-situ* tests, with different morphologies and for different loading paths.

4.2.1 Accounting for the morphology imaged through x-rays

For each numerical simulation presented herein, the input morphology of the meso-model comes from the reference (*i.e.*, intact) x-ray 3D image of the corresponding *in-situ* test. It should be recalled that the morphologies of the studied micro-concrete samples are obtained through the segmentation procedure described in Chapter 3 (see Section 3.1). As mentioned in Section 4.1, the first step of the *non-adapted meshing* procedure is the creation of the unstructured FE mesh, independently of any morphology. The GMSH software [Geuzaine et Remacle, 2009] is used to create this mesh, based on a Delaunay triangulation of randomly positioned nodes. The generated mesh is a cylinder of the dimensions of the micro-concrete specimens consisting of 4-noded tetrahedra elements, as shown in Fig. 4.3c.

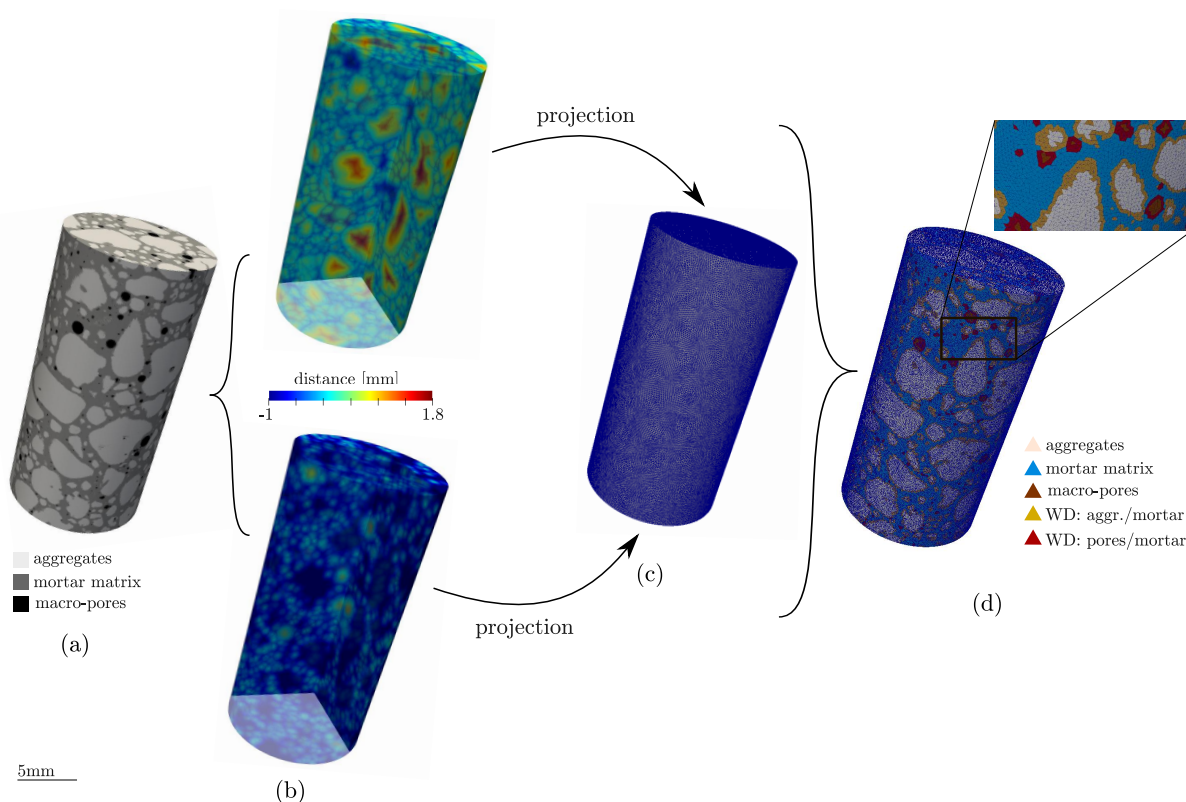


Figure 4.3: Non-adapted mesh method: (a) starting from the identified morphology (segmented image), (b) the distance fields for each inclusion phase are calculated (aggregates top and macro-pores bottom) and (c) projected onto the unstructured FE mesh (d) leading to 5 sets of FE

The second step consists in projecting the identified morphology onto the FE mesh. Directly projecting the discrete segmented image (see Fig. 4.3a), would result in an incorrect computation of the interface vectors in the elements with shared material properties (enhanced with a weak discontinuity), since a gradient is required for an accurate estimation of the orientation of these vectors. For this reason, the distance fields of each inclusion phase (aggregates and macro-pores) are calculated. This is achieved by transforming the binary images of each inclusion into scalar fields, where the values of each

voxel are inversely related to the distance from the closest boundary (see Fig. 4.3b). The calculated distance fields are signed, which means that they are positive inside the inclusions, negative outside and zero at the border of each inclusion (*i.e.*, interface). These two separate distance fields are the ones used for the projection onto the unstructured FE mesh yielding the final FE mesh which represents the heterogeneous morphology, as shown in see Fig. 4.3d.

Following the enhanced kinematics formulation described above, the projection leads to five sets of FE:

- three classical FE, falling inside aggregates, mortar matrix or macro-pores
- two FE enhanced with weak discontinuities, falling between aggregates/mortar and macro-pores/mortar, accounting for their respective interfaces.

Note that due to the projection of the two different distance fields of each inclusion phase, elements accounting for the interface between the two inclusion phases (aggregates/macro-pores) are not considered here.

The characteristic length of each tetrahedron (*i.e.*, average distance between nodes) is crucial and has a major impact on the relevance of the modelled morphology. In order to observe the relationship between the node density of the FE mesh and the corresponding representation of the morphology, a parametric analysis is performed. The morphology coming from the first *in-situ* tensile test is projected onto different FE meshes with gradually increasing node densities.

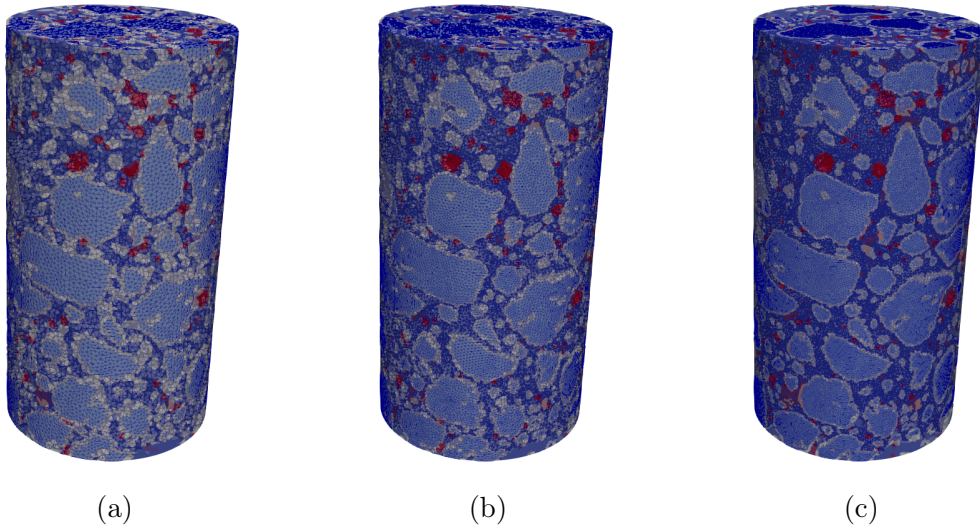


Figure 4.4: The morphology coming from the reference scan of the first *in-situ* tensile test (T-01) projected onto a FE mesh with: (a) 4.4×10^5 dof, (b) 1.6×10^6 dof and (c) 3.4×10^6 dof

As it can be seen in Fig. 4.4, if the morphology is not sufficiently discretised by the FE mesh, it is not accurately represented. The volume fraction of the different phases as a function of the mesh density is computed in Table 4.1. As a general trend, the coarser the mesh, the higher the risk of losing morphological information. In a coarse mesh (Fig. 4.4 on the left), the deterioration of the actual shape of the inclusions (mainly the aggregate's) is more significant, with some of them appearing touching each other. Moreover, the smallest heterogeneities of the considered morphology (*i.e.*, the smallest

macro-pores) are sufficiently captured only in the finest FE mesh (elements coloured red in Fig. 4.4).

This inaccurate representation of the morphology affects, in turn, the calculated macroscopic material response, as revealed from a series of preliminary uniaxial tensile simulations presented in Fig. 4.5. It can be seen that the elastic behaviour of the material is affected by the mesh density. The coarser the mesh, the stiffer the response, with the computed Young's moduli ranging from 35.6 GPa to 27.7 GPa (see also Table 4.1). A coarse FE mesh seems also to overestimate the macroscopic tensile strength, which ranges from 4.7 MPa to 3.3 MPa.

The differences in the Young's moduli and the tensile strengths can be explained from the fact that the morphology, not sufficiently discretised, exhibits unrealistically strong paths, due to the touching aggregates. The creation of these strong paths is also manifested from the stress state at the end of the loading, with the total amount of dissipated energy (area below the stress-strain curve) being significantly larger in the case of a coarse mesh. It is shown, however, that above a certain level of mesh density, the simulations converge to a similar macroscopic response. This means that aiming for an even finer mesh, would potentially only increase the computational cost, rather than enrich the mechanical solution. Note that more extended studies of mesh convergence with respect to the geometrical properties can be found in [Benkemoun *et al.*, 2010].

Table 4.1: Phases volume fraction, along with computed macroscopic Young's moduli and tensile strengths for different discretisations (*i.e.*, mesh densities) of the same morphology

Mesh dof	aggregates [%]	matrix [%]	WD aggr./matrix [%]	E [GPa]	σ_{\max} [MPa]
0.4×10^6	25.6	27.3	42.6	35.6	4.7
0.7×10^6	27.1	30.4	37.8	33.9	4.4
1.6×10^6	31.1	34.7	29.5	30.1	3.7
2.0×10^6	31.7	35.8	27.8	29.3	3.6
2.6×10^6	32.2	37.1	26.1	28.2	3.4
3.4×10^6	32.9	38.3	24.2	27.7	3.3

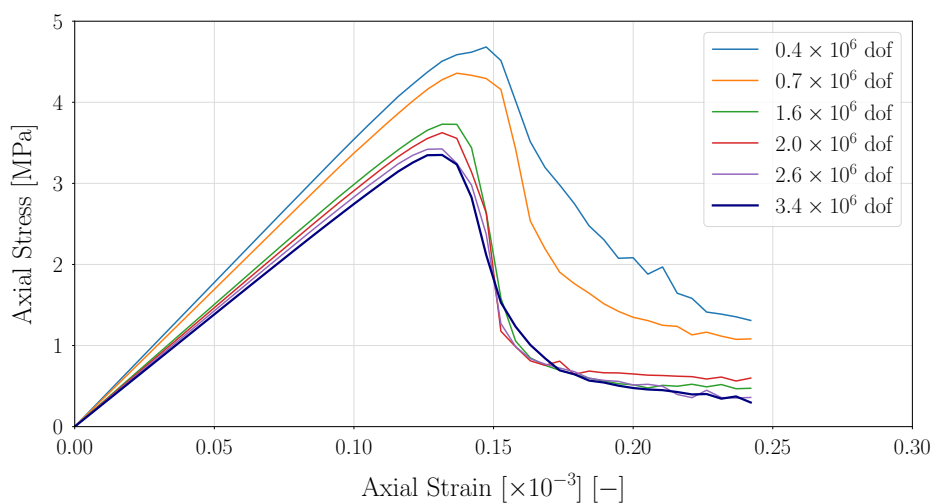


Figure 4.5: Macroscopic stress-strain responses for different discretisations (*i.e.*, mesh densities) of the same morphology under uniaxial tension

4.2.2 Application of boundary conditions

As already mentioned, the mechanical response of the micro-concrete specimens is studied under: uniaxial tension, uniaxial compression and triaxial compression. In order to accurately account for the actual experiment, the kinematic boundary conditions measured from the experimental fields (see Section 3.3) can be prescribed in the numerical simulations, an operation which for a number of reasons is not trivial.

To begin with, a local correlation in a cubic structured grid is performed in this work, where no continuity is imposed in the sought displacement field between the separate correlation windows (see Section 3.2.1). Besides, due to the compromise between the level of uncertainty and the spatial resolution of the measurements, the experimental field is evaluated in a coarse grid with a point spacing of 0.4 mm. However, as discussed in the previous section, a fine tetrahedral FE mesh is required to have a sufficient discretisation of the micro-structure, with the average distance between the nodes of the tetrahedra set to 0.1 mm. Therefore, an interpolation of the discontinuous experimental field evaluated on a coarser cubic grid to the boundary nodes of the finer tetrahedral FE mesh is required. Meanwhile, the error and noise (see Section 3.2.3) inherent in these experimental data (and especially at the points on the boundaries) should be carefully accounted for, in order on one hand not to induce non-physical damage in the FE simulations and on the other hand not to oversmooth the experimental data. It should be also mentioned that during the *in-situ* experiments scans are performed at discrete loading steps (with only two scans before failure in some cases) and thus a significantly discontinuous experimental displacement history can only be obtained.

For all these reasons and without neglecting the importance of considering the actual displacement field, a rather simpler approach is followed here. The experimental kinematic boundary conditions are not prescribed in the numerical computations presented in this work. However, the direct interplay between experimental and numerical displacement fields is discussed in the last chapter of this doctoral work. The presented simulations are performed under uniform displacement control, in order to follow the post-peak response of the numerical samples, with a description of the chosen boundary conditions for each loading path detailed in the following.

In case of uniaxial tests, the minimum constraints for blocking the rigid-body motion are applied. Displacement control computations are performed along the vertical axis of the cylindrical mesh (*i.e.*, by imposing a uniform vertical displacement on the upper surface), while the perpendicular directions are stress free. Concerning the triaxial tests, the simulations are performed in two stages. The first stage consists in reaching the level of the intended confining pressure (*i.e.*, hydrostatic phase). This is achieved by applying in the outer surface of the sample an approximately uniform pressure (*i.e.*, the intended confinement), while at the upper surface of the cylinder a vertical displacement is applied, such that by the end of this first stage, the pressure is approximately equivalent to the intended confining pressure everywhere in the cylinder. The magnitude of this applied displacement is found through an iterative process, considering an error tolerance in global equilibrium.

Note that both stages of the simulation are governed by the same elastic/brittle behaviour law (as introduced in Section 4.1.2), which means that during the application of the confinement localisation may occur in some elements. In other words, a linear-elastic behaviour is not enforced during the confinement phase, however, the global material response remains roughly linear. The end of the confining stage is illustrated in Fig. 4.6, where the accumulated deformation of two different morphologies (tests TX5-01

and TX15-01) is shown after the application of 5 MPa (on the left) and 15 MPa (on the right) confining pressures.

Once the hydrostatic stage is completed, the deviatoric loading is applied, with constraints set again to prevent the rigid-body motion. This time in order to better simulate the experimental conditions, a group of nodes in the bottom surface, circumscribed within a minimum radial sector around the axis of rotation of the cylinder (*i.e.*, 1/20 of the diameter), is fixed. The deviatoric loading is then applied through an axial displacement (along the vertical axis) in the upper surface of the cylindrical mesh, on top of the displacement applied during the confinement stage. Note that the nodes on the upper surface can move freely in non-axial directions.

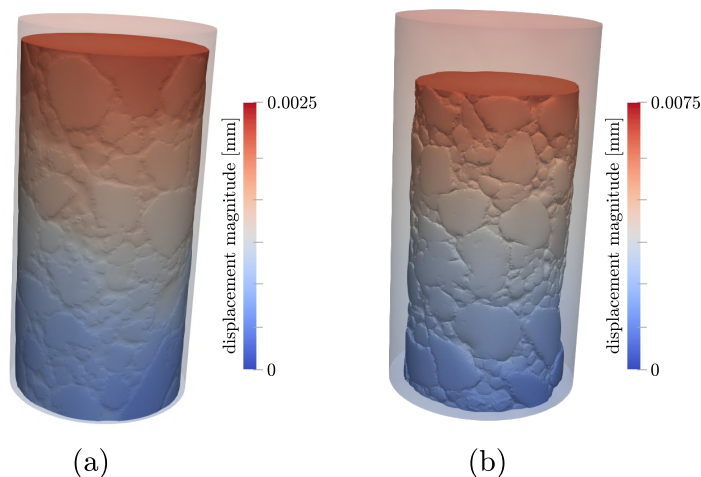


Figure 4.6: Displacement fields (amplified 500 times) at the end of the confinement stage for (a) 5 MPa (test TX5-01) and (b) 15 MPa (test TX15-01) confining pressure

4.2.3 Calibration of material parameters

As explained in the first part of this chapter, a linear-elastic continuum relationship links strain and stress fields outside the discontinuity, while for the discontinuity surface a basic single traction and brittle softening criterion is used (see Fig. 4.2). Thus, for each of the three phases (aggregates, mortar matrix, macro-pores) two elastic and two failure parameters are required: the Young's modulus (E) and the Poisson ratio (ν), and the yield stress (σ_y) and the fracture energy (\mathcal{G}_f), respectively (see Table 4.2).

Regarding the elements with shared material properties (enhanced with a weak discontinuity), no specific parameters are required in the elastic regime, whereas specific failure parameters are defined. The choice here is to assign to these elements equal failure properties with the mortar matrix, still leading to a higher stress concentration at the interfaces, due to the difference of the elastic properties between the phases. Examining the images coming from the post-peak scans, it has been observed that some of the aggregates did break. This means that crack initiation and propagation should be allowed inside these elements, but with much higher failure parameters compared to the mortar matrix.

As for the macro-pores, the physically required negligible (zero) stiffness, leads to a high contrast in material properties among the different phases, which in preliminary trial

simulations has caused numerical problems (difficulties in satisfying the global equilibrium after the post-peak) and further mechanical influences. Therefore, elements that after the morphological projection are identified as macro-pores are removed from the FE mesh, creating, thus, some cavities in the mesh. On the inside of these cavities, a free surface boundary condition is applied, which means that these nodes cannot carry any load, which does not attract any spurious stress concentrations. In the case where nodes are both in a macro-pore and the mortar matrix, the choice is made to consider the full element as part of the solid phase, instead of considering weak discontinuities with a very soft material representing the macro-pores, potentially causing numerical problems. Note that a discussion regarding the influence of the macro-pores on the mechanical response will be addressed in Chapter 5.

Moving now to the values of the material properties assigned to each phase, since the actual macroscopic responses of the micro-concrete samples are known from the *in-situ* mechanical tests (see Section 2.5), the numerical parameters used in the meso-model can be identified to better fit the numerical responses to the experimental results. It should be reminded here that in total 8 *in-situ* tests are conducted: two uniaxial tension tests, three uniaxial compression tests and three triaxial compression tests at 5 MPa, 10 MPa and 15 MPa confining pressures. The choice here is to identify the material properties based on the macroscopic response of the first uniaxial tensile test, combined, for the sake of simplicity, with arbitrary choices which are discussed below. No further identification for the different morphologies and loading paths (uniaxial or triaxial compression) is made. Note that as an alternative to this approach, the identification of the elastic material parameters could be done based for example on nanoindentation or with full-field measurements, based on the experimental kinematic fields, as discussed in Chapter 6.

Taken from bibliography, the Young's modulus of the silicious aggregates used here is set to 70 GPa (see Table 4.2). A parametric analysis is then performed by assuming, for the sake of simplicity, the same value of Poisson ratio for aggregates and mortar ($\nu_a = \nu_m = 0.2$) and keeping a constant ratio between the remaining parameters of these two phases: E_a/E_m , $\sigma_{y_a}/\sigma_{y_m}$ and $\mathcal{G}_{f_a}/\mathcal{G}_{f_m}$. This arbitrary choice is equivalent to assume that these three parameters are linearly correlated, which is not the case observed from literature. Even though a positive correlation between the Young's modulus and the tensile strength is commonly observed for cementitious materials, the fracture energy is usually negatively correlated to these two parameters. However, since only few broken aggregates are observed in the experiments, it is assumed that the fracture energy of aggregates has a weak influence in the presented study. Note also that since the experimental post-peak response is not captured in tension, the fracture energy of mortar is selected so as to reproduce a reasonably brittle behaviour in tension and a proper propagation of the micro-cracks. A high value leads to a ductile response, while a low value leads to the initiation and propagation of a large number of micro-cracks throughout the specimen, which means that a single macro-crack can no longer emerge.

After a series of uniaxial tensile simulations using different values for the material parameters ratios, the material properties that better match the numerical and experimental responses of the T-01 test are summarised in Table 4.2 (with a ratio value of 7). The comparison of the experimental and numerical stress-strain curves is shown in Fig. 4.7 with a good agreement both in terms of macroscopic strength and in terms of Young's modulus. Note that, as explained in Section 2.5, due to the use of a polycarbonate cell for the *in-situ* experiment, the loading system is not stiff enough to capture the post-peak and

thus no comparison between experimental and numerical post-peak response is possible. However, a comparison of the crack patterns observed experimentally and numerically will be addressed in detail in Chapter 5.

Table 4.2: Material parameters of each phase and their interfaces after being calibrated to better fit the experimental result of the first uniaxial tensile test

Phase	E [GPa]	ν	σ_y [MPa]	\mathcal{G}_f [Jm^{-2}]
aggregates	70	0.2	70	0.7
mortar matrix	10	0.2	10	0.1
macro-pores	-	-	-	-
aggregates/mortar matrix (WD)	-	-	10	0.1

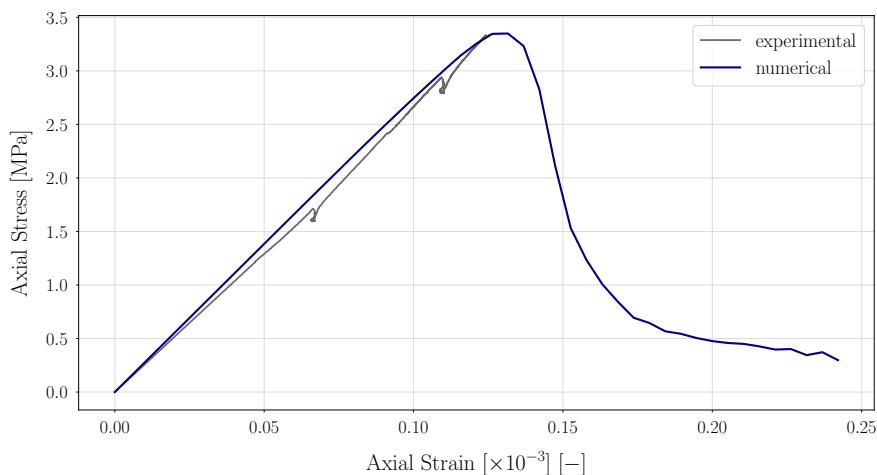


Figure 4.7: Comparison of experimental and numerical macroscopic stress-strain curves for the first uniaxial tensile test (T-01) after numerical identification

Fig. 4.8 illustrates the evolution of the displacement fields in the direction of loading during the uniaxial tensile computation. At the beginning of the loading the displacement field is rather homogeneous, while at the end, the field consists of two discrete blocks with a zone of large displacement gradient in-between them. The discontinuity in the displacement field is concentrated in a roughly horizontal plane (perpendicular to the loading direction) indicating the presence of a single macro-crack. In order to investigate the cracking network by itself, Fig. 4.9 shows the elements for which a strong discontinuity has been activated, which could be associated to a visualisation of the crack patterns predicted by the numerical model. Their evolution with the loading gives an idea about the failure process during the numerical computation. Note that as a direct consequence of the adopted formulation, the magnitude of the jump in the displacement field directly corresponds to the crack opening.

At the beginning of the loading, due to the difference in elastic moduli between the phases, a stress concentration around aggregates appears as a diffused micro-cracking throughout the specimen. Here it should be reminded that the position and the normal vectors of the discontinuities of two neighbouring elements are not constrained to match, which means that no crack path continuity is enforced. One element being locally under failure, certainly, does not correspond to any specific macroscopic feature. However,

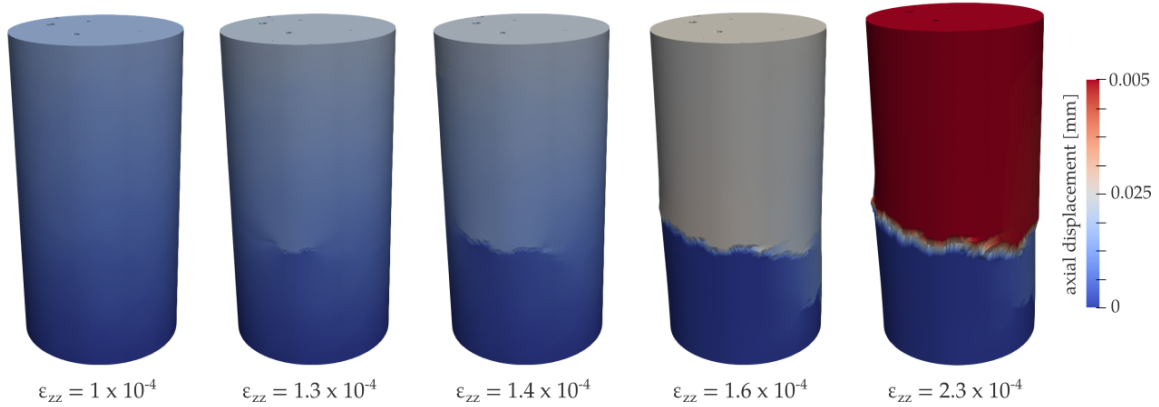


Figure 4.8: Evolution of displacement fields (amplified 200 times) in the axial direction during the T-01 test

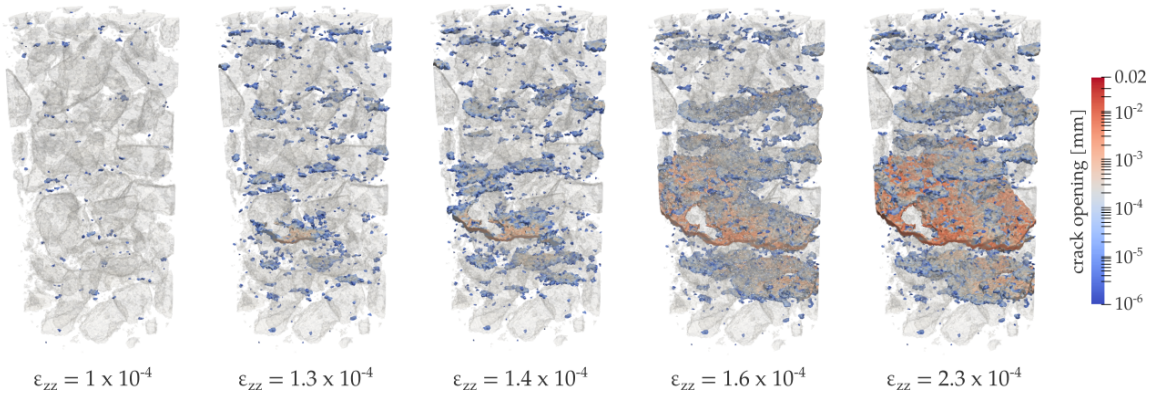


Figure 4.9: Evolution of crack patterns during the T-01 test (aggregates are shown in a faded colour)

when a large number of them appears, it can be said that a macroscopic response does emerge, providing a way to represent macroscale crack path continuity and branching. This is exactly what is shown in Fig. 4.9, where, due to the quasi-brittle behaviour of the material, the diffused micro-cracks quickly bridge into a critical macro-crack that leads finally to the macroscopic failure of the material.

Interesting additional quantitative information concerning the fracturing process can be obtained by plotting the evolution of the crack histograms during the numerical computation. As shown in Fig. 4.10 on the top, the range of the micro-cracks openings is relatively large, reaching to $10 \mu\text{m}$ by the end of the simulation. At the beginning of the loading few micro-cracks appear with relatively low displacement magnitudes, while as the load progresses both their number and their corresponding opening increase. Reaching at the end of the simulation, fewer new micro-cracks are appearing, but rather the opening of the already existing ones is increased. Note that no crack closure is considered in the formulation, even under stress release, which results in micro-cracks with small crack openings not to vanish at the end of the loading.

To highlight the impact of the heterogeneities on the localisation process, the histograms of the crack openings are calculated separately for the elements belonging to mortar matrix and for the elements with shared properties between mortar matrix and aggregates (enhanced with a weak discontinuity). Even though equal failure properties are assigned to these elements (see Table 4.2), it is worth noting that micro-cracks firstly appear in elements accounting for the interfaces between aggregates and mortar, exhibit-

ing a wide range of opening magnitudes, as shown in Fig. 4.10b. As for the mortar matrix (see Fig. 4.10c), cracks start to appear for a macroscopic loading close to the macroscopic peak stress (around 1.2×10^{-4} macroscopic axial strain), with a larger opening compared to the micro-cracks developed inside the elements enhanced with a weak discontinuity (see Fig. 4.10b). It is also worth mentioning that by the end of the simulation about 5% of both types of elements have activated a strong discontinuity.

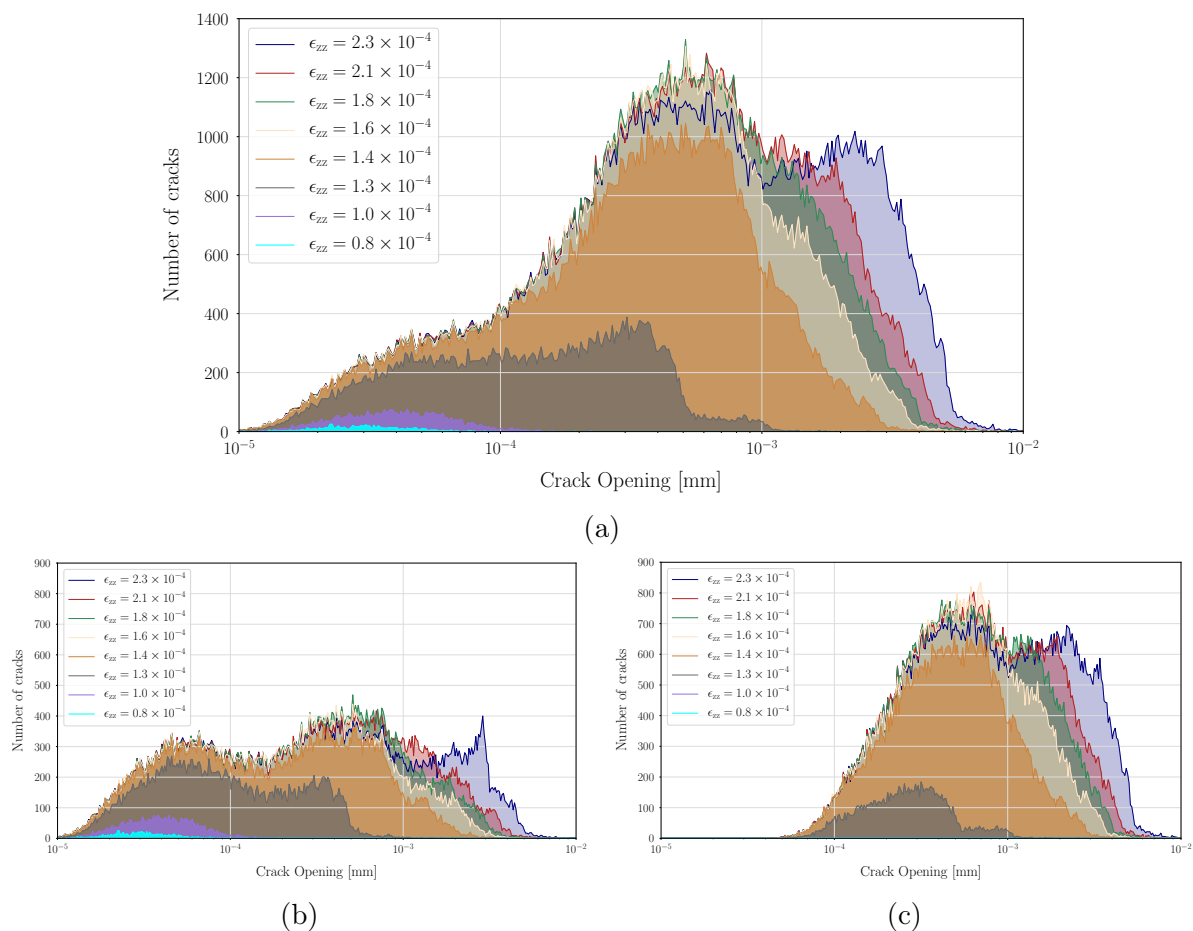


Figure 4.10: Evolution of crack openings during the T-01 test: (a) accumulated cracks developed in all different phases, (b) cracks developed in elements accounting for the interfaces between aggregates and mortar and (c) cracks developed in mortar matrix

4.2.4 Numerical prediction

In the previous section it has been shown that the meso-model is able to predict the material's macroscopic response under uniaxial tension, with the explicit representation of the meso-scale heterogeneities being its key feature. For strengthening this assumption and further challenging the model, different morphologies coming from the remaining *in-situ* mechanical tests are introduced to the meso-model. It should be mentioned that the choice here is to focus on the impact of the underlying morphology and therefore no new identification is performed. The material parameters are identical to the ones calibrated from the first *in-situ* tensile test and shown in Table 4.2.

Uniaxial compression

As an illustrative example of a uniaxial compression simulation, the morphology coming from the reference scan of the C-02 *in-situ* test is used. This time, the direction of the applied displacement is pointing downwards (compressing the top surface) and the magnitude is 10 times higher compared to the one imposed during the tensile simulation. The macroscopic response, in terms of axial stress as a function of axial strain, along with the axial displacement fields throughout the simulation are shown in Fig. 4.11.

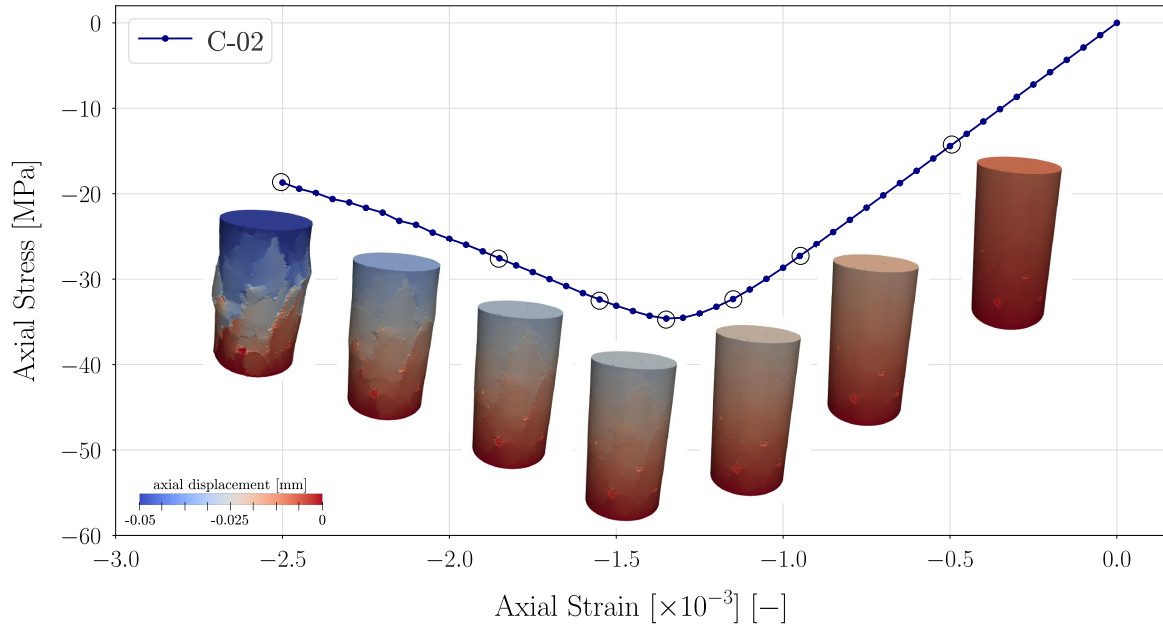


Figure 4.11: Macroscopic stress-strain curve for uniaxial compression simulation (test C-02) along with the axial displacement fields (amplified 30 times)

It is worth mentioning that even though a simple local tensile failure criterion is used, a macroscopic compressive failure is observed. This is a direct consequence of the explicit representation of the heterogeneities combined with the local behaviour of each element, which finally lead to a heterogeneous stress field. Comparing this response with the one of the uniaxial tensile simulation (see Fig. 4.7) it is observed that the typical asymmetric strength values (with their corresponding failure strain values) between tension and compression are recovered, with the ratio of compression to tension being in the order of 10. Again, at the beginning of the loading, the displacement field is rather homogeneous, while as the load increases the field becomes progressively inhomogeneous. At the end of the computation a complex displacement field has been developed, indicating several (as opposed to simple tension) macro-cracks roughly parallel to the axial (loading) direction.

The evolution of the crack patterns is shown in Fig. 4.12, indicating that this time the macroscopic failure is not in mode I. Similarly to the tensile case, displacement incompatibilities (due to the different phases) result in stress concentrations around the heterogeneities, which leads to cracks initiation at these points. Since the failure is governed by a mode I opening mechanism, the crack initiation at these points propagates in the perpendicular direction, leading to local mode I failures. It is when a large number of these local mode I failures occurs, that macroscopically a much more complex failure mechanism emerges, with micro-cracks branching around aggregates forming macro-cracks roughly parallel to the loading direction.

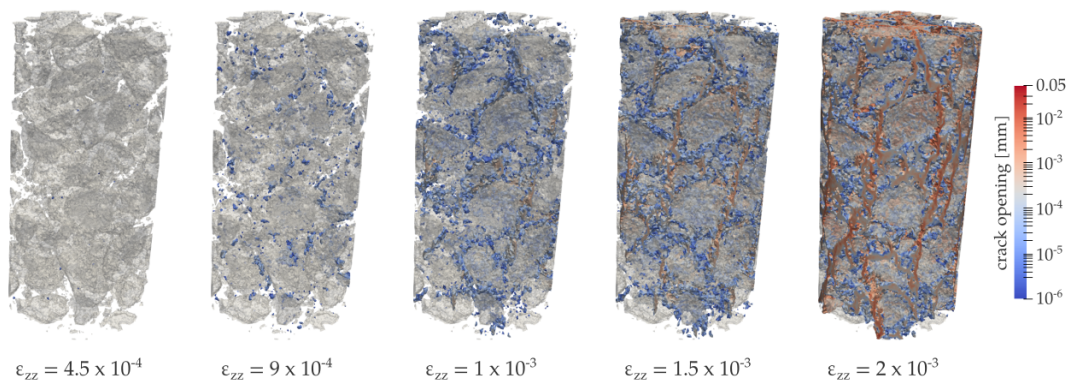


Figure 4.12: Evolution of crack patterns during the a uniaxial compression (test C-02) numerical simulation (aggregates are shown in a faded colour)

However, a noticeable weak point of the formulation should be mentioned. The post-peak part of the macroscopic response exhibits a ductile behaviour indicating that the kinematics representation should be enriched. The fact that only mode I opening mechanism is considered seems to be a phenomenological flaw of the model. A different failure mechanism which accounts for sliding, *i.e.*, mode II, or the combination of mode I and mode II (mixed-mode) should be considered to capture more accurately the local failure mechanism that occurs during a compression loading. Besides, an identification in compression (and not in tension) might be more sufficient to capture the more complex failure mechanisms that occur in this stress path.

Triaxial compression

The meso-model has been proven able so far to reproduce a macroscopic failure under uniaxial tension and compression. It is now time to further challenge it by performing triaxial compression simulations under the three different levels of confinement selected (5 MPa, 10 MPa, and 15 MPa). As above, the generated FE meshes are based on the identified morphologies coming from the reference scans of the corresponding *in-situ* tests.

Depending on the level of confinement, the failure patterns differ significantly as revealed by the displacement fields, but also by the crack patterns evolution presented in Fig. 4.16, 4.17 and 4.18. For the lower levels of confinement, the numerical specimens fail macroscopically on a sliding inclined plane, whereas the macroscopic failure of the numerical specimen under the highest level of confinement happens on a roughly horizontal shear band located at the bottom part of the sample (resembling a compaction band). Remarkably, a local tensile failure criterion combined with a mode I opening mechanism reproduce such complex macroscopic failure modes. However, when the displacement incompatibilities result in a shear loading, along with the fact that no relative sliding (*i.e.*, mode II mechanism) of the crack faces is considered, yield a rather diffused (and not localised) cracking network (as per the uniaxial compression test). This observation justifies on one hand, a future consideration of an identification in compression and on the other hand a shear (Mohr-Coulomb) localisation criterion with a sliding (mode II) opening criterion in order to characterise local shear fractures.

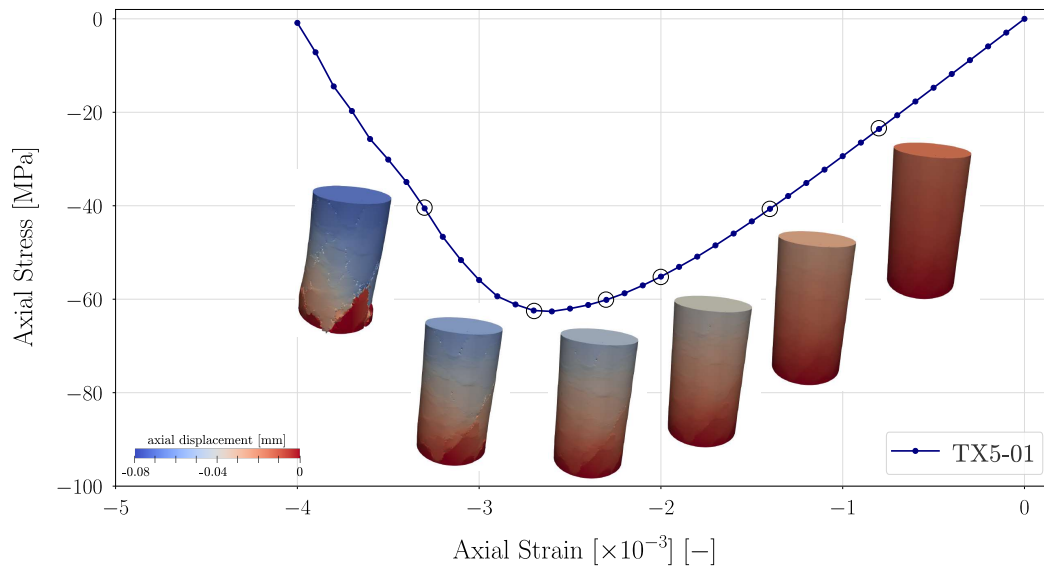


Figure 4.13: Macroscopic stress-strain curve for triaxial compression test under 5 MPa confinement along with the axial displacement fields (amplified 30 times)

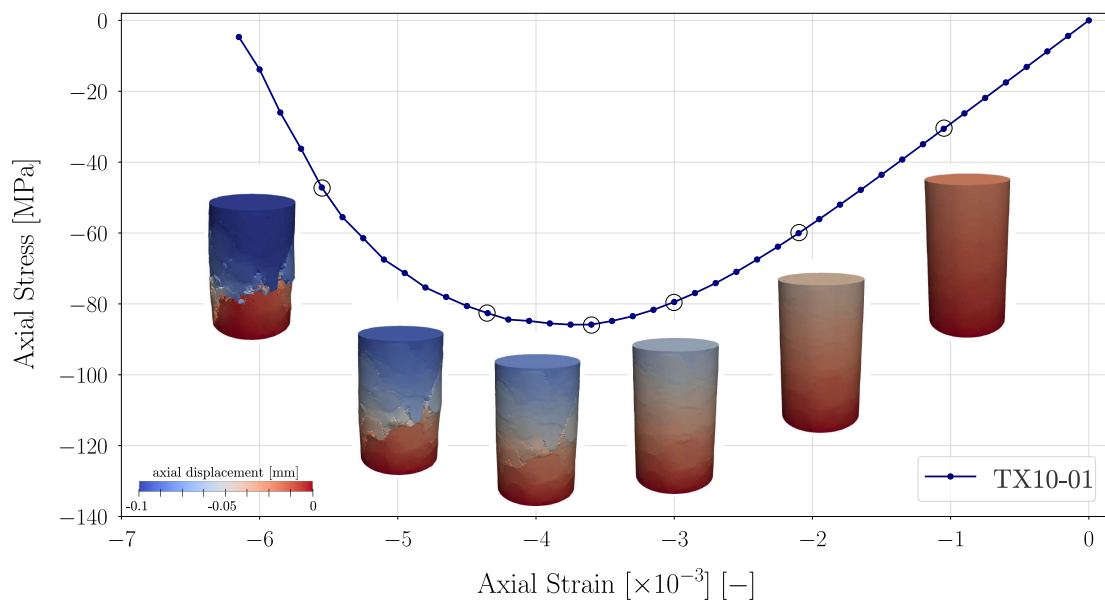


Figure 4.14: Macroscopic stress-strain curve for triaxial compression test under 10 MPa confinement along with the axial displacement fields (amplified 30 times)

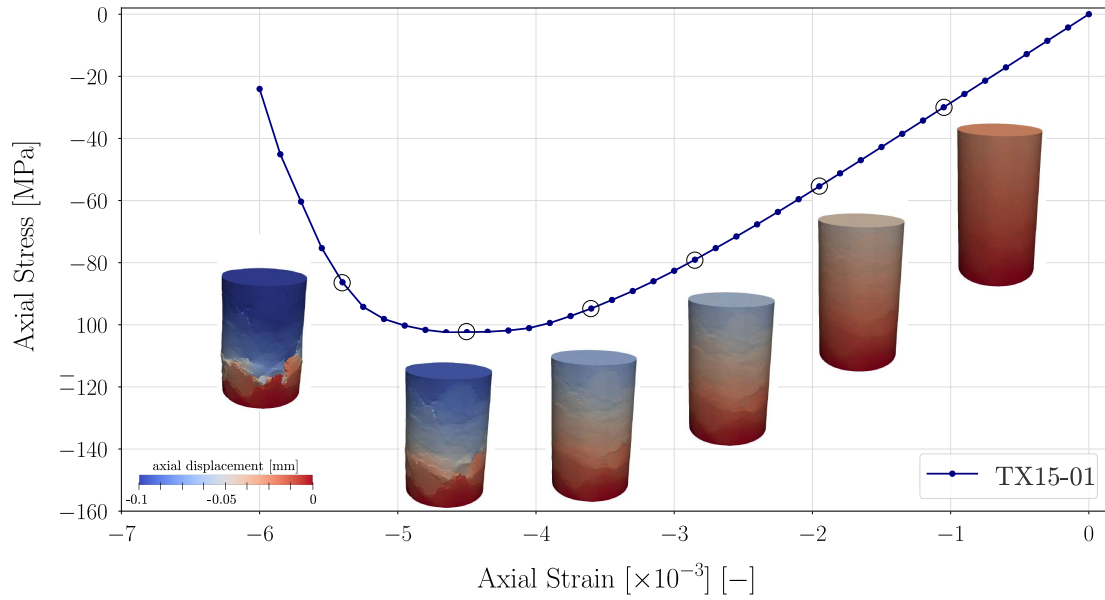


Figure 4.15: Macroscopic stress-strain curve for triaxial compression test under 15 MPa confinement along with the axial displacement fields (amplified 30 times)

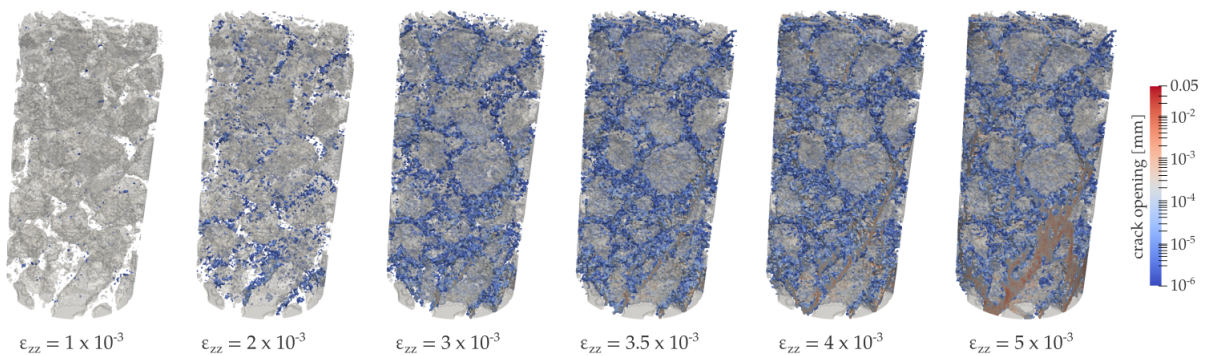


Figure 4.16: Evolution of crack patterns during the triaxial numerical simulation under 5 MPa confinement (test TX5-01). Note that aggregates are also shown in a faded colour

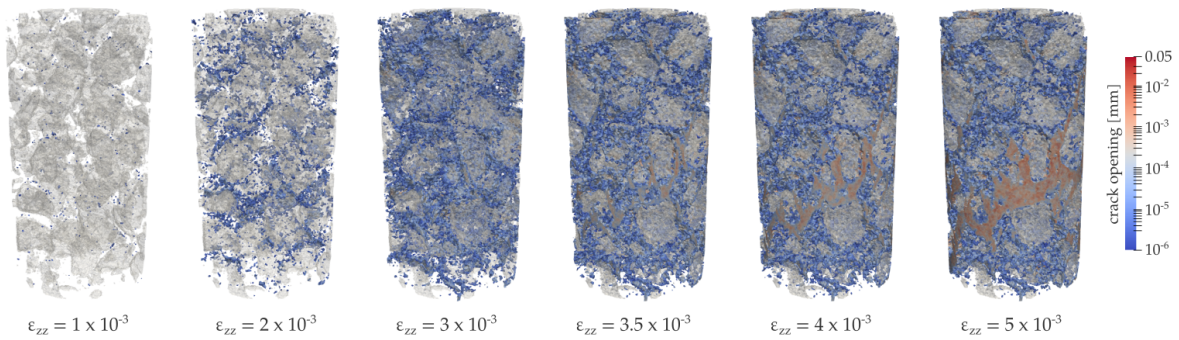


Figure 4.17: Evolution of crack patterns during the triaxial numerical simulation under 10 MPa confinement (test TX10-01). Note that aggregates are also shown in a faded colour

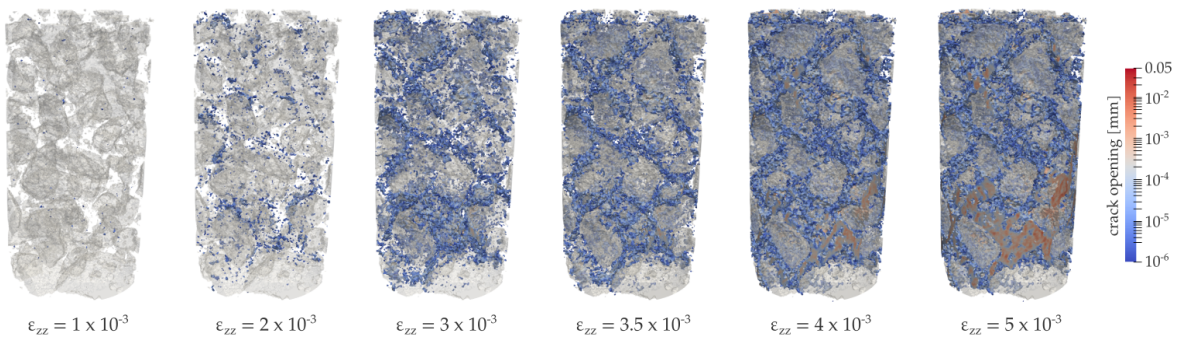


Figure 4.18: Evolution of crack patterns during the triaxial numerical simulation under 15 MPa confinement (test TX15-01). Note that aggregates are also shown in a faded colour

4.3 Concluding remarks

This fourth chapter presented the framework to numerically investigate the impact of the meso-scale heterogeneities of concrete on its macroscopic mechanical response. The first part of the chapter introduced the basic ingredients of the FE meso-model used in this study. On one hand, in order to account for the complex heterogeneous aspects of the morphology (explicit representation of aggregates and macro-pores), a non-adapted mesh projection was used leading to discontinuities in the strain field (weak discontinuities), which was handled by a local kinematics enhancement. On the other hand, in order to account for the quasi-brittle behaviour of the material, a second set of local discontinuities was introduced, this time in the displacement field (strong discontinuities), accounting for micro-cracking. The coalescence and bridging of these micro-cracks lead to the macroscopic failure of the material. These two discontinuities were combined within the same Embedded Finite Element Model (E-FEM) and a simple tensile failure criterion coupled with a mode I failure mechanism were considered.

The second part of this chapter focused on the application of the presented meso-model to the micro-concrete specimens studied (introduced in Chapter 2). The identified morphologies (see Chapter 3) coming from the reference scans of each *in-situ* test served as the input morphologies of the meso-model and an illustrative example of the creation of the heterogeneous FE mesh was given. The calibration of the meso-model was then presented, based on the macroscopic response of the first *in-situ* tensile test (see Section 2.5), which revealed the capability of the model to reproduce the actual material response. Without any new identification, the prediction of the model was asked for the different morphologies and loading paths considered (uniaxial and triaxial compression).

A local tensile failure criterion combined with a mode I opening mechanism reproduced complex macroscopic failure modes, such as sliding shear bands for the lowest levels of confinement and a roughly horizontal shear band (resembling a compaction band) for the highest level of confinement. However, a less realistic post-peak response was observed, principally for the compression tests, with a development of a rather diffused cracking network. On one hand, this indicates a limitation of the model to capture displacement incompatibilities that yield shear loadings, suggesting a future consideration of a sliding (*i.e.*, mode II) failure mechanism (or even better a combination of mode I and mode II) and a shear (*i.e.*, Mohr-Coulomb) failure criterion. On the other hand, an identification in compression (and not in tension) might be more sufficient to capture the more complex failure mechanisms that occur under these loading paths.

Chapter 5

Link between experimental and numerical observations

The conducted *in-situ* mechanical tests on micro-concrete specimens have been detailed in Chapter 2 and the analysis of the 3D images coming from these experiments has been addressed in the subsequent Chapter 3. The macroscopic responses, as well as the first stages of the fracturing process at the scale of the largest heterogeneities (aggregates and macro-pores), along with the failure patterns at the end of the loading observed experimentally have been discussed in detail.

The subsequent Chapter 4 has presented the framework to numerically investigate the mechanical response of the studied material, that accounts both for the meso-scale heterogeneities and the local failure mechanisms. The morphologies coming from the reference scans of each *in-situ* test have been used as the input morphologies of a 3D FE meso-model with enhanced discontinuities. After a numerical identification based on the first *in-situ* uniaxial tensile experiment, the meso-model has successfully reproduced complex failure modes, capturing some of the characteristic features of the mechanical response of micro-concrete under the different loading paths studied. A direct comparison between the numerical predictions and the experimental measurements is now possible, based on the tools and techniques described so far in this study.

The first part of this chapter focuses on the comparison between simulations and experiments in terms of macroscopic responses, displacement fields, fracturing processes and failure patterns. The predictive ability of the meso-model is challenged for the different morphologies and loading paths considered, taking into account that the identification of the material parameters is done in simple tension and that only a local simple tensile failure criterion coupled with a mode I failure mechanism are considered. It should be also recalled here that the boundary displacements of the measured experimental fields are not prescribed as displacement boundary conditions to the numerical simulations (see Section 4.2.2). While validating the numerical results and through a combination of numerical and experimental observations, the impact of the meso-scale heterogeneities on the local failure mechanisms is systematically investigated. The second part of this chapter focuses on the role of the underlying morphology on the mechanical macroscopic response. Illustrative example applications of the meso-model based on virtual morphologies are presented with the objective of obtaining some further insight into the impact of the different phases on the macroscopic response.

5.1 Macroscopic responses comparison

This section discusses the macroscopic responses obtained experimentally and numerically. Note that the former are coming from the stress-strain curves measured during the *in-situ* tests after subtracting the considerable displacement corresponding to the elastic stiffness of the apparatus used for each test (see Section 2.5). It should be also recalled that for the *in-situ* uniaxial tests, the loading system is not stiff enough to capture the post-peak and thus no comparison between experimental and numerical post-peak responses is possible.

As detailed in Chapter 4 (see Section 4.2.3), the calibrated material properties that best match the numerical and experimental responses of the first uniaxial tensile test are summarised in Table 4.1. Although discussed in the previous chapter, the comparison between the experimental and numerical stress-strain curves for the first tensile test is briefly recalled here in Fig. 5.1a, which shows a good agreement both in terms of macroscopic strength and in terms of Young’s modulus. Without modifying the material parameters, different morphologies coming from the remaining *in-situ* mechanical tests have been introduced to the meso-model and their numerical responses have been computed.

Starting from uniaxial tension, Fig. 5.1b shows the comparison between experimental and numerical macroscopic stress-strain curves for the second *in-situ* tensile test. Similarly to the first tensile test, a good agreement both in terms of macroscopic strength and in terms of Young’s modulus is observed. Despite the identical material parameters and the fact that the volume fraction of each phase is very close for both morphologies (see Table 3.1), the slightly higher measured strength (compared to the T-01 test) is also numerically reproduced (3.5 MPa compared to 3.2 MPa). The predicted response of the T-02 sample appears to be slightly stiffer, with a computed Young’s modulus of 29.8 GPa, compared to 27.7 GPa of the T-01 test. However, this numerical difference (in the order of 2 GPa) can not be experimentally validated, since due to the soft loading system used, the elastic moduli measurement uncertainties are in the order of 8 GPa (see Section 2.5.3). Note also that for the tensile tests, the Young’s modulus is not possible to be safely evaluated from the experimental kinematic fields, with errors reaching 400 GPa (see Section 3.2.3).

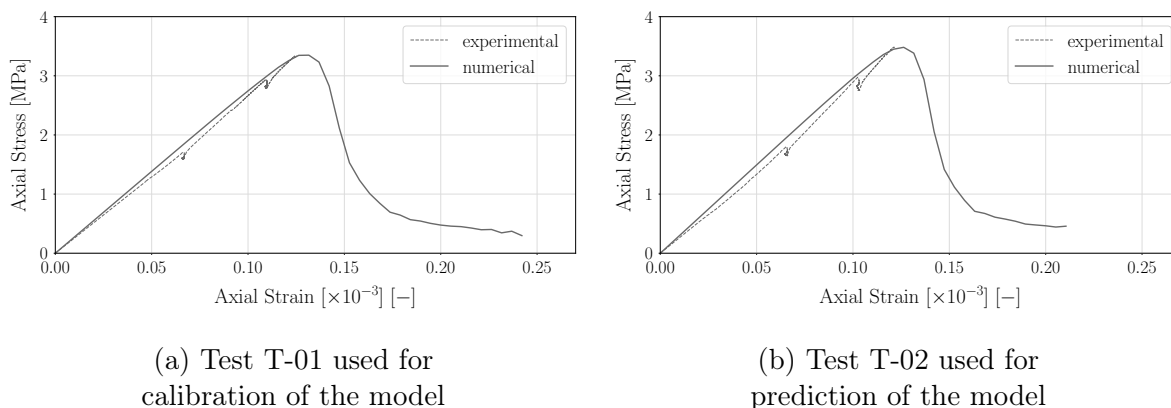


Figure 5.1: Comparison of experimental-numerical macroscopic stress-strain curves for the (a) first and (b) second uniaxial tensile tests

Moving now to the three uniaxial compression tests, Fig. 5.2 gathers the macroscopic responses, in terms of axial stress as a function of axial strain, obtained both experimentally and numerically. Note that for the experimental curves only the part starting from the second loading cycle is shown. As already mentioned in the previous chapter, even

though a Rankine failure criterion is considered by the meso-model, a macroscopic failure of the material is also observed in simple compression. Although a good agreement both in terms of macroscopic strength and in terms of Young's moduli between experiments and simulations is observed, for all the three tests the numerically predicted compressive strengths are slightly lower compared to the experimentally measured ones.

In particular, the numerical strengths are 32 MPa, 34.5 MPa and 34.0 MPa, whereas the experimental ones are 33 MPa, 39 MPa and 39.5 MPa, respectively. This means that the uniaxial compressive strengths are underestimated by 3%, 11.5% and 14%, respectively. It is worth mentioning that for the C-01 test (see Fig.5.2a) the relatively lower compressive strength measured experimentally is also numerically reproduced, indicating that it is a direct consequence of the morphology.

The numerical Young's moduli are 28 GPa, 29 GPa and 26.5 GPa for each test respectively, which are in a good agreement both with the ones measured directly from the experimental macroscopic responses (27.5 GPa, 25.5 GPa and 26 GPa) and with ones measured through the experimental displacement fields (24.5 GPa, 27 GPa and 26.5 GPa, with a corresponding error of ± 4 GPa). Due to the low stiffness of the loading system, a direct comparison of the post-peak regime is again not possible, yet it is obvious that the numerical response after the peak exhibits a ductile behaviour.

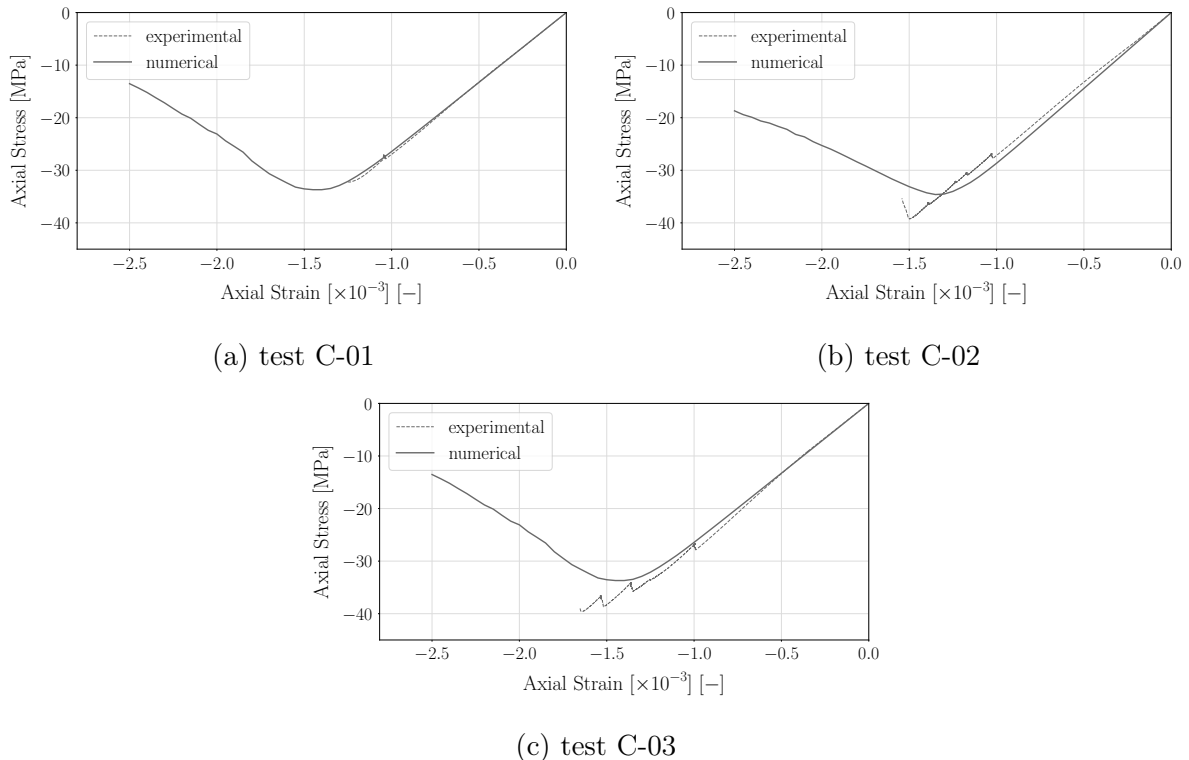


Figure 5.2: Comparison of experimental-numerical macroscopic stress-strain curves for the (a) first, (b) second, and (c) third uniaxial compression tests

The comparison between the deviatoric part of the experimental and numerical macroscopic responses under 5 MPa, 10 MPa and 15 MPa confining pressures is presented in Fig. 5.3, in terms of axial stress, as a function of axial strain. Similarly to the simple compression tests, the numerical responses seem to underestimate the actual strength of the material. In particular, for an increasing level of confinement the numerical deviatoric strengths are 62.5 MPa, 86 MPa and 102.5 MPa, whereas the experimental ones are

67.5 MPa, 98 MPa and 111.5 MPa, respectively. This means that the maximum deviatoric stresses are underestimated by 8%, 12% and 8%, respectively. It can be seen that the range of underestimation is of about the same percentage as per simple compression, meaning that it does not seem to be affected by the increasing peak compressive strength. The predicted numerical response is slightly stiffer, with the Young's moduli ranging between 29.5 GPa, 29 GPa and 28.5 GPa, compared to the ones measured directly from the experimental macroscopic responses (25.5 GPa, 25.5 GPa and 26.5 GPa) and to the ones measured through the experimental displacement fields (24.5 GPa, 25.5 GPa and 26.5 GPa, with a corresponding error of ± 3 GPa).

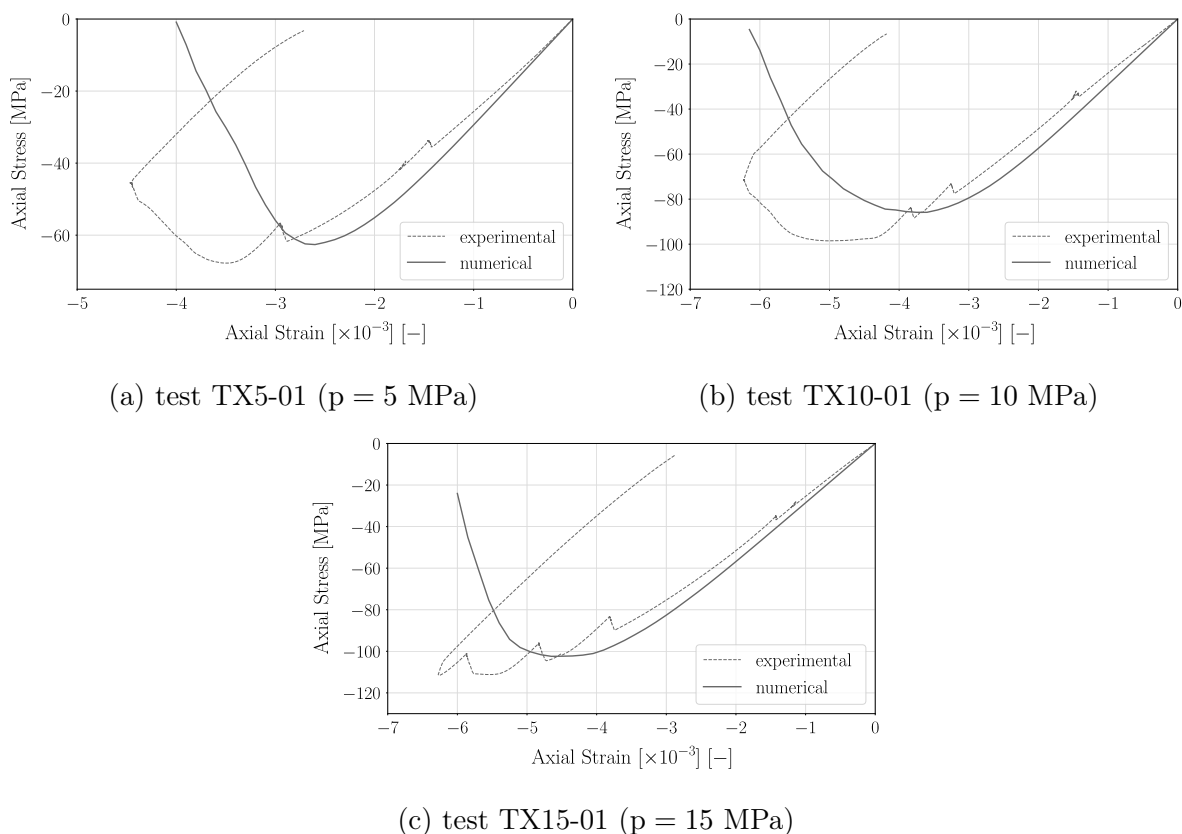
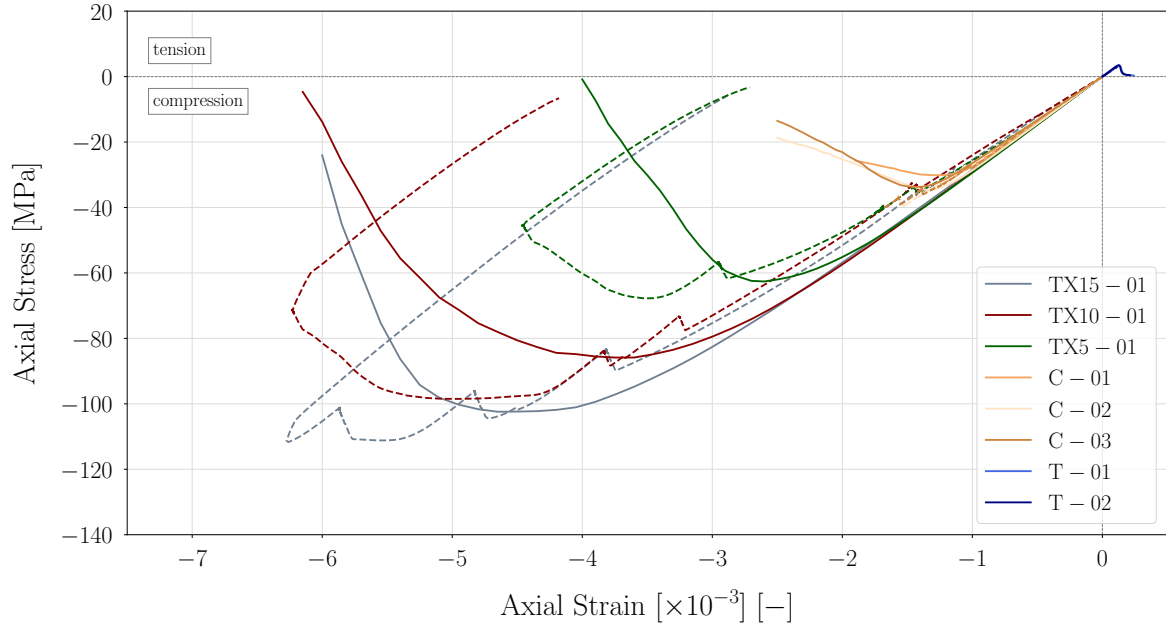


Figure 5.3: Comparison of the deviatoric part of the experimental-numerical macroscopic stress-strain curves for the triaxial compression tests under: (a) 5 MPa, (b) 10 MPa, and (c) 15 MPa confinement

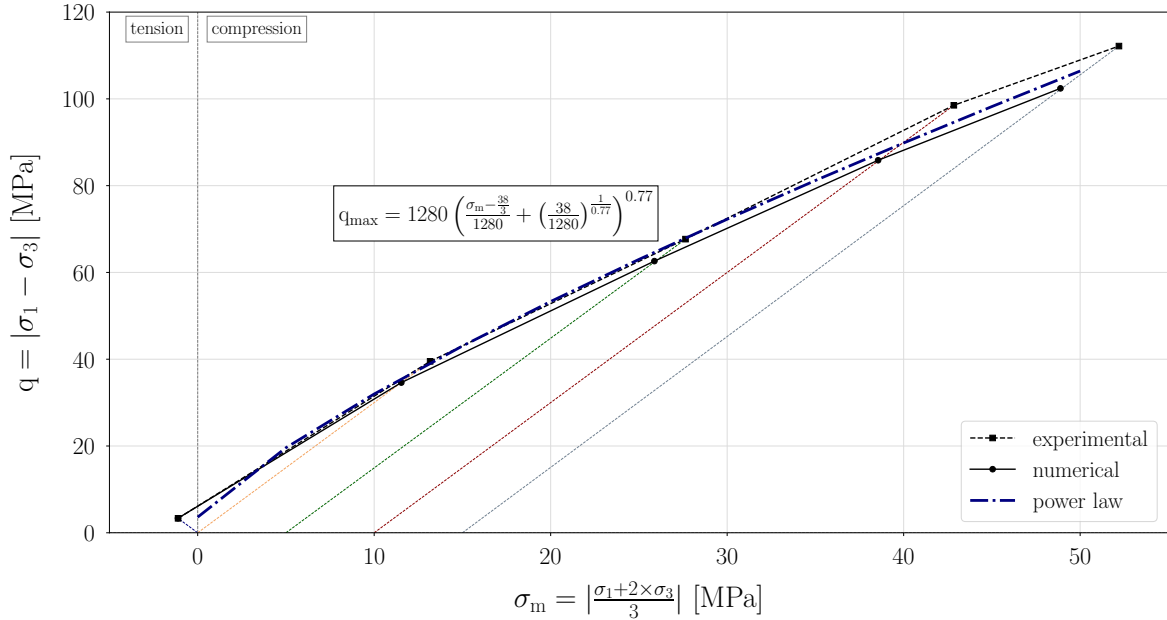
The experimental and numerical macroscopic responses for all the *in-situ* tests are gathered and compared in Fig. 5.4. In general, the meso-model seems to underestimate the strength of the material under simple and triaxial compression. However, the typical asymmetric behaviour of concrete in tension and compression, as well as the increase of strength and ductility with the increase of confinement are well captured numerically. With an identification of the material parameters only in simple tension and a consideration of a simple tensile failure criterion coupled with a mode I failure mechanism, the meso-model is able to satisfactorily predict the macroscopic response of the studied micro-concrete samples under the different loading paths considered.

Fig. 5.4b depicts the studied loading paths in the stress space (meridian plain) using the first two stress invariants: the deviatoric stress, *i.e.*, $q = |\sigma_1 - \sigma_3|$, as a function of the mean stress, *i.e.*, $\sigma_m = |(\sigma_1 + 2 \times \sigma_3)/3|$. A stress limit state curve (*i.e.*, failure surface) can then be obtained both experimentally and numerically, by plotting the evolution of

the maximum deviatoric stress versus the maximum mean stress for the different loading paths studied. As it can be clearly seen, the curve of strength at failure is strongly non-linear.



(a)



(b)

Figure 5.4: Comparison between experimental and numerical results of all the different tests in terms of: (a) axial strain as a function of axial stress and (b) loading paths and failure surface (blue colour) in the meridian plane (deviatoric stress versus mean stress)

Among the various ways that exist to describe the failure surface of concrete, three types of meridian cross-sections of the failure surface are the most common: (a) linear

(Mohr-Coulomb, Druker-Prager, Willam-Warnke), (b) parabolic [Pontiroli *et al.*, 2010] and (c) power law [Kang et Willam, 1999]. A study of [Vu *et al.*, 2009] demonstrated that for high mean stresses (above 100 MPa) the three types of failure criteria are very close, with a nearly linear limit state curve. However, for lower mean stress levels, linear or parabolic criteria are incapable of fitting the unconfined compressive strength and tend to overestimate the strength of concrete. A better fitting is achieved with a power law over a range of different mean stress levels. For this reason, a two-parameter power law is used here, as a function of the unconfined compressive strength (*i.e.*, f_{ck}), which is introduced in [Malecot *et al.*, 2019] and is written as:

$$q_{\max} = q_1 \left(\frac{\sigma_m - \frac{f_{ck}}{3}}{q_1} + \left(\frac{f_{ck}}{q_1} \right)^{\frac{1}{\alpha}} \right)^\alpha \quad (5.1)$$

where the two parameters q_1 and α depend on the behaviour of the fully compacted concrete, called granular stacking (aggregates and cement paste without any strength or residual porosity) varying according to the aggregate type and size [Vu *et al.*, 2011].

Herein, the value of f_{ck} is directly extracted from the simple compression tests conducted in this work, while the values of the two parameters of Eq. (5.1) are initially taken from [Malecot *et al.*, 2019] and adjusted to fit the presented data. In particular, f_{ck} is set to 38 MPa and the obtained unique set of the power law criterion parameters are $q_1 = 1280$ MPa and $\alpha = 0.77$ (see Table 5.1). The predicted q_{\max} based on the above criterion is then plotted for a range of mean stresses and a very good fit both with the experimental and the numerical responses is obtained for the compression regime. Even though only a limited number of tests is examined here, this power law could be used to predict the failure criterion of concrete in the (q_{\max}, σ_m) plane.

Table 5.1: Set of fitting parameters for the power law criterion given in Eq. (5.1) and shown in Fig. 5.4b

Parameter	Symbol	Value
Unconfined compressive strength	f_{ck}	38 MPa
Slope of the criterion on a logarithmic scale	α	0.77
Critical shear stress of dry concrete	q_1	1280 MPa

To conclude the comparison of the macroscopic responses, as a general remark, the choice to identify the material parameters in tension, due to the simple mechanisms involved, is proven insufficient to capture the more complex failure mechanisms in compression. Apart from the phenomenological enrichment of the model, an identification in compression should be a considerable future perspective.

In the same context, the simple arbitrary choices made in this study regarding the values of the material properties assigned to each phase should be also further investigated (see Section 4.2.3). The choice, for example, to assign the same value of Poisson ratio to aggregates and mortar, as well as the equal failure properties between mortar and the elements accounting for the mortar/aggregates interface should be further studied. Moreover, an identification of all the material parameters is needed, including the fracture energy. This means that experimental post-peak information is required, which is available herein for the triaxial tests. The identification of the material parameters

from the experimental kinematic fields, can be also a promising alternative as discussed in Chapter 6.

Without neglecting the importance of the above remarks, it should be mentioned that the principal objective of this work is to proceed into a first comparison between numerical and experimental results, while focusing on the role of the underlying morphology, which is legitimate for a meso-model. Therefore, after the comparison of the experimental and numerical macroscopic responses, the question that naturally arises is related to the predictive ability of the model in terms of the complex fracture initiation and evolution until failure, along with the characteristics of the fracture patterns at the end of the loading, which is the subject of the following section.

5.2 Fracturing process and failure patterns comparison

As discussed in Chapter 3, the DVC technique coupled with the data coming from the *in-situ* experiments have produced the full 3D kinematic fields throughout the mechanical tests. Consequently, a straightforward comparison between the experimental and numerical kinematic fields is possible. Provided that the experimental fields are computed only for discrete loading steps during each test (for which the loading is interrupted and tomographic scans are performed), the comparison is made at the same level of the corresponding macroscopic axial strain.

It should be recalled here that micro-cracking is the local failure mechanism that numerically accounts for the degradation of the material. The FE are enhanced by a set of strong discontinuities, introducing jumps in the displacement field, representing thus the discontinuous aspect of the micro-cracks. One element being under failure, certainly, does not correspond to any specific macroscopic response. However, when a large number of them appears, then it can be said that a macroscopic feature does emerge, providing a way to represent macro-scale crack path continuity and branching. Experimentally, the transition from a spatially continuous deformation process to a discontinuous one can be revealed by regions of localised deformations in the measured strain fields (*i.e.*, strain localisation). It is worth reminding that the experimental strain fields are a result of a total and not incremental analysis, meaning that the reference scan of each test is mapped into each of the subsequent scans captured throughout the test.

The distinction between strain localisation and cracking is not trivial and highly depends on the observation scale. Considering that one of the main objectives of this work is to observe and quantify the first stages of the fracturing process at the scale of the largest heterogeneities, the choice herein is to compare the evolution of the measured experimental strain fields to the micro-cracking evolution predicted by the numerical model. Note that correlation residual fields are also examined to reveal non-linear transformations (*i.e.*, cracks) in the experimental kinematic fields, but mainly in order to characterise the fracture patterns at the end of the loading.

In what follows, for selected mechanical tests, the experimental and numerical axial displacement fields are firstly compared, after subtracting the calculated rigid-body motion from the former ones (see for example Fig. 5.5). The evolution of the experimental strain fields during the loading is then compared to the evolution of the crack patterns predicted by the model. To facilitate the interpretation of the localisation process, vertical slices from both fields are shown, oriented to include the specimens' axis and prominent

deformation patterns, along with the corresponding 2D greyscale slices extracted from the tomographic scans at each loading step (see for example Fig. 5.6).

A qualitative comparison of the 3D fracture patterns at the end of the loading follows, as revealed from the post-peak scans (or the correlation residual fields in case of triaxial tests) and from the cracking network predicted by the meso-model at the end of the simulations (see for example Fig. 5.8). For a quantitative analysis of the fracture patterns, the local orientation of the cracking network at the end of the loading is examined both experimentally and numerically, as explained below.

Regarding the numerical model, it should be kept in mind that the predicted cracking network consists of a large number of independent micro-cracks (planes), each represented by an activated strong discontinuity locally inside an element, without enforcing any crack path continuity. In case of an element with shared material properties, the orientation of the crack coincides with the orientation of the material interface (*i.e.*, the crack is forced to open following the material geometry), whereas for elements without shared material properties, the crack opens following the direction of the largest principal stress. In both cases, when the localisation occurs inside an element, the orientation of the crack is recorded and remains fixed (see Section 4.1.2).

Concerning the experimental fracture patterns at the end of the loading, they are either extracted from the post-peak x-rays images or from the correlation residual fields of the last loading step, both resulting in binary 3D objects discretised in voxels. The local orientations of these 3D objects need thus to be computed, which is achieved here by a meshing of their outer surface. More specifically, following the *non-adapted meshing* technique detailed in Section 4.2.1, the distance field of each extracted 3D object is calculated and *projected* onto an unstructured FE mesh, resulting in a discretisation of the crack patterns with 4-noded tetrahedra elements (see for example Fig. 5.9). After this morphological projection, the vectors of the elements falling between the 3D object and background are directly computed, corresponding to the geometrical orientation of the experimental cracking network's outer surface. Note that in order to keep the same FE discretisation between numerical and experimental cracks, the experimental crack patterns are projected onto the same FE meshes used for the projection of the morphologies coming from the corresponding reference scans.

Once the local orientations of both the experimental and the numerical crack patterns are obtained, a quantitative comparison is possible. In order to visualise the distribution of the 3D crack orientation vectors, among the different ways that exist to plot 3D vectors, a Lambert azimuthal equal area projection [Hinks, 1921] is used here, as implemented in `spam`. A detailed illustration of this technique can be found in [Jaquet *et al.*, 2013] and [Wiebicke *et al.*, 2019]. Herein is briefly mentioned that the crack vectors are placed into a unit z -positive half-sphere (*i.e.*, each vector is flipped such that it has a positive vertical axis) and the Lambert azimuthal equal area projection is used to project (map) the sphere onto a plane. In the presented case, considering the complex crack patterns and thus the large number of local orientations that are examined, the plotted vectors are binned, so as to detect clusters easily (see for example Fig. 5.9).

5.2.1 Uniaxial tension

The evolution of the 3D axial experimental and numerical displacement fields during the first uniaxial tensile test is shown in Fig. 5.5, together with the displacement profiles along the specimen's axis. The range of the displacements are in a good accordance, with

a relative axial displacement inside the micro-concrete sample of around $2\ \mu\text{m}$. Note that the axial macroscopic failure strain is in the level of 1.3×10^{-4} for both numerical and experimental responses. Even at the first loading step (at 50% of the maximum experimental and numerical failure load), both responses show a heterogeneous displacement field, however, the slight bending (due to the experimental boundary conditions) reflected in the experimental field is not reproduced in the numerical one. At 75% of the maximum failure load (and about 1.0×10^{-4} of macroscopic axial strain), the experimental field is increasingly inhomogeneous, showing a large displacement gradient, which suggests strain localisations and crack initiations.

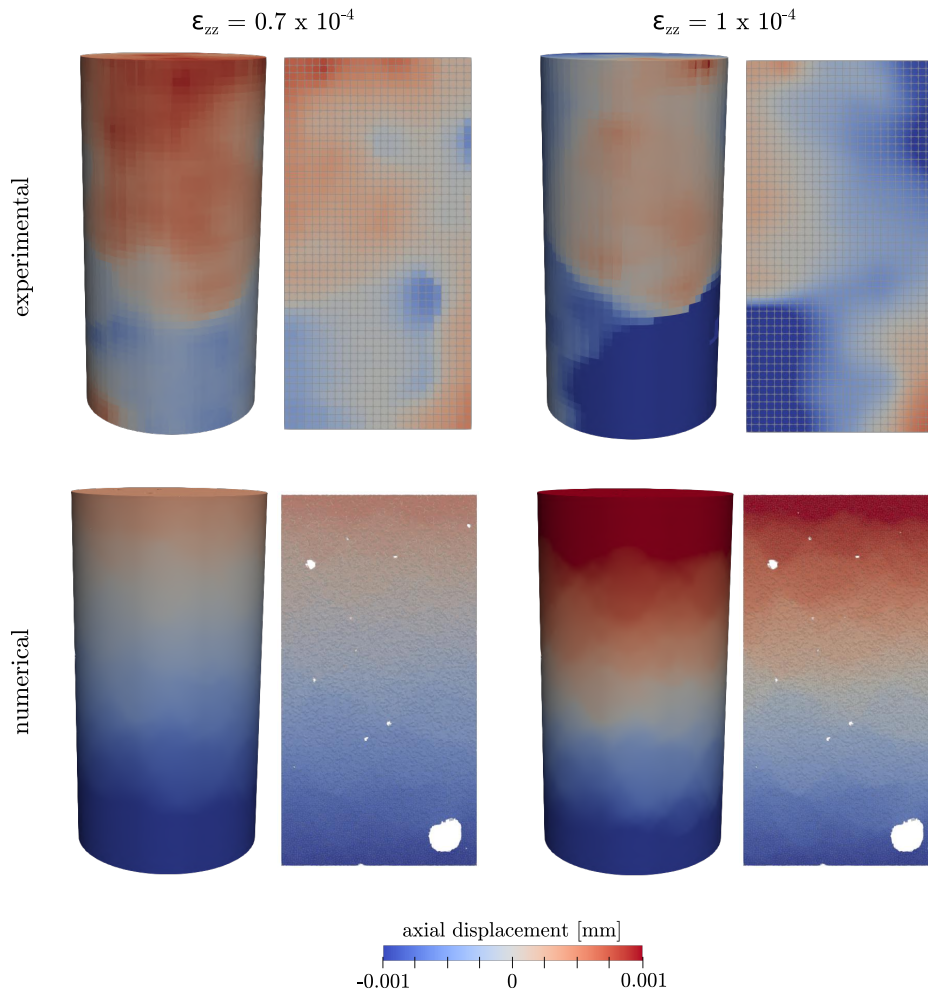


Figure 5.5: Comparison between experimental (top) and numerical (bottom) axial displacement fields during the T-01 test. Vertical profiles (with their respective discretisations) are also shown. The comparison is made at the axial strain levels for which a tomographic scan is performed. The cavities shown in the numerical fields correspond to elements removed from the FE mesh accounting for the macro-pores

The bending which occurred experimentally is clearly visible in the vertical displacement profile (upper row on the right), but is not reflected in the corresponding numerical field (lower row on the right), which exhibits a roughly constant gradient of axial displacement along the specimen's axis. This observation highlights the importance of a future consideration of the actual experimental kinematic boundary conditions in the numerical

simulation. Although the numerical displacement field at this stage shows some heterogeneities, dominant localisation features in the numerical response seem to occur for a bit higher macroscopic axial strain (above 1.25×10^{-4}) and very close to the failure one.

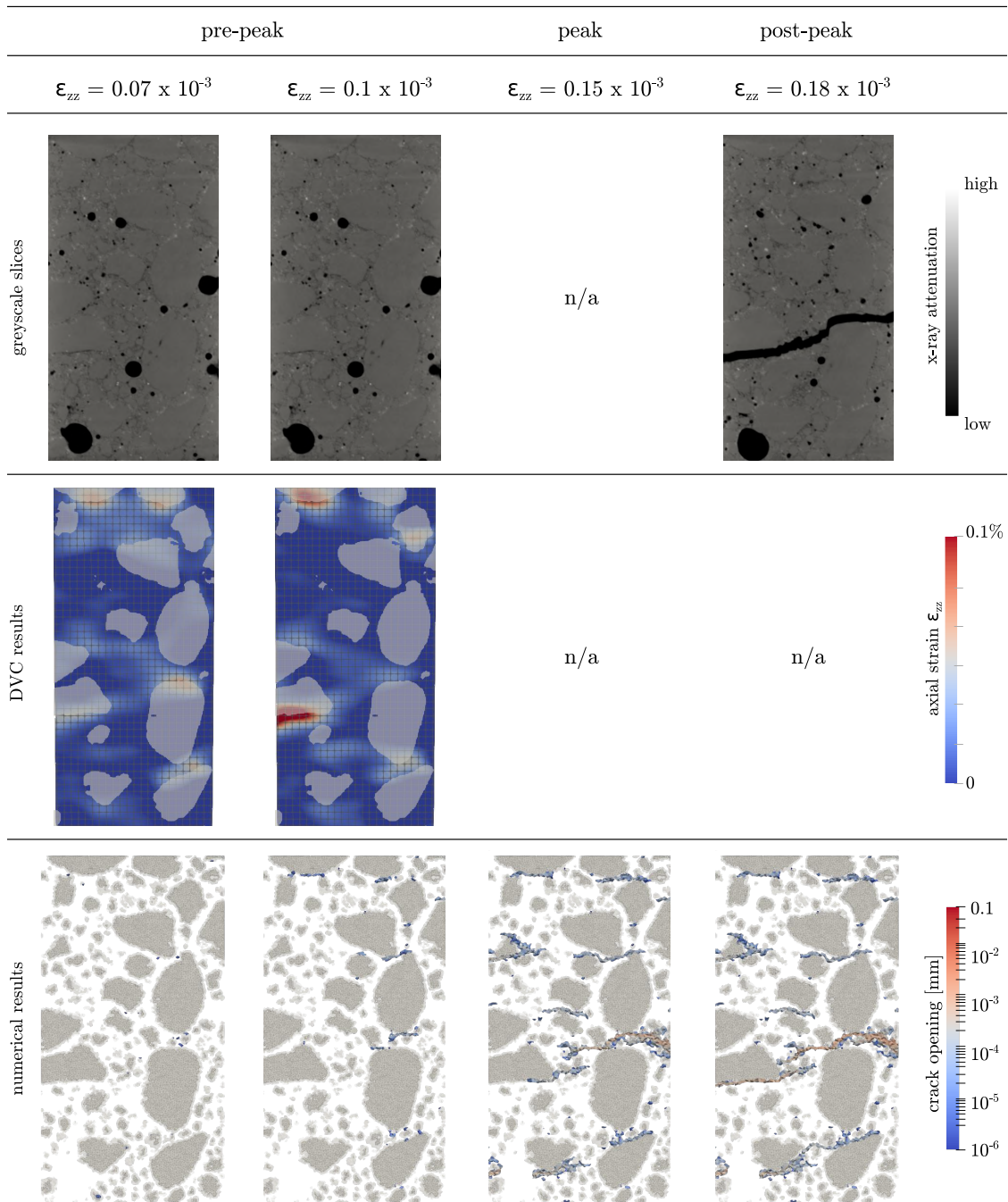


Figure 5.6: Fracturing process evolution during the first uniaxial tensile test. (Top): greyscale slices coming from the tomographic scans, (Middle): axial strain fields measured with DVC for the scans before failure, overlaid with the segmented largest aggregates of the reference scan, (Bottom): crack patterns predicted by the meso-model. The comparison is performed at the same macroscopic axial strain levels for which a tomographic scan is performed. The discretisation of each field (rectangles for the experimental and triangles for the numerical) is shown

To justify the above statement, Fig. 5.6 presents the evolution of the measured experimental axial strain field along with the evolution of the crack patterns predicted by the meso-model, as well as the vertical greyscale slices coming from the x-rays scans. The first two columns correspond to the levels of macroscopic axial strain for which the tomographic scans are performed, whereas the last two columns follow the evolution of the fracturing process for higher macroscopic axial strains, only possible in the numerical simulation. In order to highlight the different spatial resolutions between experimental and numerical observations, the underlying cubic grid (for the experimental field) and (the much finer) tetrahedral mesh (for the numerical one) are also shown.

Concentrations of positive axial strains can be observed around aggregates in the experimental field at 50% of the loading (middle left of Fig. 5.6), indicating local extension at these points. At this stage, only a very small number of micro-cracks have initiated in the numerical simulation (bottom left of Fig. 5.6). The number of micro-cracks is significantly increased at 75% of the loading (second column of Fig. 5.6), whereby they mostly appear at the interfaces between aggregates and mortar matrix. It is worth noting that the region which exhibits the highest strain concentration in the experimental field (below the aggregate on the middle left of the vertical slice) does not seem to exhibit yet any initial micro-cracking in the numerical simulation. It is only at the peak (third column of Fig. 5.6), that micro-cracks appear below that particular aggregate and the localisation becomes pronounced. After this stage and downwards on the softening regime, the interfacial micro-cracks bridge through the initiation of new cracks in the mortar and form the dominant macro-crack. It can be seen that the dominant macro-crack in the numerical response reproduces well the localisation patterns observed in the experimental strain fields and corresponds well with the location of the final-macro crack shown in the post-peak scan (top right of Fig. 5.6).

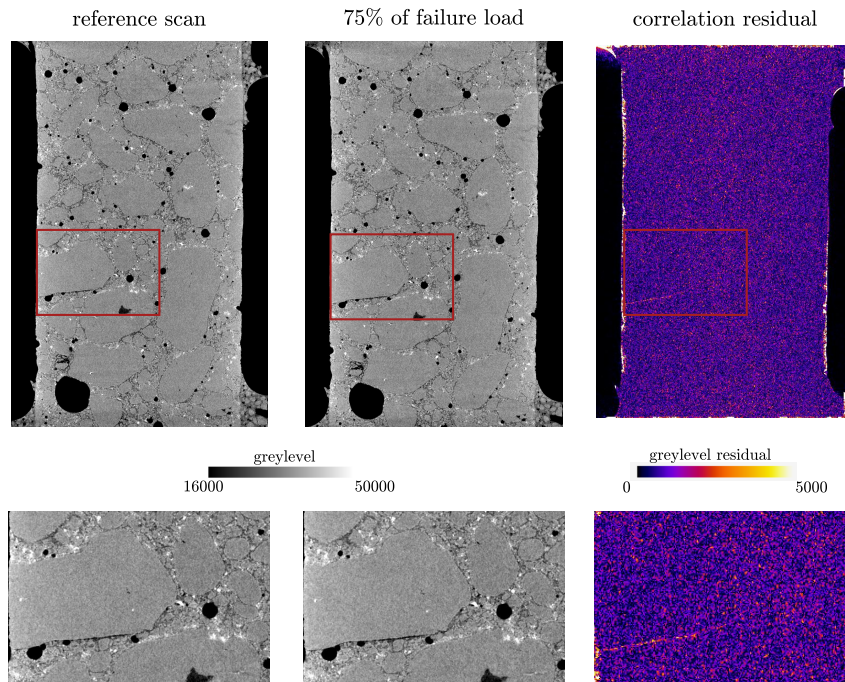


Figure 5.7: Zoom into the zone of identified high strain concentration measured for the T-01 test. (Left): greyscale slice of reference scan, (Middle): greyscale slice of last scan before the peak, (Right): correlation residual field between the two scans

A zoom into the identified region of strain localisation in the experimental field is shown in Fig. 5.7. No obvious micro-structural change is visible below the aggregate on the middle left of the greyscale slices, even when observing the cropped images zooming into this zone (bottom row). However, a concentration of high correlation residual values can be seen (Fig. 5.7 on the right), indicating that indeed a non-linear transformation has occurred and a crack has initiated.

To allow a direct observation of the entire region of interest, Fig. 5.8 presents a qualitative comparison between the crack patterns in the end of the numerical simulation and the extracted macro-crack coming from the post-peak scan. A very good agreement between the two responses is observed despite the different kinematics on the boundaries. Without imposing any *a priori* assumption concerning the location or the continuity of the numerical crack path, the ability of the numerical meso-model to predict the macro-crack's location highlights the influence of the heterogeneities on the failure process of concrete. It is shown that the shape and location of aggregates is one of the key parameters that forms the geometry of the macro-crack, which as illustrated in Fig. 5.6, propagates by bridging the interfacial micro-cracks. It should be noted here, that at the observed scale, one single critical macro-crack has been extracted from the post-peak 3D image, whereas in the numerical model there are certainly regions with concentrated micro-cracks outside the dominant macro-crack. These regions, as shown in Fig. 5.6, correspond well with the ones exhibiting high axial strain concentrations in the experimental field.

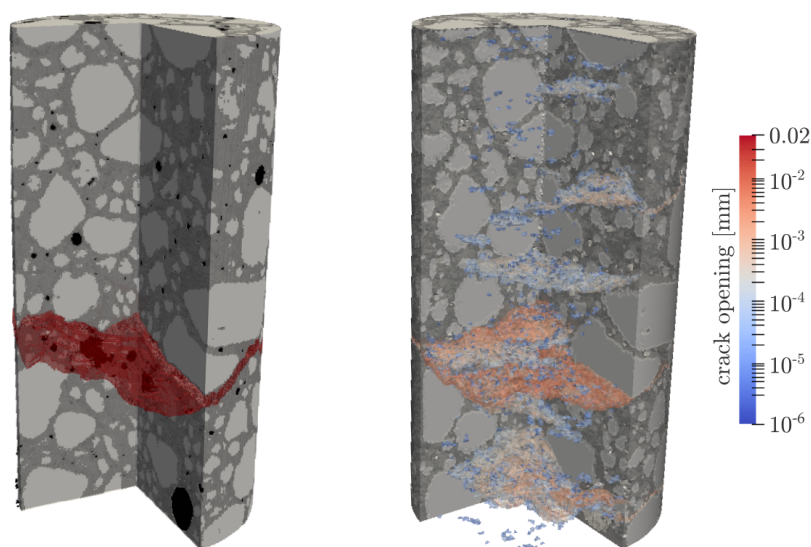


Figure 5.8: Comparison between experimental (left) and numerical (right) crack patterns at the end of the loading for the first uniaxial tensile test (T-01). Note that the experimental macro-crack is extracted from the segmented 3D image of the post-peak x-ray scan

For a quantitative comparison of the fracture patterns, the orientation of the crack networks at the end of the loading observed both experimentally and numerically is presented in Fig. 5.9. The micro-cracks predicted by the numerical model along with their orientation vectors, as well as the discretisation of the experimental macro-crack's outer surface with the corresponding vectors are shown on the left. Provided that the extracted experimental macro-crack is a 3D object of some voxels width, the choice herein is to

consider only the vectors of the upper surface of the crack for the comparison with the orientation of the numerical micro-cracks (planes). The distribution of the binned orientations plotted as a Lambert azimuthal projection is shown on the middle of Fig. 5.9. The histograms of the inclination (*i.e.*, polar angle) of the orientation vectors are shown on the right. Note that a zero inclination means that the vector is aligned to the positive z-axis. It can be seen that the mean polar angles are close, 27° and 18° for the experimental and the numerical response, respectively. Both responses show a clear vertical alignment of the orientations, corresponding to a typical mode I failure in uniaxial tension.

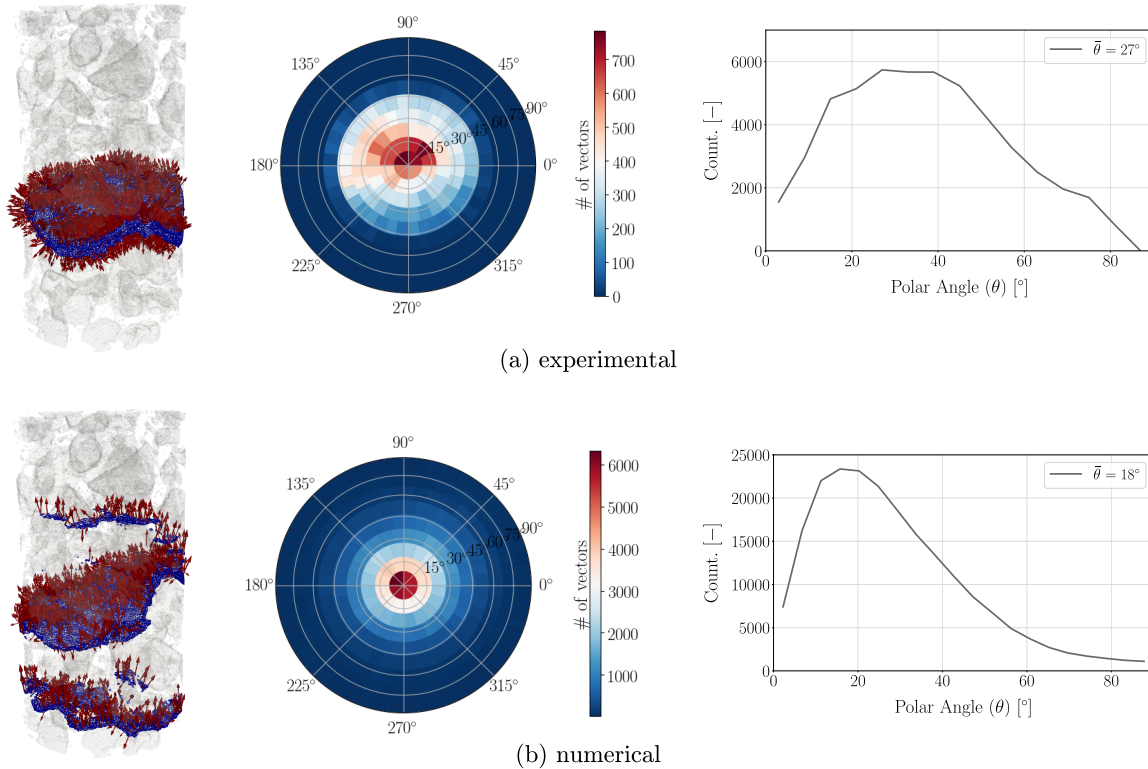


Figure 5.9: Comparison of experimental (top) and numerical (bottom) crack orientation vectors at the end of the loading for the first uniaxial tensile test. The crack patterns with their corresponding local orientation vectors are shown on the left. The binned Lambert azimuthal equal area plots of these 3D vectors are shown on the middle, along with the histograms of the polar angles on the right

5.2.2 Uniaxial compression

Moving now to uniaxial compression, the progressive development of the experimental and numerical axial displacement fields of the second *in-situ* uniaxial compression test (C-02) is depicted in Fig. 5.10. Note that experimentally the specimen reached a higher compressive strength (and corresponding macroscopic axial strain) compared to the numerical ones (see Fig. 5.2(b)). The last scan has been performed at 93% of the maximum experimental failure load, which corresponds to a macroscopic axial strain at the peak of the numerical stress-strain curve (about 1.4×10^{-3}). For the scans performed at 1×10^{-3} and 1.2×10^{-3} macroscopic axial strain levels, higher relative local axial displacements are calculated inside the specimen in the experimental fields compared to the numerical ones.

Displacement incompatibilities (due to the heterogeneities) can be observed in both fields, especially at the bottom part of the cylindrical sample. Due to the contrast in the elastic properties between the different phases, the position and shape of the stiffer (compared to mortar matrix) aggregates are revealed both in the numerical and the experimental fields.

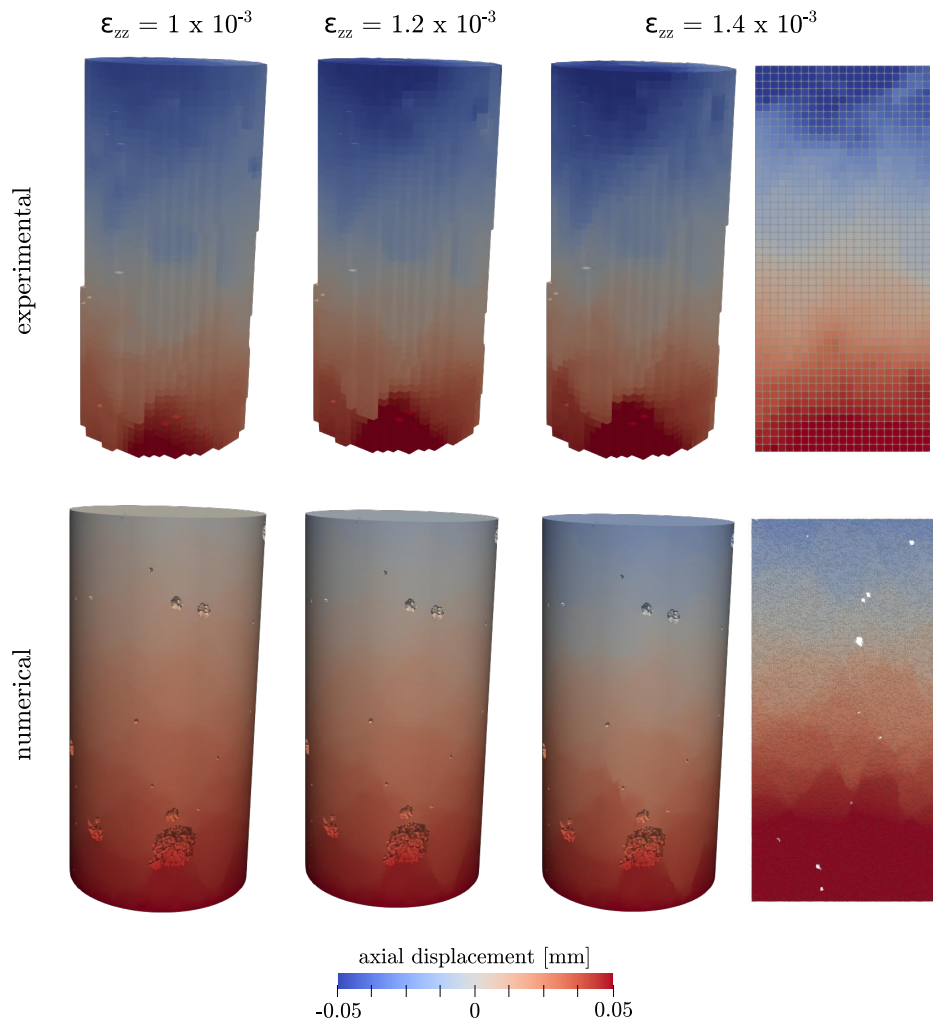


Figure 5.10: Comparison between experimental (top) and numerical (bottom) axial displacement fields for the C-02 uniaxial compression test. Vertical profiles (with their respective discretisations) are also shown for the last step. The comparison is made at the same macroscopic axial strain levels for which a tomographic scan is performed

In order to get a better insight on the localisation process during this test, the experimentally derived volumetric strain fields are compared to the numerically predicted crack patterns and presented in Fig. 5.11. The corresponding 2D greyscale slices extracted from the tomographic scans are also shown. Note again that although no obvious microstructural change is visible in these greyscale images, the progressive development of the fracturing process is underlined both in the numerical crack patterns and the experimental strain fields.

During the first stage (first column of Fig. 5.11), the specimen is mostly under uniform compression, resulting in negative volumetric strain. Only in some few weak points

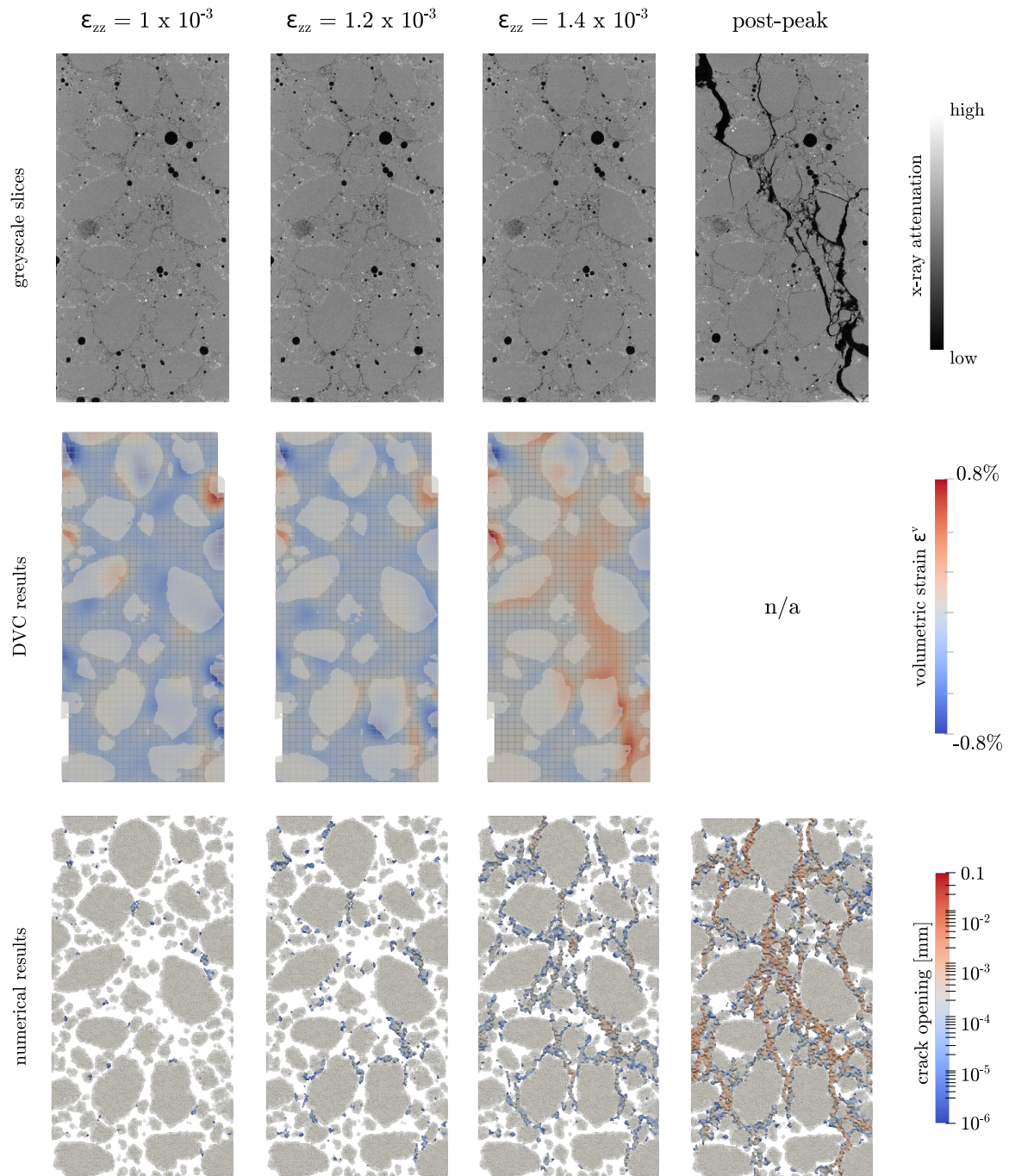


Figure 5.11: Fracturing process evolution during the C-02 test. (Top): greyscale slices coming from the tomographic scans, (Middle): volumetric strain fields measured with DVC overlaid with the segmented largest aggregates of the reference scan, (Bottom): crack patterns predicted by the model. The comparison is performed at the same macroscopic axial strain levels for which a tomographic scan is performed. The discretisation of each field (rectangles for the experimental and triangles for the numerical) is shown

displacement incompatibilities lead to stress concentrations, which in turn result to local expansion (*i.e.*, positive volumetric strain). Strain localisation is thus initially observed, both experimentally and numerically, in the interfaces between aggregates and mortar matrix (weakest points due to material heterogeneities) scattered throughout the speci-

men. It is manifested as diffused micro-cracks (in the numerical response) and regions of positive volumetric strains (in the experimental response). As the compressive load increases (second column of Fig. 5.11), the regions of transverse tensile strains around aggregates become more pronounced in the experimental response, which numerically is reproduced by the initiation of new micro-cracks around aggregates. Reaching close (93%) to the peak experimental axial stress (third column of Fig. 5.11), the experimental strain field is highly heterogeneous indicating the formation of several macro-cracks. The corresponding numerical response (which is at the peak axial stress) exhibits a complex cracking network which coincides well with the identified regions of strain localisation observed in the experimental field. The comparison of both responses with the 2D greyscale slice extracted from the post-peak scan shows a broad similarity, demonstrating that the interfacial micro-cracks around aggregates (identified in both responses) have propagated and bridged through the development of new micro-cracks in the mortar matrix, leading to the development of the depicted cracking network.

It is worth mentioning here that in reality some cracks have propagated through single aggregates, which is also reproduced in the numerical response, but only in very few cases. As an illustration, Fig. 5.12 shows some examples of fractured aggregates, which are extracted from the post-peak x-ray image. Fig. 5.13 depicts the same identified aggregate, along with the cracks propagating through it experimentally and numerically. On the left it is shown how the aggregate fractured during the experiment, while on the right the numerical micro-cracks which have appeared inside the same particle (although not in the same place). For the numerical response, all the activated strong discontinuities inside aggregates at the end of the loading are also depicted.

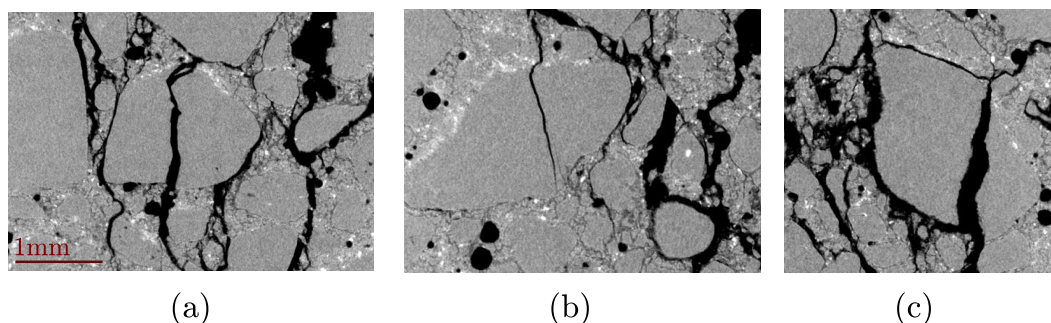


Figure 5.12: Examples of fractured aggregates extracted from the post-peak scan of the C-02 test

A 3D visualisation of the fracture patterns observed experimentally and numerically is presented in Fig. 5.14 by comparing the extracted macro-cracks from the post-peak scan with the numerical crack patterns at the end of the simulation. The complex failure patterns of both responses consist of several macro-cracks (as opposed to simple tension) branching around aggregates roughly parallel to the axial (loading) direction. A large number of local mode I failures in the numerical response has resulted in the emergence of the depicted complex failure mechanism. Even though it has been shown that the model follows well the progressive development of strain localisation before the peak, the rather diffused cracking network predicted at the end of the simulation indicates that the kinematics representation should be enriched (consider for example mode II combined with crack closure) in order to better reproduce the softening post-peak behaviour during this stress path.

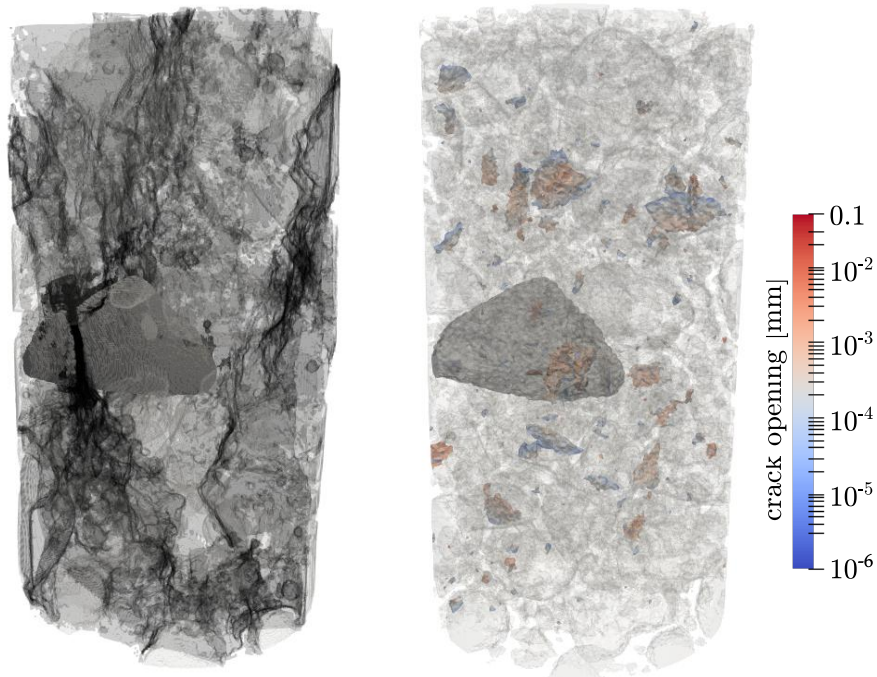


Figure 5.13: Comparison between the same fractured aggregate observed experimentally (left) and numerically (right) at the end of the C-02 test. All the strong discontinuities which have been activated inside aggregates at the end of the numerical simulation are also shown

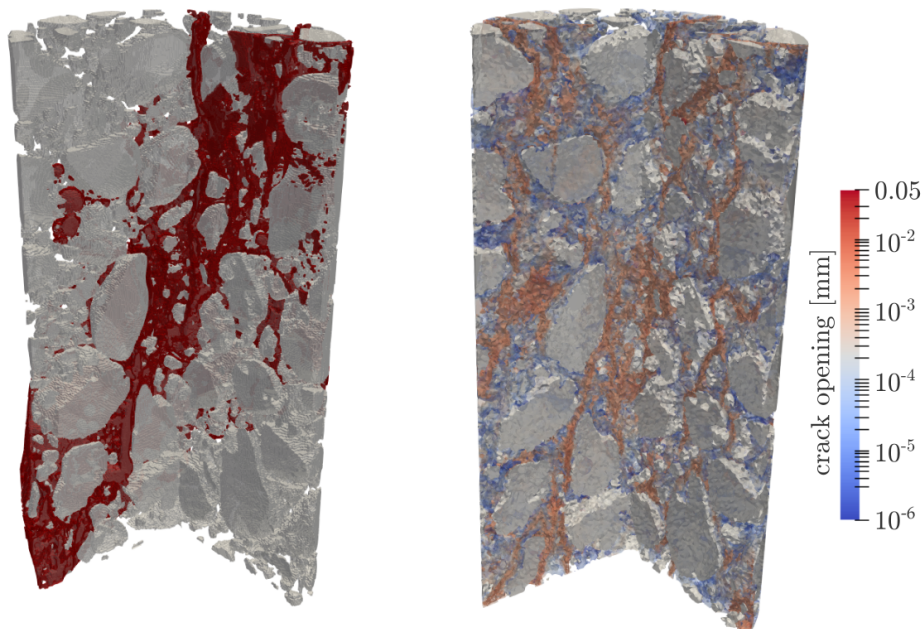


Figure 5.14: Comparison between experimental (left) and numerical (right) crack patterns at the end of the loading for the C-02 test. Note that the experimental crack patterns are extracted from the segmented 3D image of the post-peak x-ray scan. For visualisation, in the numerical result crack openings smaller than 0.002 mm are faded

The diffused cracking network predicted by the meso-model is also depicted in Fig. 5.15 by comparing the orientations of the cracks at the end of the loading. As shown on the histograms of Fig. 5.15 on the right, the calculated mean polar angles are close, 89° and 102° for the experimental and the numerical response, respectively. Note that a zero (or 180°) inclination means that the vector is aligned to the z-axis. Both responses show a clear horizontal alignment of the crack orientation vectors, indicating local mode I openings perpendicular to the direction of the vertical compressive loading. However, a greater number of experimental local crack orientation vectors can be seen that deviate from the horizontal x-y plane. As observed from the Lambert azimuthal equal area plots (Fig. 5.15 on the middle), the crack vectors of the numerical prediction seem rather randomly distributed without reflecting the polarisation observed in the experimental cracks (perhaps due to the experimental boundary conditions), which tend towards 135° with respect to the Cartesian axes.

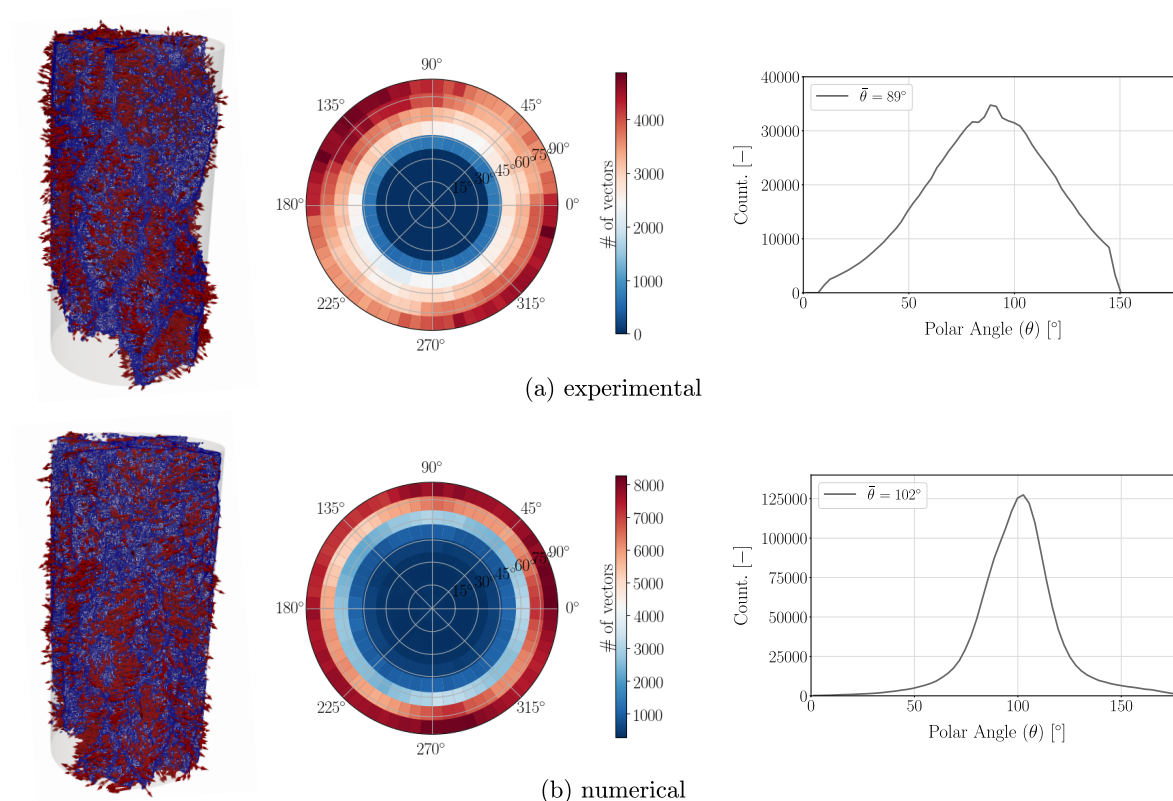


Figure 5.15: Comparison of experimental (top) and numerical (bottom) crack orientations at the end of the loading for the C-02 test. The crack patterns with their corresponding local orientation vectors are shown on the left. The binned Lambert azimuthal equal area plots of these 3D vectors are shown on the middle, along with the histograms of the polar angles on the right

5.2.3 Triaxial compression

Concerning the triaxial tests, the choice herein is to compare experimental and numerical tests that exhibit different deformation patterns. Provided that for the triaxial tests under 5 MPa and 10 MPa confinement a similar failure pattern has occurred (sliding shear band as shown in Sections 3.3.3 and 4.2.4), the TX5-01 and TX15-01 tests are analysed in the following. The comparison between experimental and numerical axial displacement fields

for the deviatoric part of these two tests is presented in Fig. 5.16 and Fig. 5.17, respectively, for the same levels of macroscopic deviatoric axial strains at which tomographic scans are performed.

A good agreement is shown for both tests before the peak, with slightly higher level of relative displacements inside the micro-concrete samples measured experimentally. Heterogeneities in experimental and numerical fields start to appear even at low macroscopic axial strain levels (*i.e.*, 1.4×10^{-3} for both tests), which become more pronounced as the deviatoric load increases. Different deformation patterns are observed for each test, with the shape and location of the significant displacement gradients observed in the experimental fields reproduced well in the corresponding numerical responses. As per the simple compression test presented above, the position and shape of the stiffer (compared to mortar matrix) aggregates is revealed, both in the experimental and the numerical fields.

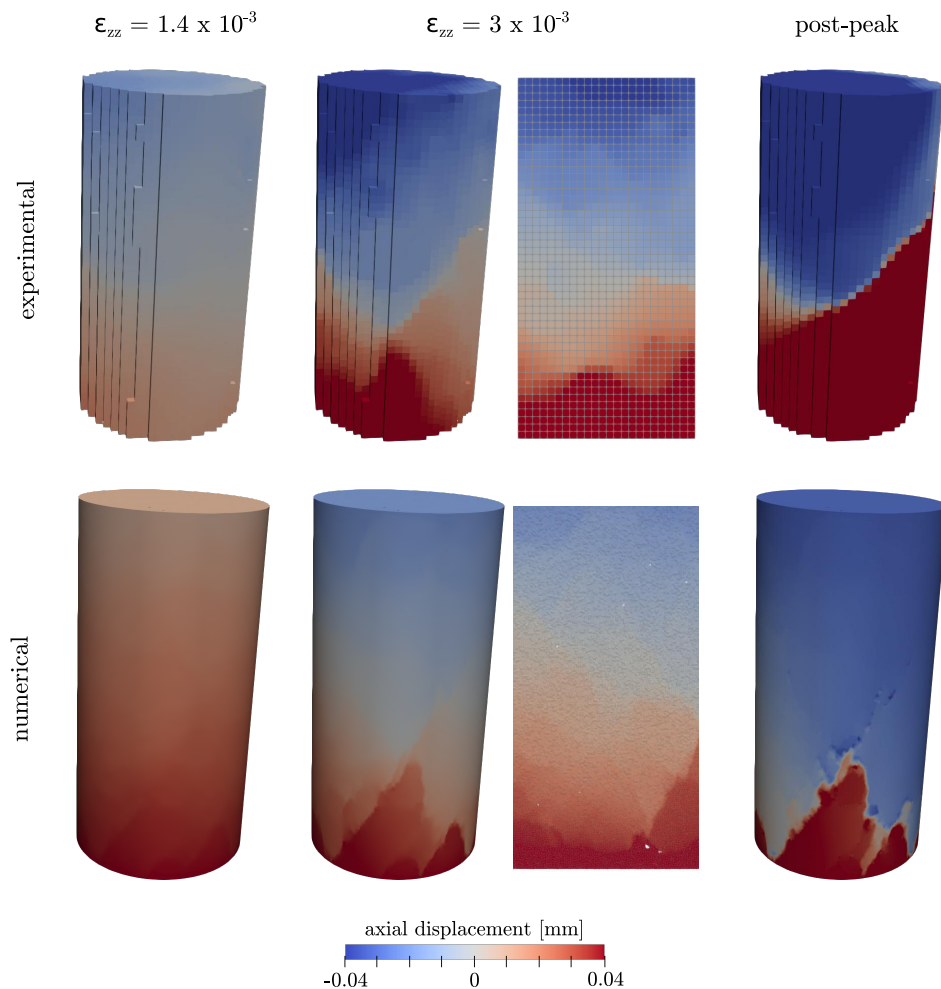


Figure 5.16: Comparison between experimental (top) and numerical (bottom) axial displacement fields during the deviatoric part of the TX5-01 triaxial compression test. Vertical profiles (with their respective discretisations) are also shown for the last step before the peak. The comparison is made at the same macroscopic axial strain levels for which a tomographic scan is performed

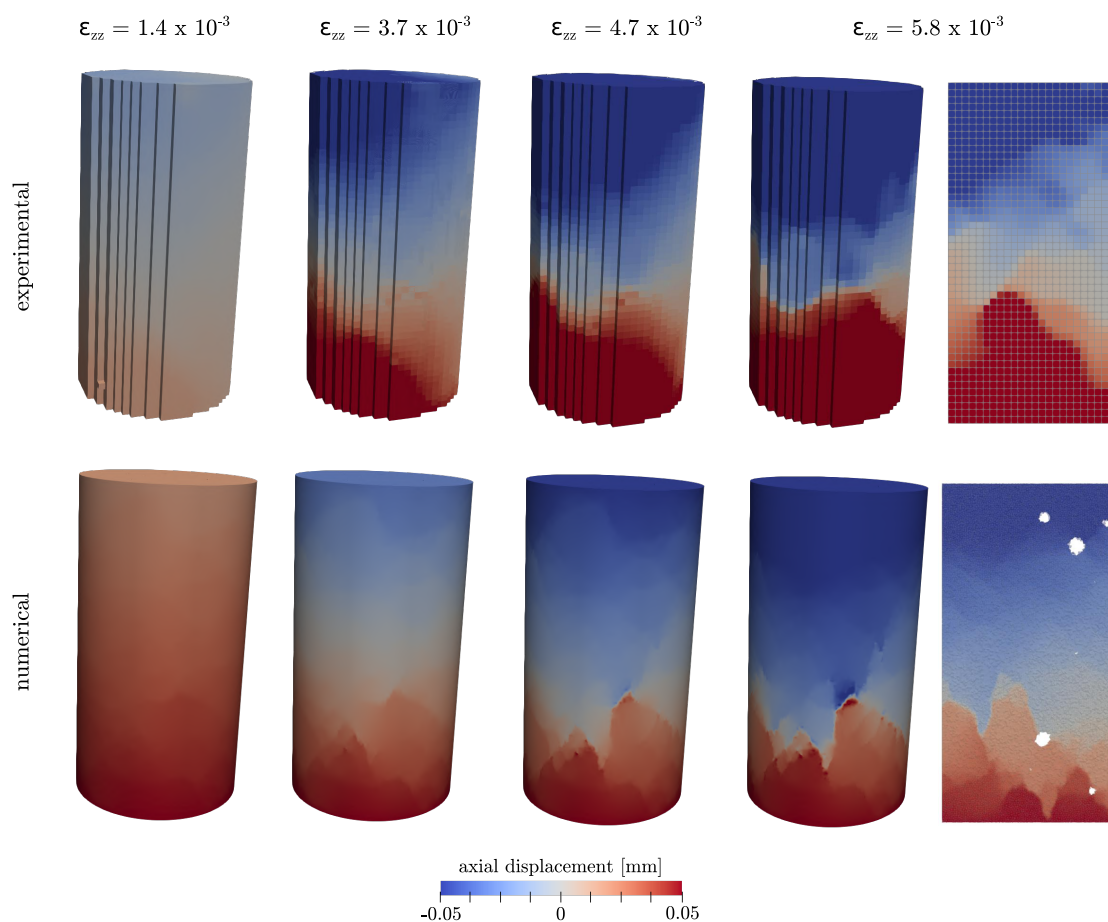


Figure 5.17: Comparison between experimental (top) and numerical (bottom) axial displacement fields during the deviatoric part of the TX15-01 triaxial compression test (highest confining pressure). Vertical profiles (with their respective discretisations) are also shown for the last step. The comparison is made at the same macroscopic axial strain levels for which a tomographic scan is performed

To highlight exactly this impact of the underlying micro-structures, Fig. 5.18 and Fig. 5.19 present the evolution of the fracturing process observed experimentally and predicted numerically for both tests. Slices through the evolving deviatoric strain fields are shown, along with the corresponding numerical crack patterns and the greyscale slices extracted from the tomographic scans.

Regarding the TX5-01 test, at 1.4×10^{-3} macroscopic deviatoric axial strain (see Fig. 5.18 left column), few regions of relatively high deviatoric strain are distributed in the specimen, which in the numerical response are reproduced by a diffused micro-cracking (again around the aggregates). As the test evolves, the middle column of Fig. 5.18 shows regions of significant localised deviatoric strains in the experimental field, in the orientation of the final inclined shear band (see Fig. 5.18 right column), which are also captured by the model. However, a region with high concentration of micro-cracks starts to appear in the bottom right of the numerical specimen, which is not observed in the experimental field. It should be mentioned that at this strain level, the numerical sample has already passed the peak. This region of widespread cracking could, thus, partially reflect the identified phenomenological flaw of the meso-model, which is related to the

importance of improving the post-peak behaviour. Meanwhile, by examining the greyscale images, an aggregate with a different chemical composition can be seen at the bottom of the sample, exhibiting a different distribution of greyvalues (appears darker). This particular aggregate is not captured through the segmentation procedure and consequently is modelled as part of the mortar matrix in the numerical simulation. The widespread cracking network appearing close to the location of this aggregate might also partially be explained by the fact that its presence is ignored in the numerical simulation.

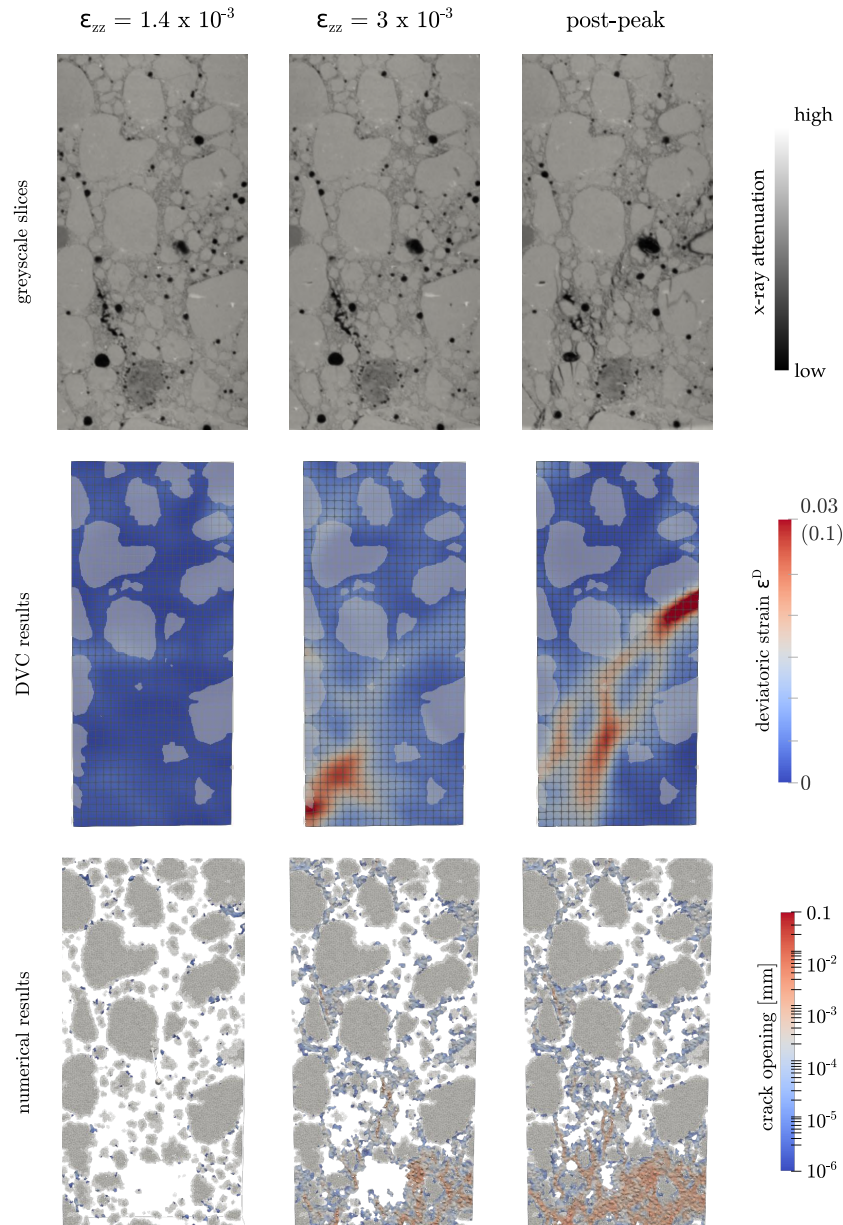


Figure 5.18: Fracturing process evolution during the TX5-01 triaxial compression test. (Top): greyscale slices coming from the tomographic scans, (Middle): deviatoric strain fields (different scale bar after failure) measured with DVC overlaid with the segmented largest aggregates of the reference scan, (Bottom): crack patterns predicted by the model. The comparison is performed at the same macroscopic axial strain levels for which a tomographic scan is performed. The discretisation of each field (rectangles for the experimental and triangles for the numerical) is shown

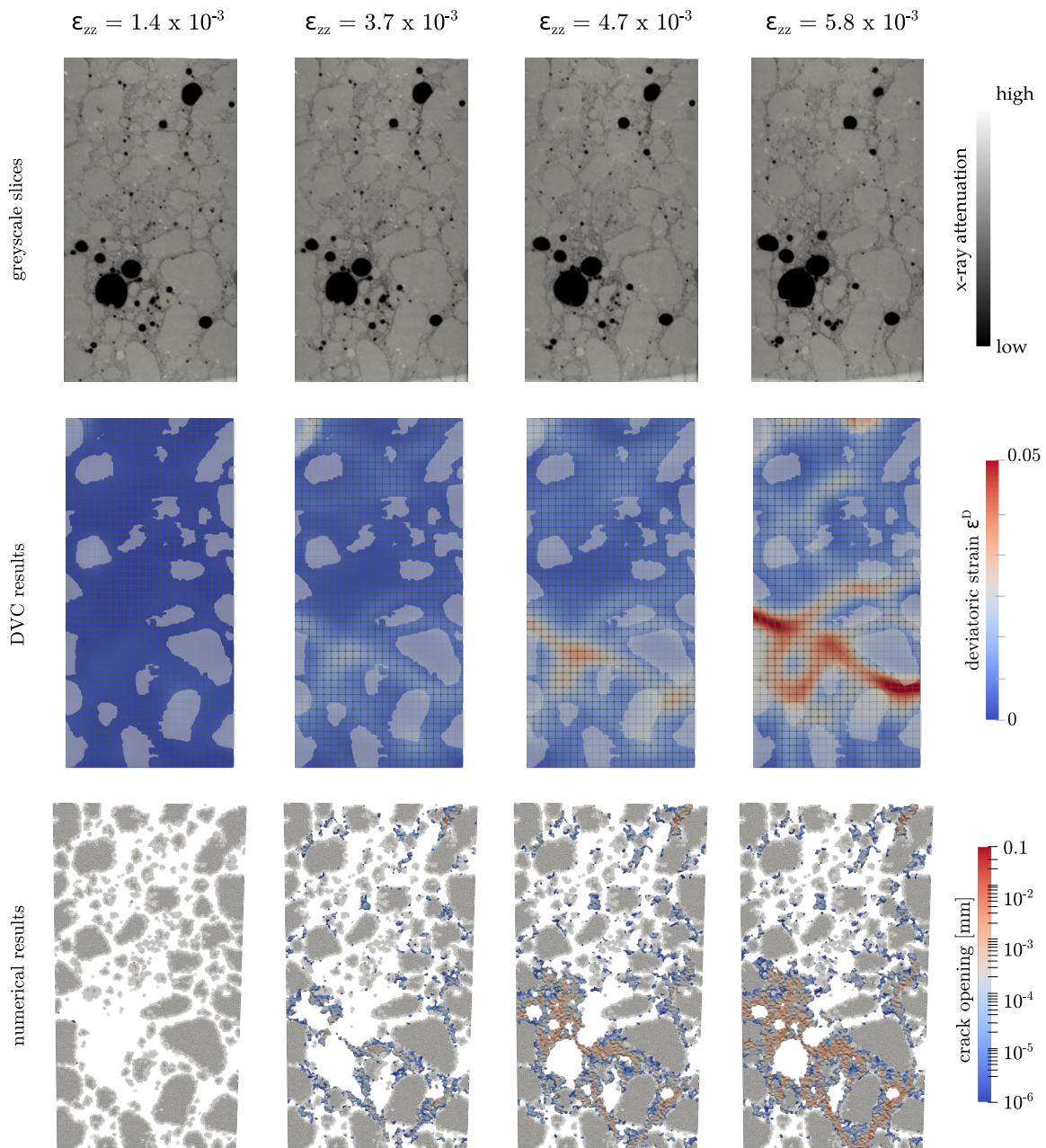


Figure 5.19: Fracturing process evolution during the TX15-01 triaxial compression test (highest confining pressure). (Top): greyscale slices coming from the tomographic scans, (Middle): deviatoric strain fields measured with DVC overlaid with the segmented largest aggregates of the reference scan, (Bottom): crack patterns predicted by the model. The comparison is performed at the same macroscopic axial strain levels for which a tomographic scan is performed. The discretisation of each field (rectangles for the experimental and triangles for the numerical) is shown

Concerning the TX15-01 test, for low strain levels (see Fig. 5.19 left column) no strain localisation is observed in the experimental field, which is in accordance with the numerical prediction, whereby very few micro-cracks have appeared. With the increase of the deviatoric loading, strain concentrations are observed around aggregates, mainly at the bottom part of the specimen, which coincide well with the concentrations of micro-cracks

predicted by the model. Reaching closer to the plateau of the experimental deviatoric axial stress (third column of Fig. 5.19) the localisation gets more pronounced in both fields, with the predicted numerical cracking network resembling well the complexity of the experimental strain field. At the stage of the last scan, the formation of a compactive shear band can be observed experimentally (see also Fig. 3.30 for a 3D visualisation), the location and geometry of which are captured well by the numerical prediction. It is worth mentioning here that the impact of the largest macro-pores in the progressive development of this compactive shear band is highlighted both experimentally and numerically.

Regarding the failure patterns themselves, it should be recalled that for the *in-situ* triaxial compression tests, the detection of the experimental fracture patterns at the end of the loading is based on the greylevel residual fields coming from the correlation between the reference and the last scan of each experiment (see Section 3.3). Note that high residual values indicate discontinuities on the experimental displacement fields, corresponding to cracks. A qualitative comparison between the correlation residual fields and the crack patterns predicted by the numerical model at the end of the loading is presented in Fig. 5.20 and Fig. 5.21 for the TX5-01 and the TX15-01 test, respectively.

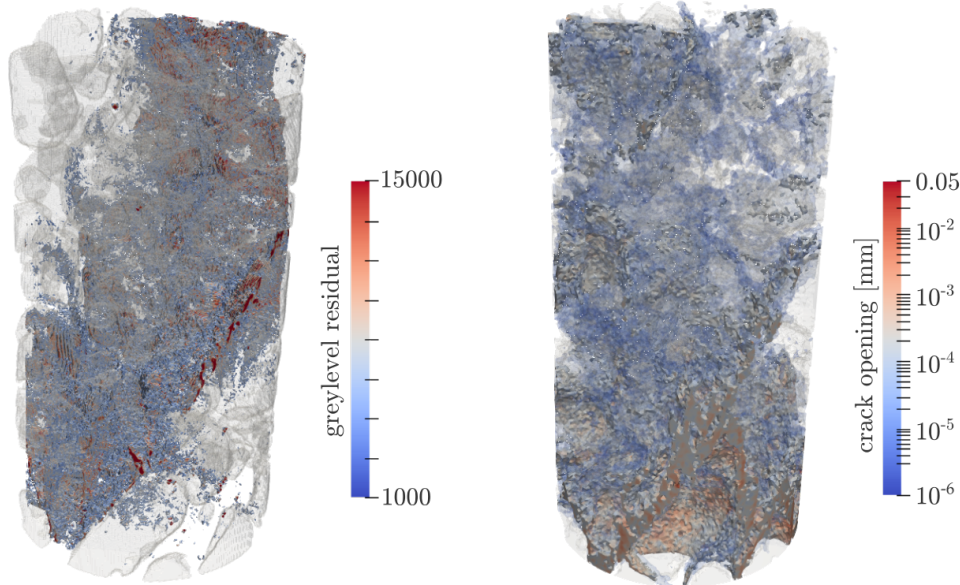


Figure 5.20: Comparison of experimental (left) and numerical (right) crack patterns at the end of the loading for the triaxial test under 5 MPa confinement. The experimental crack patterns correspond to regions of high residual values coming from the correlation between the reference and the post-peak scan

Despite the rather simple phenomenology considered, the model is able to satisfactorily reproduce the basic characteristics of the fracture patterns observed in these experiments. The inclination and location of the shear band observed in the TX5-01 *in-situ* experiment are roughly reproduced numerically. The concentration of high correlation residuals values in the bottom part of the sample observed in the TX15-01 *in-situ* experiment is reflected in the numerical prediction by a concentration of micro-cracks with relatively large openings

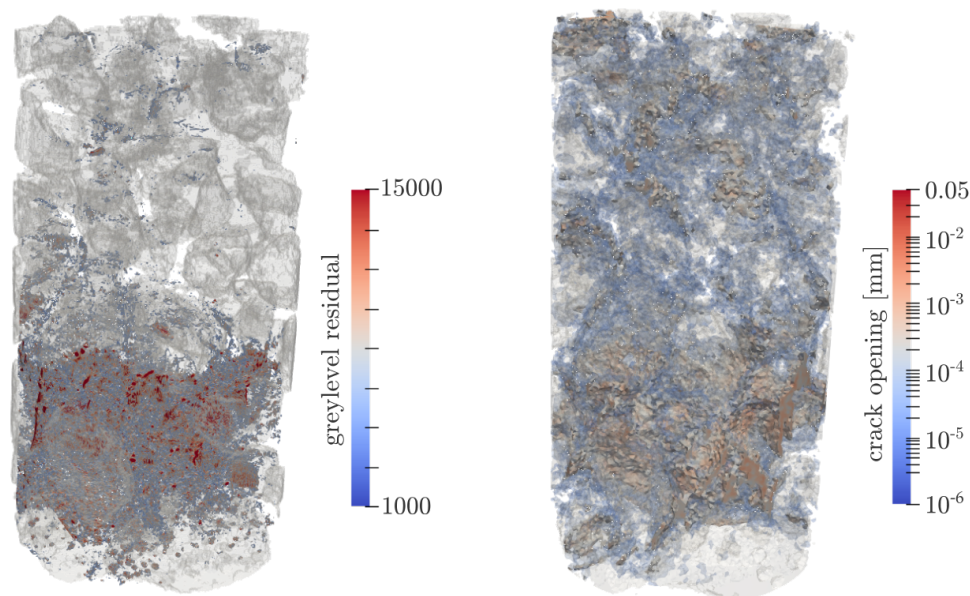


Figure 5.21: Comparison of experimental (left) and numerical (right) crack patterns at the end of the loading for the triaxial test under the highest (15 MPa) confinement level. The experimental crack patterns correspond to regions of high residual values coming from the correlation between the reference and the post-peak scan

in the same location. It should be mentioned, however, that in both numerical responses a rather diffused cracking network is predicted, with regions of high concentrations of micro-cracks existing outside the regions of high residual values observed experimentally. On one hand, the fact that the model captures the onset and evolution of the localisation process observed experimentally indicates that the Rankine localisation criterion used is suitable for mortar at low mean stress levels. On the other hand, the less realistic post-peak response, renders once again the improvement of the local phenomenology a justified future consideration.

The orientation of the numerical and experimental fracture patterns at the end of the loading are compared in Fig. 5.22 and Fig. 5.23 for both levels of confinement. As per the simple compression test, a horizontal alignment of the orientations is depicted, while again a smaller number of vectors deviate from the horizontal x-y plane in the numerical response. However, unlike uniaxial compression, the crack vectors of the numerical predictions do not seem randomly distributed, indicating a less diffused cracking network at the end of the loading. This can be attributed to the lateral restriction of the specimen during the triaxial simulations. As shown on the histograms of the calculated polar angles of the orientation vectors, for both tests, the mean polar angles are close, about 90° and 107° for the experimental and the numerical responses, respectively. Regarding the TX5-01 test, the clear polarisation observed in the experimental cracks which tend towards the xx' Cartesian axes is not well reproduced by the numerical response. On the contrary, a clustering of the orientation vectors towards the yy' Cartesian axes can be seen in both responses for the test under the highest confinement.

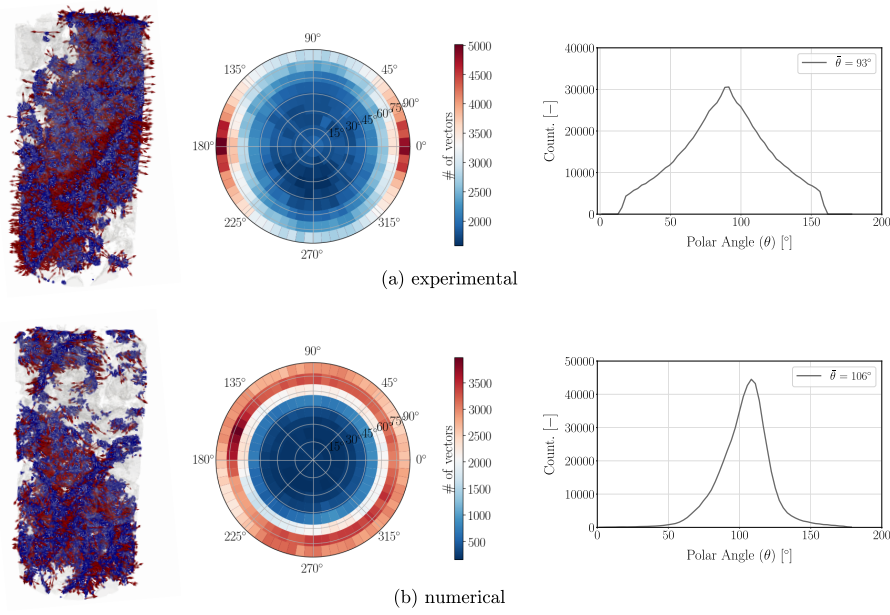


Figure 5.22: Comparison of experimental (top) and numerical (bottom) crack orientations at the end of the loading for the triaxial test under 5 MPa confining pressure. The crack patterns with their corresponding local orientation vectors are shown on the left. The binned Lambert azimuthal equal area plots of these 3D vectors are shown on the middle, along with the histograms of the polar angles on the right

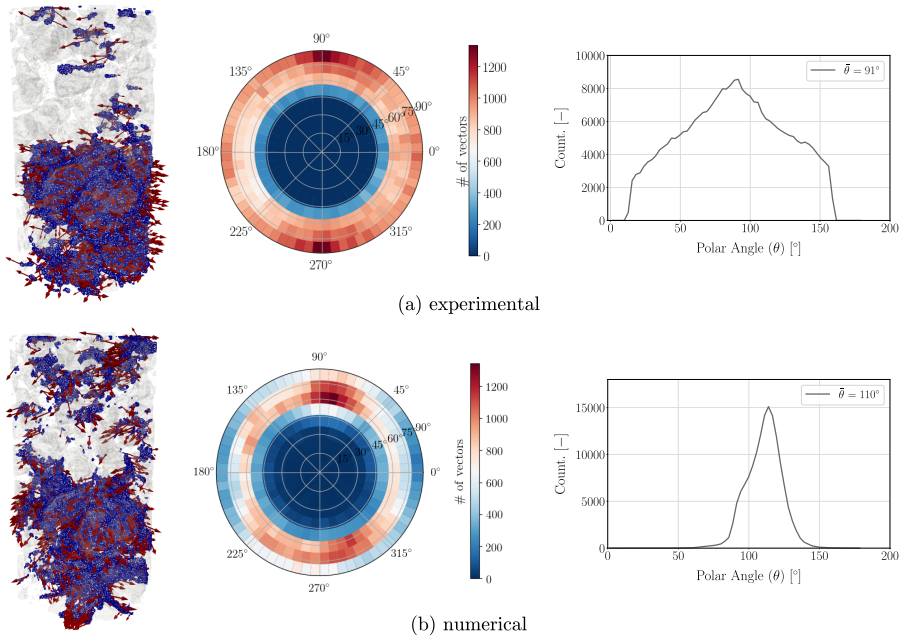


Figure 5.23: Comparison of experimental (top) and numerical (bottom) crack orientations at the end of the loading for the triaxial test under the highest (15 MPa) confining pressure. The crack patterns with their corresponding local orientation vectors are shown on the left. The binned Lambert azimuthal equal area plots of these 3D vectors are shown on the middle, along with the histograms of the polar angles on the right

Despite the patterns observed, it should be mentioned that the comparison of the local crack orientation vectors presented in this section is a first step towards the quantification of the fracture patterns. Even though quantitative information for both responses have been obtained, due to the complexity of the crack patterns, especially for the compression tests, several open questions arise. These questions are related to the different spatial resolutions of the cracking network examined experimentally and numerically, as well as the lack of a clear definition of a macro-scale crack path continuity in the numerical response. An interesting future perspective could be to define a macro-scale 3D cracking network in the numerical response, extract it and mesh its outer surface, as per the extracted experimental macro-cracks.

5.3 Further insights into the role of morphology

The predictive ability of the meso-model discussed in the previous section, considering the adopted phenomenology and the identification of model parameters only in simple tension, strongly suggests that the explicit representation of the heterogeneities seems to be its key feature. Consequently, in order to accurately predict the mechanical behaviour and the fracturing process of concrete, the actual material's meso-structure has to be taken into account. However, it is costly and time-consuming to conduct *in-situ* mechanical experiments, especially in the case when a large number of samples is required in order to provide a meaningful statistical result. As an alternative, a large number of numerical samples can be generated with relative ease and, in turn, a large number of numerical predictions can be obtained, providing promising potential for a global statistical analysis. In the presented case in particular, the numerical results directly compared to corresponding experiments, suggest interesting further practical applications of the meso-model.

In what follows, with the objective to offer a further insight into the impact of the different phases, virtual concrete meso-structures are generated by modifying the real reference morphologies coming from the x-rays scans. The aim of this section is to present some illustrative examples of virtual morphologies in order to evaluate the influence of macro-pores and aggregates. Note that a limited number of numerical predictions is produced, without intending to provide an extensive statistical analysis.

5.3.1 Influence of macro-pores

As a first step to study the impact of the different phases on the macroscopic mechanical response, the role of macro-pores is investigated under simple tension and triaxial compression. It should be recalled here, that for the numerical results presented so far, elements which after the morphological projection have been identified as macro-pores, have been removed from the FE mesh creating, thus, some cavities in the mesh (see Section 4.2.3). This time, in order to account for the impact of macro-pores, these elements are not removed and the material properties of the mortar matrix (see Table 4.2) are assigned to them. Consequently, a two-phase morphology (composed of aggregates, mortar matrix and their respective interfaces) is created, using as a base the original three-phase morphology coming from the reference scan of the corresponding *in-situ* test. It is worth mentioning that since a non-adapted meshing technique is used, whereby the FE mesh is created regardless of the heterogeneous morphology (see Section 4.1.1), there is no need to generate a new FE mesh which will account for the modified two-phase morphology.

The influence of macro-pores on the macroscopic response under uniaxial tension is depicted in Fig. 5.24, by comparing the response of the initial three-phase morphology to the modified two-phase one, in terms of axial stress as a function of axial strain. In order to justify the choice of removing the elements that account for macro-pores, the response of a third simulation is also shown, where macro-pores are modelled as a very soft material. It can be seen that, indeed, this latter case causes numerical problems, with the global solution diverging after the post-peak. The comparison of the macroscopic responses shows that a three-phase morphology results in a lower tensile strength and a slightly less stiff macroscopic behaviour. This can be justified by the fact that the presence of macro-pores reduces the effective area to resist the tensile force. Considering that the volume fraction of macro-pores measured from the reference scan is 2.6% (see Table 3.1), an increase of porosity from 0% (two-phase morphology) to 2.6% (reference morphology) reduces the tensile strength by 3.3%.

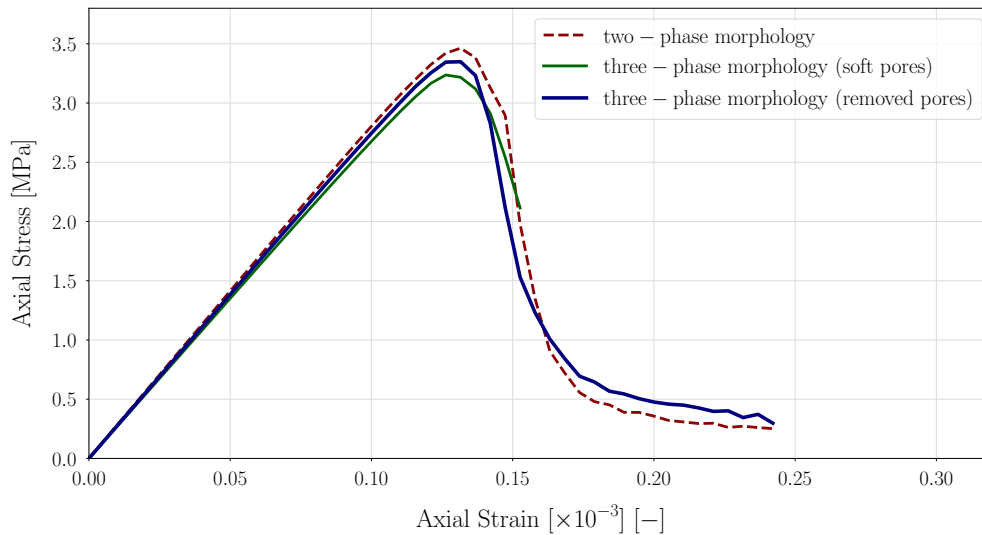


Figure 5.24: Impact of macro-pores on the macroscopic response of the first uniaxial tensile test

The pronounced effect of the presence of macro-pores is revealed by observing the cracking network at the end of the loading, as highlighted in Fig. 5.25. For the three-phase morphology, macro-pores (in a faded colour) are also overlaid with the predicted fracture patterns, in order to facilitate the interpretation of their impact. Even though the position and shape of the aggregates are identical in both simulations, it can be seen that the cracking network predicted by a two-phase morphology (see Fig. 5.25 on the right) differs significantly from the one evolved when the reference three-phase morphology is considered (see Fig. 5.25 on the left).

In the latter case, due to the interplay between the different heterogeneities, macro-pores seem to attract the evolved cracking network and a clear macro-crack appears in the specimen, propagating through them. On the contrary, in the case of a two-phase morphology, a clear macro-crack no longer appears, but rather it branches into two dominant macro-cracks. It is worth mentioning that in both cases about the same

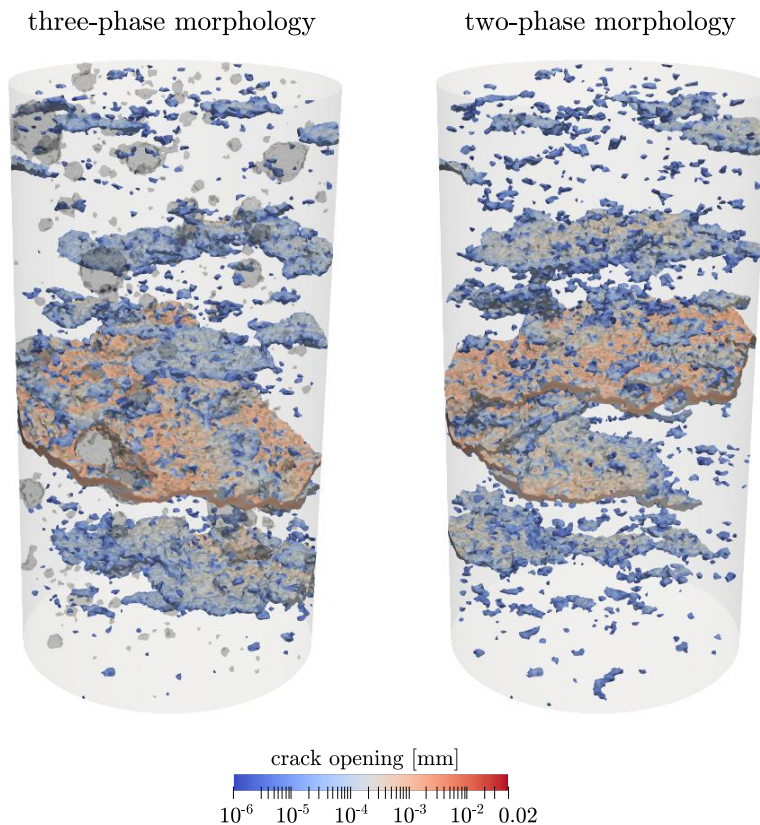


Figure 5.25: Influence of macro-pores on the fracture patterns under uniaxial tension. (Left): reference three-phase morphology with macro-pores removed from the FE mesh, but shown shown in a faded black colour only as an illustration. (Right): modified two-phase morphology with macro-pores modelled as part of the mortar matrix

number of elements have failed, with micro-cracks appearing in 3% of the total number of elements. However, it is only when the real morphology is accounted for, that the location and geometry of the predicted macro-crack correspond well to the experimental one (see Fig. 5.8), reproducing numerically the actual response of the heterogeneous material.

To further investigate the influence of porosity under uniaxial tension, the variation of the normalised area of aggregates and macro-pores along the vertical axis of the specimen is shown in Fig. 5.26. In the same graph, the variation of the normalised area of the extracted experimental macro-crack and the predicted numerical crack patterns are also depicted. By concentrating on the comparison between experiment and model, the capability of the latter to predict the macro-crack's location is highlighted again, even though there are regions with high micro-cracks concentrations outside the extracted experimental macro-crack.

As for the role of the heterogeneities, it can be seen that the experimental macro-crack appears in the part of the specimen with the lowest effective area, which is the region that exhibits high concentration of macro-pores and disproportionately low concentration of aggregates. This information combined with the evolution of the fracturing process presented in Fig. 5.6, suggest that the initiation of the localisation seems to be driven by aggregates (due to stress concentration), while the propagation of the cracking network is driven both by aggregates and macro-pores, with cracks branching around the former and propagating through the latter.

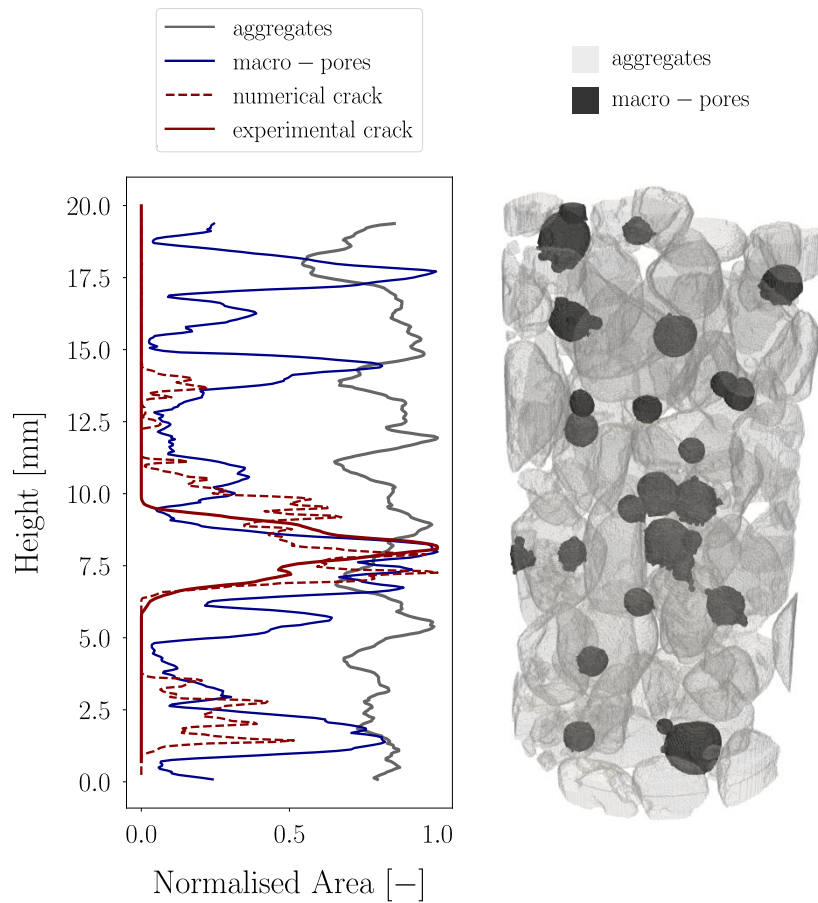


Figure 5.26: (Left): variation of normalised area of experimental and numerical crack patterns along the vertical axis of the T-01 specimen. The variation of the normalised area of aggregates and macro-pores is also shown. (Right): segmented largest heterogeneities coming from the reference scan

Concerning the TX15-01 test (highest confinement), the influence of macro-pores on the macroscopic response is depicted in Fig. 5.27. The deviatoric part of the response of the initial three-phase morphology is compared to the modified two-phase one, in terms of axial stress as a function of axial strain. It should be mentioned that, as shown in Table 3.1, the volume fraction of macro-pores measured from the reference scan of this test is 2.7%, which is very close to the one measured for the uniaxial tensile test above. Similarly with simple tension, a two-phase morphology yields a slightly stiffer response and an increase of the macroscopic strength of the material. In triaxial compression, however, the increase of porosity from 0% (two-phase morphology) to 2.7% (reference morphology) reduces the deviatoric strength by 8%, as opposed to a reduction of 3.3% obtained for simple tension.

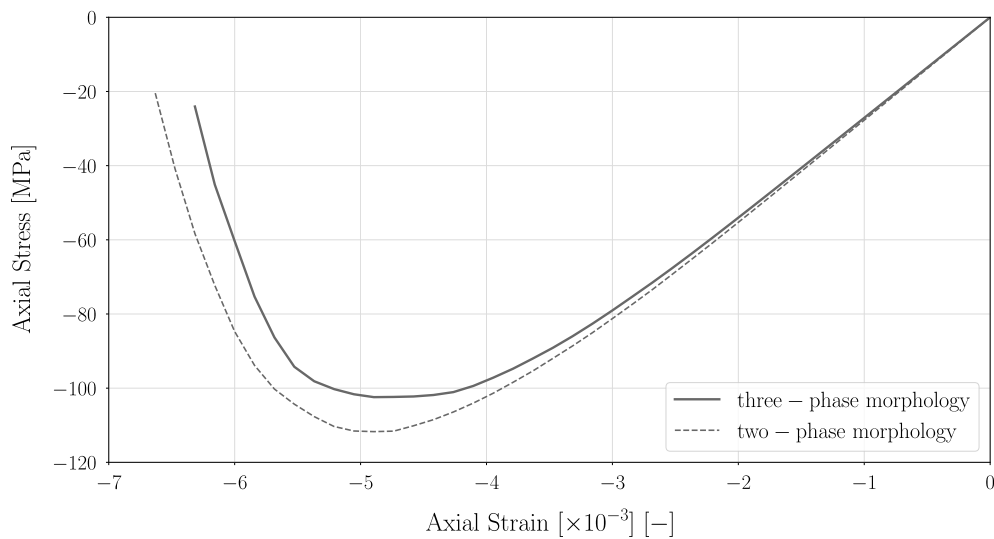


Figure 5.27: Impact of macro-pores on the macroscopic response of the TX15-01 test (highest confinement)

The effect of macro-pores in the predicted failure patterns is less pronounced in tri-axial compression compared to simple tension. This can be attributed to the fact that in the latter case the response is more brittle and the developed cracking network is more localised with only 3% of the elements having failed at the end of the loading. On the contrary, the failure under triaxial compression is more diffused with 15% of elements having failed at the end of the loading. Fig. 5.28 presents the comparison of the predicted failure patterns between the two-phase and the reference three-phase morphology. Even though in both cases high concentrations of micro-cracks at the bottom of the specimen can be observed, the presence of macro-pores alters the evolved cracking network, indicating, again, that the interaction between aggregates and macro-pores drive the development of the failure patterns.

The two example applications of the meso-model presented above have revealed interesting information regarding the role of macro-pores on the fracturing process under simple tension and triaxial compression. The influence of the other set of heterogeneities, *i.e.*, the aggregates, is investigated in the following section.

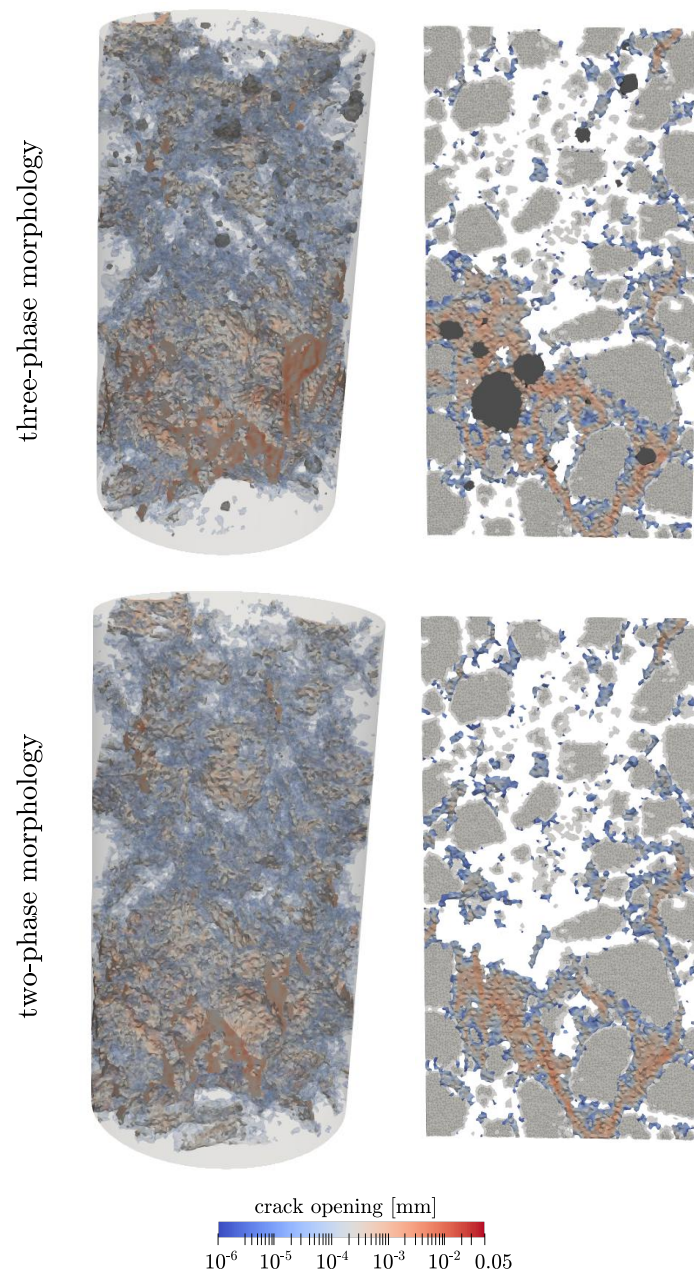
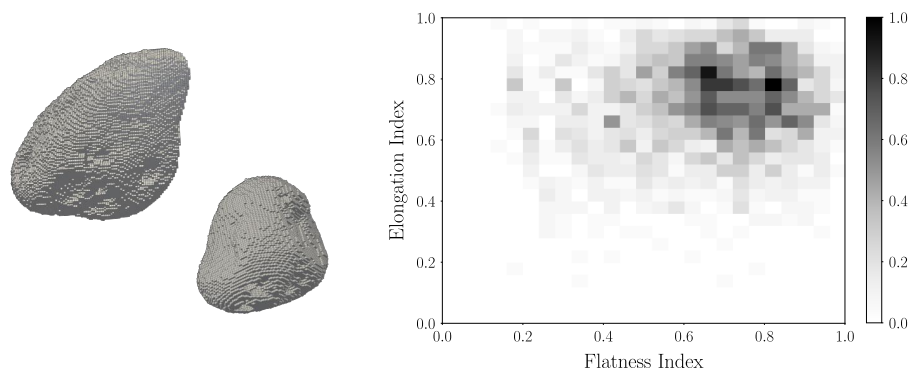


Figure 5.28: Influence of macro-pores on the fracture patterns under triaxial compression (TX15-01 test). (Top): reference three-phase morphology with macro-pores removed from the FE mesh, but shown in a faded black colour only as an illustration. (Bottom): modified two-phase morphology with macro-pores modelled as part of the mortar matrix

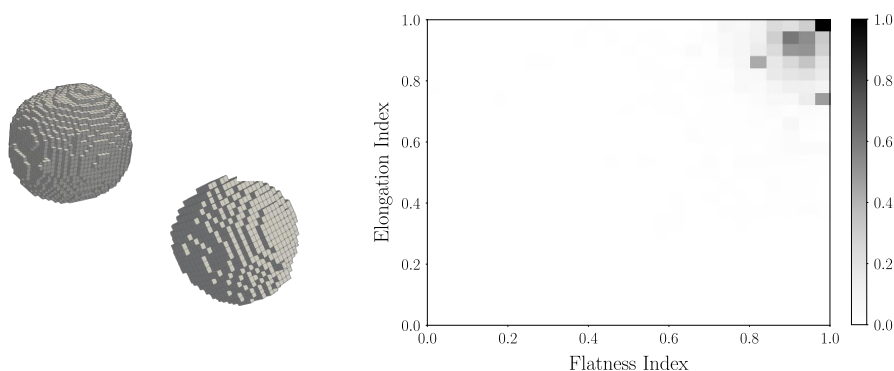
5.3.2 Modelling heterogeneities as spheres

The micro-concrete composition studied herein consists of aggregates with sizes between 0.5 and 4 mm (see Table 2.1) exhibiting a range of different shapes. The particle size distribution curves for aggregates and macro-pores measured from the segmented images of the reference scans have been presented in Fig. 3.8. In order to characterise the 3D shape of these heterogeneities, among the different methods that exist, the Zingg diagram [Zingg, 1935] is used here. Note that the Zingg diagram is a shape classification scheme that

uses the particle's dimensions along the three principal axes, measured in the presented case through the moments of inertia. If the largest, intermediate and smallest axes of each particle are defined as a , b and c , respectively, then the Zingg diagram is used to represent a relation between the *flatness* (*i.e.*, c/b) and *elongation* (*i.e.*, b/a) ratios. As an illustrative example, the Zingg diagrams of the identified aggregates and macro-pores coming from the reference scan of the T-01 test are shown in Fig. 5.29. As expected, a clear clustering of both ratios close to 1.0 can be seen for macro-pores, which roughly corresponds to a spherical shape, whereas a larger spectrum of irregular aggregates' shapes is depicted.



(a) aggregates



(b) macro-pores

Figure 5.29: Shape characterisation of the heterogeneities coming from the segmented image of the T-01 test. The computed Zingg diagrams of aggregates (top) and macro-pores (bottom) are shown along with some identified particles (discretised in voxels)

As discussed in the introduction of this work, considering the fact that a typical approach in meso-scale modelling is to represent aggregates as spheres or ellipsoids (with different aspect ratios), it is interesting to study the effect of the heterogeneities' actual shape, as opposed to an idealised one. To achieve this, the morphology coming from the reference scan of the T-01 test is considered as the reference morphology. As a first step, a modified morphology is generated, whereby the identified from the 3D image aggregates and macro-pores are converted into spheres of equivalent volume, with their positions remaining fixed, as per the reference morphology. Starting from the labelled image of each inclusion phase and for each labelled particle, the diameter of a sphere which occupies the same volume as the original particle (irregular for aggregates and roughly spherical

for macro-pores) is computed, along with the coordinates of its centre of mass. The distance fields of the “spherical” heterogeneities are then calculated and projected onto the unstructured FE mesh following the procedure detailed in Section 4.2.1.

As a further step, in order to study the impact of both the location and the shape of the heterogeneities, a set of new virtual morphologies is created, with aggregates and macro-pores still modelled as spheres, but this time randomly distributed in the numerical concrete sample. To generate these virtual morphologies, a sphere packing algorithm is used (see [Vallade, 2016a]), which is based on a collective rearrangement method [Bezrukov *et al.*, 2002], as implemented in `spam`. The basic idea is to create and randomly pack spherical aggregates and macro-pores, allowing them initially to overlap. An iterative process is then applied by moving each particle depending on the percentage of overlapping, until there is no more intersection between different particles. It should be noted here that since only the shape of the heterogeneities is modified, the volume fraction of each phase, as well as their corresponding size distribution curves are kept similar to the ones calculated from the reference morphology and presented in Section 3.1.3.

A minimum distance of 0.2 mm is set between each sphere, which is double the average distance between the nodes of each tetrahedron (*i.e.*, 0.1 mm), in order to ensure a good representation of the elements that account for the interfaces between the particles and the mortar matrix (*i.e.*, enhanced with a weak discontinuity). However, after a number of trial sphere packing realisations, it has been observed that only when the volume of the original particles is decreased, no overlapping between the generated spherical particles is finally achieved. In other words, a sphere packing of the different phases with their initial volume fraction (as measured from the x-ray scan) is hard to achieve. For this reason, a 3D erosion filter with a structuring element of 3 voxels radius (see Section 3.1.2) is applied to the segmented binary images of the heterogeneities, reducing the volume fraction from 50% to 40% for aggregates and from 2.6% to 1.3% for macro-pores. Starting from this morphology as the reference, the set of virtual morphologies with spherical heterogeneities is finally created.

Note that all the different morphologies are projected onto the same unstructured FE mesh as the one used for the reference uniaxial tensile computation (see Section 4.2.1). Fig. 5.30 presents, for three different input morphologies, the finite elements that after the morphological projection have been identified as aggregates or macro-pores. On the left, the heterogeneities of the reference morphology with the reduced volume fraction are shown. These heterogeneities are then modelled as spheres fixed at their original positions, shown in Fig. 5.31b. These spherical heterogeneities are then randomly distributed throughout the numerical concrete sample, with an example of a generated morphology shown in Fig. 5.31c. It should be mentioned here, that for the mechanical simulations to be performed, elements which account for macro-pores are finally removed from the FE meshes.

In total 10 different simulations are performed with aggregates and macro-pores modelled as spheres randomly distributed. Fig. 5.31 gathers and compares the macroscopic responses of the reference morphology (with a reduced volume fraction of the heterogeneities), the modified one with the spherical heterogeneities and the 10 different realisations, along with their mean response. It can be seen that the spherical shape of the heterogeneities facilitates the localisation, leading to an underestimation of the macroscopic strength of the material and a less stiff macroscopic response. In particular, considering aggregates as spheres fixed at their initial position reduces the macroscopic strength by 18% (from 2.8 MPa to 2.3 MPa), while the mean response of the randomly distributed

spherical heterogeneities leads to a reduction of the macroscopic strength by 10% (from 2.8 MPa to 2.5 MPa). It is worth mentioning here, that focusing only on the reference morphology (without any modification of the shape and location of the heterogeneities), the reduction of the aggregate's volume fraction from 50% to 40% results in a reduction of the tensile strength by 15% (from 3.3 MPa to 2.8 MPa) and a reduction of the computed Young's modulus by 33% (from 27 GPa to 18 GPa).

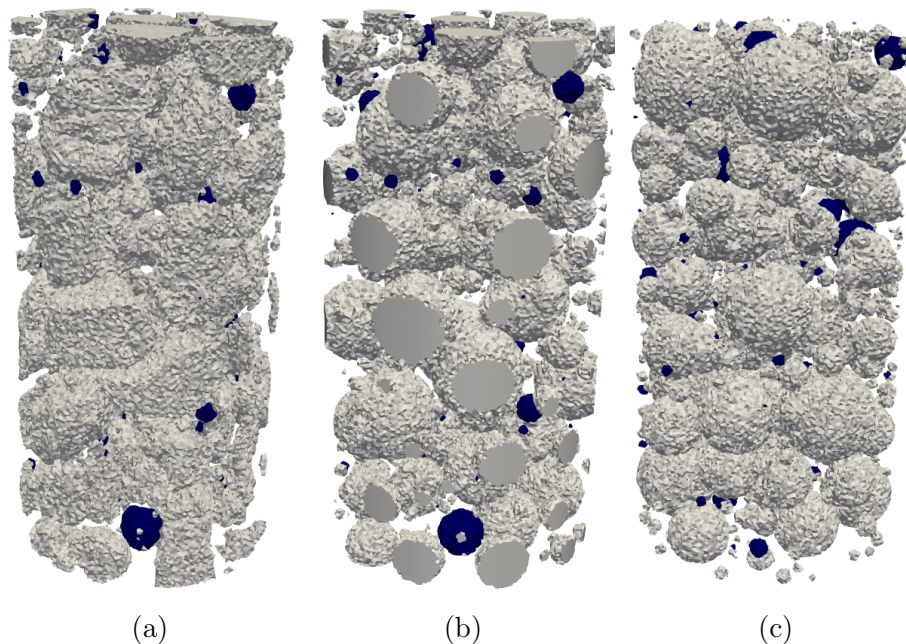


Figure 5.30: Reference and modified morphologies projected onto the same unstructured FE mesh. Only elements that after the projection correspond to aggregates (white) and macro-pores (blue) are shown. (a) Reference morphology with positions and shapes of heterogeneities as obtained from the x-ray scan, after their initial volume has been reduced, (b) heterogeneities modelled as spheres at the same positions as the reference morphology on the left, (c) heterogeneities modelled as spheres randomly distributed in the numerical concrete sample. Note that for the mechanical simulations elements in blue (macro-pores) are finally removed from the FE meshes

The fracture patterns at the end of the loading are shown in Fig. 5.32, revealing the different cracking networks developed for each morphology. As a first remark, the position of the macro-crack after reducing the volume fraction of the heterogeneities does not coincide with the one predicted based on the initial volume of the heterogeneities (see Fig. 5.8). In all cases about the same number of elements have failed, with micro-cracks appearing in 2% of the total number of elements. Even though the position of each aggregate is kept fixed, it can be seen that the location of the predicted macro-crack is different when considering idealised spherical aggregates compared to the original irregular ones. A representative example of randomly positioned spherical heterogeneities is shown on the right of Fig. 5.32, where a less localised cracking network is observed, with a single dominant macro-crack no longer appearing.

This observation might partially explain the lower tensile strength predicted for the spherical heterogeneities. While higher stress concentrations are expected around the irregular aggregates (reference morphology), the natural packing of the granular skeleton of the material combined with the initial distribution of the macro-pores might have led

to fewer weak paths that result in the emergence of a single final macro-crack. On the contrary, the idealised shape of the heterogeneities and their numerical packing might have created an increased number of weak paths resulting in the emergence of a less complex crack path topology.

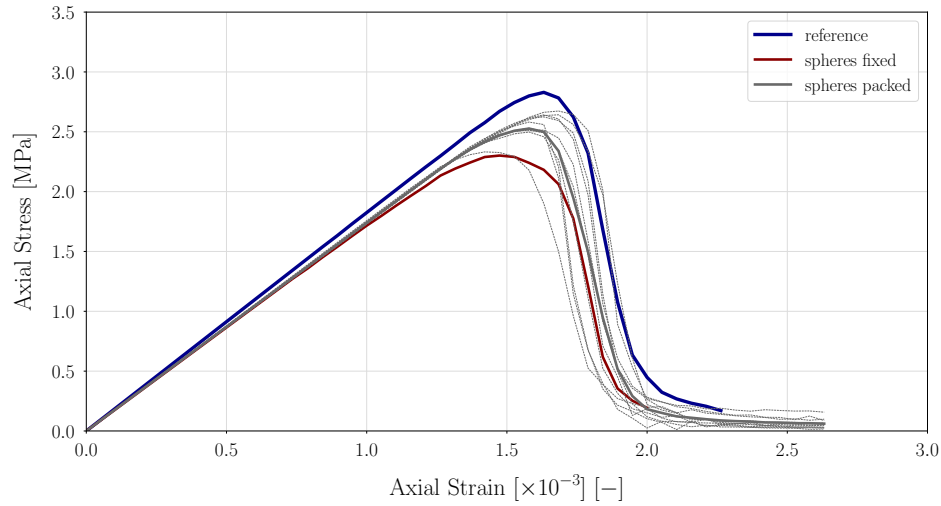


Figure 5.31: Comparison of macroscopic responses under simple tension between reference morphology and heterogeneities modelled as spheres at the same position (fixed) and randomly distributed (packed)

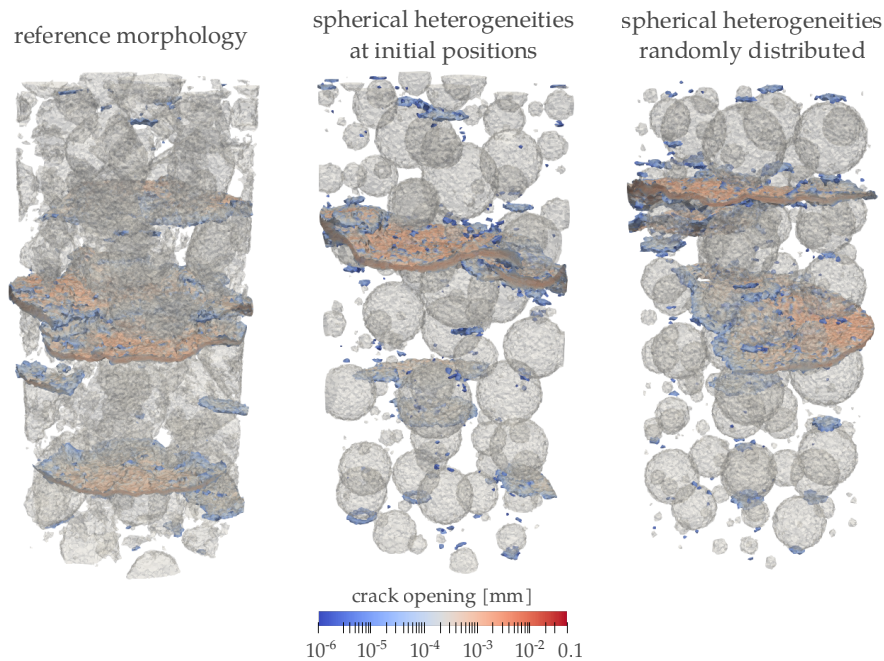


Figure 5.32: Comparison of failure patterns at the end of the loading for reference and modified heterogeneous morphologies under uniaxial tension. (Left): reference morphology with positions and shapes of heterogeneities as obtained from the x-ray scan but after their initial volume has been reduced, (Middle): heterogeneities modelled as spheres at the same positions as the reference morphology on the left, (Right): heterogeneities modelled as spheres randomly distributed in the numerical concrete sample

5.4 Concluding remarks

This chapter presented a comparison between experimental and numerical observations of the mechanical behaviour of the micro-concrete specimens, in terms of macroscopic responses, displacement fields, fracturing processes and failure patterns. For the different stress paths studied, a power law was fitted in the experimental and numerical data that can be used to predict the failure criterion of concrete in the (q_{\max}, σ_m) plane. Starting from an x-ray scan, it was shown that the meso-model was able to satisfactorily predict the macroscopic response of the studied material in terms of macroscopic strengths and Young's moduli. The typical asymmetric behaviour of concrete in tension and compression, as well as the increase of strength and ductility with the increase of confinement were sufficiently captured numerically.

With an identification of the material parameters only in simple tension and a consideration of a simple tensile failure criterion coupled with a mode I failure mechanism, some of the basic characteristic features of the different failure modes observed experimentally were also numerically reproduced. In simple tension, the meso-model was able to predict the location and geometry of the single macro-crack occurred experimentally, despite the different kinematics in the boundaries. More complex failure patterns, such as the inclined shear band observed in triaxial compression under 5 MPa confinement, but also the compactive shear band observed in triaxial compression under the highest confinement were satisfactorily reproduced by the meso-model.

Meanwhile, for the different loading paths, the model was capable of following the onset and evolution of the localisation process observed experimentally, indicating that the Rankine localisation criterion used is suitable for mortar at low mean stress levels. A quantitative comparison of the cracking networks local orientation vectors at the end of the loading revealed a clear vertical alignment of the orientations in uniaxial tension, corresponding to a typical macroscopic failure in mode I. A horizontal alignment of the orientations was observed for the compression tests, even though a more diffused (compared to the more localised experimental one) cracking network was predicted by the model. Considering the complexity of the failure patterns in compression, the presented comparison of the local crack orientation vectors is a first step towards the quantification of the fracture patterns, while several open questions arise, mainly regarding the lack of a clear definition of a macro-scale crack path continuity in the numerical model.

Despite the predictive ability of the model, the strength of the material was underestimated in compression and a less realistic post-peak behaviour was reproduced. The choice to identify the material parameters in simple tension, even though allowing a first comparison between experimental and numerical results, is proven not sufficient to capture the more complex failure mechanisms occurring in compression. Moreover, an improvement of the local phenomenology should be examined, by considering for example a sliding, *i.e.*, mode II, failure mechanism (or even better a combination of mode I and mode II) and a combination of Rankine and Mohr-Coulomb localisation criterion.

While validating the numerical results and through a combination of numerical and experimental observations, the significant impact of the meso-scale heterogeneities on the local failure mechanisms was revealed. The localisation originated from the interfaces among aggregates and mortar, with the shape and location of the largest aggregates and macro-pores essentially driving the propagation of fracture patterns under simple tension, simple compression and triaxial compression. The predictive ability of the model strongly suggested that the explicit representation of these heterogeneities seems to be its key

feature.

A further insight into the impact of the meso-structure was obtained by modifying the real morphologies coming from the scans. The presence of macro-pores was shown to attract the fracture patterns under simple tension, with the location and geometry of the predicted macro-crack corresponding well to the experimental one only when the real morphology was accounted for. Under simple tension and triaxial compression, macroporosity inversely affected the macroscopic strength of the material. The role of macro-pores in the fracture patterns was less pronounced in triaxial compression compared to simple tension, yet it was shown that the interaction between aggregates and macro-pores drove the developed cracking network.

The location and shape of the heterogeneities was then studied by predicting the response of virtual morphologies with aggregates and macro-pores both modelled as spheres randomly distributed throughout the numerical specimen. It was shown that modelling the heterogeneities with an idealised shape (*i.e.*, spherical) underestimated the macroscopic strength of the material and altered the predicted failure patterns, probably due to the creation of more weak paths resulting in an emergence of less complex crack path topology. However, a limited number of artificial meso-structures were investigated, serving only as a first attempt to highlight the pronounced importance of morphology and, in turn, the value of meso-scale modelling in the prediction of the material's mechanical response.

Chapter 6

Conclusions and Perspectives

In this doctoral work, a combination of numerical and experimental techniques has highlighted the pronounced impact of the meso-scale heterogeneities of small specimens of concrete on their local failure mechanisms.

Part of the originality of this study lies in the exploration of multiple loading paths (uniaxial tension, uniaxial compression and triaxial compression) on micro-concrete samples of realistic composition (including cement, sand, aggregates and water) and in the *in-situ* nature of the experiments conducted. Based on a developed three-phase segmentation procedure, the identified morphologies coming from the intact x-rays scans were given as an input to a FE meso-model so that a direct quantitative comparison between experimental and numerical observations was possible. It has been shown that in order to accurately describe the fracturing process of concrete and obtain a fundamental understanding of its failure mechanisms, the actual material's meso-structure (composed of aggregates, mortar matrix and macro-pores) has to be taken into account.

This chapter wraps up this thesis by first presenting a summary (Section 6.1) of the main points in the order that they have been presented. Some of the future perspectives emerging as a result of this work are then discussed in Section 6.2. The chapter closes with some final conclusions in Section 6.3.

6.1 Summary

An experimental campaign was undertaken to characterise the mechanical behaviour of small concrete specimens under: uniaxial tension, uniaxial compression and triaxial compression. The particularity of the experiments conducted was that they were performed inside the x-ray scanner hosted at Laboratoire 3SR. The main advantage of such tests was that, apart from obtaining the typical macroscopic responses (in terms of force-displacement curves), the internal micro-structure of the material was scanned at several loading stages, from the intact until the failure state.

The use of x-ray tomography combined with a mechanical loading system imposed certain size constraints on the examined specimens, with cylindrical samples measuring 11 mm in diameter and 22 mm in height finally selected. The rather small sample's dimensions compared to the size of the largest heterogeneities (macro-pores reaching 1 mm and aggregates reaching 3 mm) was a compromise between satisfying the objective of directly giving a valuable insight into the impact of the mechanical and morphological properties of each phase (aggregates, macro-pores, mortar matrix), while obtaining a behaviour which was still representative of concrete.

For each loading path, a suitable experimental set-up compatible with the x-ray scanner of Laboratoire 3SR was developed, allowing the micro-concrete specimens to be scanned while they were under load. In total 8 *in-situ* experiments were performed: two uniaxial tension tests, three uniaxial compression tests and three triaxial compression tests at 5 MPa, 10 MPa and 15 MPa confining pressures. The typical asymmetrical macroscopic failures in tension and compression were observed, whereby starting both from a symmetric elastic behaviour, for compression the transition to a non-linear behaviour was obtained for a larger macroscopic stress compared to tension. Moreover, with an increasing level of confinement (from 0 to 15 MPa) the transition from brittle to ductile response was observed, as well as an increase of the strength of the material. While the specimens' size was admittedly small compared to their heterogeneities, their failure strengths were mechanically representative of the ordinary concrete from which the micro-concrete composition was derived.

The image analysis presented all over this work was performed with the open source software spam, whose main contributors are mostly in Laboratoire 3SR and with parts of it initially developed to cover the needs of this thesis. The 3D images were first analysed to quantitatively characterise the internal meso-structure. Macro-pores were easily identified due to their obvious density contrast compared to the solid phase. On the contrary, a segmentation procedure needed to be developed in order to address the principal technical challenge of separating the solid phase into aggregates and mortar matrix. The key of the proposed procedure was based on the *variation* of grey values inside each material (related to the homogeneity of the material), instead of the *absolute* grey values (related to the density of the material). From an image analysis point of view, the variance map of the grey scale image needed to be computed according to a selected structuring element. The validation of the proposed technique was based on a comparison of the same segmented set of aggregates coming from x-rays and neutron scans. Once the different phases were identified, a quantitative characterisation of the meso-structure was possible. The volume fraction of each phase, as well as the size distribution curves were some examples of the measurements made.

The series of 3D images coming from each *in-situ* experiment were then analysed as timeseries. A local DVC approach was employed by subdividing the region of interest into a set of independent correlation windows and computing a linear homogeneous deformation function evaluated at the centre of each window. To overcome the problem of unsuccessfully correlating the textureless coarse aggregates, a new procedure was proposed. A discrete correlation was performed on the coarse aggregates and the computed deformation field was afterwards merged with the regularly-spaced one. The level of uncertainty in the measured kinematic fields (both displacement and strains) was estimated through a correlation of a "repeated" scan.

The first stages of the fracturing process at the scale of the largest aggregates and macro-pores were followed and quantified through the measured displacement and the derived strain fields. In case of uniaxial tension, relative displacements inside the samples in the range of 1/5 of the voxel size (2 to 4 μm) were measured, indicating that the adopted DVC procedure was capable of capturing kinematic inhomogeneities even for such stiff and low strength specimens. Typical macro-cracks for fracture mode I were observed, crossing the cylindrical specimens roughly horizontally, formed around the aggregates, sometimes propagating through macro-pores. More complex failure modes were observed for the compression tests (confined or unconfined). A notable example was the test under

the highest level of confinement (15 MPa), where even though the experiment had to be interrupted since the limit of the forcemeter load capacity was reached, the measured kinematic fields revealed that a compaction-like shear band was created.

A FE meso-model with enhanced discontinuities was employed to numerically investigate the mechanical response of the studied material using as an input the identified morphologies coming from the intact x-rays scans. On one hand, in order to account for the explicit representation of aggregates and macro-pores, a non-adapted mesh projection was used, leading to discontinuities in the strain field (weak discontinuities), handled by a local kinematics enhancement. On the other hand, in order to account for the quasi-brittle behaviour of the material, another set of local kinematics enhancement was introduced, this time in the displacement field (strong discontinuities), accounting for micro-cracking. These two discontinuities were combined within the same Embedded Finite Element Method (E-FEM) and a simple tensile failure criterion coupled with a mode I failure mechanism were considered. The material parameters of the meso-model were selected so as to best match the macroscopic response of the first uniaxial tensile test together with a set of arbitrary choices. The predictive ability of the model was then challenged for the different morphologies and loading paths considered, without a new identification.

A systematic comparison was presented between experimental and numerical observations, in terms of macroscopic responses, displacement fields, fracturing processes and failure patterns. For the different stress paths studied, a power law was fitted in the experimental and numerical data that can be used to predict the failure criterion of concrete in the (q_{\max}, σ_m) plane. Remarkably, despite the rough parameter identification, combined with the simple behaviour law and failure mode used locally, some of the basic characteristic features of the different failure modes observed experimentally were well reproduced numerically. The typical asymmetric behaviour of concrete in tension and compression, as well as the increase of strength and ductility with the increase of confinement were sufficiently captured numerically. In simple tension, the location and geometry of the single macro-crack occurred experimentally was predicted by the meso-model, despite some differences in the kinematic boundary conditions. More complex failure patterns, such as the inclined shear band in triaxial compression under 5 MPa confinement, but also the compaction-like shear band under the 15 MPa confinement were satisfactorily reproduced by the meso-model. The model was able to capture the onset and evolution of the localisation process observed experimentally, indicating that the selected Rankine localisation criterion was suitable for mortar at low mean stress levels. A quantitative comparison of the cracking networks local orientation vectors at the end of the loading revealed a clear vertical alignment of the orientations in uniaxial tension and a horizontal alignment for the stress paths in compression. However, the real strength of the material was underestimated in compression and a more diffused (compared to the more localised experimental one) cracking network was predicted. The numerical responses exhibited a rather ductile post-peak behaviour, suggesting on one hand that the improvement of the post-peak behaviour should be a considerable future perspective and on the other hand that an identification in compression (and not in tension) might be more sufficient to capture the more complex failure mechanisms that occur under these stress paths.

Numerical and experimental observations highlighted the significant impact of the meso-scale heterogeneities on the local failure mechanisms. For the different loading paths

studied, it was shown that localisation mainly originated from the interfaces between aggregates and mortar matrix, with the shape and location of the largest aggregates and macro-pores essentially driving the propagation of the cracking network. The predictive ability of the model strongly suggested that the explicit representation of these heterogeneities seems to be the key feature that allows this predictive power. A further insight into the impact of the meso-structure was obtained by investigating virtual concrete morphologies, generated by modifying the real meso-structures coming from the scans. Under simple tension and triaxial compression macro-porosity inversely affected the macroscopic strength of the material. In simple tension, in particular, the presence of macro-pores clearly attracted the developed cracking network, demonstrating that only when the real morphology was accounted for, the location and geometry of the predicted macro-crack corresponded well to the experimental one. In the same context, considering idealised morphologies (modelling the heterogeneities as spheres) underestimated the macroscopic strength of the material under uniaxial tension, probably due to the development of a less complex crack path topology. The value and efficiency of meso-scale modelling was manifested through these illustrative examples, rendering a parametric analysis of different material properties and morphologies a promising future perspective to further evaluate the presented observations and to obtain a meaningful statistical result.

6.2 Perspectives

A number of perspectives come as a result of this work, some of which are discussed in the following.

6.2.1 Elastic properties identification based on experimental kinematic fields

Despite the direct comparison between numerical and experimental observations presented in Chapter 5, the possibilities provided by the experimental kinematic fields have been explored only to a certain depth during this thesis. It should be recalled that the material parameters of the meso-model are selected so as to best match the macroscopic response of the first uniaxial tensile experiment, based on simple arbitrary choices. As an alternative to this approach and in order to reduce the number of arbitrary choices, the identification of the elastic material parameters can be done based on the experimental kinematic fields. Over the years, different identification methods based on kinematics measurements have been developed, such as the virtual fields method [Grédiac, 1989], the equilibrium gap method [Claire *et al.*, 2004] or the Finite Element Updating (FEMU) method [Kavanagh et Clough, 1971]. In the following, a first attempt towards exploring the possibilities that the latter method brings in this study is made.

Very briefly, the FEMU method consists in updating the parameters of a FE model in order to minimise the difference between measured and simulated fields. Herein, FEMU is based on the minimisation of the discrepancy between the displacement field as measured by the DVC procedure and as predicted by the meso-model for every nodal position of the mesh. The displacement boundary conditions extracted from the experimental field are prescribed in the numerical simulations and the minimisation is based on a set of trial values of material parameters.

It should be mentioned, however, that in the presented case there is a fundamental difference in the kinematic hypotheses between experimental and numerical displacement

fields. The former is evaluated in a cubic structured grid, with a point spacing of 0.4 mm, whereby no continuity is imposed in the sought displacements between the separate correlation windows, while the latter is evaluated in a 4-noded tetrahedral mesh, with the average distance between the nodes of each tetrahedron set to 0.1 mm.

Local DVC

As a first attempt to evaluate the displacement discrepancy between the two fields, an interpolation of the coarser discontinuous (between adjacent correlation windows) experimental field to the nodes of the finer tetrahedral FE mesh is made. An illustration on a 6 mm^3 cube extracted from the reference scan of the third uniaxial compression test is given. Following the non-adapted meshing technique (see Section 4.2), this morphology is projected onto a 6 mm^3 cubical unstructured tetrahedral mesh consisted of 2×10^6 4-noded tetrahedra elements and 386×10^3 degrees of freedom, with the characteristic length of each tetrahedron set to 0.1 mm. Elements that after the morphological projection are identified as aggregates or macro-pores are shown in Fig. 6.1 on the left. Again, for the subsequent simulations, macro-pores (red colour in Fig. 6.1) are finally removed from the FE mesh. The principal idea of focusing on this cropped realistic morphology is the attempt to identify the elastic properties of aggregates and mortar matrix in a subvolume where the largest heterogeneities have a direct impact on the displacement incompatibilities.

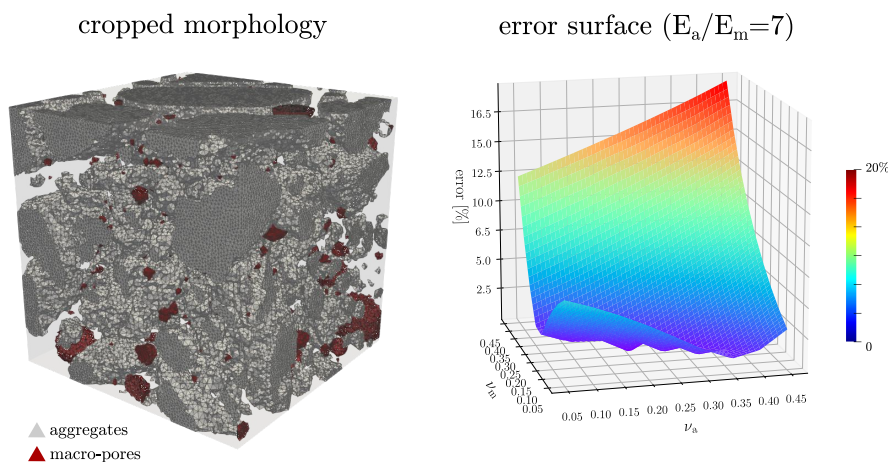


Figure 6.1: Elastic properties identification in a cropped cube based on a synthetic case using a numerical displacement field (uniaxial compression) as reference

As a first step, a synthetic case is studied. An arbitrary set of elastic material parameters is assigned to each phase and a *reference* compressive elastic computation is performed along the vertical axis of the cube (corresponding to the axis of the original cylindrical sample), while the remaining four faces in the perpendicular directions are stress-free. The displacement field coming from this computation is considered the *reference* one, replacing thus for this synthetic case the experimental field. A number of elastic simulations follow with trial values of elastic material parameters, while the boundary conditions are kept the same as per the reference simulation. For each of these computations the difference between the reference displacement field and the one predicted based on the trial parameters is calculated. This difference corresponds to the displacement residual

field, *i.e.*, $R(\alpha)$ and is computed for every displacement component, u_i , of each node, n , of the mesh:

$$R(\alpha_j, i) = \|u_i^{\text{FEref}} - u_i^{\text{FE}\alpha_j}\| \quad (6.1)$$

where α_j is the set of the trial elastic material parameters of each phase that needs to be identified: E_a , ν_a and E_m , ν_m . Since only the relative stiffness of the two phases affects the inhomogeneity of the displacements, the residual field coming from this parametric analysis can be visualised in a 3D space, as a function of: E_a/E_m , ν_a and ν_m . For a quantitative interpretation of the residual, the global error is computed as the arithmetic mean of the relative error of each component of the displacement residual over all the nodes:

$$\text{error}(\alpha_j, i) = \frac{1}{N} \sum_{n=1}^N \frac{\|u_i^{\text{FEref}} - u_i^{\text{FE}\alpha_j}\|}{u_i^{\text{FEref}}} \quad (6.2)$$

The error function can then be evaluated and plotted in the parameter space. As an illustration, Fig. 6.1 shows the interpolated magnitude error surface for a trial constant stiffness ratio $E_a/E_m = 7$ as a function of trial Poisson ratio values of each phase. The shape of this curve indicates that a global minimum exists and through the minimisation of the interpolated error function, the retrieval of the reference set of elastic parameters is obtained.

As a following step, for the same cropped morphology, the measured experimental displacement field coming from the correlation of the first step of the C-03 test is considered. After subtracting the rigid-body motion, the experimental field is smoothed with a 3D median filter of 2 voxels radius in order to avoid introducing non-physical damage in the FE simulations. This resultant field is then cropped to the corresponding subvolume and a trilinear interpolation to the nodes of the 6 mm³ cubical FE mesh follows, as shown on the top row of Fig. 6.2 on the right. This interpolated field is the reference experimental field to which the numerical one should match. The boundary displacements of this field are the prescribed displacement boundary conditions of the elastic FE computations that follow.

As above, for each trial set of elastic parameters, every nodal position and each displacement component, the displacement residual is calculated as:

$$R(\alpha_j, i) = \|u_i^{\text{DVC}} - u_i^{\text{FE}\alpha_j}\| \quad (6.3)$$

The magnitude of the residual displacement field estimated for the whole region of interest is shown on the bottom row on the left of Fig. 6.2 for the trial elastic material parameters that correspond to the ones identified from simple tension (see Table 4.1). Again as an illustration, for a constant stiffness ratio $E_a/E_m = 7$ the interpolated magnitude error surface in the parameter space is depicted on the bottom right of Fig. 6.2. It can be seen that, as opposed to the synthetic case above, the interpolated error function is rather smooth. This time, the minimisation of the global error function does not lead to a unique optimal set of parameters.

A possible explanation comes from the fact that the displacement residual, as defined in Eq. (6.3) (and also in Eq. (6.1)) does not account for the noise and error inherent in the experimental field, meaning that all nodes are equally weighted for the minimisation. However, it is worth recalling (see Chapter 3) that the uncertainty of the experimental field is spatially varying, attributed to the fact that the texture is not uniform. A future work

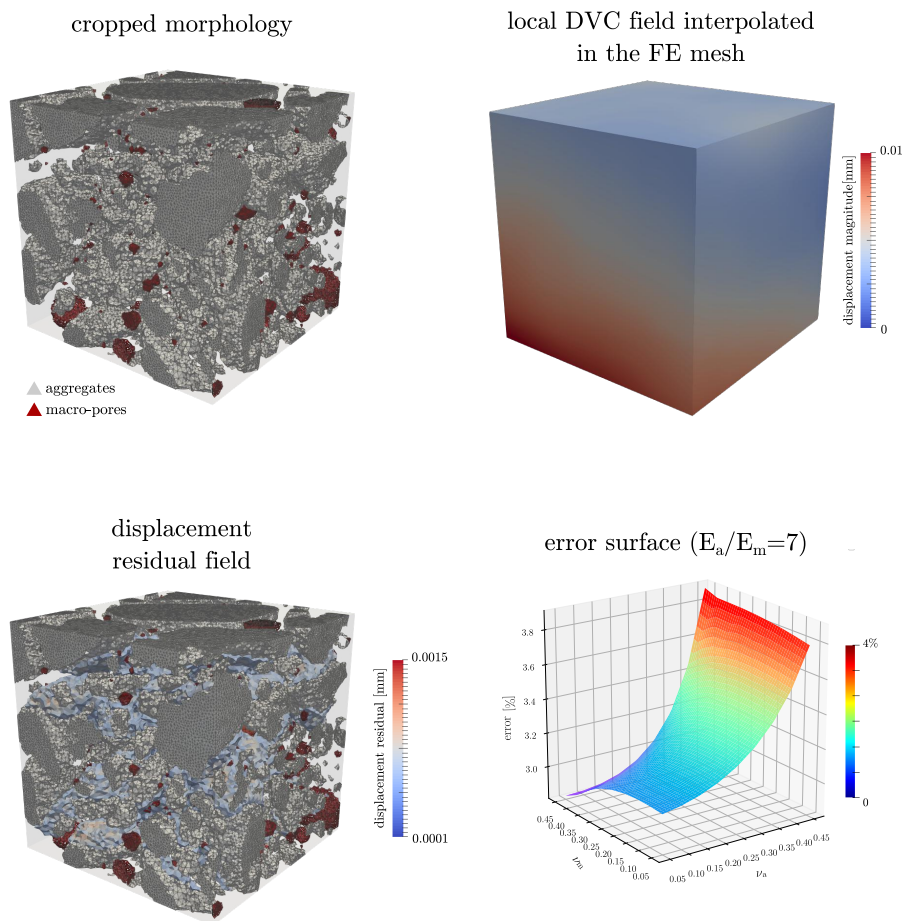


Figure 6.2: Elastic properties identification in a cropped cube coming from the C-03 test based on a local DVC approach

should point towards a minimisation based on a weighted residual functional, so that zones associated with high uncertainty are not considered in the identification. Moreover, it is possible that the spatial resolution of the experimental displacement field, especially after the filtering, may not be fine enough to allow the distinction between the different phases of the material. Future work should focus on a quantitative analysis of the filtering of the local DVC field and its interpolation to the FE mesh by creating for instance synthetic images of simplified morphologies affected by random noise and subjected to artificial transformations.

Global DVC

A different strategy that can be a very promising future perspective and is a work in progress, is to proceed into a global DVC approach [Besnard *et al.*, 2006, Hild et Roux, 2012]. Unlike the local approach, the global one imposes a continuity on the sought displacement field between elements. The measured field is then consistent with a FE simulation, since the same kinematic descriptions both for the experimental and the numerical field can be chosen. It is worth mentioning that the FE shape functions are only used as a convenient way to regularise the sought displacement field, with no mechanical modelling (constitutive law for example) involved at this stage.

The global DVC approach as implemented in `spam` discretises the region of interest

with 4-noded tetrahedral elements, so that in the present case the sought experimental displacement field is interpolated with the same linear tetrahedron shape functions as the numerical one. The global correlation approach consists in solving for the nodal displacements that minimise a weak form of the greylevel conservation law (see Eq. (3.2)). Please note that details on the formulation and implementation of the global DVC technique in `spam` is out of the scope of this perspectives section. It should be mentioned, however, that the adopted formulation leads again to an incremental solution of a linear system, similar to the one described by Eq. (3.8), for small displacement increments.

As per the local DVC formulation, there is a trade-off between the measurement uncertainty and the smallest possible characteristic length of the tetrahedral elements. Again, below a certain element size, high measurement uncertainties can dominate the signal, however, this time any displacement measurement is no longer possible (the solution of the linear system does not exist) [Leclerc *et al.*, 2011]. As a future perspective, a sensitivity analysis of the uncertainty level as a function of the characteristic element size should be considered, in the style of what presented for the local approach (see Section 3.2.3).

An example of a potential use of global DVC for the elastic properties identification is given for the first pair of images coming from the second uniaxial compression test. A cuboid ($19.5\text{ mm}^3 \times 7.5\text{ mm}^3 \times 7.5\text{ mm}^3$) is cropped inside this pair of images so as to perform the global DVC computation. The central greyscale vertical slice of the reference cuboid is shown on the top left of Fig. 6.3. The smallest possible characteristic length of each tetrahedron is 30 voxels (*i.e.*, 0.4 mm), which discretises the region of interest with 76×10^3 4-noded tetrahedra elements and 15×10^3 degrees of freedom. Similarly to the local approach, the deformation function that accounts for the registration between the two images (see Section 3.2.1) is passed as an initial guess to each node of the mesh. Considering that this time a continuity is imposed between the nodal displacements, nodes that happen to fall inside the textureless coarse aggregates prevent the convergence of the iterative global correlation algorithm. For this reason, the displacements already measured through the discrete DVC approach (see Section 3.2.2) are prescribed to each of these nodes, meaning that they are excluded from the vector containing the degrees of freedom of the linear system.

The iterative scheme of the global correlation converges to a solution, which after the subtraction of the rigid-body motion is set as the reference experimental displacement field. The central vertical slice of the measured axial displacement field is shown on the top row of Fig. 6.3 on the right. For the FE simulations to be performed, the morphology of the reference cropped cuboid is projected onto the same unstructured FE mesh which has been used for the global correlation. As depicted on the top row of Fig. 6.3 on the left, due to the larger element size, the discretisation is coarse and thus the morphological representation of the meso-structure is less good. The boundary displacements measured through the global correlation are used as the prescribed displacement boundary conditions and a number of elastic FE computations with trial material parameters follows. For every trial set of parameters, the displacement residual field is calculated based on Eq. (6.3), still without considering a weighted functional.

For the elastic material parameters of Table 4.1, the central vertical slice of the computed axial displacement field is shown on the top right of Fig. 6.3. For the same set of parameters, the central vertical slice of the axial displacement residual field is shown on the bottom left of Fig. 6.3. It can be seen that the measured and calculated axial displacement fields are very close. Again as an illustration, the interpolated global error magnitude is shown for a trial constant stiffness ratio $E_a/E_m = 7$ as a function of trial

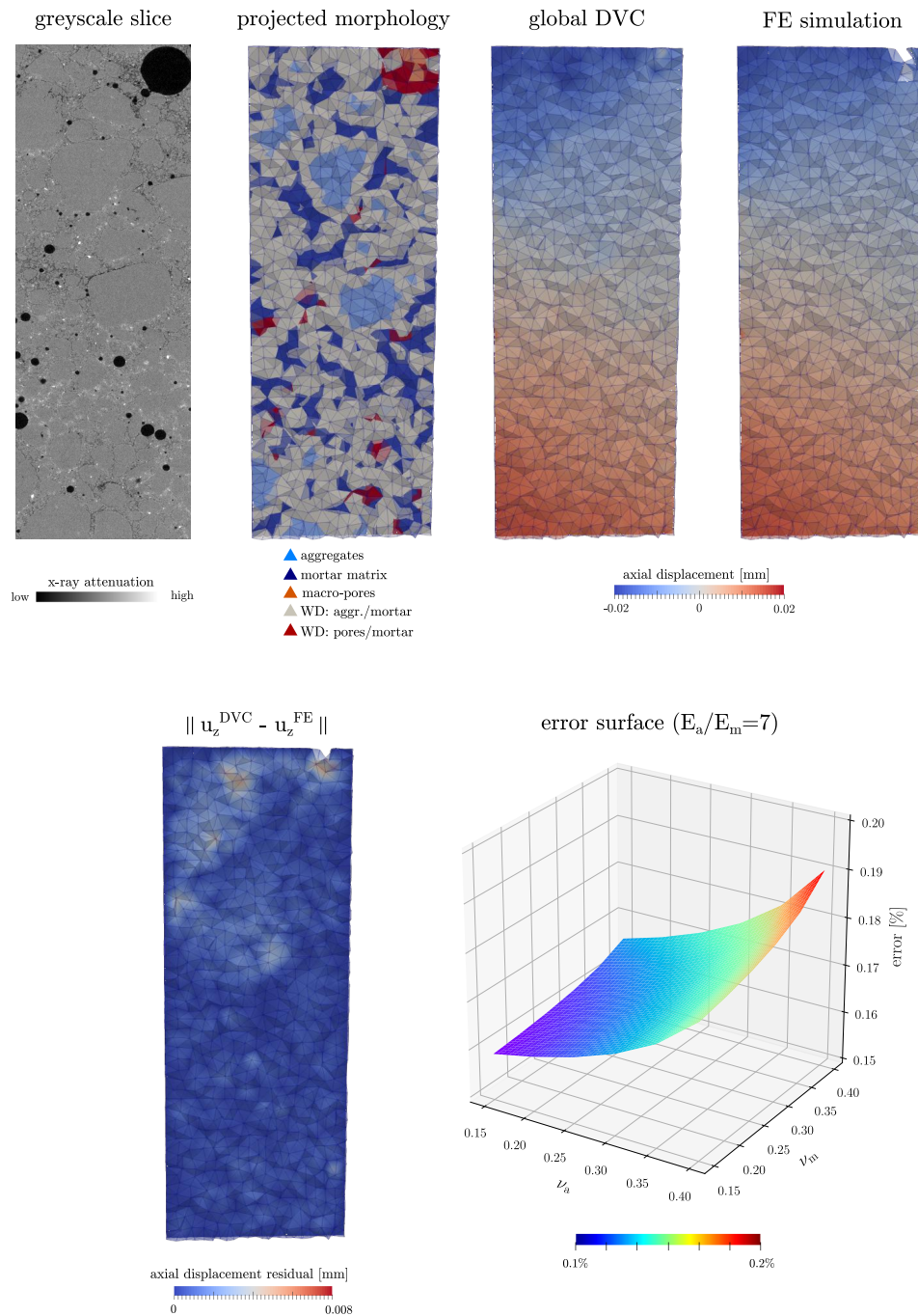


Figure 6.3: Elastic properties identification on the C-02 test based on a global DVC approach

Poisson ratio values of each phase (see bottom right of Fig. 6.3). Even though both fields are evaluated at the same FE mesh and their difference is small, the minimisation of the interpolated error function, again, does not lead to a unique set of solution. For the case studied, the noise inherent in the experimental data and the spatial resolution of the sought displacement field render the identification of the elastic material parameters a non-trivial problem.

To sum up this section regarding the elastic material properties identification, there are several weak points of the presented approaches which require further improvements. For the experimental fields, the first load step of the *in-situ* experiments is considered, while assuming that the behaviour of the material remains elastic. This means that the relative displacements inside the specimen are of a low magnitude, which in turn results in a higher noise level in the experimental data. Focusing particularly on global DVC, necessary future steps should be a quantitative study of the measurement uncertainties and a minimisation based on a weighted functional by taking into account the covariance matrix of the displacement measurements, in the style of [Besnard *et al.*, 2006, Leclerc *et al.*, 2011]. Moreover, a careful implementation of the prescribed displacements for the nodes falling inside coarse aggregates should be considered by using, for instance, Lagrange multipliers as additional constraints.

Furthermore, one of the limitations of the presented global DVC example is the restriction to a coarse FE mesh, due to the noise sensitivity. However, a complex heterogeneous kinematic field requires a fine discretisation in order to be accurately described and the fact that no unique set of solution could be found in the previous example, may well come from the spatial resolution of the displacement field which is not fine enough to capture displacement incompatibilities between the phases. A future perspective to overcome the well-known compromise between spatial resolution and uncertainty can be to introduce a mechanical regularisation in the sought displacement field, performed in a fully integrated way and known as integrated DVC [Hild et Roux, 2006]. Instead of measuring experimentally the kinematic field and successively performing an identification procedure, a direct coupling with mechanical simulations can be used to regularise the correlation procedure. A combination of the correlation and mechanical residuals allows for very fine meshes to be used, with the advantage of obtaining mechanically admissible solutions.

A promising line of development towards the same direction is the enrichment of the displacement interpolation functions with discontinuities. Enriched kinematics following the X-FEM approaches have been used for example to validate X-FEM simulations against measured displacement fields by comparing measured and predicted profiles of stress intensity factors [Rannou *et al.*, 2010, Réthoré *et al.*, 2011]. In the presented case, the strong discontinuities introduced in the meso-model in the context of the E-FEM can be considered to enhance the global DVC kinematic basis in order to account for the presence of the cracks that appear during the mechanical tests.

As a general remark, the direction that certainly deserves to be explored is the direct coupling between the FE meso-model and the full-field kinematics measurements, overcoming the limitations of each individual method, with the objective to gain a fundamental understanding of the mechanical response of the studied material.

6.2.2 Numerical meso-model

Parametric analysis

The numerical results presented in this work, directly compared to corresponding experiments, strongly suggest that the explicit representation of the meso-structure is the key feature of the meso-model that allows its predictive power. This predictive ability highlights the value of the meso-scale modelling, as well as suggests interesting future applications. The examples of virtual concrete morphologies presented in the last part of Chapter 5 explored some of these possibilities.

More specifically, the example application based on the spherical heterogeneities has revealed interesting results regarding the response of a realistic morphology as opposed to an idealised one that are certainly worth enriching and exploring further. However, it should be recalled that, due to the sphere packing algorithm used, the initial volume of the heterogeneities needed to be reduced in order to avoid overlapping. A future study considering an isotropic compression step in the style of DEM simulations could initialise the positions of the spherical particles, while preserving their original volume.

Meanwhile, for different loading paths (not necessarily only the ones studied in this work) and through a parametric analysis of different morphologies and material properties, valuable information about the quantitative and qualitative influence of each phase on the global response can be obtained. In the same context, provided that in reality the material properties are not constant for a given phase, inserting spatial discrepancy in the material properties of each phase could be also a promising line of development. Empowered by the value and efficiency of meso-scale modelling, a future work towards a parametric analysis should involve a large number of numerical concrete samples in order to provide a meaningful statistical result. In the engineering context, such a statistical result can provide quantitative recommendations for improving the strength and ductility of the material, leading to a better design of concrete mixtures.

It is worth mentioning here that despite the predictive ability of the meso-model and its potential applications, there is certainly some room for improvement. Considering the fact that the primary objective of this study was to focus on the role of the underlying morphology, the identification of the material parameters in simple tension coupled with a set of arbitrary choices has been a legitimate choice for a meso-model, allowing a first comparison between experimental and numerical results. However, it has been shown that the strength of the material was underestimated in compression and a ductile post-peak response was predicted. Therefore, a future work that focuses on an identification of all the material parameters (including the fracture energy) in compression rather than in tension should be considered. The previous discussion concerning the elastic properties identification through the kinematic fields supplements well the necessity of further exploring the choice of the material parameters used in the meso-model.

Phenomenological enrichment

Concentrating now on the local phenomenology considered, it should be reminded that following the general spirit of simplicity in meso-scale modelling, a Rankine criterion and a brittle softening behaviour law was used. For each phase of the morphology only two failure parameters were required: the fracture energy and the tensile strength. The choice, however, of using this rather simple criterion combined with a mode I opening came at a cost. A less realistic post-peak response was observed principally for the compression tests (confined or unconfined), with a rather diffused and not localised cracking network.

As already discussed, such a behaviour indicates the limitation of the current formulation to capture displacement incompatibilities that yield shear loadings. The Ph.D. theses of Paul Hausseux [Hausseux, 2015] and Alexis Vallade [Vallade, 2016b] focused on addressing this issue, achieving to implement in the presented meso-model a Mohr-Coulomb failure criterion coupled with a mode II sliding mechanism. Retaining the light local framework, the associated failure parameters for each phase are the fracture energy (in mode II), the cohesion and the friction angle. In the ongoing Ph.D. thesis of Alejandro Ortega the combination of a Mohr-Coulomb failure criterion coupled with a mode II frictional sliding has been applied to the micro-concrete specimens studied herein.

As an illustration, Fig. 6.4 depicts the predicted cracking network by the end of the loading for the test under the highest level of confinement (15 MPa) both for a mode I and mode II failure mechanisms. For the sake of comparison, the experimental crack extracted from the correlation residual of the last pair of x-ray images is also shown in Fig. 6.4 on the left. A promising result is depicted, since a sliding criterion yields, indeed, a more localised cracking network.

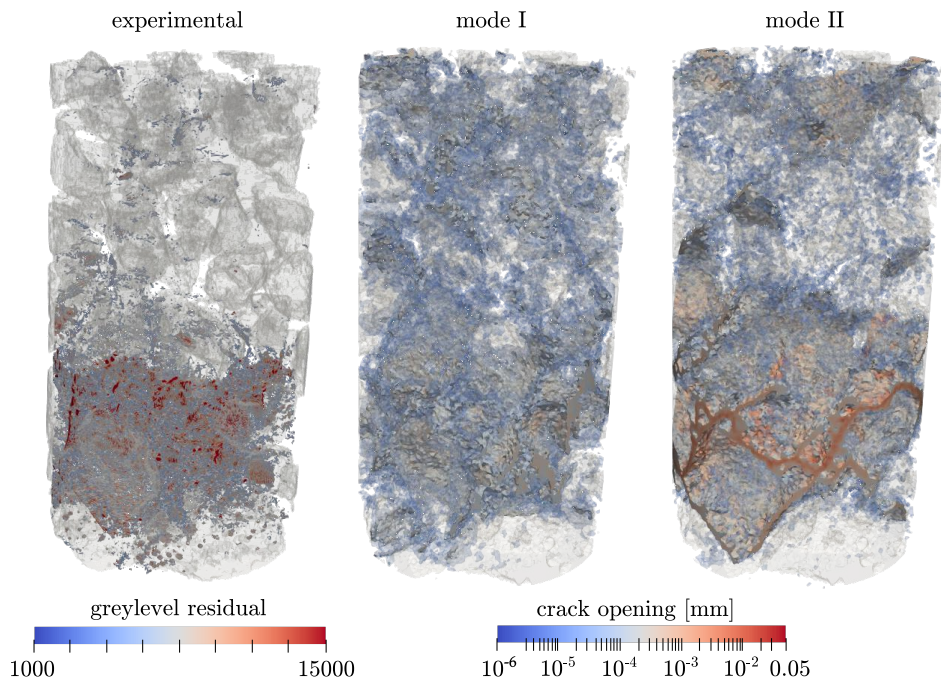


Figure 6.4: Comparison of crack patterns at the end of the loading for the triaxial test under the highest confining pressure (15 MPa). On the left the experimental crack, on the middle the numerical crack patterns with a local mode I opening mechanism (considered in this study) and on the right the numerical crack patterns with a local mode II sliding mechanism

Meanwhile, in her recent Ph.D. work, Yue Sun has implemented in the existing formulation a crack closure mechanism both for mode I and mode II failure modes. The implementation of the crack closure mechanism is formulated within an empirical consideration, without requiring any additional parameters. According to this work, crack closure leads to a more localised crack pattern, however, only simple synthetic morphologies were tested. It would be interesting, thus, to evaluate the effect of crack closure on the realistic morphologies considered in the present study.

To summarise, a future consideration of a mixed-mode local failure mechanism combined with a crack closure mechanism can be a particularly promising phenomenological enrichment of the meso-model.

6.3 Conclusions

This thesis has presented a continuous dialogue between experiments and modelling from specimen preparation and morphological modelling based on the real meso-structure to comparison of experimental and numerical local crack orientation vectors, allowing a systematic investigation of the impact of the meso-scale heterogeneities on the fracturing process of concrete. It was shown that the shape and location of the largest aggregates and macro-pores essentially drive the fracture patterns under simple tension, simple compression and triaxial compression. In order to accurately describe the fracturing process and obtain a fundamental understanding of the failure mechanisms, the actual material's meso-structure has to be taken into account. Despite the significant progress made over the years, the investigation of the failure mechanisms of concrete is a long standing scientific challenge that still remains widely open. Hopefully the contribution of this thesis is a step towards understanding these complex fracturing process phenomena.

Bibliography

- [Alikarami *et al.*, 2015] ALIKARAMI, R., ANDÒ, E., GKIOUSAS-KAPNISIS, M., TORABI, A. et VIGGIANI, G. (2015). Strain localisation and grain breakage in sand under shearing at high mean stress: insights from in situ x-ray tomography. *Acta Geotechnica*, 10(1):15–30.
- [Andò *et al.*, 2012] ANDÒ, E., HALL, S. A., VIGGIANI, G., DESRUES, J. et BÉSUELLE, P. (2012). Experimental micromechanics: grain-scale observation of sand deformation. *Géotechnique Letters*, 2(3):107–112.
- [Ashby, 2012] ASHBY, M. F. (2012). *Materials and the environment: eco-informed material choice*. Elsevier.
- [ASTM, 2003] ASTM (2003). Standard test method for obtaining and testing drilled cores and sawed beams of concrete.
- [Azevedo *et al.*, 2008] AZEVEDO, N. M., LEMOS, J. et de ALMEIDA, J. R. (2008). Influence of aggregate deformation and contact behaviour on discrete particle modelling of fracture of concrete. *Engineering Fracture Mechanics*, 75(6):1569–1586.
- [Barenblatt, 1962] BARENBLATT, G. I. (1962). The mathematical theory of equilibrium cracks in brittle fracture. In *Advances in applied mechanics*, volume 7, pages 55–129. Elsevier.
- [Baruchel *et al.*, 2000] BARUCHEL, J., BUFFIERE, J.-Y. et MAIRE, E. (2000). X-ray tomography in material science.
- [Basheer *et al.*, 2005] BASHEER, L., BASHEER, P. et LONG, A. (2005). Influence of coarse aggregate on the permeation, durability and the microstructure characteristics of ordinary portland cement concrete. *Construction and Building Materials*, 19(9):682–690.
- [Bay *et al.*, 1999] BAY, B. K., SMITH, T. S., FYHRIE, D. P. et SAAD, M. (1999). Digital volume correlation: three-dimensional strain mapping using x-ray tomography. *Experimental mechanics*, 39(3):217–226.
- [Bažant et Belytschko, 1985] BAŽANT, Z. P. et BELYTSCHKO, T. B. (1985). Wave propagation in a strain-softening bar: exact solution. *Journal of Engineering Mechanics*, 111(3):381–389.
- [Bažant *et al.*, 1990] BAŽANT, Z. P., TABBARA, M. R., KAZEMI, M. T. et PIJAUDIER-CABOT, G. (1990). Random particle model for fracture of aggregate or fiber composites. *Journal of engineering mechanics*, 116(8):1686–1705.

- [Beare et Lehmann, 2006] BEARE, R. et LEHMANN, G. (2006). The watershed transform in itk-discussion and new developments. *The Insight Journal*, 1:1–24.
- [Benkemoun et al., 2010] BENKEMOUN, N., HAUTEFEUILLE, M., COLLIAT, J.-B. et IBRAHIMBEGOVIC, A. (2010). Failure of heterogeneous materials: 3d meso-scale fe models with embedded discontinuities. *International Journal for Numerical Methods in Engineering*, 82(13):1671–1688.
- [Besnard et al., 2006] BESNARD, G., HILD, F. et ROUX, S. (2006). “Finite-Element” Displacement Fields Analysis from Digital Images: Application to Portevin–Le Châtelier Bands. *Experimental Mechanics*.
- [Bezrukov et al., 2002] BEZRUKOV, A., BARGIEL, M. et STOYAN, D. (2002). Statistical analysis of simulated random packings of spheres. *Particle & Particle Systems Characterization: Measurement and Description of Particle Properties and Behavior in Powders and Other Disperse Systems*, 19(2):111–118.
- [Bornert et al., 2009] BORNERT, M., BRÉMAND, F., DOUMALIN, P., DUPRÉ, J.-C., FAZZINI, M., GRÉDIAC, M., HILD, F., MISTOU, S., MOLIMARD, J., ORTEU, J.-J. et al. (2009). Assessment of digital image correlation measurement errors: methodology and results. *Experimental mechanics*, 49(3):353–370.
- [Bradski, 2000] BRADSKI, G. (2000). The OpenCV Library. *Dr. Dobb’s Journal of Software Tools*.
- [Brisard et al., 2020] BRISARD, S., SERDAR, M. et MONTEIRO, P. J. (2020). Multiscale x-ray tomography of cementitious materials: A review. *Cement and Concrete Research*, 128:105824.
- [BSI, 2004] BSI (2004). Bs en 1992-1-1: 2004+ a1: 2014: Eurocode 2: Design of concrete structures. general rules and rules for buildings.
- [Buljac et al., 2018] BULJAC, A., JAILIN, C., MENDOZA, A., NEGGERS, J., TAILLANDIER-THOMAS, T., BOUTERF, A., SMANIOTTO, B., HILD, F. et ROUX, S. (2018). Digital volume correlation: review of progress and challenges. *Experimental Mechanics*, 58(5):661–708.
- [Burlion et al., 2006] BURLION, N., BERNARD, D. et CHEN, D. (2006). X-ray microtomography: application to microstructure analysis of a cementitious material during leaching process. *Cement and Concrete Research*, 36(2):346–357.
- [Bushberg et Boone, 2011] BUSHBERG, J. T. et BOONE, J. M. (2011). *The essential physics of medical imaging*. Lippincott Williams & Wilkins.
- [Chateau et al., 2018] CHATEAU, C., NGUYEN, T. T., BORNERT, M. et YVONNET, J. (2018). Dvc-based image subtraction to detect microcracking in lightweight concrete. *Strain*, 54(5):e12276.
- [Claire et al., 2004] CLAIRE, D., HILD, F. et ROUX, S. (2004). A finite element formulation to identify damage fields: the equilibrium gap method. *International journal for numerical methods in engineering*, 61(2):189–208.

- [Cnudde *et al.*, 2009] CNUDDE, V., CWIRZEN, A., MASSCHAELE, B. et JACOBS, P. (2009). Porosity and microstructure characterization of building stones and concretes. *Engineering geology*, 103(3-4):76–83.
- [Dautriat *et al.*, 2011] DAUTRIAT, J., BORNERT, M., GLAND, N., DIMANOV, A. et RAPHANEL, J. (2011). Localized deformation induced by heterogeneities in porous carbonate analysed by multi-scale digital image correlation. *Tectonophysics*, 503(1-2):100–116.
- [Davis et Elliott, 2006] DAVIS, G. et ELLIOTT, J. (2006). Artefacts in x-ray microtomography of materials. *Materials science and technology*, 22(9):1011–1018.
- [Doumalin et Bornert, 2000] DOUMALIN, P. et BORNERT, M. (2000). Micromechanical applications of digital image correlation techniques. In *Interferometry in Speckle Light*, pages 67–74. Springer.
- [Dupray *et al.*, 2009] DUPRAY, F., MALECOT, Y., DAUDEVILLE, L. et BUZAUD, E. (2009). A mesoscopic model for the behaviour of concrete under high confinement. *International Journal for Numerical and Analytical Methods in Geomechanics*, 33(11):1407–1423.
- [Dvorkin *et al.*, 1990] DVORKIN, E. N., CUITIÑO, A. M. et GIOIA, G. (1990). Finite elements with displacement interpolated embedded localization lines insensitive to mesh size and distortions. *International journal for numerical methods in engineering*, 30(3):541–564.
- [Feldkamp *et al.*, 1984] FELDKAMP, L. A., DAVIS, L. C. et KRESS, J. W. (1984). Practical cone-beam algorithm. *J. Opt. Soc. Am. A*, 1(6):612–619.
- [Gabet, 2006] GABET, T. (2006). *Comportement triaxial du béton sous fortes contraintes: Influence du trajet de chargement*. Thèse de doctorat.
- [Gabet *et al.*, 2008] GABET, T., MALÉCOT, Y. et DAUDEVILLE, L. (2008). Triaxial behaviour of concrete under high stresses: Influence of the loading path on compaction and limit states. *Cement and Concrete Research*, 38(3):403–412.
- [Gallucci *et al.*, 2007] GALLUCCI, E., SCRIVENER, K., GROSO, A., STAMPANONI, M. et MARGARITONDO, G. (2007). 3d experimental investigation of the microstructure of cement pastes using synchrotron x-ray microtomography (μ ct). *Cement and Concrete Research*, 37(3):360–368.
- [Garboczi et Bentz, 1993] GARBOCZI, E. et BENTZ, D. (1993). Computational materials science of cement-based materials. *MRS Bulletin*, 18(3):50–54.
- [Garboczi, 2002] GARBOCZI, E. J. (2002). Three-dimensional mathematical analysis of particle shape using x-ray tomography and spherical harmonics: Application to aggregates used in concrete. *Cement and concrete research*, 32(10):1621–1638.
- [Geuzaine et Remacle, 2009] GEUZAINÉ, C. et REMACLE, J.-F. (2009). Gmsh: A 3-d finite element mesh generator with built-in pre-and post-processing facilities. *International journal for numerical methods in engineering*, 79(11):1309–1331.

- [Grédiac, 1989] GRÉDIAC, M. (1989). Principe des travaux virtuels et identification. *Comptes rendus de l'Académie des sciences. Série 2, Mécanique, Physique, Chimie, Sciences de l'univers, Sciences de la Terre*, 309(1):1–5.
- [Grédiac et Hild, 2013] GRÉDIAC, M. et HILD, F. (2013). *Full-field measurements and identification in solid mechanics*. Wiley Online Library.
- [Häfner et al., 2006] HÄFNER, S., ECKARDT, S., LUTHER, T. et KÖNKE, C. (2006). Mesoscale modeling of concrete: Geometry and numerics. *Computers & structures*, 84(7):450–461.
- [Hall et al., 2010] HALL, S., BORNERT, M., DESRUES, J., PANNIER, Y., LENOIR, N., VIGGIANI, G. et BÉSUELLE, P. (2010). Discrete and continuum experimental study of localised deformation in hostun sand under triaxial compression using x-ray ct and 3d digital image correlation. *Géotechnique*, 60(5):315–322.
- [Hauseux, 2015] HAUSEUX, P. (2015). *Propagation d'incertitudes paramétriques dans les modèles numériques en mécanique non linéaire: applications à des problèmes d'excavation*. Thèse de doctorat, Lille 1.
- [Hautefeuille et al., 2009] HAUTEFEUILLE, M., MELNYK, S., COLLIAT, J.-B. et IBRAHIM-BEGOVIC, A. (2009). Failure model for heterogeneous structures using structured meshes and accounting for probability aspects. *Engineering Computations*, 26(1/2):166–184.
- [Helfen et al., 2007] HELFEN, L., MYAGOTIN, A., RACK, A., PERNOT, P., MIKULÍK, P., DI MICHIEL, M. et BAUMBACH, T. (2007). Synchrotron-radiation computed laminography for high-resolution three-dimensional imaging of flat devices. *physica status solidi (a)*, 204(8):2760–2765.
- [Hild et Roux, 2006] HILD, F. et ROUX, S. (2006). Digital image correlation: from displacement measurement to identification of elastic properties—a review. *Strain*, 42(2):69–80.
- [Hild et Roux, 2012] HILD, F. et ROUX, S. (2012). Comparison of local and global approaches to digital image correlation. *Experimental Mechanics*, 52(9):1503–1519.
- [Hild et al., 2013] HILD, F., ROUX, S., BERNARD, D., HAUSS, G. et REBAI, M. (2013). On the use of 3d images and 3d displacement measurements for the analysis of damage mechanisms in concrete-like materials.
- [Hillerborg, 1991] HILLERBORG, A. (1991). Application of the fictitious crack model to different types of materials. *In Current Trends in Concrete Fracture Research*, pages 95–102. Springer.
- [Hinks, 1921] HINKS, A. (1921). Map projections, 2nd edit. *Cambridge, England*, page 29.
- [Hsieh et al., 2009] HSIEH, J. et al. (2009). *Computed tomography: principles, design, artifacts, and recent advances*. SPIE Bellingham, WA.
- [Huang et al., 2015] HUANG, Y., YANG, Z., REN, W., LIU, G. et ZHANG, C. (2015). 3d meso-scale fracture modelling and validation of concrete based on in-situ x-ray computed tomography images using damage plasticity model. *International Journal of Solids and Structures*, 67:340–352.

- [Huet, 1993] HUET, C. (1993). An integrated approach of concrete micromechanics. *Micromechanics of concrete and cementitious composites*, Presses Polytechniques et Universitaires Romandes, Lausanne, pages 117–146.
- [Hurley et Pagan, 2019] HURLEY, R. et PAGAN, D. (2019). An in-situ study of stress evolution and fracture growth during compression of concrete. *International Journal of Solids and Structures*, 168:26–40.
- [Ibrahimbegovic et Melnyk, 2007] IBRAHIMBEGOVIC, A. et MELNYK, S. (2007). Embedded discontinuity finite element method for modeling of localized failure in heterogeneous materials with structured mesh: an alternative to extended finite element method. *Computational Mechanics*, 40(1):149–155.
- [Ioannidou et al., 2014] IOANNIDOU, K., PELLENQ, R. J.-M. et DEL GADO, E. (2014). Controlling local packing and growth in calcium–silicate–hydrate gels. *Soft Matter*, 10(8):1121–1133.
- [Jaquet et al., 2013] JAQUET, C., ANDÓ, E., VIGGIANI, G. et TALBOT, H. (2013). Estimation of separating planes between touching 3d objects using power watershed. In *International Symposium on Mathematical Morphology and Its Applications to Signal and Image Processing*, pages 452–463. Springer.
- [Kang et Willam, 1999] KANG, H. D. et WILLAM, K. J. (1999). Localization characteristics of triaxial concrete model. *Journal of engineering mechanics*, 125(8):941–950.
- [Kavanagh et Clough, 1971] KAVANAGH, K. T. et CLOUGH, R. W. (1971). Finite element applications in the characterization of elastic solids. *International Journal of Solids and Structures*, 7(1):11–23.
- [Ketcham et Carlson, 2001] KETCHAM, R. A. et CARLSON, W. D. (2001). Acquisition, optimization and interpretation of x-ray computed tomographic imagery: applications to the geosciences. *Computers & Geosciences*, 27(4):381–400.
- [Kim et Al-Rub, 2011] KIM, S.-M. et AL-RUB, R. K. A. (2011). Meso-scale computational modeling of the plastic-damage response of cementitious composites. *Cement and Concrete Research*, 41(3):339–358.
- [Landis et al., 1999] LANDIS, E. N., NAGY, E. N., KEANE, D. T. et NAGY, G. (1999). Technique to measure 3d work-of-fracture of concrete in compression. *Journal of engineering mechanics*, 125(6):599–605.
- [Landis et al., 2007] LANDIS, E. N., ZHANG, T., NAGY, E. N., NAGY, G. et FRANKLIN, W. R. (2007). Cracking, damage and fracture in four dimensions. *Materials and Structures*, 40(4):357–364.
- [Leclerc et al., 2011] LECLERC, H., PÉRIÉ, J.-N., ROUX, S. et HILD, F. (2011). Voxel-scale digital volume correlation. *Experimental Mechanics*, 51(4):479–490.
- [Leite et al., 2004] LEITE, J., SLOWIK, V. et MIHASHI, H. (2004). Computer simulation of fracture processes of concrete using mesolevel models of lattice structures. *Cement and concrete research*, 34(6):1025–1033.

- [Lilliu et van Mier, 2003] LILLIU, G. et van MIER, J. G. (2003). 3d lattice type fracture model for concrete. *Engineering Fracture Mechanics*, 70(7):927–941.
- [Lu et al., 2006] LU, S., LANDIS, E. et KEANE, D. (2006). X-ray microtomographic studies of pore structure and permeability in portland cement concrete. *Materials and structures*, 39(6):611–620.
- [Lucas et al., 1981] LUCAS, B. D., KANADE, T. et al. (1981). An iterative image registration technique with an application to stereo vision.
- [Lukic, 2018] LUKIC, B. (2018). *Mise au point d’une technique de mesure de champs pour la caractérisation du comportement dynamique du béton en traction*. Thèse de doctorat, Grenoble Alpes.
- [Malecot et al., 2019] MALECOT, Y., ZINGG, L., BRIFFAUT, M. et BAROTH, J. (2019). Influence of free water on concrete triaxial behavior: The effect of porosity. *Cement and Concrete Research*, 120:207–216.
- [Malhotra et Carino, 2003] MALHOTRA, V. M. et CARINO, N. J. (2003). *Handbook on nondestructive testing of concrete*. CRC press.
- [Man et van Mier, 2008] MAN, H.-K. et van MIER, J. G. (2008). Size effect on strength and fracture energy for numerical concrete with realistic aggregate shapes. *International journal of fracture*, 154(1-2):61–72.
- [Markovic et al., 2005] MARKOVIC, D., NIEKAMP, R., IBRAHIMBEGOVIĆ, A., MATTHIES, H. G. et TAYLOR, R. L. (2005). Multi-scale modeling of heterogeneous structures with inelastic constitutive behaviour: Part i–physical and mathematical aspects. *Engineering Computations*, 22(5/6):664–683.
- [Markowicz, 1993] MARKOWICZ, A. A. (1993). X-ray physics. *In Handbook of x-ray spectrometry: Methods and techniques*.
- [Masad, 2004] MASAD, E. (2004). X-ray computed tomography of aggregates and asphalt mixes. *Materials Evaluation*, 62(7):775–783.
- [Mehta, 1986] MEHTA, P. K. (1986). *Concrete. structure, properties and materials*.
- [Moës et al., 2003] MOËS, N., CLOIREC, M., CARTRAUD, P. et REMACLE, J.-F. (2003). A computational approach to handle complex microstructure geometries. *Computer Methods in Applied Mechanics and Engineering*, 192(28):3163 – 3177. Multiscale Computational Mechanics for Materials and Structures.
- [Moës et al., 1999] MOËS, N., DOLBOW, J. et BELYTSCHKO, T. (1999). A finite element method for crack growth without remeshing. *International Journal for Numerical Methods in Engineering*.
- [Mukunoki et al., 2004] MUKUNOKI, T., OTANI, J., OBARA, Y. et KANEKO, K. (2004). Soils artifacts of x-ray ct data in the analysis of geomaterial properties. *In Xray CT for Geomaterials*, pages 106–113. CRC Press.
- [Needleman, 1988] NEEDLEMAN, A. (1988). Material rate dependence and mesh sensitivity in localization problems. *Computer methods in applied mechanics and engineering*, 67(1):69–85.

- [Neville *et al.*, 1995] NEVILLE, A. M. *et al.* (1995). *Properties of concrete*, volume 4. longman London.
- [Nguyen *et al.*, 2016] NGUYEN, T. T., YVONNET, J., BORNERT, M. et CHATEAU, C. (2016). Initiation and propagation of complex 3d networks of cracks in heterogeneous quasi-brittle materials: Direct comparison between in situ testing-microct experiments and phase field simulations. *Journal of the Mechanics and Physics of Solids*, 95:320–350.
- [Nitka et Tejchman, 2018] NITKA, M. et TEJCHMAN, J. (2018). A three-dimensional meso-scale approach to concrete fracture based on combined dem with x-ray μ ct images. *Cement and Concrete Research*, 107:11–29.
- [Obara *et al.*, 2016] OBARA, Y., TANIKURA, I., JUNG, J., SHINTANI, R. et WATANABE, S. (2016). Evaluation of micro-damage of concrete specimens under cyclic uniaxial loading by x-ray ct method. *Journal of Advanced Concrete Technology*, 14(8):433–443.
- [Oliver, 1989] OLIVER, J. (1989). A consistent characteristic length for smeared cracking models. *International Journal for Numerical Methods in Engineering*, 28(2):461–474.
- [Oliver, 1996] OLIVER, J. (1996). Modelling strong discontinuities in solid mechanics via strain softening constitutive equations. *International Journal for Numerical Methods in Engineering*.
- [Oliver, 2000] OLIVER, J. (2000). On the discrete constitutive models induced by strong discontinuity kinematics and continuum constitutive equations. *International Journal of Solids and Structures*, 37(48):7207 – 7229.
- [Oliver *et al.*, 2006] OLIVER, J., HUESPE, A. E. et SÁNCHEZ, P. J. (2006). A comparative study on finite elements for capturing strong discontinuities: E-fem vs x-fem. *Computer methods in applied mechanics and engineering*, 195(37-40):4732–4752.
- [Ortiz *et al.*, 1987] ORTIZ, M., LEROY, Y. et NEEDLEMAN, A. (1987). A finite element method for localized failure analysis. *Computer methods in applied mechanics and engineering*, 61(2):189–214.
- [Pan *et al.*, 2014] PAN, B., WANG, B., WU, D. et LUBINEAU, G. (2014). An efficient and accurate 3d displacements tracking strategy for digital volume correlation. *Optics and Lasers in Engineering*, 58:126–135.
- [Peerlings *et al.*, 1996] PEERLINGS, R. H., BORST, R. d., BREKELMANS, W. A., VREE, J. H. et SPEE, I. (1996). Some observations on localization in non-local and gradient damage models. *European Journal of Mechanics, A/Solids*, 15(6):937–953.
- [Perona et Malik, 1990] PERONA, P. et MALIK, J. (1990). Scale-space and edge detection using anisotropic diffusion. *IEEE Transactions on pattern analysis and machine intelligence*, 12(7):629–639.
- [Peters et Ranson, 1982] PETERS, W. et RANSON, W. (1982). Digital imaging techniques in experimental stress analysis. *Optical engineering*, 21(3):213427.
- [Pietruszczak et Mroz, 1981] PIETRUSZCZAK, S. et MROZ, Z. (1981). Finite element analysis of deformation of strain-softening materials. *International Journal for Numerical Methods in Engineering*, 17(3):327–334.

- [Pijaudier-Cabot et Bažant, 1987] PIJAUDIER-CABOT, G. et BAŽANT, Z. P. (1987). Non-local damage theory. *Journal of engineering mechanics*, 113(10):1512–1533.
- [Piotrowska, 2013] PIOTROWSKA, E. (2013). *Role of coarse aggregates in the triaxial behavior of concrete: experimental and numerical*. Thèse de doctorat, PhD thesis, L’Université de Grenoble.
- [Poinard *et al.*, 2012] POINARD, C., PIOTROWSKA, E., MALECOT, Y., DAUDEVILLE, L. et LANDIS, E. N. (2012). Compression triaxial behavior of concrete: the role of the mesostructure by analysis of x-ray tomographic images. *European Journal of Environmental and Civil Engineering*, 16(sup1):s115–s136.
- [Poinard *et al.*, 2011] POINARD, C., PIOTROWSKA, E., MARIN, P., MALECOT, Y. et DAUDEVILLE, L. (2011). Mesoscopic scale modeling of concrete under triaxial loading using x-ray tomographic images. *2nd International Conference on Particle-Based Methods - Fundamentals and Applications (Particles) Location: Barcelona, SPAIN Date: OCT 26-28, 2011 Sponsor(s):Tech Unive Catalonia; Swansea Univ; European Community Computat Methods Appl Sci (ECCOMAS); Int Assoc Computat Mech (IACM)*, pages 117–129.
- [Pontiroli *et al.*, 2010] PONTIROLI, C., ROUQUAND, A. et MAZARS, J. (2010). Predicting concrete behaviour from quasi-static loading to hypervelocity impact: an overview of the prm model. *European Journal of Environmental and Civil Engineering*, 14(6-7):703–727.
- [Radon, 1917] RADON, J. (1917). über die bestimmung von funktionen durch ihre integralwerte längs gewisser mannigfaltigkeiten. *Mathematisch-Physische Klasse*, 69:262–277.
- [Rannou *et al.*, 2010] RANNOU, J., LIMODIN, N., RÉTHORÉ, J., GRAVOUIL, A., LUDWIG, W., BAÏETTO-DUBOURG, M.-C., BUFFIERE, J.-Y., COMBESURE, A., HILD, F. et ROUX, S. (2010). Three dimensional experimental and numerical multiscale analysis of a fatigue crack. *Computer methods in applied mechanics and engineering*, 199(21-22):1307–1325.
- [Ren *et al.*, 2015] REN, W., YANG, Z., SHARMA, R., ZHANG, C. et WITHERS, P. J. (2015). Two-dimensional x-ray ct image based meso-scale fracture modelling of concrete. *Engineering Fracture Mechanics*, 133:24–39.
- [Réthoré *et al.*, 2011] RÉTHORÉ, J., LIMODIN, N., BUFFIERE, J.-Y., HILD, F., LUDWIG, W. et ROUX, S. (2011). Digital volume correlation analyses of synchrotron tomographic images. *The Journal of Strain Analysis for Engineering Design*, 46(7):683–695.
- [Reynouard *et al.*, 2010] REYNOUARD, J.-M., PIJAUDIER-CABOT, G. et TORRENTI, J.-M. (2010). *Mechanical behavior of concrete*. Wiley, New-York.
- [Roubin, 2013] ROUBIN, E. (2013). *Meso-scale FE and morphological modeling of heterogeneous media : applications to cementitious materials ”*. Theses, École normale supérieure de Cachan - ENS Cachan.
- [Roubin *et al.*, 2019] ROUBIN, E., ANDO, E. et ROUX, S. (2019). The colours of concrete as seen by x-rays and neutrons. *Cement and Concrete Composites*, page 103336.

-
- [Roubin *et al.*, 2015a] ROUBIN, E., COLLIAT, J.-B. et BENKEMOUN, N. (2015a). Meso-scale modeling of concrete: A morphological description based on excursion sets of random fields. *Computational Materials Science*, 102(Supplement C):183 – 195.
- [Roubin *et al.*, 2015b] ROUBIN, E., VALLADE, A., BENKEMOUN, N. et COLLIAT, J.-B. (2015b). Multi-scale failure of heterogeneous materials: A double kinematics enhancement for Embedded Finite Element Method. *International Journal of Solids and Structures*.
- [Roux et Hild, 2006] ROUX, S. et HILD, F. (2006). Stress intensity factor measurements from digital image correlation: post-processing and integrated approaches. *International journal of fracture*, 140(1-4):141–157.
- [Roux *et al.*, 2008] ROUX, S., HILD, F., VIOT, P. et BERNARD, D. (2008). Three-dimensional image correlation from x-ray computed tomography of solid foam. *Composites Part A: Applied science and manufacturing*, 39(8):1253–1265.
- [Salvatore *et al.*, 2016] SALVATORE, E., ANDÒ, E., MODONI, G. et VIGGIANI, G. (2016). Micromechanical study of cyclically loaded sands with x-ray microtomography and digital image correlation. *Procedia Engineering*, 158:92–97.
- [Salvo *et al.*, 2003] SALVO, L., CLOETENS, P., MAIRE, E., ZABLER, S., BLANDIN, J. J., BUFFIÈRE, J.-Y., LUDWIG, W., BOLLER, E., BELLET, D. et JOSSEROND, C. (2003). X-ray micro-tomography an attractive characterisation technique in materials science. *Nuclear instruments and methods in physics research section B: Beam interactions with materials and atoms*, 200:273–286.
- [Sandler et Wright, 1984] SANDLER, I. et WRIGHT, J. (1984). *Theoretical Foundations for Large Scale Computations of Nonlinear Material Behavior*. Martinus Nijhoff, Netherlands.
- [Schlangen, 2008] SCHLANGEN, E. (2008). Crack development in concrete, part 1: Fracture experiments and ct-scan observations. *In Key Engineering Materials*, volume 385, pages 69–72. Trans Tech Publ.
- [Schlangen et Van Mier, 1992] SCHLANGEN, E. et VAN MIER, J. (1992). Simple lattice model for numerical simulation of fracture of concrete materials and structures. *Materials and Structures*, 25(9):534–542.
- [Schreier *et al.*, 2000] SCHREIER, H. W., BRAASCH, J. R. et SUTTON, M. A. (2000). Systematic errors in digital image correlation caused by intensity interpolation. *Optical engineering*, 39.
- [Schreier et Sutton, 2002] SCHREIER, H. W. et SUTTON, M. A. (2002). Systematic errors in digital image correlation due to undermatched subset shape functions. *Experimental Mechanics*, 42(3):303–310.
- [Serra, 1983] SERRA, J. (1983). *Image analysis and mathematical morphology*. Academic Press, Inc.
- [Simo et Oliver, 1994] SIMO, J. et OLIVER, J. (1994). A new approach to the analysis and simulation of strain softening in solids. *Fracture and damage in quasibrittle structures*, pages 25–39.

- [Simo *et al.*, 1993] SIMO, J. C., OLIVER, J. et ARMERO, F. (1993). An analysis of strong discontinuities induced by strain-softening in rate-independent inelastic solids. *Computational mechanics*, 12(5):277–296.
- [Stamati *et al.*, 2020] STAMATI, O., ANDÒ, E., ROUBIN, E., CAILLETAUD, R., WIEBICKE, M., PINZON, G., COUTURE, C., HURLEY, R. C., CAULK, R., CAILLERIE, D., MATSUSHIMA, T., BÉSUELLE, P., BERTONI, F., ARNAUD, T., LABORIN, A. O., RORATO, R., SUN, Y., TENGATTINI, A., OKUBADEJO, O., COLLIAT, J.-B., SAADATFAR, M., GARCIA, F. E., PAPAZOGLU, C., VEGO, I., BRISARD, S., DIJKSTRA, J. et BIRMPILIS, G. (2020). ‘spam’: Software for practical analysis of materials. *Journal of Open Source Software*, 5(51):2286.
- [Stamati *et al.*, 2019] STAMATI, O., ROUBIN, E., ANDÒ, E. et MALECOT, Y. (2019). Tensile failure of micro-concrete: from mechanical tests to fe meso-model with the help of x-ray tomography. *Meccanica*, 54(4-5):707–722.
- [Stamati *et al.*, 2018] STAMATI, O., ROUBIN, E., ANDÒ, E. et MALECOT, Y. (2018). Phase segmentation of concrete x-ray tomographic images at meso-scale: Validation with neutron tomography. *Cement and Concrete Composites*, 88:8 – 16.
- [Stock *et al.*, 2002] STOCK, S. R., NAIK, N., WILKINSON, A. et KURTIS, K. (2002). X-ray microtomography (microct) of the progression of sulfate attack of cement paste. *Cement and Concrete Research*, 32(10):1673–1675.
- [Suchorzewski *et al.*, 2017] SUCHORZEWSKI, J., TEJCHMAN, J. et NITKA, M. (2017). Discrete element method simulations of fracture in concrete under uniaxial compression based on its real internal structure. *International Journal of Damage Mechanics*, page 1056789517690915.
- [Sukumar *et al.*, 2001] SUKUMAR, N., CHOPP, D. L., MOËS, N. et BELYTSHKO, T. (2001). Modelling holes and inclusions by level sets in the extended finite element method. *Computer Methods in Applied Mechanics and Engineering*.
- [Sutton *et al.*, 1983] SUTTON, M., WOLTERS, W., PETERS, W., RANSON, W. et MCNEILL, S. (1983). Determination of displacements using an improved digital correlation method. *Image and vision computing*, 1(3):133–139.
- [Sutton *et al.*, 2009] SUTTON, M. A., ORTEU, J. J. et SCHREIER, H. (2009). *Image correlation for shape, motion and deformation measurements: basic concepts, theory and applications*. Springer Science & Business Media.
- [Suzuki *et al.*, 2010] SUZUKI, T., AOKI, M. et OHTSU, M. (2010). Damage identification of cracked concrete by x-ray computed tomography method. *Proceedings of FraMCoS-7*, pages 1143–1148.
- [Taylor, 1987] TAYLOR, R. L. (1987). *FEAP-ein finite element analysis programm*. Ing.-Gemeinschaft Klee & Wrigges.
- [Tejchman *et al.*, 2010] TEJCHMAN, J. *et al.* (2010). Calculations of fracture process zones on meso-scale in notched concrete beams subjected to three-point bending. *European Journal of Mechanics-A/Solids*, 29(4):746–760.

- [Trtik *et al.*, 2011] TRTIK, P., MÜNCH, B., WEISS, W. J., KAESTNER, A., JERJEN, I., JOSIC, L., LEHMANN, E. et LURA, P. (2011). Release of internal curing water from lightweight aggregates in cement paste investigated by neutron and x-ray tomography. *Nuclear Instruments and Methods in Physics Research Section A: Accelerators, Spectrometers, Detectors and Associated Equipment*, 651(1):244–249.
- [Tudisco *et al.*, 2017] TUDISCO, E., JAILIN, C., MENDOZA, A., TENGATTINI, A., ANDÒ, E., HALL, S. A., VIGGIANI, G., HILD, F. et ROUX, S. (2017). An extension of digital volume correlation for multimodality image registration. *Measurement Science and Technology*, 28(9):095401.
- [Vallade, 2016a] VALLADE, A. (2016a). *Modélisation multi-échelles des shales: influence de la microstructure sur les propriétés macroscopiques et le processus de fracturation*. Thèse de doctorat, Lille 1.
- [Vallade, 2016b] VALLADE, A. (2016b). *Modélisation multi-échelles des shales : influence de la microstructure sur les propriétés macroscopiques et le processus de fracturation*. Thèse de doctorat. Thèse de doctorat dirigée par Shao, Jianfu et Colliat, Jean-Baptiste Génie civil Lille 1 2016.
- [Vu, 2007] VU, X. H. (2007). *Caractérisation expérimentale du béton sous fort confinement: influences du degré de saturation et du rapport eau/ciment*. Thèse de doctorat.
- [Vu *et al.*, 2011] VU, X. H., DAUDEVILLE, L. et MALECOT, Y. (2011). Effect of coarse aggregate size and cement paste volume on concrete behavior under high triaxial compression loading. *Construction and Building Materials*, 25(10):3941–3949.
- [Vu *et al.*, 2009] VU, X. H., MALECOT, Y., DAUDEVILLE, L. et BUZAUD, E. (2009). Effect of the water/cement ratio on concrete behavior under extreme loading. *International Journal for Numerical and Analytical Methods in Geomechanics*, 33(17):1867–1888.
- [Wang *et al.*, 2014] WANG, H., HUANG, Z., LI, L., YOU, Z. et CHEN, Y. (2014). Three-dimensional modeling and simulation of asphalt concrete mixtures based on x-ray ct microstructure images. *Journal of Traffic and Transportation Engineering (English Edition)*, 1(1):55–61.
- [Wang *et al.*, 2003] WANG, L., FROST, J., VOYIADJIS, G. et HARMAN, T. (2003). Quantification of damage parameters using x-ray tomography images. *Mechanics of Materials*, 35(8):777–790.
- [Wang *et al.*, 2015] WANG, X., YANG, Z. J., YATES, J., JIVKOV, A. et ZHANG, C. (2015). Monte carlo simulations of mesoscale fracture modelling of concrete with random aggregates and pores. *Construction and Building Materials*, 75:35–45.
- [Wang *et al.*, 1999] WANG, Z., KWAN, A. et CHAN, H. (1999). Mesoscopic study of concrete i: generation of random aggregate structure and finite element mesh. *Computers & structures*, 70(5):533–544.
- [Weerheijm, 2013] WEERHEIJM, J. (2013). *Understanding the tensile properties of concrete*. Elsevier.

- [Wells et Sluys, 2001] WELLS, G. et SLUYS, L. (2001). Three-dimensional embedded discontinuity model for brittle fracture. *International Journal of Solids and Structures*, 38(5):897–913.
- [Wiebicke *et al.*, 2019] WIEBICKE, M., ANDÒ, E., ŠMILAUER, V., HERLE, I. et VIGGIANI, G. (2019). A benchmark strategy for the experimental measurement of contact fabric. *Granular Matter*, 21(3):54.
- [Wilson, 1974] WILSON, E. L. (1974). The static condensation algorithm. *International Journal for Numerical Methods in Engineering*, 8(1):198–203.
- [Wittmann *et al.*, 1985] WITTMANN, F., ROELFSTRA, P. et SADOUKI, H. (1985). Simulation and analysis of composite structures. *Materials science and engineering*, 68(2):239–248.
- [Wriggers et Moftah, 2006] WRIGGERS, P. et MOFTAH, S. (2006). Mesoscale models for concrete: Homogenisation and damage behaviour. *Finite elements in analysis and design*, 42(7):623–636.
- [Yang *et al.*, 2017] YANG, Z., REN, W., SHARMA, R., McDONALD, S., MOSTAFAVI, M., VERTYAGINA, Y. et MARROW, T. (2017). In-situ x-ray computed tomography characterisation of 3d fracture evolution and image-based numerical homogenisation of concrete. *Cement and Concrete Composites*, 75:74–83.
- [Yang *et al.*, 2009] YANG, Z., SU, X., CHEN, J. et LIU, G. (2009). Monte carlo simulation of complex cohesive fracture in random heterogeneous quasi-brittle materials. *International Journal of Solids and Structures*, 46(17):3222–3234.
- [Yu *et al.*, 2018] YU, Q., LIU, H., YANG, T. et LIU, H. (2018). 3d numerical study on fracture process of concrete with different itz properties using x-ray computerized tomography. *International Journal of Solids and Structures*, 147:204 – 222.
- [Zaitsev et Wittmann, 1981] ZAITSEV, Y. et WITTMANN, F. (1981). Simulation of crack propagation and failure of concrete. *Materiaux et Construction*, 14(5):357–365.
- [Zaitsev, 1985] ZAITSEV, Y. V. (1985). Inelastic properties of solids with random cracks. *In Mechanics of geomaterials*, pages 89–128. Wiley Chicester.
- [Zingg, 1935] ZINGG, T. (1935). Beitrag zur schotteranalyse: Schweizerische mineralogische und petrologische mitteilungen, v. 15.

Appendix A

Technical drawings of the 7075 T6 aluminium alloy cell

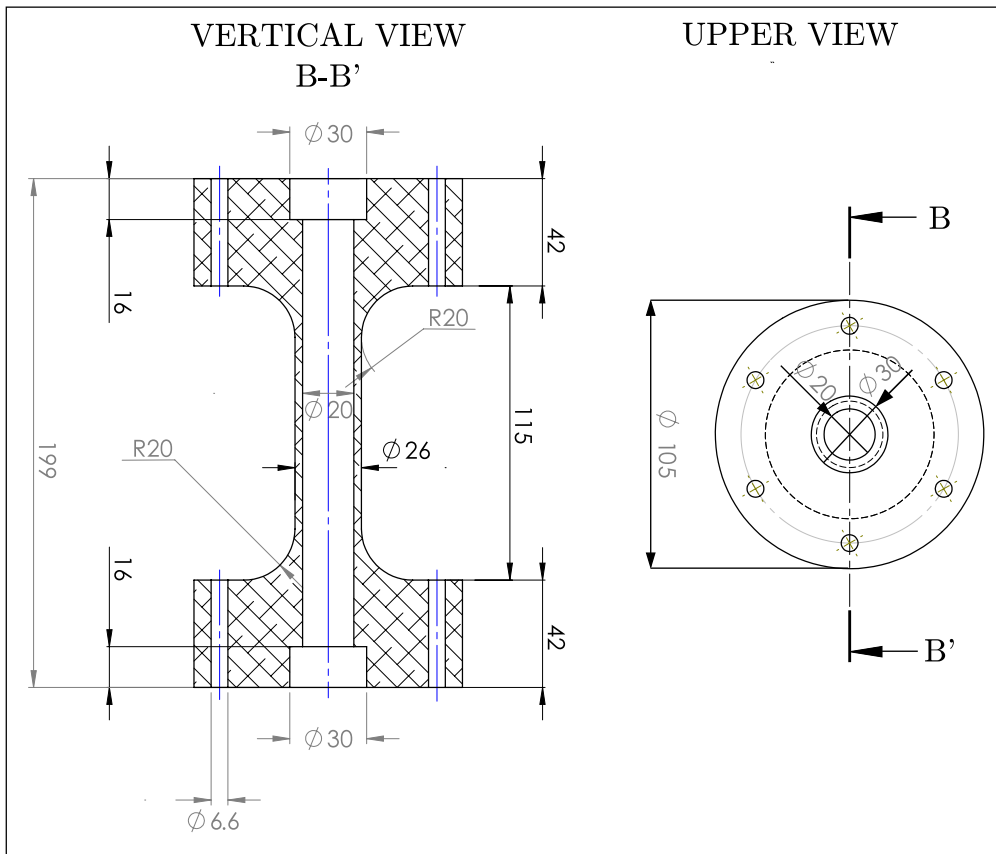


Figure A.1: Vertical and upper view of the cell

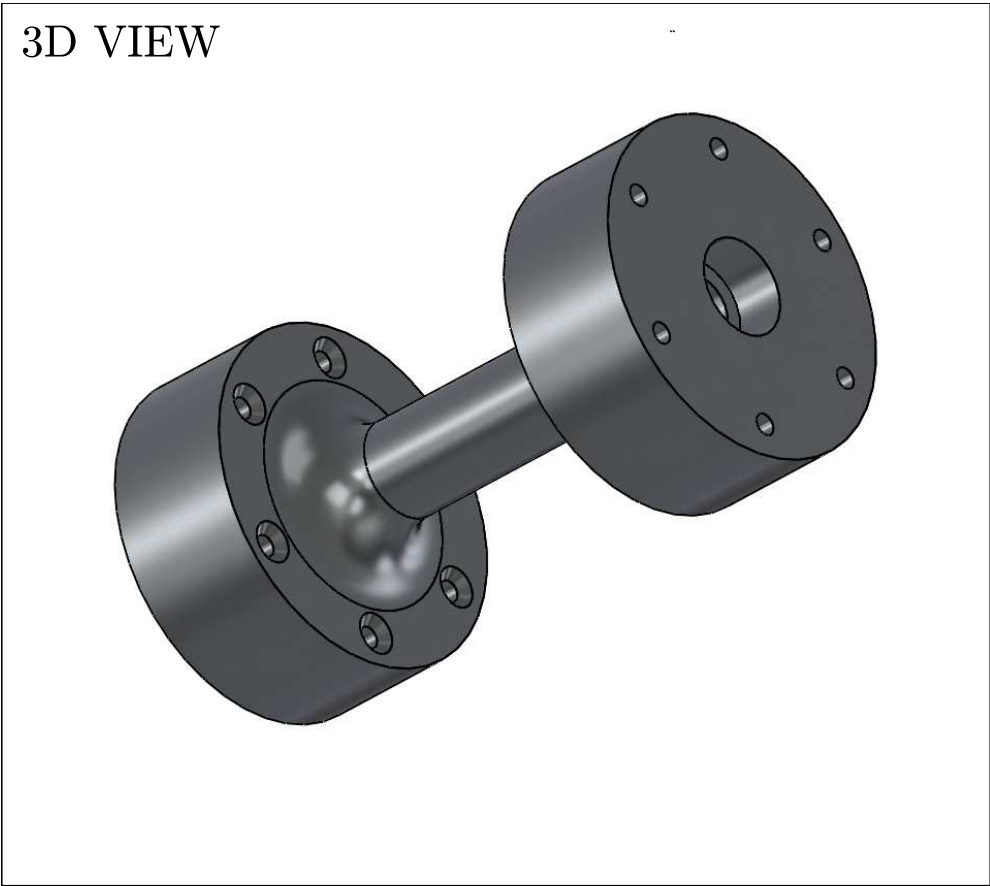


Figure A.2: 3D view of the cell

Appendix B

Mechanical tests outside of the x-ray cabin

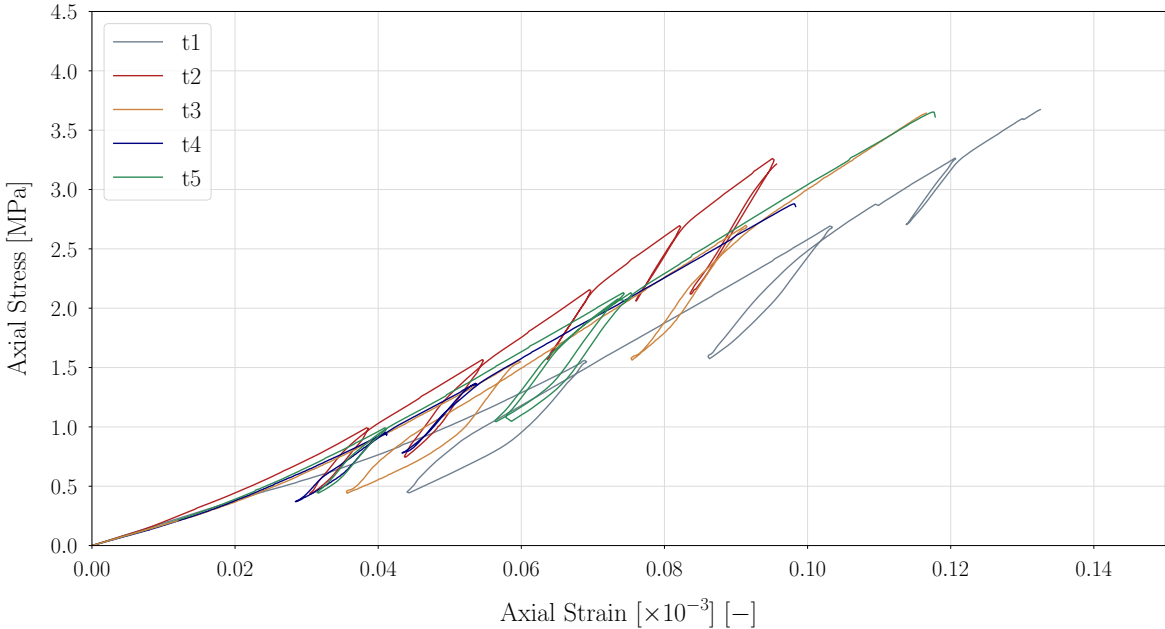


Figure B.1: Macroscopic responses of preliminary uniaxial tension tests outside the x-ray cabin

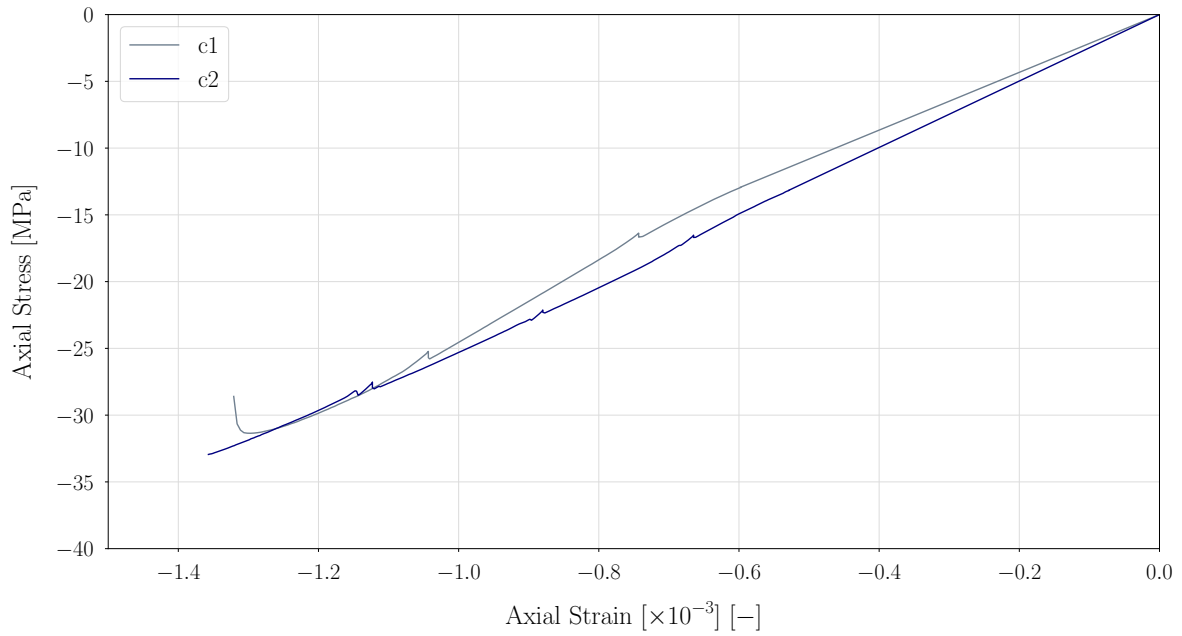


Figure B.2: Macroscopic responses of preliminary uniaxial compression tests outside the x-ray cabin

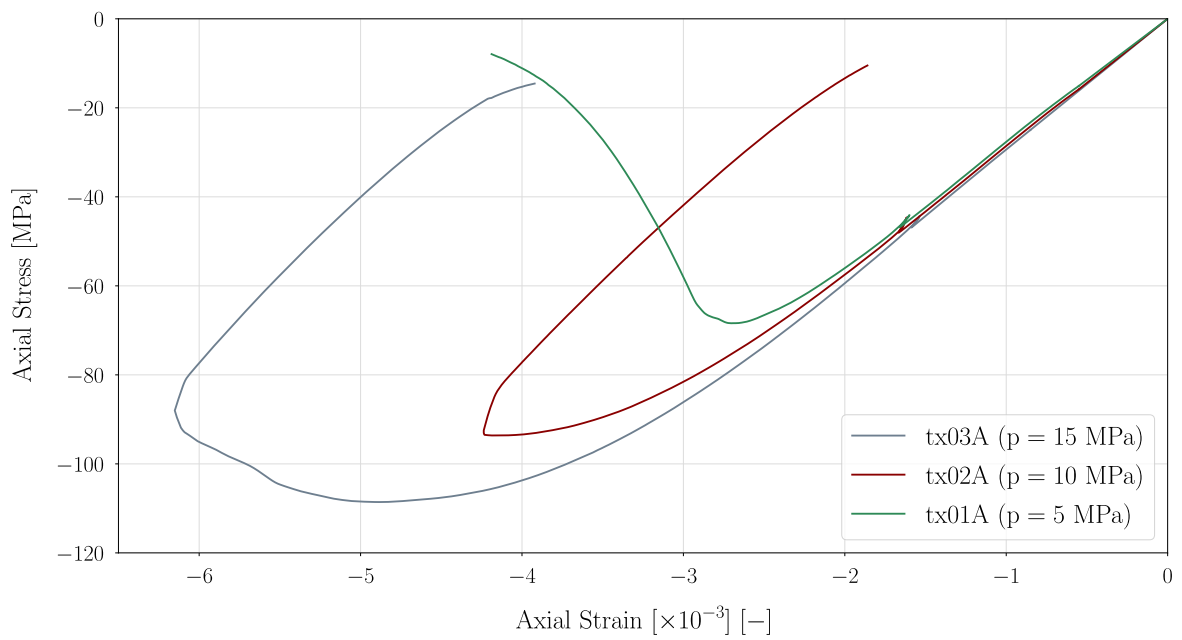


Figure B.3: Macroscopic responses of preliminary triaxial compression tests outside the x-ray cabin